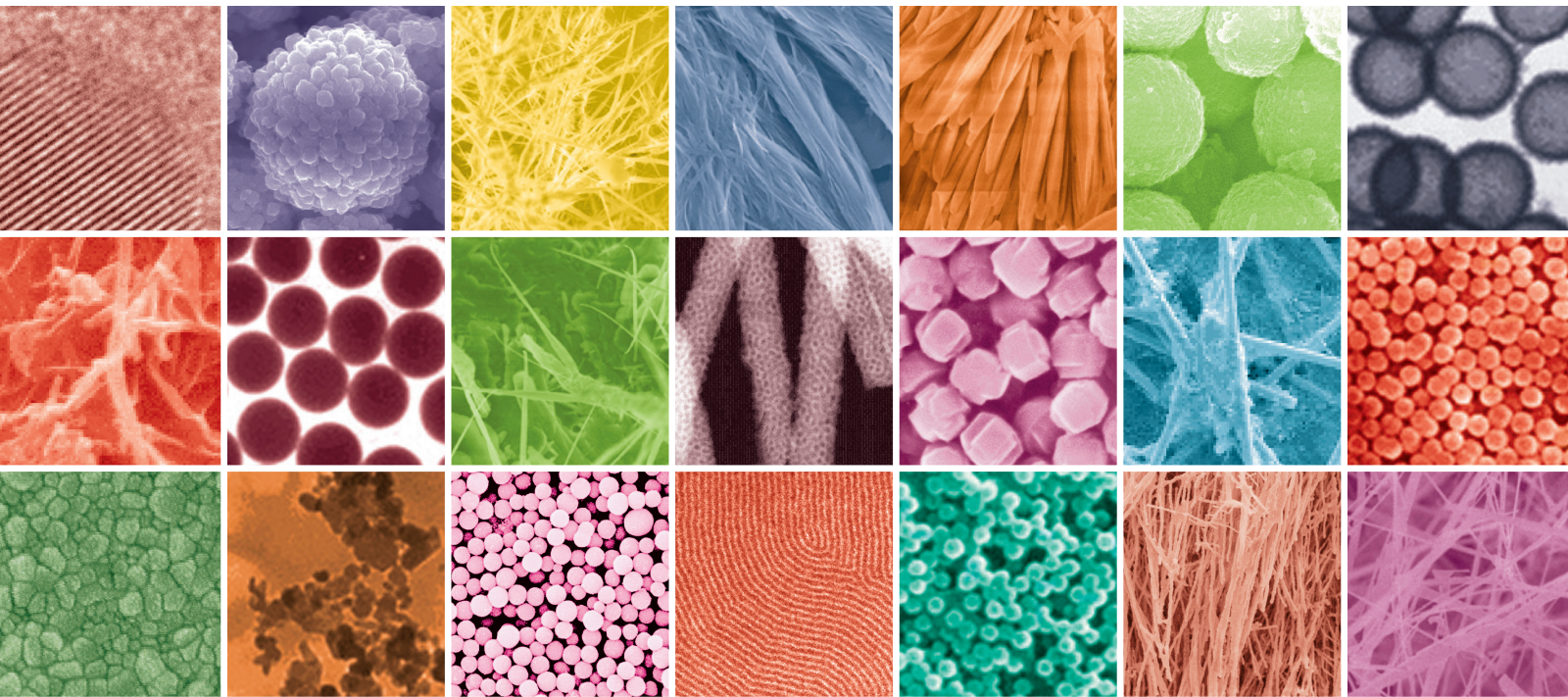


Chemical Functionalization, Self-Assembly, and Applications of Nanomaterials and Nanocomposites 2014

Guest Editors: Xingbin Yan, Tifeng Jiao, Lavinia Balan, Xinqing Chen,
Michael Z. Hu, and Wenwen Liu





**Chemical Functionalization, Self-Assembly,
and Applications of Nanomaterials
and Nanocomposites 2014**

Journal of Nanomaterials

**Chemical Functionalization, Self-Assembly,
and Applications of Nanomaterials
and Nanocomposites 2014**

Guest Editors: Xingbin Yan, Tifeng Jiao, Lavinia Balan,
Xinqing Chen, Michael Z. Hu, and Wenwen Liu



Copyright © 2015 Hindawi Publishing Corporation. All rights reserved.

This is a special issue published in "Journal of Nanomaterials." All articles are open access articles distributed under the Creative Commons Attribution License, which permits unrestricted use, distribution, and reproduction in any medium, provided the original work is properly cited.

Editorial Board

- Domenico Acierno, Italy
Katerina Aifantis, USA
Sheikh Akbar, USA
Nageh K. Allam, USA
Margarida Amaral, Portugal
Raul Arenal, Spain
Ilaria Armentano, Italy
Lavinia Balan, France
Thierry Baron, France
Andrew R. Barron, USA
Hongbin Bei, USA
Stefano Bellucci, Italy
Enrico Bergamaschi, Italy
Debes Bhattacharyya, New Zealand
Giovanni Bongiovanni, Italy
Theodorian Borca-Tasciuc, USA
Mohamed Bououdina, Bahrain
Torsten Brezesinski, Germany
C. Jeffrey Brinker, USA
Christian Brosseau, France
Yibing Cai, China
Chuanbao Cao, China
Victor M. Castaño, Mexico
Albano Cavaleiro, Portugal
Bhanu P. S. Chauhan, USA
Wei Chen, China
Yuan Chen, Singapore
Tupei Chen, Singapore
Shafiul Chowdhury, USA
Kwang-Leong Choy, UK
Jin-Ho Choy, Korea
Yu-Lun Chueh, Taiwan
Elisabetta Comini, Italy
Giuseppe Compagnini, Italy
David Cornu, France
Miguel A. Correa-Duarte, Spain
P. Davide Cozzoli, Italy
Majid Darroudi, Iran
Shadi A. Dayeh, USA
Luca Deseri, USA
Yong Ding, USA
Bin Dong, China
Zehra Durmus, Turkey
Joydeep Dutta, Oman
Ali Eftekhari, USA
Samy El-Shall, USA
Farid El-Tantawy, Egypt
Ovidiu Ersen, France
Claude Estournès, France
Andrea Falqui, Saudi Arabia
Xiaosheng Fang, China
Bo Feng, China
Matteo Ferroni, Italy
Wolfgang Fritzsche, Germany
Alan Fuchs, USA
Peng Gao, China
Miguel A. Garcia, Spain
Siddhartha Ghosh, Singapore
P. K. Giri, India
Russell E. Gorga, USA
Jihua Gou, USA
Jean M. Greneche, France
Changzhi Gu, China
Lin Guo, China
John Zhanhu Guo, USA
Smrati Gupta, Germany
Kimberly Hamad-Schifferli, USA
Michael Harris, USA
Jr-Hau He, Taiwan
Nguyen D. Hoa, Vietnam
Michael Z. Hu, USA
Nay Ming Huang, Malaysia
Qing Huang, China
Shaoming Huang, China
David Hui, USA
Zafar Iqbal, USA
Balachandran Jeyadevan, Japan
Xin Jiang, Germany
Rakesh Joshi, Australia
Myung-Hwa Jung, Korea
Jeong-won Kang, Korea
Hassan Karimi-Maleh, Iran
Antonios Kelarakis, UK
Alireza Khataee, Iran
Ali Khorsand Zak, Iran
Wonbaek Kim, Korea
Dojin Kim, Korea
Philippe Knauth, France
Ralph Krupke, Germany
Christian Kbel, Germany
Sushil Kumar, India
Sanjeev Kumar, India
Prashant Kumar, UK
Subrata Kundu, India
Michele Laus, Italy
Eric Le Bourhis, France
Burtrand Lee, USA
Jun Li, Singapore
Shijun Liao, China
Meiyong Liao, Japan
Silvia Licocchia, Italy
Wei Lin, USA
Jun Liu, USA
Zainovia Lockman, Malaysia
Songwei Lu, USA
Jue Lu, USA
Ed Ma, USA
Malik Maaza, South Africa
Lutz Mdlar, Germany
Gaurav Mago, USA
Morteza Mahmoudi, Iran
Mohammad A. Malik, UK
Devanesan Mangalaraj, India
Sanjay R. Mathur, Germany
Paulo Cesar Morais, Brazil
Mahendra A. More, India
Paul Munroe, Australia
Jae-Min Myoung, Korea
Rajesh R. Naik, USA
Albert Nasibulin, Russia
Toshiaki Natsuki, Japan
Koichi Niihara, Japan
Sherine Obare, USA
Won-Chun Oh, Republic of Korea
Atsuto Okamoto, Japan
Abdelwahab Omri, Canada
Ungyu Paik, Republic of Korea
Edward A. Payzant, USA
Ton Peijs, UK
Oscar Perales-Prez, Puerto Rico
Wenxiu Que, China
Peter Reiss, France
Orlando Rojas, USA
Marco Rossi, Italy
Cengiz S. Ozkan, USA

Vladimir epelk, Germany
Huaiyu Shao, Japan
Prashant Sharma, USA
Donglu Shi, USA
Bhanu P. Singh, India
Surinder Singh, USA
Vladimir Sivakov, Germany
Yanlin Song, China
Ashok Sood, USA
Marinella Striccoli, Italy
Xuping Sun, Saudi Arabia
Jing Sun, China
Ashok K. Sundramoorthy, USA
Nyan-Hwa Tai, Taiwan

Bo Tan, Canada
Ion Tiginyanu, Moldova
Valeri P. Tolstoy, Russia
Muhammet S. Toprak, Sweden
Ramon Torrecillas, Spain
Takuya Tsuzuki, Australia
Tamer Uyar, Turkey
Bala Vaidhyanathan, UK
Luca Valentini, Italy
Rajender S. Varma, USA
Antonio Villaverde, Spain
Ajayan Vinu, Australia
Shiren Wang, USA
Yong Wang, USA

Ruibing Wang, Macau
Magnus Willander, Sweden
Ping Xiao, UK
Zhi Li Xiao, USA
Shuangxi Xing, China
Yangchuan Xing, USA
Doron Yadlovker, Israel
Piaoping Yang, China
Yoke K. Yap, USA
Ramin Yousefi, Iran
William W. Yu, USA
Kui Yu, Canada
Renyun Zhang, Sweden

Contents

Chemical Functionalization, Self-Assembly, and Applications of Nanomaterials and Nanocomposites 2014, Xingbin Yan, Tifeng Jiao, Lavinia Balan, Xinqing Chen, Michael Z. Hu, and Wenwen Liu
Volume 2015, Article ID 953926, 1 page

The Structural and Magnetic Properties of Gadolinium Doped CoFe_2O_4 Nanoferrites, Qing Lin, Jinpei Lin, Yun He, Ruijun Wang, and Jianghui Dong
Volume 2015, Article ID 294239, 6 pages

The Gelation Ability and Morphology Study of Organogel System Based on Calamitic Hydrazide Derivatives, Xia Ran, Lili Shi, Kun Zhang, Jie Lou, Bo Liu, and Lijun Guo
Volume 2015, Article ID 357875, 6 pages

Experiment Investigation on Fretting Wear and Wear Debris Performance for the Stem-Cement Interface, Lanfeng Zhang, Shirong Ge, and Hongtao Liu
Volume 2015, Article ID 945259, 14 pages

Ball Milling to Build the Hybrid Mesocrystals of Ibuprofen and Aragonite, Kyoung A Cho, Insil Choi, and Il Won Kim
Volume 2015, Article ID 163190, 9 pages

A Novel Porous Carrier Found in Nature for Nanocomposite Materials Preparation: A Case Study of *Artemia* Egg Shell-Supported TiO_2 for Formaldehyde Removal, Sufeng Wang, Fengjing Lv, Tifeng Jiao, Jingfen Ao, Xiaochun Zhang, and Fengdan Jin
Volume 2015, Article ID 963012, 6 pages

Preparation and Investigation of the Microtribological Properties of Graphene Oxide and Graphene Films via Electrostatic Layer-by-Layer Self-Assembly, Yongshou Hu, Haibing Ma, Wei Liu, Qianqian Lin, and Bin Liu
Volume 2015, Article ID 282369, 8 pages

Fluorescent Gold Nanoclusters: Synthesis and Recent Biological Application, Xiaochao Qu, Yichen Li, Lei Li, Yanran Wang, Jingning Liang, and Jimin Liang
Volume 2015, Article ID 784097, 23 pages

Mössbauer Spectroscopy, Structural and Magnetic Studies of Zn^{2+} Substituted Magnesium Ferrite Nanomaterials Prepared by Sol-Gel Method, Yun He, Xingxing Yang, Jinpei Lin, Qing Lin, and Jianghui Dong
Volume 2015, Article ID 854840, 8 pages

Morphological Investigation of Calcium Carbonate during Ammonification-Carbonization Process of Low Concentration Calcium Solution, Huaigang Cheng, Xiaoxi Zhang, and Huiping Song
Volume 2014, Article ID 503696, 7 pages

Gold Nanoparticles: Synthesis, Stability Test, and Application for the Rice Growth, Aiwu Wang, Hoi Pong Ng, Yi Xu, Yuyu Li, Yuhong Zheng, Jingping Yu, Fugui Han, Feng Peng, and Li Fu
Volume 2014, Article ID 451232, 6 pages

Synthesis and Catalytic Performance of Graphene Modified $\text{CuO-ZnO-Al}_2\text{O}_3$ for CO_2 Hydrogenation to Methanol, Zheng-juan Liu, Xing-jiang Tang, Shan Xu, and Xiao-lai Wang
Volume 2014, Article ID 690514, 6 pages



Study on Thermal Insulation Zeolite by Coal Fly Ash, Huiping Song, Nan Zheng, Fangbin Xue,
and Fangqin Cheng

Volume 2014, Article ID 875940, 6 pages

Editorial

Chemical Functionalization, Self-Assembly, and Applications of Nanomaterials and Nanocomposites 2014

**Xingbin Yan,¹ Tifeng Jiao,² Lavinia Balan,³ Xinqing Chen,⁴
Michael Z. Hu,⁵ and Wenwen Liu⁶**

¹Laboratory of Clean Energy Chemistry and Materials and State Key Laboratory of Solid Lubrication, Lanzhou Institute of Chemical Physics, Chinese Academy of Sciences, Lanzhou 730000, China

²School of Environmental and Chemical Engineering, Yanshan University, Qinhuangdao 066004, China

³Institute of Materials Science of Mulhouse (IS2M), rue Jean Starcky, BP 2488, 68057 Mulhouse Cedex, France

⁴Department of Chemical and Biomolecular Engineering, Hong Kong University of Science and Technology, Clear Water Bay, Kowloon 00852, Hong Kong

⁵Energy and Transportation Science Division, Oak Ridge National Laboratory, Oak Ridge, TN 37831, USA

⁶School of Electrical and Electronic Engineering, Nanyang Technological University, Singapore 639798

Correspondence should be addressed to Xingbin Yan; xbyan@licp.cas.cn

Received 10 March 2015; Accepted 10 March 2015

Copyright © 2015 Xingbin Yan et al. This is an open access article distributed under the Creative Commons Attribution License, which permits unrestricted use, distribution, and reproduction in any medium, provided the original work is properly cited.

The growing interests in nanomaterials and nanocomposites call for the development of processing techniques to obtain multiple functionalization nanostructures and achieve the tailoring of specific features of the nanometer size. Functional nanomaterials and nanocomposites will expand the applied range of the original material and at the same time promote the development of interdisciplinary. Thus, the chemical functionalization and bottom-up assemblies of nanomaterials and subsequent applications will accelerate the development of nanoscience and nanotechnology.

This special issue continues to focus on chemical functionalization, self-assembly, and applications of nanomaterials and nanocomposites in 2014. The issue compiles thirteen exciting manuscripts. It is to refer to multiple functional nanomaterials and nanocomposites such as magnetic materials Mg-Zn-Ferrite and $\text{CoGd}_x\text{Fe}_{2-x}\text{O}_4$, graphene-based material for the biological and catalytic application, supramolecular material soluble glutathione peroxidase, thermal insulation zeolite that uses the coal fly ash as the raw material under a two-step synthesis, *Artemia* egg shell-supported TiO_2 high efficiency formaldehyde removal material, and hybrid mesocrystals of ibuprofen and aragonite for medical application. In addition, two of the manuscripts deal with morphology studies about organogel system based on calamitic hydrazide derivatives and calcium carbonate,

respectively. The paper by A. Wang et al. explores the bioapplication of gold nanoparticles. The engineering applications about the fretting wear mechanism and debris analysis are in depth researched by L. Zhang et al. Furthermore, X. Qu et al. review the recent advances of fluorescent gold nanoclusters-based applications in biological sensing, biolabeling, and bioimaging and finally discuss the current challenges of fluorescent gold nanoclusters in controllable synthesis and biological application.

Altogether, by compiling these papers, we hope to arouse our readers and researchers' interest with respect to chemical functionalization, self-assembly, and applications of nanomaterials and nanocomposites.

Acknowledgment

Moreover, sincere thanks are extended to all the authors for their contribution and all reviewers for their time.

Xingbin Yan
Tifeng Jiao
Lavinia Balan
Xinqing Chen
Michael Z. Hu
Wenwen Liu

Research Article

The Structural and Magnetic Properties of Gadolinium Doped CoFe_2O_4 Nanoferrites

Qing Lin,^{1,2} Jinpei Lin,¹ Yun He,¹ Ruijun Wang,² and Jianghui Dong³

¹College of Physics and Technology, Guangxi Normal University, Guilin 541004, China

²Department of Information Technology, Hainan Medical College, Haikou 571101, China

³School of Natural and Built Environments, University of South Australia, Adelaide, SA 5095, Australia

Correspondence should be addressed to Yun He; hy@gxnu.edu.cn

Received 8 August 2014; Accepted 26 August 2014

Academic Editor: Xinqing Chen

Copyright © 2015 Qing Lin et al. This is an open access article distributed under the Creative Commons Attribution License, which permits unrestricted use, distribution, and reproduction in any medium, provided the original work is properly cited.

Gadolinium substituted cobalt ferrite $\text{CoGd}_x\text{Fe}_{2-x}\text{O}_4$ ($x = 0, 0.04, 0.08$) powders have been prepared by a sol-gel autocombustion method. XRD results indicate the production of a single cubic phase of ferrites. The lattice parameter increases and the average crystallite size decreases with the substitution of Gd^{3+} ions. SEM shows that the ferrite powders are nanoparticles. Room temperature Mössbauer spectra of $\text{CoGd}_x\text{Fe}_{2-x}\text{O}_4$ are two normal Zeeman-split sextets, which display ferrimagnetic behavior. The saturation magnetization decreases and the coercivity increases by the Gd^{3+} ions.

1. Introduction

Cobalt ferrite is a hard magnetic material, and it has moderate saturation magnetization of about 80 emu/g, high coercivity of 5000 Oe, high Curie temperature T_C of 793.15 K (520°C), high anisotropy constant of $2.65 \times 10^6 \sim 5.1 \times 10^6$ erg/cm³, and high magnetostrictive of -225×10^{-6} [1, 2]. Moreover, cobalt ferrite exhibits high electromagnetic performance, large magneto-optic effect, excellent chemical stability, and mechanical hardness [3, 4]. In the materials containing 3d transition metals, the magnetism carriers are the electrons from the 3d shell that are considered to migrate from one atom to another. In rare earth (RE) metals, the magnetism carriers are the 4f electrons which are protected by the $5s^2 5p^6$ shells, so their magnetic moments are well localized at individual atoms [5–7]. Small amounts of RE element gadolinium can affect the magnetic properties and the magnetic coercivity of Co ferrites. Peng et al. [8] and Rana et al. [9] investigated the effect of Gd^{3+} substitution on dielectric properties and saturation magnetization of nanocobalt ferrite.

In this paper, nanoferrites $\text{CoGd}_x\text{Fe}_{2-x}\text{O}_4$ ($x = 0, 0.04, 0.08$) were prepared by a sol-gel autocombustion method. The aim of this study is to investigate variation structural and

magnetic properties of cobalt ferrite powders by replacement of small amounts gadolinium.

2. Experimental

2.1. Sample Preparation. RE ions substituted cobalt ferrite $\text{CoGd}_x\text{Fe}_{2-x}\text{O}_4$ ($x = 0, 0.04, 0.08$) powders were prepared by a sol-gel autocombustion method. The analytical grades $\text{Co}(\text{NO}_3)_2 \cdot 6\text{H}_2\text{O}$, $\text{Fe}(\text{NO}_3)_3 \cdot 9\text{H}_2\text{O}$, $\text{Gd}(\text{NO}_3)_3 \cdot 6\text{H}_2\text{O}$, citric acid ($\text{C}_6\text{H}_8\text{O}_7 \cdot \text{H}_2\text{O}$), and ammonia ($\text{NH}_3 \cdot \text{H}_2\text{O}$) were used as raw materials. The molar ratio of metal nitrates to citric acid was taken as 1 : 1. The metal nitrates and citric acid were, respectively, dissolved into deionized water to form solution. Ammonia was added to the solution of metal nitrates to change the pH value from 7 to 9. The mixed solution was poured into a thermostat water bath and heated at 80°C under constant stirring to transform into a dried gel [9]. Citric acid was dropped continually in the process of heating. The gel was dried at 120°C in a dry-oven for 2 h, being ignited in the air at room temperature, and the dried gel burnt in a self-propagating combustion way to form loose powder. The powder was ground and annealed at temperatures 800°C for 3 h.

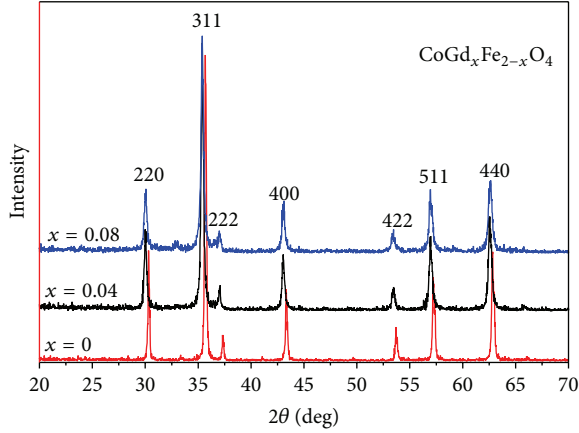


FIGURE 1: Room temperature X-ray diffraction patterns of $\text{CoGd}_x\text{Fe}_{2-x}\text{O}_4$ ($x = 0, 0.04, 0.08$) annealed at 800°C .

TABLE 1: Lattice parameters, average crystallite size, and X-ray densities of $\text{CoGd}_x\text{Fe}_{2-x}\text{O}_4$ ($x = 0, 0.04, 0.08$) ferrites annealed at 800°C .

Sample (x)	Lattice parameter (\AA)	Average crystallite size (\AA)	Density ($\text{g}\cdot\text{cm}^{-3}$)
0	8.35497	556	5.3468
0.04	8.39787	343	5.3536
0.08	8.39755	316	5.4452

2.2. Characterization. The crystalline structure was investigated by X-ray diffraction (Rigaku D/max-2500V/PC) with $\text{Cu K}\alpha$ radiation ($\lambda = 0.15405 \text{ nm}$). The micrographs were obtained by scanning electron microscopy (NoVa Nano SEM 430). The Mössbauer spectrum was performed at room temperature, using a conventional Mössbauer spectrometer (Fast Com Tec PC-mossII), in constant acceleration mode. The γ -rays were provided by a ^{57}Co source in a rhodium matrix. Magnetization measurements were carried out with superconducting quantum interference device (MPMS-XL-7, Quantum Design) at room temperature.

3. Results and Discussion

3.1. XRD Patterns Analysis. Figure 1 shows the XRD patterns of $\text{CoGd}_x\text{Fe}_{2-x}\text{O}_4$ ($x = 0, 0.04, 0.08$) ferrites calcined at 800°C for 3 h. The XRD patterns show that all the samples are single phase and all diffraction peaks can be indexed to the cubic spinel structure of CoFe_2O_4 (JCPDS card number 22-1086). No impurity peak was detected in these samples. Table 1 indicates that the lattice constant of Co ferrite substituting the Gd^{3+} sample is larger than that of the pure cobalt ferrite; it is due to the fact that the ionic radius of Gd^{3+} ions (0.938 \AA) is larger than that of Fe^{3+} ions (0.645 \AA) [8–11]. However, lattice parameter does not increase monotonously by increasing the gadolinium content, and it may be related to doping gadolinium having a larger radius in CoFe_2O_4 which leads to the lattice distortion [8].

The average crystallite size of the investigated samples is found to be around 31.6 to 55.6 nm by using Scherrer's formula [10, 12, 13]. The decreasing average crystallite size is with Gd^{3+} ions doping, which is in agreement with the results of literature [14–18]. They pointed out that the larger the bond energy of $\text{Gd}^{3+}-\text{O}^{2-}$ as compared to that of $\text{Gd}^{3+}-\text{O}^{2-}$, the more the energy needed to make Gd^{3+} ions enter into the lattice and form the bond of $\text{RE}^{3+}-\text{O}^{2-}$. Therefore, Gd^{3+} substituted ferrites have higher thermal stability relative to pure Co ferrite, and more energy is needed for the substituted samples to complete crystallization and grow grains.

The X-ray density was calculated using the following relation [10, 11, 17]:

$$\rho_x = \frac{8M}{Na^3}, \quad (1)$$

where M is relative molecular mass, N is Avogadro's number, and " a " is the lattice parameter. Table 1 shows that the X-ray density is tending to increase with Gd^{3+} substitution. The atomic weight of Gd is greater than that of Fe, so the relative molecular mass increases with the substitution of Gd^{3+} ions, and the lattice parameter of cobalt ferrite substituting the Gd^{3+} has no significant changes. So the increase in X-ray density is attributed to the fact that the relative molecular mass increases.

3.2. Structures and Grain Sizes. The SEM micrographs of CoFe_2O_4 ferrites annealed at 800°C for 3 h are shown in Figure 2. The distribution of grains with almost uniform size, well crystallized for the sample, can be observed. Figure 3 shows the histogram of grain size distribution of $\text{CoGd}_x\text{Fe}_{2-x}\text{O}_4$ ($x = 0$) ferrites. The average grain size estimated by a statistical method is approximately 96.26 nm. The average grain size is slightly larger than the average crystallite size determined by XRD. This shows that every particle is formed by a number of crystallites [19–21].

The SEM micrographs of $\text{CoGd}_x\text{Fe}_{2-x}\text{O}_4$ ($x = 0$) are shown in Figure 4. The distribution of grains with almost uniform size, well crystallized for $\text{CoGd}_x\text{Fe}_{2-x}\text{O}_4$ ($x = 0$), can be observed. Some particles are agglomerated due to the presence of magnetic interactions among particles [14].

3.3. Mössbauer Spectroscopy. The Mössbauer spectra recorded at room temperature are shown in Figure 5 for $\text{CoGd}_x\text{Fe}_{2-x}\text{O}_4$ ($x = 0, 0.04, 0.08$). All samples have been analyzed using Mösswinn 3.0 program. For all samples, the spectra exhibit two normal Zeeman-split sextets due to Fe^{3+} at tetrahedral and octahedral sites, indicating the ferromagnetic behavior of the samples. The sextet with the larger isomer shift is assigned to the Fe^{3+} ions at B site, and the one with the smaller isomer shift is assumed to the Fe^{3+} ions occupying A site. Maybe it is due to the difference in $\text{Fe}^{3+}-\text{O}^{2-}$ internuclear separations. For the bond separation being larger for B site Fe^{3+} ions, in comparison with A site ions, smaller overlapping of orbits for Fe^{3+} and O^{2+} ions at B site occurs, resulting in smaller covalency and larger isomer shift for B site Fe^{3+} ions [22, 23]. It is evident from

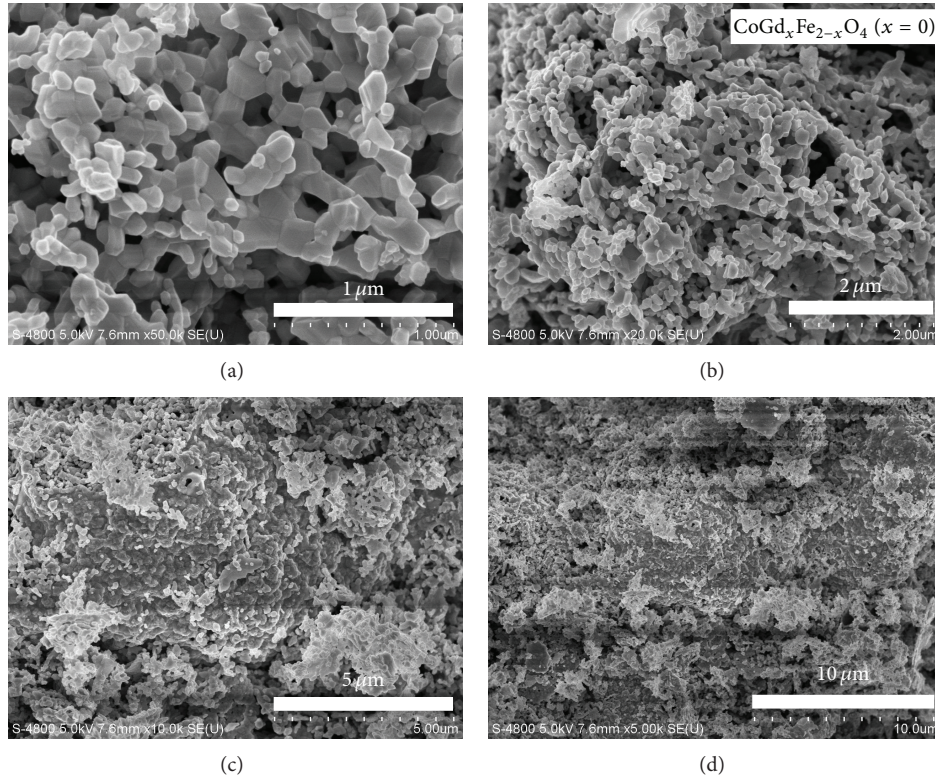


FIGURE 2: SEM micrographs depict CoFe₂O₄ ferrites with diameters of 1 μm (a), 2 μm (b), 5 μm (c), and 10 μm (d).

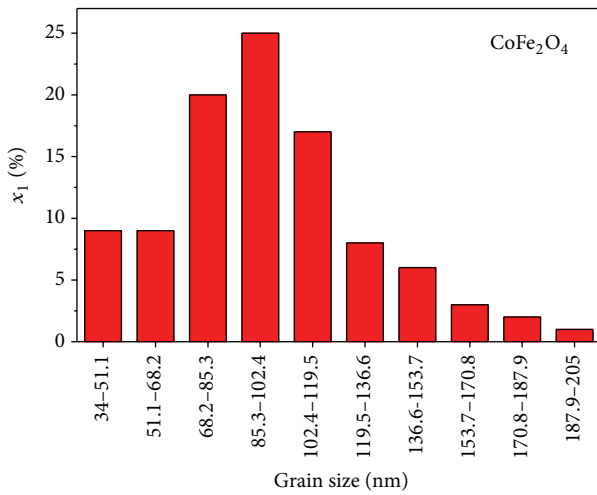


FIGURE 3: Histogram of grain size distribution for CoFe₂O₄ ferrites annealed at 800°C.

Table 2 that isomer shifts values show very little change with Gd³⁺ substitution, which indicates that s electrons charge distribution of Fe³⁺ is not much influenced by Gd³⁺ substitution [23]. It is reported that the values of IS (Isomer shift) for Fe²⁺ ions lie in the range 0.6~1.7 mm/s, while for Fe³⁺ ions they lie in the range 0.1~0.5 mm/s [24]. From

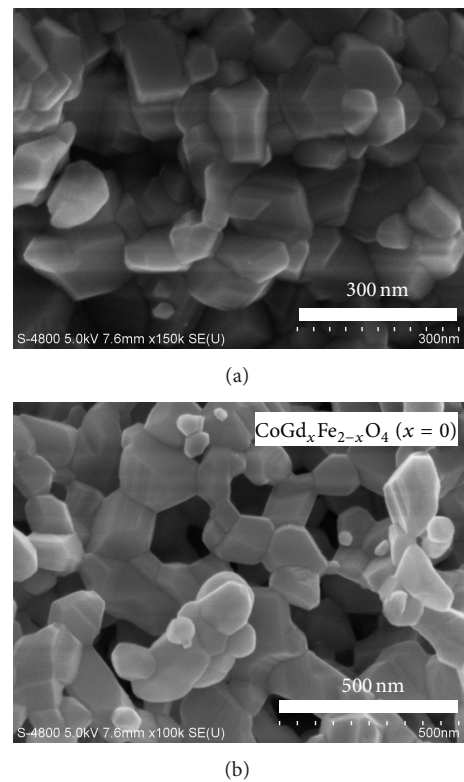


FIGURE 4: SEM micrographs of different part in CoGd_xFe_{2-x}O₄ (x = 0) ferrites with diameters of 300 nm (a) and 500 nm (b).

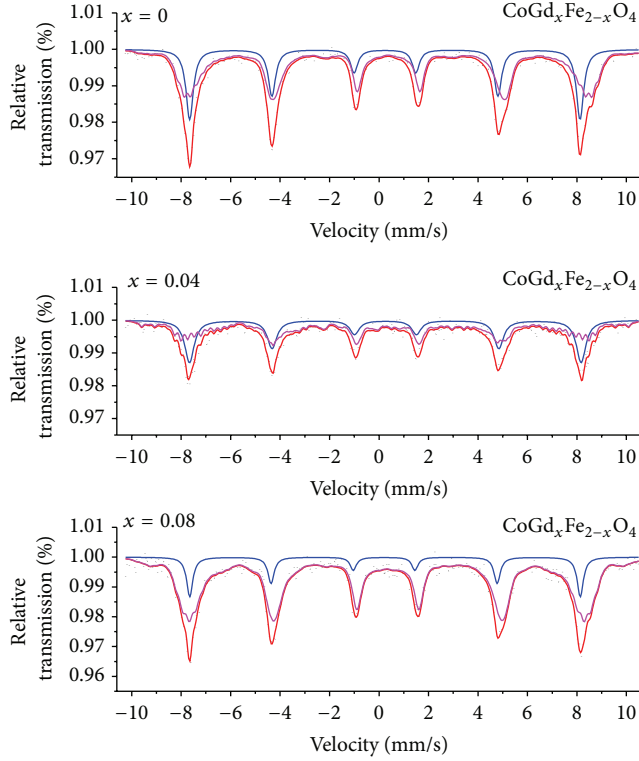


FIGURE 5: Room temperature Mössbauer spectra of $\text{CoGd}_x\text{Fe}_{2-x}\text{O}_4$ ($x = 0, 0.04, 0.08$) ferrites annealed at 800°C .

Table 2, values for IS in this paper indicate that iron is in Fe^{3+} state.

Table 3 shows that the values of magnetic hyperfine field at A site have no significant changes, and the magnetic hyperfine field at B site is tending to decrease by Gd^{3+} substitution. Maybe the Fe^{3+} ions of samples at lattice site are substituted by Gd^{3+} ions at B sites. Gd is the only RE element that has a Curie temperature T_C (293.2 K) close to room temperature [16, 25]. Magnetic dipolar orientation of the RE exhibits a disordering form at room temperature; therefore, introducing rare-earth Gd^{3+} ions in CoFe_2O_4 seems like substituting magnetic Fe^{3+} ions (in octahedral B site of spinel lattice) by nonmagnetic atoms [8].

The value of quadrupole shift of the magnetic sextet is very small in all the samples indicating that the local symmetry of the ferrites obtained is close to cubic.

3.4. Magnetic Property of Particles. Figure 6 shows hysteresis loops of $\text{CoGd}_x\text{Fe}_{2-x}\text{O}_4$ at room temperature. The magnetization of all samples nearly reaches saturation at the external field of 10000 Oe .

It is observed from Table 3 that saturation magnetization decreases as Gd content increases. The saturation magnetization could be expressed by means of the following relation [7]:

$$\sigma_s = \frac{5585 \times n_B}{M}, \quad (2)$$

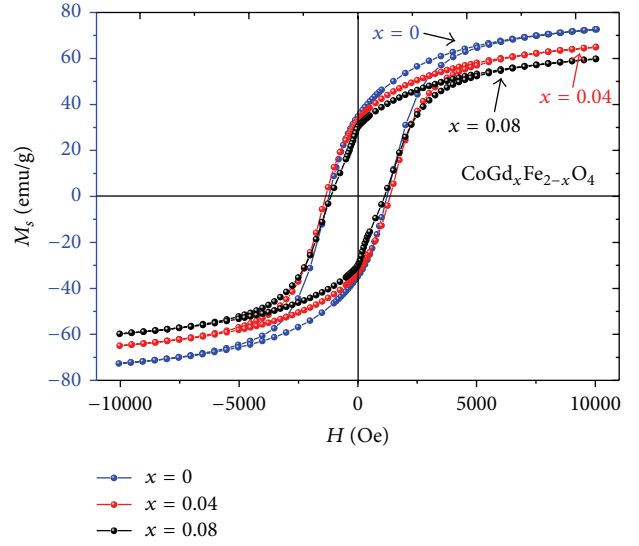


FIGURE 6: Room temperature hysteresis loops of $\text{CoGd}_x\text{Fe}_{2-x}\text{O}_4$ ($x = 0, 0.04, 0.08$) annealed at 800°C .

where n_B is the magnetic moment with Bohr magneton as the unit and M is relative molecular mass. The relative molecular mass of $\text{CoGd}_x\text{Fe}_{2-x}\text{O}_4$ increases as Gd content x increases. The change of magnetic moment n_B can be explained with Néel's theory. The magnetic moment per ion for Gd^{3+} , Co^{2+} , and Fe^{3+} ions is $7.94 \mu_B$, $3 \mu_B$, and $5 \mu_B$ [15, 16], respectively. As previously mentioned, magnetic dipolar orientation of the rare earth exhibits a disordering form at room temperature. Hence, in this paper, it may be reasonable that rare earth ions (Gd^{3+}) are considered as nonmagnetic ones at room temperature.

Since Co^{2+} prefer to occupy the octahedral site (B) in CoFe_2O_4 material of inverse spinel structure [1, 2], Gd^{3+} ions occupy only the B sites for their large ion radii [10, 16]. That is, the cation distribution is $(\text{Fe})_A[\text{CoGd}_x\text{Fe}_{1-x}]_B\text{O}_4$. According to Néel's two sublattice models of ferrimagnetism, the magnetic moment n_B is expressed as [7, 11]

$$n_B = M_B - M_A = 3 + 5(1 - x) - 5 = 3 - 5x, \quad (3)$$

where M_B and M_A are B and A sublattice magnetic moments, respectively. Figure 7 shows the change in experimental and theoretical magnetic moment with Gd content x .

From Figure 7, the experimental and theoretical magnetic moment decreases as Gd content x increases, and according to relation (2) the theoretical saturation magnetization decreases with Gd content x . The variation of the experimental and theoretical saturation magnetization is in a good agreement with each other for all samples.

It is observed from Table 3 that the variation of coercivity with Gd content x increases for $\text{CoGd}_x\text{Fe}_{2-x}\text{O}_4$. It indicates that the coercivity of Co ferrite substituting the Gd^{3+} ions is larger than that of the pure cobalt ferrite. The phenomenon can be explained as follows. Like Co^{2+} ions, rare earth ions (Gd^{3+}) have stronger s-l coupling and weaker crystal field, so they have stronger magnetocrystalline anisotropy [6, 10,

TABLE 2: Mössbauer parameters of isomer shift (IS), quadrupole splitting (QS), magnetic hyperfine field (H), linewidth (Γ), and absorption area (A_0) for $\text{CoGd}_x\text{Fe}_{2-x}\text{O}_4$ ($x = 0, 0.04, 0.08$) ferrites annealed at 800°C .

Sample (x)	Component	IS (mm/s)	QS (mm/s)	H (T)	Γ (mm/s)	A_0 (mm/s)
0	Sextet (A)	0.237	-0.004	48.946	0.360	32.4
	Sextet (B)	0.375	-0.024	45.695	0.322	67.6
0.04	Sextet (A)	0.256	-0.006	49.105	0.462	38.3
	Sextet (B)	0.298	-0.111	42.123	0.214	61.3
0.08	Sextet (A)	0.223	0.037	48.964	0.304	14.3
	Sextet (B)	0.334	-0.049	45.482	0.361	85.7

TABLE 3: Magnetic data for $\text{CoGd}_x\text{Fe}_{2-x}\text{O}_4$ ($x = 0, 0.04, 0.08$) ferrites annealed at 800°C .

Sample (x)	M_S (emu/g)	H_C (Oe)	M_r (emu/g)	n_B
0	72.58	1005.33	34.71	3.05
0.04	65.00	1365.17	33.24	2.78
0.08	59.77	1125.26	30.12	2.60

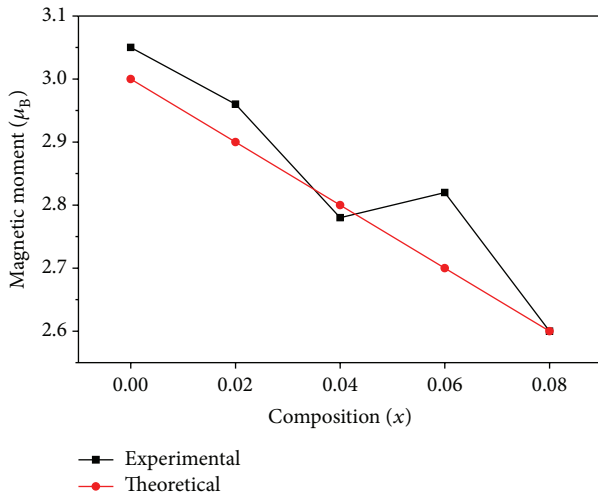


FIGURE 7: The variation in experimental and theoretical magnetic moment of $\text{CoGd}_x\text{Fe}_{2-x}\text{O}_4$ ferrites with gadolinium content x .

18, 25, 26]. Furthermore, the radii of Gd^{3+} ions are larger than that of Fe^{3+} ions, and the symmetry of crystal will be decreased after the sample was substituted by Gd^{3+} ions and hence may distort the lattice or crystalline field and generate an internal stress [13, 14]. Moreover, it is known that the grain boundary increases with decreasing crystallite size. In this study, Gd substituted ferrites have a decrease in crystallite size with the substitution of Gd^{3+} ions. The area of disordered arrangement for ions on grain boundaries may fix and hinder the domain walls motion; thus the coercivity of the samples increases with Gd^{3+} ions substituted cobalt ferrite [14]. However the coercivity does not increase monotonously by increasing the gadolinium content, and it may be related to the coercivity which is influenced by many factors, such

as crystallinity, microstrain, magnetic particle morphology and size distribution, anisotropy, and magnetic domain size [14, 27, 28].

4. Conclusion

The analysis of XRD patterns reveals the formation of single-phase cubic spinel structure for $\text{CoGd}_x\text{Fe}_{2-x}\text{O}_4$ ($x = 0, 0.04, 0.08$) ferrite annealed at 800°C . The increase in lattice constant is due to replacement of smaller Fe^{3+} ions by larger Gd^{3+} ions. SEM results indicate the distribution of grains and morphology of the samples. Some particles are agglomerated due to the presence of magnetic interactions among particles. The ferrite powers are nanoparticles. Room temperature Mössbauer spectra of $\text{CoGd}_x\text{Fe}_{2-x}\text{O}_4$ ($x = 0, 0.04, 0.08$) ferrites are two normal Zeeman-split sextets. It displays ferrimagnetic behavior for the samples. The saturation magnetization decreases and the coercivity increases with the substitution of Gd^{3+} ions. The decreases of the saturation magnetization can be explained with Néel's theory. The variation of coercivity is attributed to magneto-crystalline anisotropy, microstrain, and grain boundary.

Conflict of Interests

The authors declared that they have no conflict of interests to this work.

Acknowledgments

This work was financially supported by the National Natural Science Foundation of China (no. 11364004, 11164002) and Innovation Project of Guangxi Graduate Education under Grant (no. 2010106020702M47).

References

- [1] B. Babić-Stojić, V. Jokanović, D. Milivojević et al., "Magnetic and structural studies of CoFe_2O_4 nanoparticles suspended in an organic liquid," *Journal of Nanomaterials*, vol. 2013, Article ID 741036, 9 pages, 2013.
- [2] S. Amiri and H. Shokrollahi, "The role of cobalt ferrite magnetic nanoparticles in medical science," *Materials Science and Engineering C*, vol. 33, no. 1, pp. 1-8, 2013.

- [3] N. Sanpo, C. C. Berndt, C. Wen, and J. Wang, "Transition metal-substituted cobalt ferrite nanoparticles for biomedical applications," *Acta Biomaterialia*, vol. 9, no. 3, pp. 5830–5837, 2013.
- [4] C. H. Chia, S. Zakaria, M. Yusoff et al., "Size and crystallinity-dependent magnetic properties of CoFe_2O_4 nanocrystals," *Ceramics International*, vol. 36, no. 2, pp. 605–609, 2010.
- [5] M. M. Eltabey, A. M. Massoud, and C. Radu, "Microstructure and superparamagnetic properties of Mg-Ni-Cd ferrites nanoparticles," *Journal of Nanomaterials*, vol. 2014, Article ID 492832, 7 pages, 2014.
- [6] G. Dascalu, T. Popescu, M. Feder, and O. F. Caltun, "Structural, electric and magnetic properties of $\text{CoFe}_{1.8}\text{RE}_{0.2}\text{O}_4$ (RE=Dy, Gd, La) bulk materials," *Journal of Magnetism and Magnetic Materials*, vol. 333, pp. 69–74, 2013.
- [7] S. Kanagesan, M. Hashim, S. Tamilselvan, N. B. Alitheen, I. Ismail, and G. Bahmanrokh, "Cytotoxic effect of nanocrystalline MgFe_2O_4 particles for cancer cure," *Journal of Nanomaterials*, vol. 2013, Article ID 865024, 8 pages, 2013.
- [8] J. Peng, M. Hojamberdiev, Y. Xu, B. Cao, J. Wang, and H. Wu, "Hydrothermal synthesis and magnetic properties of gadolinium-doped CoFe_2O_4 nanoparticles," *Journal of Magnetism and Magnetic Materials*, vol. 323, no. 1, pp. 133–138, 2011.
- [9] A. Rana, O. P. Thakur, and V. Kumar, "Effect of Gd^{3+} substitution on dielectric properties of nano cobalt ferrite," *Materials Letters*, vol. 65, no. 19–20, pp. 3191–3192, 2011.
- [10] S. Amiri and H. Shokrollahi, "Magnetic and structural properties of RE doped co-ferrite (RE=Nd, Eu, and Gd) nanoparticles synthesized by co-precipitation," *Journal of Magnetism and Magnetic Materials*, vol. 345, pp. 18–23, 2013.
- [11] J. Chand, G. Kumar, P. Kumar, S. K. Sharma, M. Knobel, and M. Singh, "Effect of Gd^{3+} doping on magnetic, electric and dielectric properties of $\text{MgGd}_x\text{Fe}_{2-x}\text{O}_4$ ferrites processed by solid state reaction technique," *Journal of Alloys and Compounds*, vol. 509, no. 40, pp. 9638–9644, 2011.
- [12] M. M. Rashad, R. M. Mohamed, and H. El-Shall, "Magnetic properties of nanocrystalline Sm-substituted CoFe_2O_4 synthesized by citrate precursor method," *Journal of Materials Processing Technology*, vol. 198, no. 1–3, pp. 139–146, 2008.
- [13] L. Guo, X. Shen, F. Song, L. Lin, and Y. Zhu, "Structure and magnetic property of $\text{CoFe}_{2-x}\text{Sm}_x\text{O}_4$ ($x = 0-0.2$) nanofibers prepared by sol-gel route," *Materials Chemistry and Physics*, vol. 129, no. 3, pp. 943–947, 2011.
- [14] J. Jiang and Y.-M. Yang, "Effect of Gd substitution on structural and magnetic properties of Zn-Cu-Cr ferrites prepared by novel rheological technique," *Materials Science and Technology*, vol. 25, no. 3, pp. 415–418, 2009.
- [15] Y. Y. Meng, Z. W. Liu, H. C. Dai et al., "Structure and magnetic properties of $\text{Mn}(\text{Zn})\text{Fe}_{2-x}\text{RE}_x\text{O}_4$ ferrite nano-powders synthesized by co-precipitation and refluxing method," *Powder Technology*, vol. 229, pp. 270–275, 2012.
- [16] L. Zhao, Y. Cui, H. Yang, L. Yu, W. Jin, and S. Feng, "The magnetic properties of $\text{Ni}_{0.7}\text{Mn}_{0.3}\text{Gd}_x\text{Fe}_{2-x}\text{O}_4$ ferrite," *Materials Letters*, vol. 60, no. 1, pp. 104–108, 2006.
- [17] M. Asif Iqbal, M.-U. Islam, M. N. Ashiq, I. Ali, A. Iftikhar, and H. M. Khan, "Effect of Gd-substitution on physical and magnetic properties of $\text{Li}_{1.2}\text{Mg}_{0.4}\text{Gd}_x\text{Fe}_{(2-x)}\text{O}_4$ ferrites," *Journal of Alloys and Compounds*, vol. 579, pp. 181–186, 2013.
- [18] R. N. Panda, J. C. Shih, and T. S. Chin, "Magnetic properties of nano-crystalline Gd- or Pr-substituted CoFe_2O_4 synthesized by the citrate precursor technique," *Journal of Magnetism and Magnetic Materials*, vol. 257, no. 1, pp. 79–86, 2003.
- [19] M. M. Ruiz, J. L. Mietta, P. Soledad Antonel, O. E. Pérez, R. Martín Negri, and G. Jorge, "Structural and magnetic properties of $\text{Fe}_{2-x}\text{CoSm}_x\text{O}_4$ -nanoparticles and $\text{Fe}_{2-x}\text{CoSm}_x\text{O}_4$ -PDMS magnetoelastomers as a function of Sm content," *Journal of Magnetism and Magnetic Materials*, vol. 327, pp. 11–19, 2013.
- [20] L. B. Tahar, L. S. Smiri, M. Artus et al., "Characterization and magnetic properties of Sm- and Gd-substituted CoFe_2O_4 nanoparticles prepared by forced hydrolysis in polyol," *Materials Research Bulletin*, vol. 42, no. 11, pp. 1888–1896, 2007.
- [21] A. I. Borhan, T. Slatineanu, A. R. Iordan, and M. N. Palamaru, "Influence of chromium ion substitution on the structure and properties of zinc ferrite synthesized by the sol-gel auto-combustion method," *Polyhedron*, vol. 56, pp. 82–89, 2013.
- [22] J. Lin, Y. He, Q. Lin, R. Wang, and H. Chen, "Microstructural and Mössbauer spectroscopy studies of $\text{Mg}_{1-x}\text{Zn}_x\text{Fe}_2\text{O}_4$ ($x = 0.5, 0.7$) nanoparticles," *Journal of Spectroscopy*, vol. 2014, Article ID 540319, 5 pages, 2014.
- [23] S. S. R. Inbanathan, V. Vaithyanathan, J. Arout Chelvane, G. Markandeyulu, and K. Kamala Bharathi, "Mössbauer studies and enhanced electrical properties of R (R=Sm, Gd and Dy) doped Ni ferrite," *Journal of Magnetism and Magnetic Materials*, vol. 353, pp. 41–46, 2014.
- [24] S. Kumar, A. M. M. Farea, K. M. Batoo et al., "Mössbauer studies of $\text{Co}_{0.5}\text{Cd}_x\text{Fe}_{2.5-x}\text{O}_4$ (0.0–0.5) ferrite," *Physica B*, vol. 403, pp. 3604–3607, 2008.
- [25] T. Jiao, Y. Wang, Q. Zhang et al., "Self-assembly and headgroup effect in nanostructured organogels via cationic amphiphilic-graphene oxide composites," *PLoS ONE*, vol. 9, no. 7, Article ID e101620, 2014.
- [26] Q. Lin, Z. Ye, C. Lei, H. Huang, J. Xu, and Y. He, "Microstructure and magnetic research of NiCuZn ferrite by Co, Bi compound doped," *Materials Research Innovations*, vol. 17, no. s1, pp. s287–s291, 2013.
- [27] S. H. Hosseini and A. Asadnia, "Synthesis, characterization, and microwave-absorbing properties of polypyrrole/ MnFe_2O_4 nanocomposite," *Journal of Nanomaterials*, vol. 2012, Article ID 198973, 6 pages, 2012.
- [28] T. Jiao, Q. Huang, Q. Zhang, D. Xiao, J. Zhou, and F. Gao, "Self-assembly of organogels via new luminol imide derivatives: diverse nanostructures and substituent chain effect," *Nanoscale Research Letters*, vol. 8, article 278, 2013.

Research Article

The Gelation Ability and Morphology Study of Organogel System Based on Calamitic Hydrazide Derivatives

Xia Ran, Lili Shi, Kun Zhang, Jie Lou, Bo Liu, and Lijun Guo

Institute of Photobiophysics, School of Physics and Electronics, Henan University, Kaifeng 475004, China

Correspondence should be addressed to Lijun Guo; juneguo@henu.edu.cn

Received 1 August 2014; Accepted 19 September 2014

Academic Editor: Tifeng Jiao

Copyright © 2015 Xia Ran et al. This is an open access article distributed under the Creative Commons Attribution License, which permits unrestricted use, distribution, and reproduction in any medium, provided the original work is properly cited.

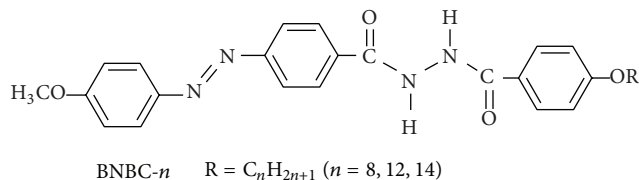
The gelation property of a series of LMOG bearing hydrazide and azobenzene groups, namely, N-4-(alkoxyphenyl)-N'-4-[(4-methoxyphenyl)azophenyl] benzohydrazide (BNBC-*n*, *n* = 8,12,14), has been systematically studied in this work. The obtained results demonstrate that the gelling ability in organic solvents is significantly influenced by the length of terminal alkoxy chain. In different organic solvents, it is hard to observe the organogel formation for BNBC-8 molecule. On the contrary, the organogelators BNBC-12 and BNBC-14 bearing longer terminal chains have shown great ability to gel organic solvents to form stable organogels. The critical gelation concentration for BNBC-12 reaches as low as 5.3×10^{-3} M, which can be considered as a supergelator. It has been manifested that the aggregation morphology of organogel strongly depends on the nature of the gelling solvents and the length of the terminal alkoxy chain. The gelation of BNBC-*n* provides an easy method for the preparation of multidimensional structure and manipulation of morphology from ribbons, hollow tube fiber to 3D net-like structure in different solvents. The cooperation of hydrogen bonding, π - π interaction, and Van der Waals force is suggested to be the main contribution to this self-assembled structure.

1. Introduction

In the past decades, low molecular mass organogelators (LMOGs) have attracted broad attention because they can self-assemble into diverse nano/microstructures, for instance, particles, tubes, fibers, and helical ribbons, through specific noncovalent interactions such as hydrogen bonding, π - π interaction, hydrophobic interaction and Van der Waals force, and so forth [1–3]. Supramolecular self-assembly is a spontaneous process of molecular aggregation into ordered nanostructures, which provides a bottom-up approach to obtain structural regularity of various morphologies [4]. However, a complete mechanism for the self-assembled supramolecular structures is still beyond our understanding. Recently, there has been a growing interest in tuning morphology by changing molecular structure [5], altering the composition of a binary gel [6, 7] and solvent [8, 9], and using ultrasound [10, 11], light [12, 13], and so on. For example, Saha et al. and coworkers reported for the first time the hierarchical tuning of one-dimensional morphology from helical bunched fibers to rods and hollow tubes, by changing

the composition of riboflavin-melamine in a hydrogel system [2]. Zhu et al. and coworkers demonstrated the structural transition from organogels to flower-like microcrystals in dipeptide self-assembling system, which can be readily induced by using ethanol as a cosolvent [8]. Our previous work reported a photoinduced fiber-vesicle morphological transition in a chloroform gel of azophenyl hydrazide derivative [12]. However, full control over the morphologies of self-assembled structures for their implementation in special applications is still a great challenge.

Among the noncovalent interactions, hydrogen bonding is most commonly used to direct self-assembly process because of its strength, directionality, reversibility, and selectivity. Meanwhile, peptide, amino acid, amide, and urea groups have been widely employed as building blocks to afford supramolecular gels. Yang et al. and coworkers reported a hydrazide quinolinone-based quadruple hydrogen-bonded building block to gelate dichloromethane/hexane at concentration higher than 2 wt % [14]. Zhao et al. and coworkers reported a new series of highly stable hydrazide-based ADDA-DAAD heterodimers, which

SCHEME 1: The molecular structure of BNBC-*n*.

represented the first successful application of hydrazide derivatives in the hydrogen-mediated supramolecular systems with well-established structures [15]. In this work, we focus on the self-assembly structure of calamitic hydrazide derivatives, N-4-(alkoxyphenyl)-N'-4-[(4-methoxyphenyl)azophenyl] benzohydrazide (BNBC-*n*, *n* = 8, 12, 14) (as shown in Scheme 1), which had been synthesized and reported in our previous work [16]. The results indicate that the gelation property and the aggregation morphology of organogel strongly depend on the nature of gelling solvents and the length of terminal alkoxy chain. The possible mechanism for the formation of nanostructural aggregates is also discussed in this paper.

2. Experimental Section

Field emission scanning electron microscopy (FE-SEM) images were taken with a JSM-6700F apparatus. Samples for FE-SEM measurement were prepared by wiping a small amount of gel onto a silicon plate, followed by drying in a vacuum for 12 h at room temperature. FT-IR spectra were recorded with a Perkin-Elmer spectrometer (Spectrum One B), in which the xerogels were prepared by freezing and pumping the organogel of BNBC-*n* for 12 h, and then pressed into a tablet with KBr for FT-IR measurement. UV-vis absorption spectra were obtained on a Shimadzu UV-2550 spectrometer.

Gelation Test. The weighted gelator was mixed in a cap sealed test tube (3.5 cm (height) × 0.5 cm (radius)) with an appropriate amount of solvent, and the mixture was heated until the solid dissolved. The sample vial was cooled to 4°C and then turned upside down. When a clear or slightly opaque gel formed, the solvent therein was immobilized at this stage. Melting temperature (T_m) was determined by the “falling drop” method [17]. An inverted gel was immersed in a water bath initially at or below room temperature and then was heated slowly up to the point at which the gel fell due to the force of gravity, that is, the T_m .

3. Results and Discussion

3.1. Molecular Design and Gelation Properties. The strategy of this work is to build up a system containing hydrogen bonding, π - π interaction, and Van der Waals force to drive the self-assembly gelation. The mentioned above interactions play mutual balance to modulate the packing arrangement

TABLE 1: Gelation properties^a of BNBC-*n*, *n* = 8, 12, 14.

Solvent	BNBC-8		BNBC-12		BNBC-14	
	State	State	CGC	State	CGC	State
Cyclohexane	I	I	—	I	—	—
Toluene	P	G	5.3×10^{-3}	G	6.7×10^{-3}	—
Benzene	P	G	8.2×10^{-3}	G	1.0×10^{-2}	—
Chloroform	P	G	1.3×10^{-2}	G	2.1×10^{-2}	—
Acetone	P	G	2.5×10^{-2}	G	4.8×10^{-2}	—
Methanol	P	P	—	P	—	—
DMSO	P	S	—	S	—	—

^aG: stable gel formed at room temperature; I: insoluble; P: precipitated; S: soluble; CGC: critical gelation concentration (mol/L), the minimum solute concentration necessary for gelation.

of molecules and eventually construct a particular superstructure. For this purpose, we had designed and synthesized the calamitic oxadiazole derivative BNBC-*n*, which contains hydrazide, azobenzene, and an alkyl chain with different length (as shown in Scheme 1). The numerous interactions in BNBC-*n* should offer, at least to some extent, the possibility of controlling the aggregation morphology of organogel. A certain solubility of a gelator in solvents is a prerequisite for gelation, whereas microphase segregation from dissolved solvents will induce gelation, in which different types of intermolecular interactions underpin the self-assembly of gelators. The length of alkyl chain is expected to regulate the intermolecular interaction with solvent to achieve a suitable solubility in solvent and thus the self-assembled nanostructures of organogel. We have investigated the gelation ability of BNBC-*n* in various organic solvents at room temperature, and the relevant minimum gel concentrations of BNBC-*n* are summarized in Table 1.

The obtained results indicate that the BNBC-8 bearing shorter terminal chain is difficult to dissolve in organic solvents with weak polarity, such as 1,2-dichloroethane and cyclohexane, but dissolves in medium and strong polarity such as benzene, chloroform, tetrahydrofuran, ethanol, and dimethylsulfoxide (DMSO) by heating and precipitates with cooling. In contrast, compounds BNBC-12 and BNBC-14 bearing longer terminal chain can form a stable gel in polar solvents such as aromatic solvents chloroform, while both of them dissolve in methanol by heating but precipitate with cooling as well. A possible reason for the precipitation from protic solvents might be that the potential supramolecular aggregation through intermolecular hydrogen bonding is prevented in this case. In other words, the above gelation property in different solvents manifests that intermolecular hydrogen bonding between the hydrazide groups is the driving force for the gelation and subsequent nanostructure. Among these three calamitic hydrazide derivatives, BNBC-12 bearing appropriate length of terminal chain shows the strongest gelation ability in toluene, and the critical gel concentration (CGC) can reach as low as 5.3×10^{-3} mol/L, which can be considered as a supergelator. Moreover, the sol-gel transition of BNBC-12 and BNBC-14 is fully thermoreversible even after several cycles of heating and cooling.

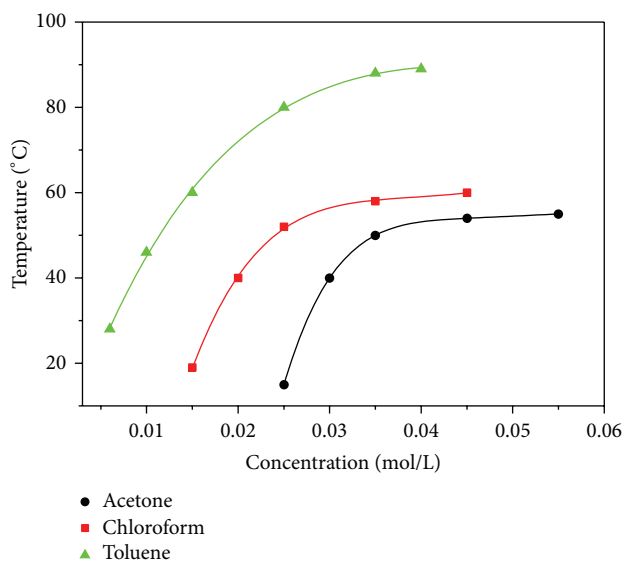


FIGURE 1: Concentration-dependent melting temperature (T_m) of BNBC-12 gelling in toluene, chloroform, and acetone, respectively.

The organogels are remarkably stable and can be stored for months without showing any decomposition.

Figure 1 shows the gel-sol transition temperature (T_m) of BNBC-12 gels in benzene, chloroform, and acetone as a function of concentration, respectively. The T_m increases with the concentration until a plateau region is reached (denoted by a concentration-independent T_m), which is determined by the “falling drop” method [17]. With changing the solvent, the T_m value in the “plateau region” decreases from 89°C (in toluene) to 60°C (in chloroform) and then to 55°C (in acetone). The most dramatic feature is that the morphologies of xerogels formed by BNBC-12 display a strong dependence on the nature of gelling solvent. From the summary listed in Table 1, it can be seen that the gelation ability of BNBC- n manifests an apparent dependence on the length of terminal chain of BNBC- n and intermolecular interaction with solvents, which will modify their self-assembled morphology structures as well.

3.2. Morphologies of the Xerogels. In order to investigate the aggregation morphology of organogel, the xerogels of BNBC- n were prepared and subjected to scanning electron microscope (SEM). As shown in Figure 2(a), the organogel of BNBC-12 from acetone consists of flexible root-like fibers with the width of 100–500 nm and length of tens of micrometers. The more entangled and dense fiber morphology with the width of 30–50 nm is observed for xerogel BNBC-12 from toluene (Figure 2(b)), and these fibers further assemble into thick fiber bundles and then constitute a highly developed and entangled network, indicating that the interactions between individual fibers are stronger in toluene. Meanwhile, the gel of BNBC-12 in toluene exhibits better transparency. Interestingly, the morphologies of the BNBC-12 xerogel from chloroform show a quite different packing from that of other xerogels. As shown in Figure 2(c), the xerogel of

BNBC-12 from toluene consists of coral-shaped aggregation morphology and reveals 3D cross-linking network structure. From the zoom-in of top right corner in Figure 2(c) (as shown in Figure 2(d)), it can be seen that the coralloid aggregation structure is composed by hillocks with the size of 50 nm in diameter and 50–200 nm in length. As to the xerogel of BNBC-14 from toluene (Figure 2(f)), the morphology image exhibits straight and dense fibrous aggregates with the diameter of 30–80 nm and tens of micrometers in length. The aggregate structure of BNBC-14 xerogel from acetone (Figure 2(e)) is composed of flat ribbons with the width ranging from 1 μm to 5 μm , and some ribbons bent to form hollow tube as shown in the inset of Figure 2(e). The observed morphology results indicate the gelation ability of BNBC-12 in different organic solvents is stronger than that of BNBC-14. Correspondingly, the assembled fiber or ribbon of BNBC-12 would capture more solvent molecules and would demonstrate a lower CGC value as well.

On the basis of the above results, it can be concluded that the morphology of the BNBC- n xerogels strongly depends on the nature of gelling solvents. These observations of tunable organogel structure are consistent with the CGC in different solvents shown in Table 1 for BNBC-12 and BNBC-14. The formation of elongated fiber-like and coral-shaped aggregates indicates that the self-assembly of BNBC- n is driven by strong intermolecular interactions.

3.3. The Interactions in the Gels. To investigate hydrogen bonding and alkyl chain conformations in the gelation process, the Fourier transform infrared (FT-IR) measurements on the xerogels of BNBC-12 from toluene, chloroform, and acetone were carried out, respectively. FT-IR spectroscopy of BNBC-12 xerogel from toluene (Figure 3(a)) shows that the N–H stretching vibrations are at around 3220 cm^{-1} and amide I at around 1641 cm^{-1} and 1679 cm^{-1} , respectively, indicating that the N–H groups are associated with C=O groups via N–H...O=C hydrogen bonding in the xerogel [18, 19]. For the acetone xerogel (Figure 3(c)), the N–H stretching vibrations locate at 3230 cm^{-1} , and the peak slightly shifts to higher wavenumbers along with a shift of amide I bands to 1683 cm^{-1} and 1645 cm^{-1} , respectively. Thus, it can be concluded that intermolecular hydrogen bonding exists in BNBC-12 xerogel from acetone, though it is somewhat weaker compared with that in the corresponding xerogel from toluene. On the other hand, the $\nu_s(\text{CH}_2)$ and $\nu_{as}(\text{CH}_2)$ in the xerogel of BNBC-12 appear at around 2855 cm^{-1} and 2925 cm^{-1} , respectively, implying that the alkyl chains are closely packed to form quasi-crystalline domain [20].

Electronic UV-vis absorption spectra of the gels were studied to obtain information about the aggregated state of azobenzene on the molecular scale. As shown in Figure 4, the absorption spectra of BNBC-12 manifest a slight but detectable dependence on concentration in acetone. With a dilute (1×10^{-5} M) solution of BNBC-12 in acetone, the π - π^* absorption maximum of the azobenzene group of BNBC-12 (Figure 4) locates at 351 nm. With the concentration increasing from 1×10^{-5} M to 1×10^{-3} M, the absorption maximum is slightly red-shifted from 351 nm to 357 nm, indicating

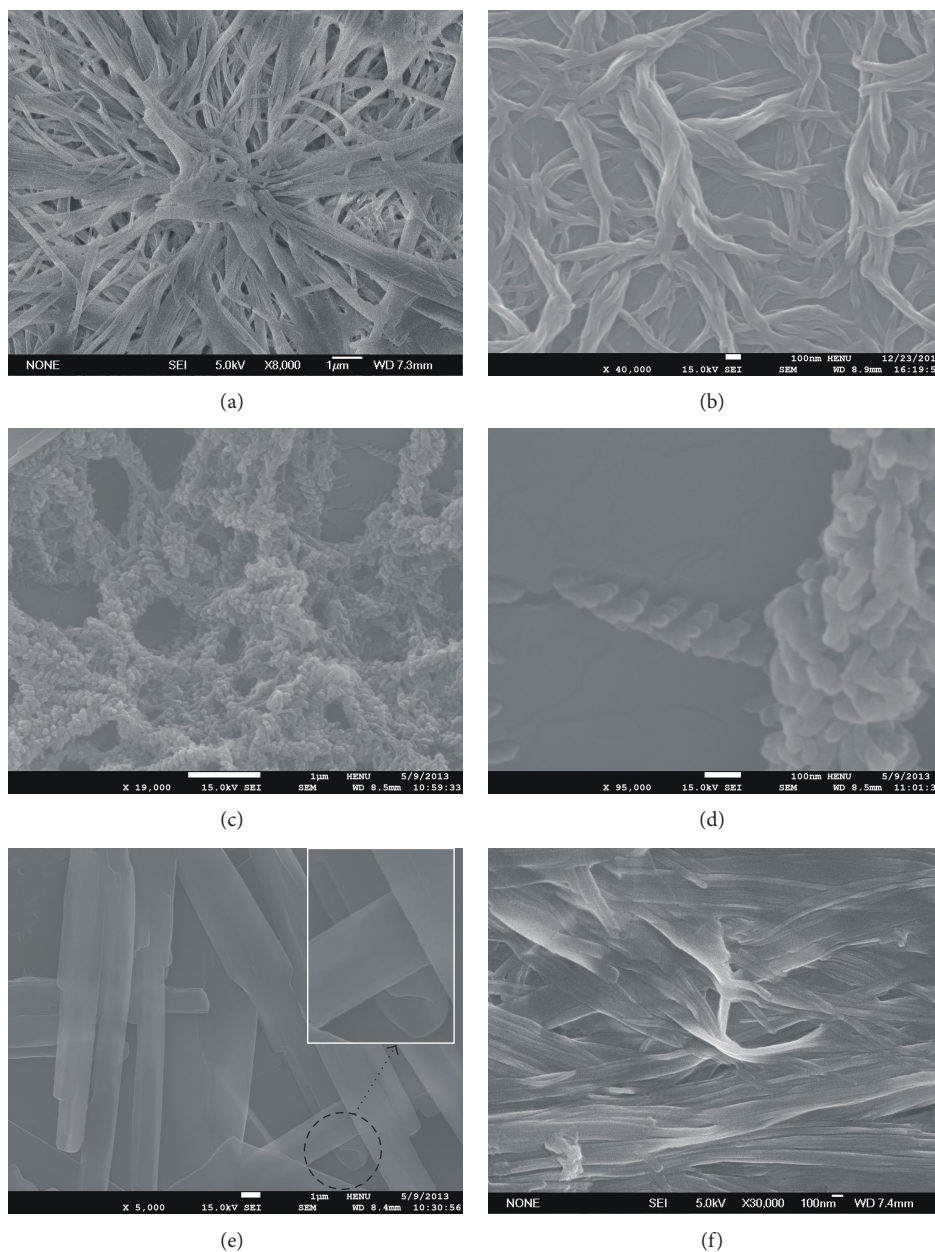


FIGURE 2: SEM images of (a) BNBC-12 xerogels from acetone (3.0×10^{-2} M), (b) BNBC-12 xerogels from toluene (5.8×10^{-3} M), (c, d) BNBC-12 xerogels from chloroform (3.0×10^{-2} M), (e) BNBC-14 xerogels from acetone (5.0×10^{-2} M), and (f) BNBC-14 xerogels from toluene (8.0×10^{-3} M).

that the azobenzene units are arranged into J-type aggregates through π - π interactions in gels [21]. Similar results were observed for BNBC-14 in acetone.

The self-assembled gelation is a complex process in which several noncovalent interactions are involved in the formation of aggregation structure. The above spectroscopic results with respect to the gelation ability and tunable morphology of BNBC-12 and BNBC-14 indicate that the cooperation of hydrogen bonds, π - π interaction, and Van der Waals force plays an important role in self-assembly. The gelation of BNBC- n provides an easy method for preparation of multidimensional structure and manipulation of morphology

ranging from ribbons, hollow tubes, fibers to even 3D net-like structure in different solvents.

4. Conclusions

We have studied the gelation ability and morphology of a series of LMOG (BNBC- n , $n = 8, 12, 14$) containing hydrazide, azobenzene, and alkyl chain with different length. BNBC-8 demonstrates a nonorganogel compound in any solvents or at different temperature. The organogelators BNBC-12 and BNBC-14 bearing longer terminal chains show strong gelation ability in organic solvents, such as toluene,

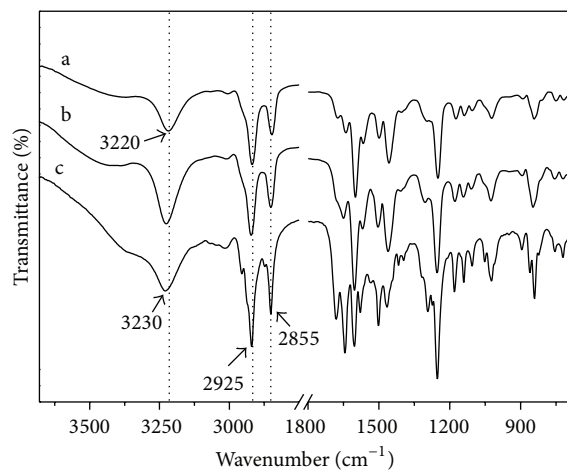


FIGURE 3: FT-IR spectra of BNBC-12 xerogel from (a) toluene, (b) chloroform, and (c) acetone.

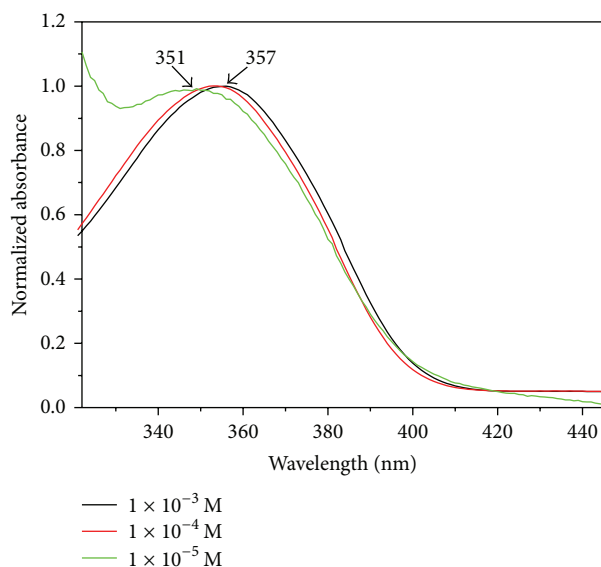


FIGURE 4: Normalized UV-vis absorption spectra of BNBC-12 in acetone at different concentrations.

chloroform and acetone, and so forth. The minimum gel concentration of BNBC-12 in toluene is as low as 5.3×10^{-3} M, which can be considered as a supergelator. It also has been demonstrated that the morphology of the xerogels strongly depends on the nature of gelling solvents, and the self-assembled nanostructure is tunable by the intermolecular interactions between molecule unit with different length of terminal chain and solvents. Based on these observations, the cooperation of hydrogen bonds, π - π interaction, and Van der Waals force might be crucially involved in the process of self-assembly. The unique and tunable aggregation morphology could be applied to surface modification such as superhydrophobicity and distinguish the obtained organogels as a novel class of functional materials.

Conflict of Interests

The authors declare that there is no conflict of interests regarding the publication of this paper.

Acknowledgments

The authors are grateful to the National Science Foundation Committee of China (Project nos. 21173068 and 21373077) and the Program for Innovative Research Team in University of Henan Province (no. 13IRTSTHN017) for their financial support of this work.

References

- [1] D. J. Abdallah and R. G. Weiss, "Organogels and low molecular mass organic gelators," *Advanced Materials*, vol. 12, no. 17, pp. 1237–1347, 2000.
- [2] A. Saha, S. Manna, and A. K. Nandi, "Hierarchical tuning of 1-D macro morphology by changing the composition of a binary hydrogel and its influence on the photoluminescence property," *Chemical Communications*, no. 32, pp. 3732–3734, 2008.
- [3] J. H. van Esch and B. L. Feringa, "Functional functional materials based on self-assembling organogels: from serendipity towards design," *Angewandte Chemie International Edition*, vol. 39, no. 13, pp. 2263–2266, 2000.
- [4] J. M. Lehn, *Supramolecular Chemistry: Concepts and Perspectives*, Wiley-VCH, Weinheim, Germany, 1995.
- [5] S. Qu, L. Zhao, Z. Yu et al., "Nanoparticles, helical fibers, and nanoribbons of an achiral twin-tapered bi-1,3,4-oxadiazole derivative with strong fluorescence," *Langmuir*, vol. 25, no. 3, pp. 1713–1717, 2009.
- [6] K. Jang, J. M. Kinyanjui, D. W. Hatchett, and D.-C. Lee, "Morphological control of one-dimensional nanostructures of T-shaped asymmetric bisphenazine," *Chemistry of Materials*, vol. 21, no. 10, pp. 2070–2076, 2009.
- [7] B. Roy, P. Bairi, and A. K. Nandi, "Supramolecular assembly of melamine and its derivatives: nanostructures to functional materials," *RSC Advances*, vol. 4, no. 4, pp. 1708–1734, 2014.
- [8] P. Zhu, X. Yan, Y. Su, Y. Yang, and J. Li, "Solvent-induced structural transition of self-assembled dipeptide: from organogels to microcrystals," *Chemistry—A European Journal*, vol. 16, no. 10, pp. 3176–3183, 2010.
- [9] W. Cai, G.-T. Wang, Y.-X. Xu, X.-K. Jiang, and Z.-T. Li, "Vesicles and organogels from foldamers: a solvent-modulated self-assembling process," *Journal of the American Chemical Society*, vol. 130, no. 22, pp. 6936–6937, 2008.
- [10] T. Naota and H. Koori, "Molecules that assemble by sound: an application to the instant gelation of stable organic fluids," *Journal of the American Chemical Society*, vol. 127, no. 26, pp. 9324–9325, 2005.
- [11] R.-Y. Wang, X.-Y. Liu, and J.-L. Li, "Engineering molecular self-assembled fibrillar networks by ultrasound," *Crystal Growth & Design*, vol. 9, no. 7, pp. 3286–3291, 2009.
- [12] X. Ran, H. Wang, P. Zhang et al., "Photo-induced fiber-vesicle morphological change in an organogel based on an azophenyl hydrazide derivative," *Soft Matter*, vol. 7, no. 18, pp. 8561–8566, 2011.
- [13] L. Frkanec, M. Jokić, J. Makarević, K. Wolsperger, and M. Žinić, "Bis(PheOH) maleic acid amide-fumaric acid amide photoisomerization induces microsphere-to-gel fiber morphological transition: the photoinduced gelation system," *Journal of the American Chemical Society*, vol. 124, no. 33, pp. 9716–9717, 2002.

- [14] Y. Yang, H.-J. Yan, C.-F. Chen, and L.-J. Wan, "Quadruply hydrogen-bonded building block from hydrazide-quinolinone motif and gelation ability of its analogous oxalic monoester-monoamide derivative," *Organic Letters*, vol. 9, no. 24, pp. 4991–4994, 2007.
- [15] X. Zhao, X.-Z. Wang, X.-K. Jiang, Y.-Q. Chen, Z.-T. Li, and G.-J. Chen, "Hydrazide-based quadruply hydrogen-bonded heterodimers. Structure, assembling selectivity, and supramolecular substitution," *Journal of the American Chemical Society*, vol. 125, no. 49, pp. 15128–15139, 2003.
- [16] X. Ran, H. Wang, P. Zhang et al., "Anticlinic smectic phase formed by calamitic hydrazide derivatives with terminal hydroxyl group," *Liquid Crystals*, vol. 38, no. 10, pp. 1227–1237, 2011.
- [17] D. J. Abdallah and R. G. Weiss, "n-Alkanes gel n-alkanes (and many other organic liquids)," *Langmuir*, vol. 16, no. 2, pp. 352–355, 2000.
- [18] S. Qu, F. Li, H. Wang et al., "Twin-tapered molecules containing Bi-dihydrazine units: self-assembly through intermolecular quadruple hydrogen bonding and liquid crystalline behavior," *Chemistry of Materials*, vol. 19, no. 20, pp. 4839–4846, 2007.
- [19] H. Shen, K.-U. Jeong, H. Xiong et al., "Phase behaviors and supra-molecular structures of a series of symmetrically tapered bisamides," *Soft Matter*, vol. 2, no. 3, pp. 232–242, 2006.
- [20] N. V. Venkataraman and S. Vasudevan, "Conformation of methylene chains in an intercalated surfactant bilayer," *Journal of Physical Chemistry B*, vol. 105, no. 9, pp. 1805–1812, 2001.
- [21] M. Shimomura and T. Kunitake, "Fluorescence and photoisomerization of azobenzene-containing bilayer membranes," *Journal of the American Chemical Society*, vol. 109, no. 17, pp. 5175–5183, 1987.

Research Article

Experiment Investigation on Fretting Wear and Wear Debris Performance for the Stem-Cement Interface

Lanfeng Zhang,¹ Shirong Ge,¹ and Hongtao Liu²

¹ School of Mechatronic Engineering, China University of Mining and Technology, Xuzhou 221116, China

² School of Material Science and Engineering, China University of Mining and Technology, Xuzhou 221116, China

Correspondence should be addressed to Lanfeng Zhang; lanfeng_zhang8888@126.com

Received 7 August 2014; Accepted 27 August 2014

Academic Editor: Tifeng Jiao

Copyright © 2015 Lanfeng Zhang et al. This is an open access article distributed under the Creative Commons Attribution License, which permits unrestricted use, distribution, and reproduction in any medium, provided the original work is properly cited.

After the interface debonding, the body protein fluid is subsequently pumped into stem-cement fretting wear interface, serving as the lubricant. On the stem surface, whether there is the influence of protein absorption on fretting wear or not is considered in this study. The biotribological properties at the stem-cement interface were investigated by SEM. The result of hysteresis loops shows that elasticity and plasticity performance of the frictional interface materials can be damaged by fretting fatigue and material energy dissipation will increase periodically. The wear quantity of cement is mainly influenced by load and displacement. The maximum wear loss of bone cement could reach 1.997 mg. Bone cement and titanium alloy wear debris, whose size distributions are widely spread from 1 to 110 μm and 5 to 150 μm , respectively, are shaped like tuber, tear, sheet, strip, and sphere, which will induce the osteocyte damage.

1. Introduction

The failure of cement type total hip replacement (THR) is mainly due to loose interface caused by different modulus of elasticity of contact materials and the patients' debris disease caused by the continuous friction and wear between components' interfaces [1–3]. Though scholars differ greatly in the complicated causes for the loosening and wear after THR, they have widely accepted the continuous fretting wear at the bone cement-stem interface [4]. The results of Jasty and Zhang showed that the stem-bone cement interface has been cited as a weak link, and it has been indicated from clinical and experimental studies that debonding of this interface may be inevitable [5, 6]. Lennon and Prendergast and Goodman demonstrated that the bone cement solidifying technology, human body environment, and the mechanical fretting of bone cement-stem interface work together, which make the influence process of interfacing wears more complicated [7, 8]. In addition, impacted by the tiny interface and metal shadow, it is hard to inspect whether there are fretting wears on interface through X-ray and CT scanning which has been verified by Ryd et al., whereas the stem's sinking distance,

interface's normal load, and microdislocation can damage the elastic-plastic characteristics of replacement components on one hand [9–11] and induce the growth of fibrous tissue and the appearance of wear debris on interface, which initiate aseptic inflammation finally [12, 13]. Therefore, it is urgent to make analysis on fretting wear characteristics of bone cement-stem interface.

Earlier researchers mainly conducted with mechanical fixation and the implantation of prosthesis [14–16], which will induce fretting fatigue and then fretting wear. Later on, researchers discovered that fretting wear is related not only to fatigue but also to environment [15–19], let alone studying the fatigue damage process of implant material through the hysteresis loops, which was complemented by this paper. Accordingly, numerous researches of Geringer et al. focused on the effects of serum on fretting wear interface and found that without albumin the interface wear quantity of concave and convex points increase as the chloride converges, whereas protein not only can protect the interface from being worn but prevent erosion [20–24]. Being influenced by the electrochemistry of the body, Kim et al. find that chloride can increase the quantity of concave and convex points in wear



FIGURE 1: Equipment for the tribology experiment between simulated femoral stem and bone cement: (a) UMT-III universal multifunction tester; (b) titanium alloy and bone cement samples for tests.

region and then generate wear debris, among which 80% are less than 100 nm. These debris are the key ones that induce the growth of fibrous tissue [25–28].

Though clinical reports and instigations revealed the bioreaction, which means reconstruction of femur, of the destruction of human bone caused by wear debris, few researches interpreted the wear mechanism over the course of micromotion and studied the morphology and size of wear debris. This study, which aims to act as a supplement, provides further investigation of bioreaction of wear debris with proof.

2. Materials and Methods

2.1. Experiment Equipment and Materials. The experiment will be made on UMT-III microfriction and wear tester (as illustrated in Figure 1(a), UMT-III, Centre for Tribology Inc., Campbell, CA, USA) produced by USA Center Company. Medical titanium alloy Ti6Al4V pins are adopted with a diameter of 4 mm and a height of 10 mm, which were manufactured to simulate the femoral stem; the average roughness arranges from 0.03~0.06 μm [17]. Bone cement is made into rectangle blocks of 12 mm long, 8 mm wide, and 4 mm high in model making process (as illustrated in Figure 1(b), Synthetic Material Research Institute, Tianjin, China), and the surface roughness is 0.3 μm . Mechanical property and compositions of the tested materials are as follows in Tables 1, 2, and 3 [29, 30].

2.2. Tribological Experiment. Orthogonal fretting wear test of twenty-four samples on titanium alloy and bone cement interface is conducted under different loads and amplitudes. Flat-flat contact model wear test is made in the following conditions (as illustrated in Figure 2), 25°C indoor temperature, 55%~60% humidity, dry friction, and 25% calf serum lubricants (Sijiqing Biological Engineering Materials Co. Ltd., Hangzhou, China) in nylon mould: D (displacement) = ± 30 , ± 40 and ± 50 μm ; F_n (contact normal loads) = 20 N, 40 N, 60 N, and 80 N; the corresponding pressure is 2.75 MPa, 3.89 MPa, 4.72 MPa, and 5.45 MPa [16, 17, 19], respectively. According to the ISO5833 standard, Zhang and Ge found the maximum compression strength of bone cement researched

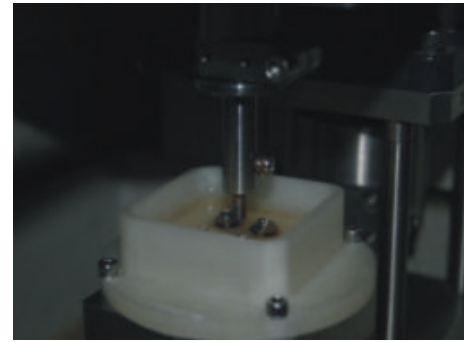


FIGURE 2: Reciprocating fretting friction test.

96.26 MPa [31]. Compared with the maximum contact pressure 64.9 MPa in the study conducted by Zhang et al., this contact pressure could be accepted for the fretting wear test [17]. This was calculated on the basis of the following equations for the contact pressure of cylindrical pads on a plane specimen configuration, according to the Hertz theory [14]. The contact pressure was comparable to the normal contact stress at the stem-bone cement interface, which would be dominant following debonding of the femoral stem from the cement mantle [6, 19]:

$$P_0 = \sqrt{\frac{PE^*}{\pi R}}, \quad (1)$$

$$\frac{1}{E^*} = \left(\frac{1 - \nu_1^2}{E_1} + \frac{1 - \nu_2^2}{E_2} \right).$$

In order to accelerate the test of the gait cycle frequency of 1 Hz, fretting frequency $f = 3$ Hz and the cycle period of 5×10^4 times were selected. This frequency was chosen to accelerate the wear simulation but not to affect the results much [23].

A total of forty-eight samples were divided into two groups to conduct two tests, and each one contains 24 orthogonal tests. Before each test, the specimens including the metallic pin and the bone cement disk were cleaned in an ultrasonic bath using acetone and deionized water for 15 min

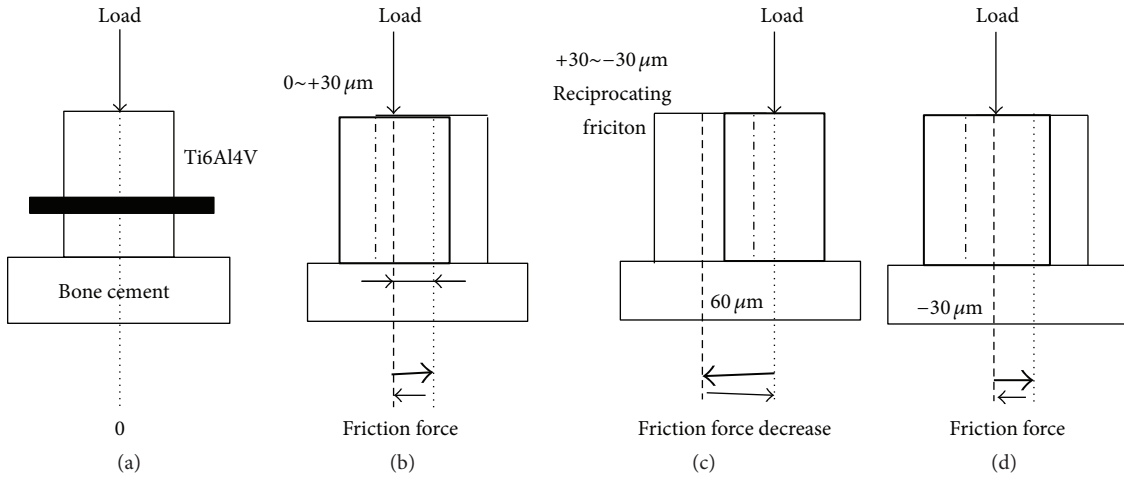


FIGURE 3: Titanium alloy and bone cement interface fretting wear operation illustration: (a) under the load of 20 N, 40 N, 60 N, and 100 N, respectively, Ti6Al4V and bone cement interface contact; (b) fretting starting amplitude; (c) 60 μm move back; (d) to lateral 30 μm , namely, move back to the original location, forming a wear cycle period.

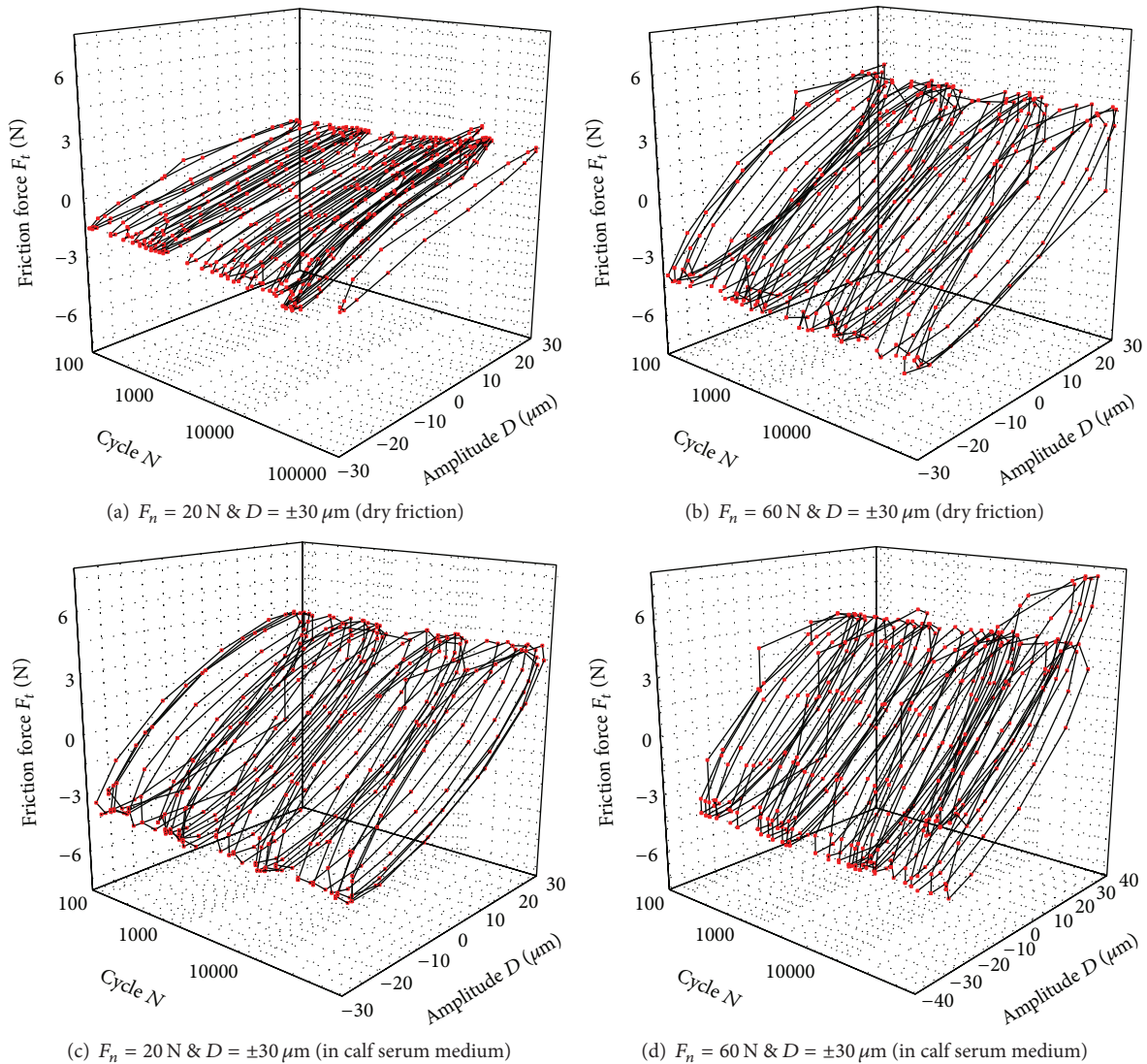
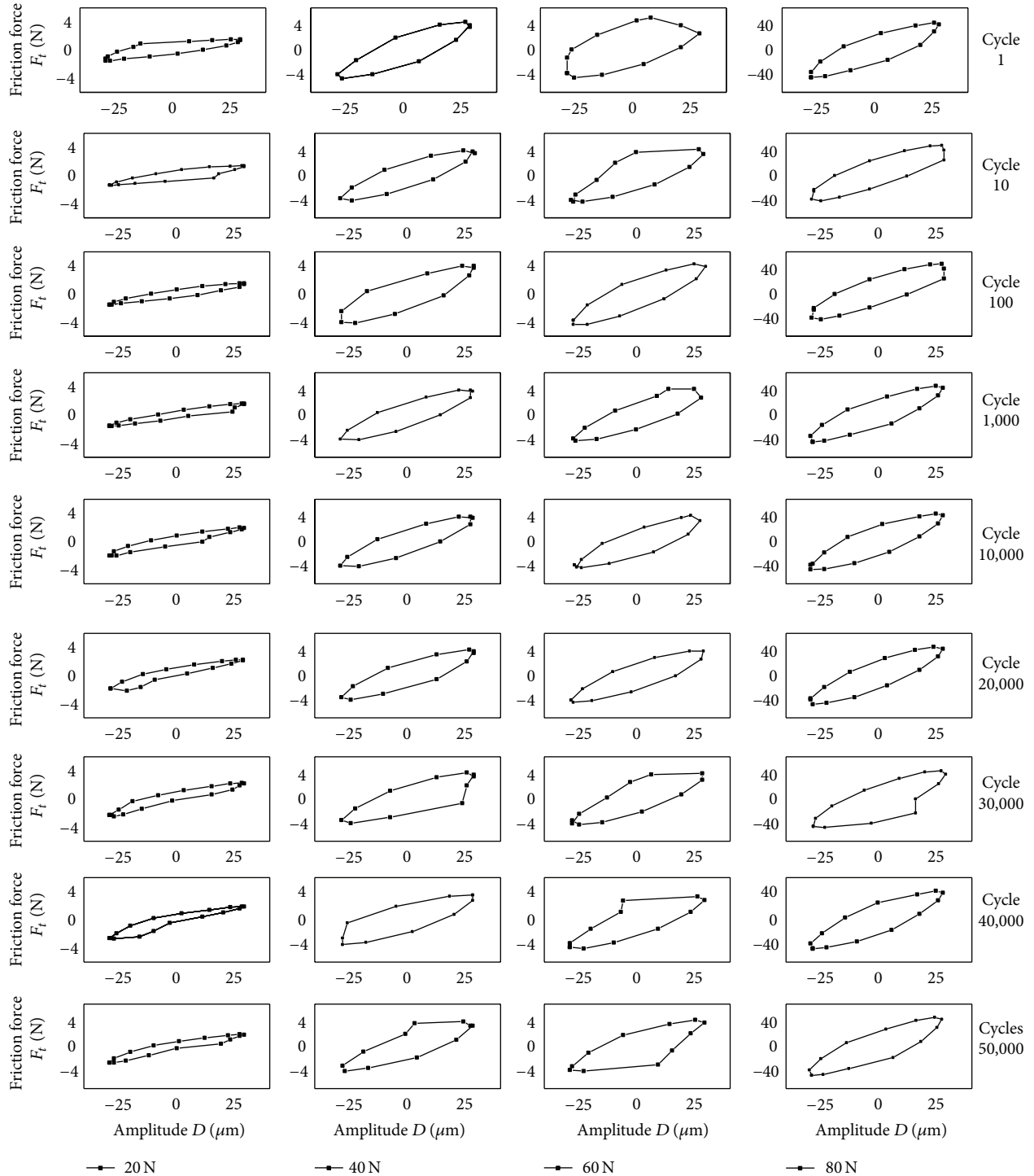


FIGURE 4: F_t - D - N 3D curves of fretting wear of titanium alloy and bone cement in different medium and under different loads.

TABLE 1: Mechanical property of the tested materials.

Mechanical properties	Yong's modulus E (GPa)	Poisson's ratio	Yield stress (MPa)	Ultimate tesnile strength (MPa)	Hardness (Hv)
Ti6Al4V	110	0.3	830	902	331
PMMA	2.5	0.39	65	75	21

FIGURE 5: F_t - D hysteresis loops ($\pm 30 \mu\text{m}$) of titanium alloy and bone cement under different loads in dry test.

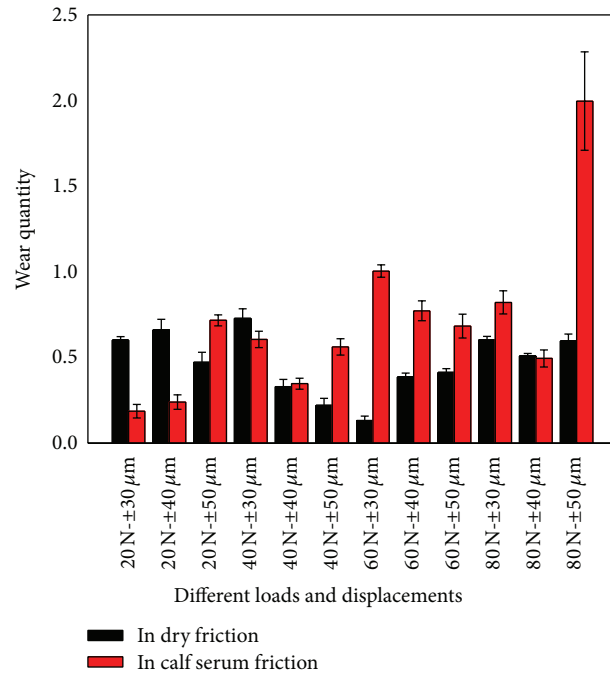


FIGURE 6: Bone cement sample fretting wear quantity.

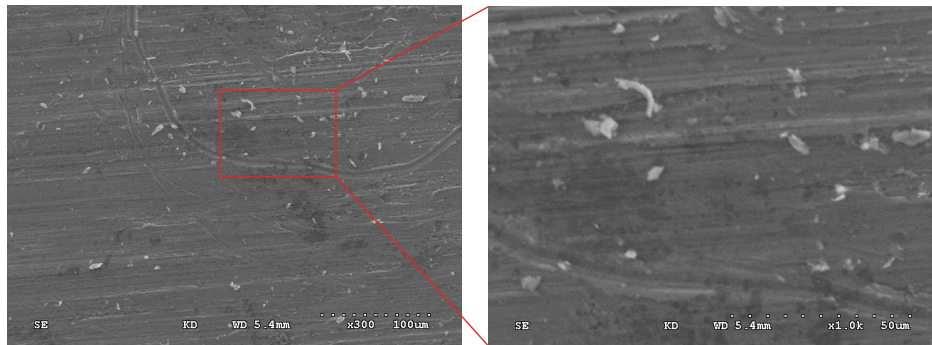


FIGURE 7: SEM graph of bone cement wear debris group.

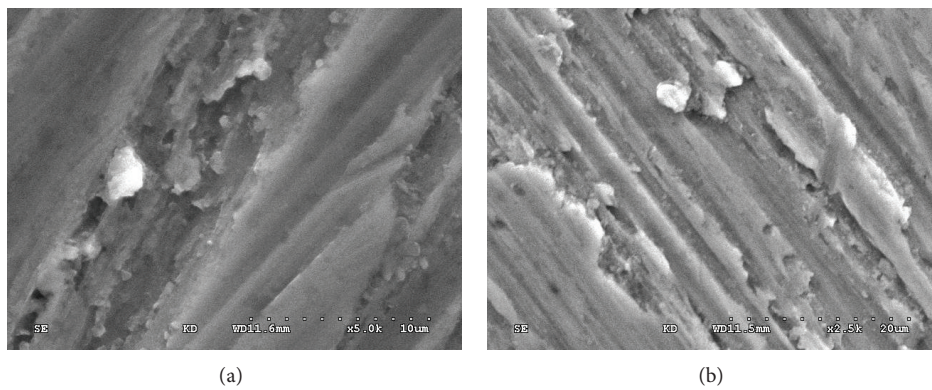


FIGURE 8: Morphology figure of bone cement spherical wear debris.

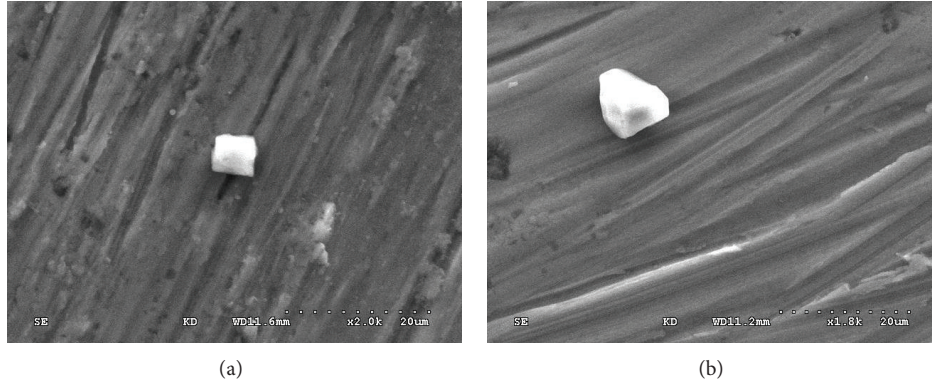


FIGURE 9: Tuberos wear debris of bone cement.

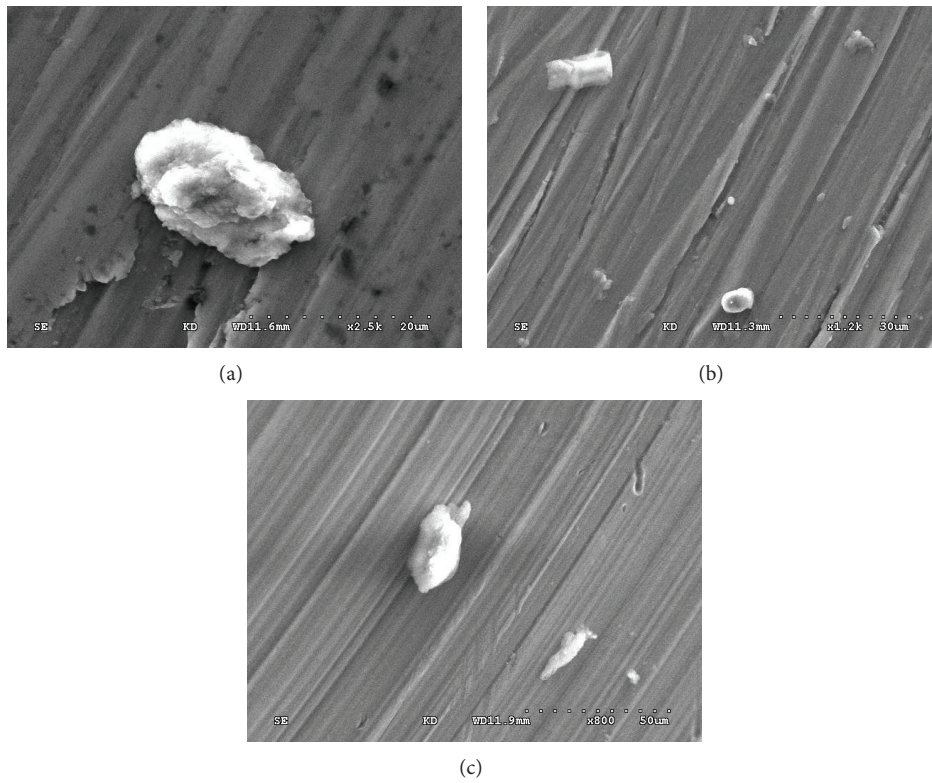


FIGURE 10: Morphology figure of bone cement mussy ellipse wear debris.



FIGURE 11: Lacerated wear debris of bone cement.

TABLE 2: Chemical composition of Ti6Al4V (%).

Al	V	Fe	O	C	N	H	Ti
6.02	4.1	0.168	0.043	0.16	0.02	0.001	89,488

each followed by drying with an N₂ gas jet. After each test, the metallic pin and the bone cement disk were removed from the testing apparatus, dried with the N₂ gas jet [17].

2.3. Evaluation of the Experiment. Draw fretting movement figure (F_t - D - N) on the basis of experiment data (F_t stands for Friction stress and N stands for cycles), analyze the

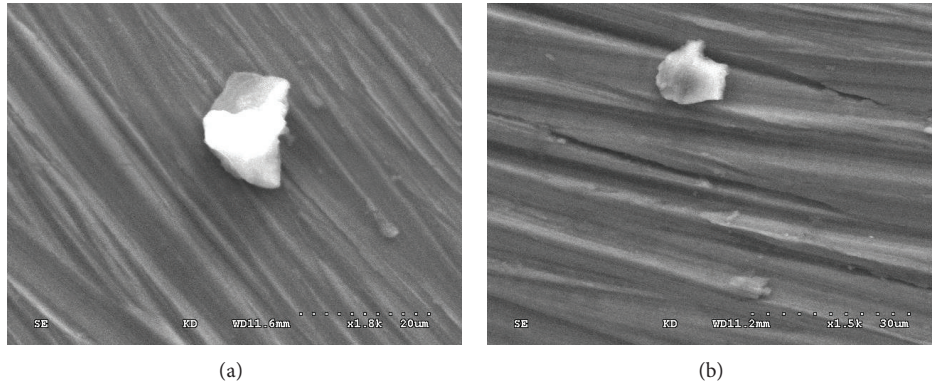


FIGURE 12: Sheet wear debris of bone cement.

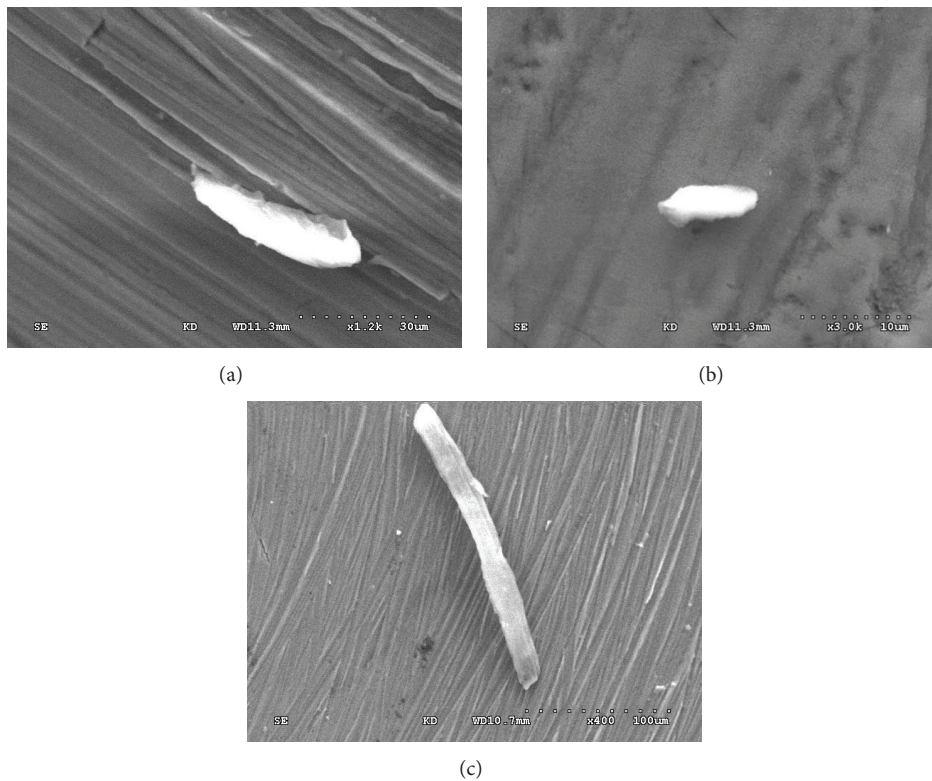


FIGURE 13: Morphology figure of bone cement strip wear debris.

TABLE 3: Composition of CEMEXXL bone cement.

Liquid ingredients	18.33 g
Methyl methacrylate	98.20%
Dimethyl acetal toluic acid	1.80%
Hydroquinone	$7.5 \times 10^{-5}\%$
Powder ingredients	50 g
BaSO ₄	85.00%
Polymethyl methacrylate	12.00%
Benzoyl peroxide	3.00%

movement characteristics of fretting wear region on friction

interface, make statistics on bone cement matrix's wear extent, and draw wear microgram further. Quanta 200 ESEM FEG scanning electron microscope (SEM, FEI, Eindhoven, Netherlands) is applied separately in collecting wear scar feature on the stem-bone cement interface, and analysis is made on the debris shape and its generating mechanism.

Titanium alloy and bone cement interface fretting is a reciprocating process (Figure 3(a)). Take 30 μm starting fretting amplitude for instance, move 30 μm aside and the friction force occurs, the rear end of Ti6Al4V metal material wears with bone cement, which makes an edge wear of 30 μm approximately and the wear scrap accumulation (Figure 3(b)). Shift back 60 μm in unloading; the titanium



FIGURE 14: Morphology figure of bone cement pole-shaped wear debris.

alloy has tip shift back and wear at $\pm 30 \mu\text{m}$ place and makes $30 \mu\text{m}$ wear (Figure 3(c)). Shift the detector aside $30 \mu\text{m}$ to its original place, and forms a wear cycle motion (Figure 3(d)).

3. Results

3.1. Mechanism of Fretting Operation. In purpose of analyzing the process of fretting movement, F_t - D - N curves are being analyzed when $F_n = 20 \text{ N}$ and $D = \pm 30 \mu\text{m}$ and $F_n = 60 \text{ N}$ and $D = \pm 30 \mu\text{m}$, respectively. Figure 4 shows the fretting operation of titanium alloy surface and bone cement matrix under the circumstances of dry friction and calf serum lubricants. In dry friction, when $F_n = 20 \text{ N}$ and $D = \pm 30 \mu\text{m}$, F_t - D curve is in shape of parallelogram at early stage, while with the increase of fretting cycle, when $N \approx 2000$, F_t - D curve transforms into straight line gradually (Figure 4). When $F_n = 60 \text{ N}$ and $D = \pm 30 \mu\text{m}$ (in Figure 4(b)), the distance between loading upper curve and unloading lower curve increases, which illustrates the energy consumption at early stage is slightly higher; meanwhile, when $N \approx 1000$, F_t - D curve transforms into ellipse. When $N = 5000$, the distance between loading upper curve and unloading lower curve decreases, which illustrates the energy consumption drop, whereas in calf serum lubricants, when $F_n = 20 \text{ N}$ and $D = \pm 30 \mu\text{m}$, the F_t - D curve transforms from parallelogram into ellipse ($0 \leq N \leq 1000$), and when $N \approx 5000$, the curve transforms into flat ellipse (Figure 4(d)).

The F_t - D curve transforming into parallelogram at early stage indicates that the contact area is completely in slippage and wear region, and because elasticity and plasticity transformations of different materials occur in contacting and cooperating process, three-matrix abrasion has not formed in friction surface; therefore, the energy consumption of microamplitude is slightly higher. When the load and cycle increase to a certain extent, the F_t - D curve turns into ellipse gradually, which indicates that the tangential fretting operates in mixed region (the medium transition phase between the overall slippage and partial slippage of the interface). With the cycle increase, F_t - D curve will close and transforms into flat ellipse, which indicates that the interface is in balance between elasticity and plasticity transformation and contact stiffness, partial slippage region, and adhesion region come into being on wear interface.

The size of fretting contact area, stress distribution, wear depth, and wear quantity are all determined by loads; F_t - D curve in the same cycle changes with the increase of contact loads. As illustrated in Figure 5, when $N = 1$ (1 cycle), F_t - D curve ($\pm 30 \mu\text{m}$) is basically parallelogram at the early stage, except that under 80 N load is ellipse at the early stage. There is no change when cycle period reaches $N = 10$ (Figure 5) and under 20 N load, which indicates that the surface is still in the elastic area, whereas, when under the loads of 40 N and 60 N , the F_t - D curve transforms from parallelogram into ellipse gradually; for it is just the early stage of wear period, there is no obvious change in fretting diagram. When the load reaches 80 N , obvious elasticity and plasticity transformations occur on the bone cement surface; yet F_t - D curve remains unchanged. When the cycle period reaches $N = 100 \sim 1000$ (Figure 5), F_t - D curves under different loads change gradually. When under 20 N load, the F_t - D curve seems like parallelogram, while under 40 N and 60 N loads, the curves will change alternately between parallelogram and ellipse, which indicates that the wear interface begins to transit from slippage to partial slippage. Analyzing from Figure 4, we can find out from the fretting figure in hysteresis loops of $N = 20,000 \sim 40,000$ and under 20 N load that the original ellipse turns into lines gradually with the influence of cycles, which illustrates that the straight line slopes in the loading and unloading process are the same and the wear quantity remains stable. When under 40 N , 60 N , and 80 N , the F_t - D curve has transformed into stable ellipse. When the cycle period reaches $5,000$ cycles, F_t - D curve remains stable; the fretting diagram under 20 N loads is linear while that under 40 N , 60 N , and 80 N turns into stable ellipse.

3.2. Fretting Wear Quantity Analysis of Bone Cement Matrix. As illustrated in Figure 6, the wear quantity of bone cement sample increases with adding contact loads in different wear conditions, amplitudes, and loads. Some researches demonstrated that the proteins in fretting tribological behavior play a passive role in protecting the wear region [20–28]. Under the same contact load, the wear quantity of bone cement in the calf serum is greater than that in the air.

3.3. Morphology Study on Wear Debris

3.3.1. Morphology Study on Bone Cement Wear Debris. After transplanting the artificial stem into human's body, for the extremely rigid biological friction and wear environment on titanium alloy and bone cement interface, friction interrelated biomechanical changes are unpredictable and the wear period is relatively long; therefore wear types can be found out through the study on the interrelated wear debris appearance produced in friction. As shown in Figure 7, the bone cement wear debris are in various shapes, including the wear debris in strip, block, sheet, and ball shape and the different particle sizes. Some basic rules can be found out that the larger the size of the wear debris is, the more complicated the surface becomes, and the appearance of wear debris with smaller particle size transforms gradually into spherality or near spherality. After studying and observing the wear debris for

several times, we find that it is a common and universal rule. The matrix of wear debris in SEM picture is titanium alloy, because the wear debris are so small that they could not be deprived from the friction contact surface.

(I) *Spherical Wear Debris*. The maximum and minimum debris sizes of spherical wear debris are basically $10\ \mu\text{m}$ and $1\ \mu\text{m}$ approximately, which distributes widely and is one kind of wear debris that exist in greatest amount. It can be found in Figure 8 that the surface texture of the spherical wear debris is quite smooth. It is inspected that wear debris with large particle sizes usually exist in shapes of block, sheet, or strip, whereas those with small particle sizes tend to be in spherical or near spherical shapes, which results from the cooperation of repeated rubbing in the reciprocating fretting wear and the debris wear, which is formed in the late period of wear debris abrasion. When the wear debris accumulate to a certain degree, they will be attached to bone bed and induce osteoclast activating factor to make broken bone physiological response under the joint capsule press and they are the main wear debris that induce hip aseptic joint replacement loosening.

(II) *Tuberous Wear Debris*. The length and width ratio of tuberous wear debris (Figure 9) is nearly $2\ \mu\text{m}$ with the spindle-shaped or flat tuberous appearance, and obvious lines rise and fall on its surface. Water prop shaped wear debris is mainly formed by adhesion wear and is always ripped or torn in the process, and its particle size is about $5\ \mu\text{m}$, while flat wear debris originate from the crack nuclear on friction surface caused by fatigue stress on the friction interrelated surface, which rips off at the weak bonding point of bone cement matrix under the friction interrelated adhesion, and its particle size is about $2\sim 20\ \mu\text{m}$. The debris are formed at the interface debonding period, attached to the titanium alloy surface, and are the early product of fretting wear.

(III) *Ellipse Wear Debris*. The width and length ratio of ellipse wear debris is from 2 to 5 and the appearance takes the shape of ellipse (Figure 10). Obvious lines rise and fall on wear debris surface, which is mainly produced and developed from bone cement tuberous wear debris. Tuberous debris are polished into ellipsoid gradually under the reciprocating wear model and long term three-matrix abrasion, and the ellipsoid wear debris are the early forms of spherical wear debris with the particle size of 2 to $15\ \mu\text{m}$ approximately. This type of wear debris is formed under the repeated roller compacted damage of large bone cement tuberous wear debris ripped off.

(IV) *Lacerated Wear Debris*. Lacerated wear debris originates from the dropping of asperity slippage wear which makes cracks on matrix surfaces, for wear debris produces in the same direction with that of crack extension, the existing parts peel off from matrix under cutting and furrowing, together with fatigue wear, lacerated wear debris come into being. This type of debris has irregular and coarse edge line and the particle size is $5\sim 35\ \mu\text{m}$ (Figure 11), which is formed at the fatigue wear stage.

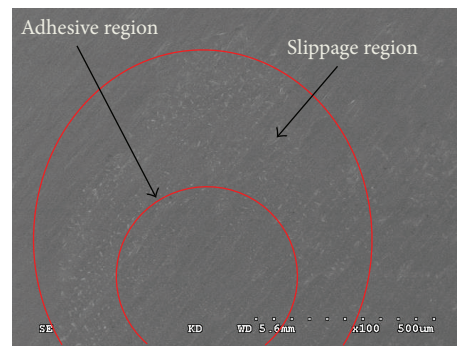


FIGURE 15: SEM Morphology graph of Ti6Al4V alloy wear debris group.

(V) *Sheet Wear Debris*. Sheet wear debris has relatively large area and small thickness and takes the shape of irregular polygon (Figure 12). It is mainly because the tiny materials peel off between surface and subsurface under fatigue effect and then, attached to material surface, sheet wear debris is formed after reciprocating press, and its particle size is 20 to $50\ \mu\text{m}$. This kind of wear debris is formed at the fatigue wear stage.

(VI) *Strip Wear Debris*. Pole-shaped wear debris has a diversified structure in appearance. There are mainly three formation reasons for strip wear debris; firstly, the matrix is ripped off the matrix in scraping action; secondly, wear debris are formed in the friction process; thirdly, sheet wear debris are rubbed into rope shaped wear debris in friction interrelated motion, which reflects the motion state of reciprocating fretting wear, and the length of wear debris is 15 to $110\ \mu\text{m}$ (Figure 13). It is the derived product of ellipsoid wear debris and it is formed at the middle and late stages.

(VII) *Pole-Shaped Wear Debris*. Pole-shaped wear debris has a diversified structure in appearance, curvy edge line, and stable surface lines, and its size is 5 to $30\ \mu\text{m}$. There are two main reasons for the formation of pole-shaped wear debris; firstly, debris are produced in thermoplastic transformation and microcutting. Pole-shaped wear debris are usually produced in breaking in period with the size of $10\sim 50\ \mu\text{m}$. Secondly, it is formed because of the falling furrow edge drop in surface cutting, and its size is 10 to $80\ \mu\text{m}$ (Figure 14). Pole-shaped wear debris are generated at the same stage with strip wear debris and then suffer from abrasive wear.

3.3.2. *Morphology Study on Titanium Alloy Wear Debris*. It can be found in Figure 15 that titanium alloy wear debris are small in size and most of which take the irregular

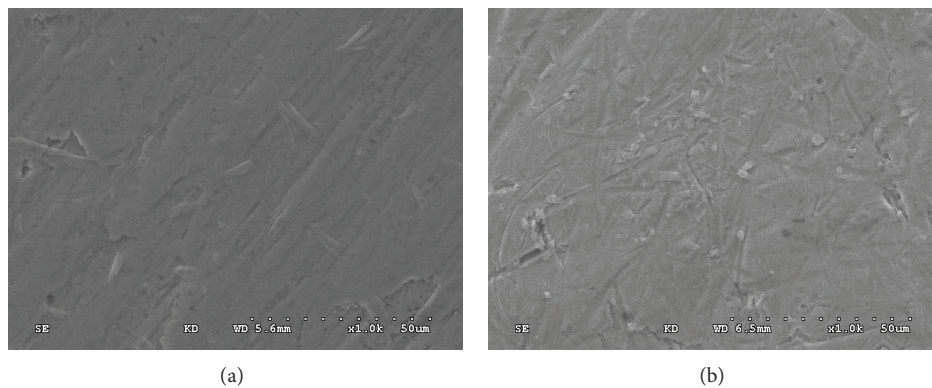


FIGURE 16: Morphology figure of titanium alloy strip wear debris: (a) debris in dry condition; (b) debris calf serum.

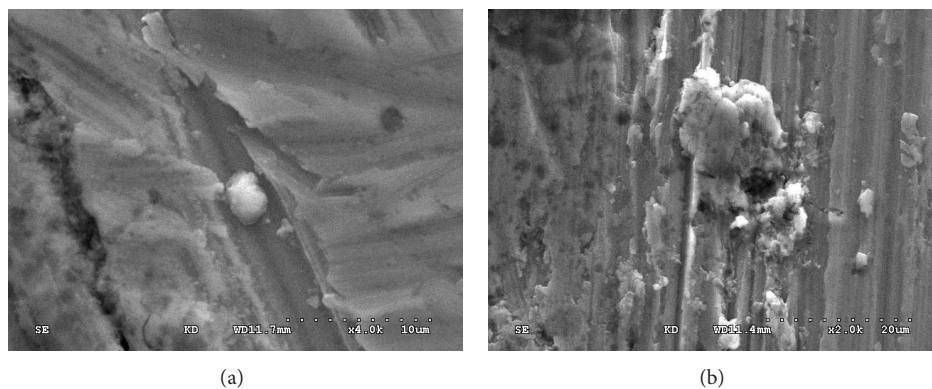


FIGURE 17: Morphology figure of titanium alloy spherical wear debris.

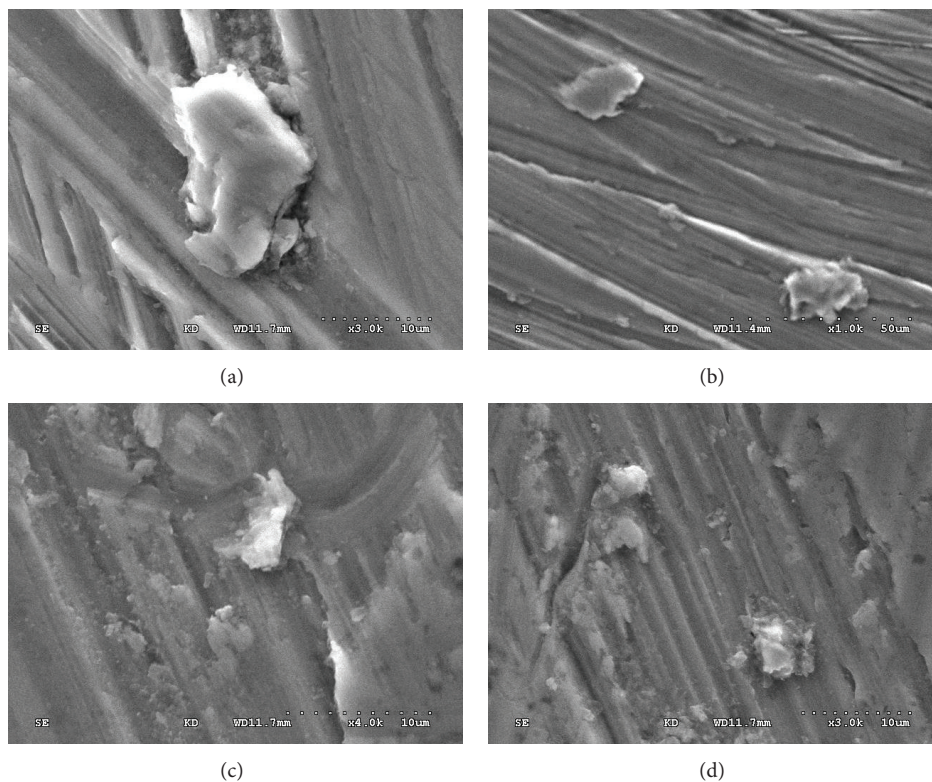


FIGURE 18: Morphology figure of titanium alloy tuberosus wear debris.

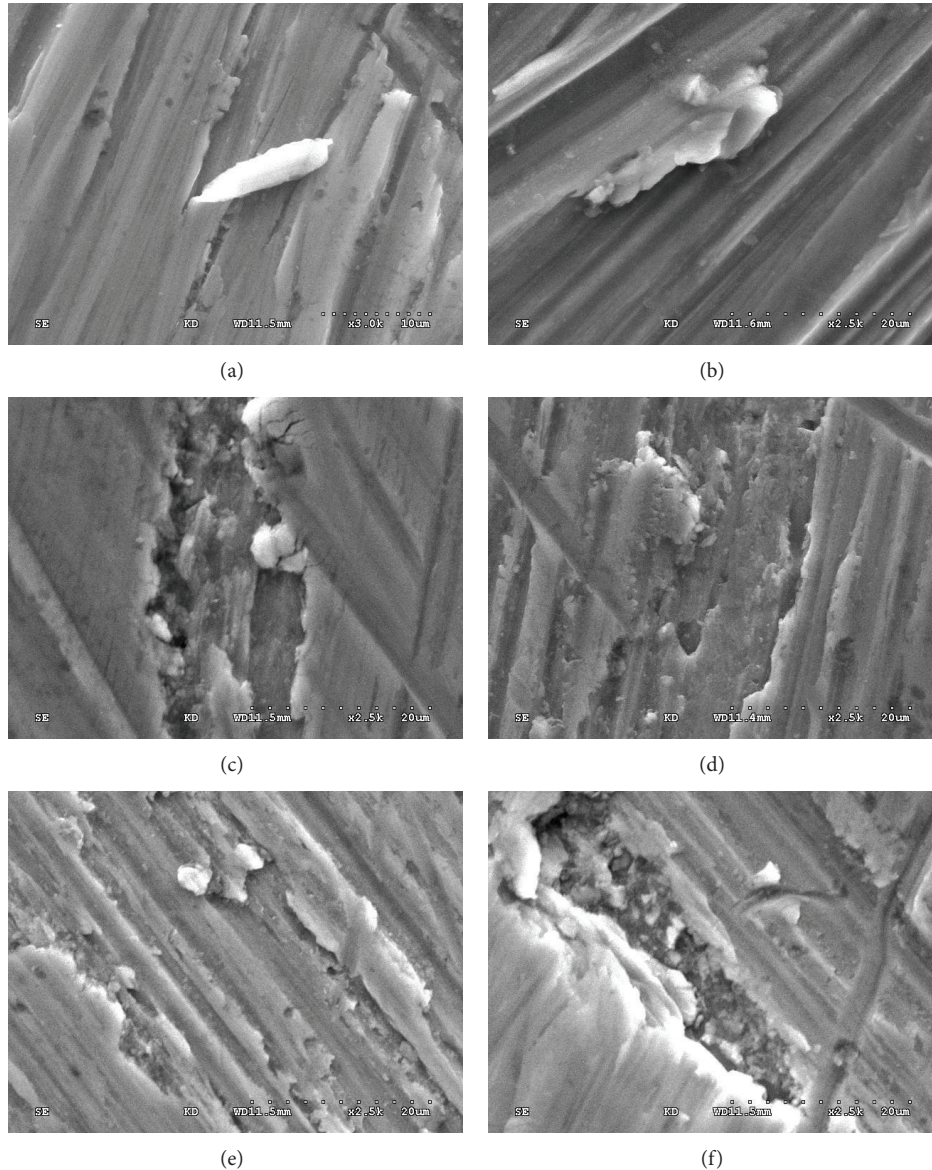


FIGURE 19: Morphology figure of titanium alloy lacerated wear debris.

shapes. Though its modulus of elasticity is higher than that of the bone cement, the inserted metals exist in long-term complicated fatigue damage conditions, which will accelerate the crack extension on wear surface and lead to the formation of wear debris at last and the generation of osteoclast factors. Therefore, study on titanium alloy wear debris' forms is quite significant.

(I) Strip Wear Debris. Strip wear debris is commonly seen in titanium alloy wear debris group with the size of 10 to 50 μm . It has rather smooth surfaces and there are various reasons for its formation. First of all, the previously ripped small titanium alloy wear debris transform gradually into abrasive wear form in fatigue wear process. On the other hand, the large sheet wear debris' edges are hardened and become thin and sharp

which scrapes titanium alloy matrix in friction process. Such kind of wear debris has rather sharp wings; the existing wear debris on friction surface generated in fretting wear process come into being (Figure 16) at the late stage.

(II) Spherical Wear Debris. Spherical wear debris of titanium alloy in spherical shape are shown in Figure 17(a) which are small in size and whose distribution scopes are usually smaller than 15 μm . There are uneven lines on the surface and many debris gather around. (Figure 17(b)). They are mainly the products of fatigue wear and adhesion wear caused by the broken large wear debris which come into being in titanium alloy fretting wear. In addition, the falling debris cannot escape from wear region easily and finally the spherical wear debris comes into being with the size of 1 to 30 μm approximately. This type of wear debris is formed in the late period of fatigue wear.

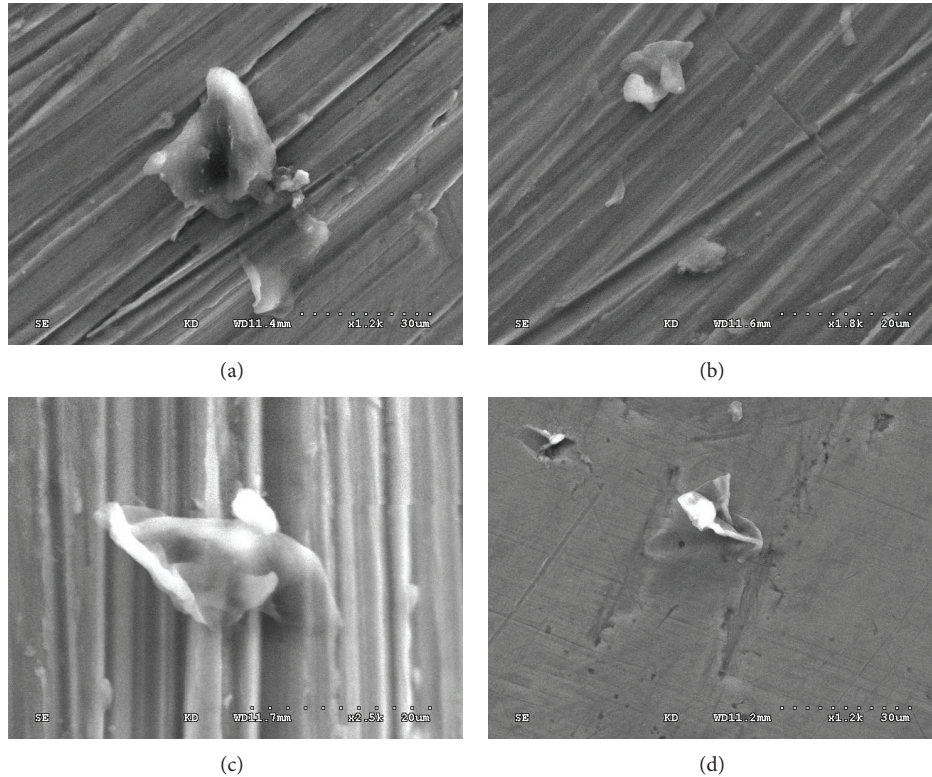


FIGURE 20: Morphology figure of titanium alloy sheet wear debris.

(III) *Tuberous Wear Debris*. Wear debris of this type are spindle-shaped (Figures 18(a) and 18(b)) or in flat shape (Figures 18(c) and 18(d)) with a small width and length ratio and complicated edge outlines, and there are uneven lines even obvious scars. Spindle-shaped wear debris come mainly from adhesion wear with a size of 5 to 100 μm , while the flat wear debris are formed because the crack nuclei formed on friction surface under the fatigue stress on the friction interrelated surface peel off and tear away from matrix at the weak bonding point of matrix materials under the effect of interface adhesion, and their distribution scopes are 5 to 50 μm . They originate from lacerated wear formation and come into being at the mid-term stage of fatigue wear.

(IV) *Lacerated Wear Debris*. Lacerated wear debris are the products of friction interrelated reciprocating motion with irregular and coarse surface and uneven lines on the surface which give people the sense of hierarchy and mainly from the falling debris from titanium alloy matrix under the fretting fatigue effect (Figures 19(a) and 19(b)). With the cycle load, cracks on fatigue wear edges extend in vertical direction with wear direction (Figures 19(c) and 19(d)). The successive wear accelerates the ripping of titanium alloy surface and then the wear debris come into being. The common size distribution scope is 5 to 50 μm and titanium alloy extends in different sizes from partial peeling to complete peeling which makes the wide distribution of wear particle size (Figures 19(e) and

19(f)). This kind of wear debris is formed at the early stage of fatigue wear.

(V) *Sheet Wear Debris*. The titanium alloy sheet wear debris have relatively wide size distribution ranging within the scope between 5 and 60 μm and smooth surface. There are two reasons for the formation. On the one hand, the early stripping tuberous debris of titanium alloy transform and harden in fretting wear process, and for the hardness and tension are higher than those of the matrix, therefore this type of wear debris comes into being. On the other hand, the fatigue peeling occurs on the wear surface of large titanium alloy under the effect of fretting wear which is broken into wear debris in smaller sizes in the reciprocating wear motion (Figure 20). This type of wear debris originates from tuberous wear debris and forms at the late stage of fatigue wear.

These results, which were consistent with other clinical results in other literature, proved that the particles shaped like spherical, sheet, and so forth were the main reason why a series of bioresponses like the increase of osteoclast were induced [32, 33]. Also, through the analysis of the morphology of wear debris, not only did this paper refine the research used to be analyzed just from the aspect of size in clinic but also it provided further analysis of the bioresponses induced by different morphology and size of the wear debris with evidence.

4. Conclusions

In this study, the fretting wear mechanism and debris analysis at the stem-bone cement interface under fretting wear were investigated through a series of frictional tests. The following conclusions can be drawn from this work.

- (1) Compared with hysteresis loops under different loads and displacements, the result shows that elasticity and plasticity performance of the frictional interface materials can be damaged by fretting fatigue. In addition, material energy dissipation will increase periodically.
- (2) The wear quantity of the bone cement is mainly influenced by load and displacement. As load increases, the albumin passive film gradually fails to protect the wear interface. The maximum of the wear loss between stem and bone cement for displacement 100 μm and load 80 N could reach 1.997 mg.
- (3) Bone cement wear debris' size distribution is relatively widely spread from 1 to 110 μm . The bone cement wear debris in tuberous, tear, and sheet shapes are formed at the early interface ripping stage, while sheet and strip wear debris will be affected by fatigue wear and reciprocating acts, respectively. The spherical wear debris is the main wear debris. Titanium alloy wear debris's size ranges from 5 to 150 μm , and tuberous and sheet wear debris are formed at the early and middle stage. Tear-shaped wear debris are affected by fatigue wear while sphere and trip wear debris are formed at the late stage under the influence of wear acts. In this paper, fretting wear properties and morphology and the size distribution of the wear debris were detected in fretting wear test [32–39], which was consistent with the results of the size of wear debris in other literature. Moreover, different morphology of titanium alloy and bone cement debris was listed in this paper according to the classification of morphology, which served as a complement in this research.

Conflict of Interests

The authors declared that they have no conflict of interests regarding the publication of this work.

Acknowledgments

This work is supported and sponsored by Qing Lan Project and the Scientific Innovation Research of College Graduate in Jiangsu Province (no. KYLX.1376).

References

- [1] W. H. Harris, "The problem is osteolysis," *Clinical Orthopaedics and Related Research*, no. 311, pp. 46–53, 1995.
- [2] C. H. Rorabeck, R. B. Bourne, B. D. Mulliken et al., "The Nicolas Andry award: comparative results of cemented and cementless total hip arthroplasty," *Clinical Orthopaedics and Related Research*, no. 325, pp. 330–344, 1996.
- [3] Y. T. Konttinen, J.-W. Xu, H. Pätälä et al., "Cytokines in aseptic loosening of total hip replacement," *Current Orthopaedics*, vol. 11, no. 1, pp. 40–47, 1997.
- [4] D. Bin and P. C. Noble, "Aseptic loosening of cemented stem following cemented hip arthroplasty: analysis of 36 revised specimens," *Journal of Clinical Rehabilitative Tissue Engineering Research*, vol. 13, no. 26, pp. 5176–5180, 2009.
- [5] M. Jasty, W. J. Maloney, C. R. Bragdon, D. O. O'Connor, T. Haire, and W. H. Harris, "The initiation of failure in cemented femoral components of hip arthroplasties," *Journal of Bone and Joint Surgery—Series B*, vol. 73, no. 4, pp. 551–558, 1991.
- [6] L.-F. Zhang, S.-R. Ge, H.-T. Liu, K.-J. Guo, S.-Y. Han, and J.-Y. Qi, "Bond strength analysis of the bone cement-stem interface of hip arthroplasties," *Asian Pacific Journal of Tropical Medicine*, vol. 7, no. 2, pp. 153–159, 2014.
- [7] A. B. Lennon and P. J. Prendergast, "Evaluation of cement stresses in finite element analyses of cemented orthopaedic implants," *Journal of Biomechanical Engineering*, vol. 123, no. 6, pp. 623–628, 2001.
- [8] S. B. Goodman, "The effects of micromotion and particulate materials on tissue differentiation: bone chamber studies in rabbits," *Acta orthopaedica Scandinavica. Supplementum*, vol. 65, no. 258, pp. 1–43, 1994.
- [9] L. Ryd, "Roentgen stereophotogrammetric analysis of prosthetic fixation in the hip and knee joint," *Clinical Orthopaedics and Related Research*, no. 276, pp. 56–65, 1992.
- [10] J. Kärrholm, B. Borssen, G. Lowenhielm, and F. Snorrason, "Does early micromotion of femoral stem prostheses matter? 4–7-year stereoradiographic follow-up of 84 cemented prostheses," *Journal of Bone and Joint Surgery—Series B*, vol. 76, no. 6, pp. 912–917, 1994.
- [11] C. A. Engh, D. O'Connor, M. Jasty, T. F. McGovern, J. D. Bobyn, and W. H. Harris, "Quantification of implant micromotion, strain shielding, and bone resorption with porous-coated anatomic medullary locking femoral prostheses," *Clinical Orthopaedics and Related Research*, no. 285, pp. 13–29, 1992.
- [12] M. Jasty, C. Bragdon, D. Burke, D. O'Connor, J. Lowenstein, and W. H. Harris, "In vivo skeletal responses to porous-surfaced implants subjected to small induced motions," *Journal of Bone and Joint Surgery A*, vol. 79, no. 5, pp. 707–714, 1997.
- [13] X. Cai, J. Wang, and S. Lu, "Comparative study of PDGF-B and BMP-7 receptors distribution on histiocytes of interface membranes around aseptic loosened prostheses," *Chinese Journal of Orthopaedics*, vol. 6, no. 1, pp. 26–28, 2001.
- [14] D. Nowell and D. Dini, "Stress gradient effects in fretting fatigue," *Tribology International*, vol. 36, no. 2, pp. 71–78, 2003.
- [15] L. A. Blunt, H. Zhang, S. M. Barrans, X. Jiang, and L. T. Brown, "What results in fretting wear on polished femoral stems," *Tribology International*, vol. 42, no. 11–12, pp. 1605–1614, 2009.
- [16] H. Zhang, L. Brown, L. Blunt, X. Jiang, and S. Barrans, "The contribution of the micropores in bone cement surface to generation of femoral stem wear in total hip replacement," *Tribology International*, vol. 44, no. 11, pp. 1476–1482, 2011.
- [17] H. Y. Zhang, J. B. Luo, M. Zhou, Y. Zhang, and Y. L. Huang, "Biotribological properties at the stem-cement interface lubricated with different media," *Journal of the Mechanical Behavior of Biomedical Materials*, vol. 20, pp. 209–216, 2013.

- [18] H. Zhang, L. T. Brown, L. A. Blunt, X. Jiang, and S. M. Barrans, "Understanding initiation and propagation of fretting wear on the femoral stem in total hip replacement," *Wear*, vol. 266, no. 5-6, pp. 566-569, 2009.
- [19] H. Y. Zhang, L. A. Blunt, X. Q. Jiang, L. T. Fleming, and S. M. Barrans, "The influence of bone cement type on production of fretting wear on the femoral stem surface: a preliminary study," *Clinical Biomechanics*, vol. 27, no. 7, pp. 666-672, 2012.
- [20] J. Geringer, B. Forest, and P. Combrade, "Fretting-corrosion of materials used as orthopaedic implants," *Wear*, vol. 259, no. 7-12, pp. 943-951, 2005.
- [21] J. Geringer, K. Kim, and B. Boyer, "14-Fretting corrosion in biomedical implants," in *Tribocorrosion of Passive Metals and Coatings*, D. Landolt and S. Mischler, Eds., pp. 401-423, Woodhead Publishing, 2011.
- [22] J. Geringer, M. T. Mathew, M. A. Wimmer, and D. D. Macdonald, "2-Synergism effects during friction and fretting corrosion experiments—focusing on biomaterials used as orthopedic implants," in *Biomaterials and Medical Tribology*, J. P. Davim, Ed., pp. 133-180, Woodhead Publishing, 2013.
- [23] J. Geringer, J. Pellier, F. Cleymand, and B. Forest, "Atomic force microscopy investigations on pits and debris related to fretting-corrosion between 316L SS and PMMA," *Wear*, vol. 292-293, pp. 207-217, 2012.
- [24] J. Geringer, K. Kim, J. Pellier, and D. D. Macdonald, "Fretting corrosion processes and wear mechanisms in medical implants," in *Bio-Tribocorrosion in Biomaterials and Medical Implants*, Y. Yan, Ed., pp. 45-73, Woodhead Publishing, Cambridge, UK, 2013.
- [25] K. Kim and J. Geringer, "Analysis of energy dissipation in fretting corrosion experiments with materials used as hip prostheses," *Wear*, vol. 296, pp. 497-503, 2012.
- [26] J. Pellier, J. Geringer, and B. Forest, "Fretting-corrosion between 316L SS and PMMA: influence of ionic strength, protein and electrochemical conditions on material wear. Application to orthopaedic implants," *Wear*, vol. 271, no. 9-10, pp. 1563-1571, 2011.
- [27] B. R. Zhang, Z. B. Cai, X. Q. Gan, M. H. Zhu, and H. Y. Yu, "Dual motion fretting wear behaviors of titanium and its alloy in artificial saliva," *Transactions of Nonferrous Metals Society of China*, vol. 24, no. 1, pp. 100-107, 2014.
- [28] M. Bryant, R. Farrar, K. Brummitt, R. Freeman, and A. Neville, "Fretting corrosion of fully cemented polished collarless tapered stems: the influence of PMMA bone cement," *Wear*, vol. 301, no. 1-2, pp. 290-299, 2013.
- [29] J.-H. Yi, X.-Z. Lin, Z.-B. Cai, M.-X. Shen, L.-P. He, and M.-H. Zhu, "Study on torsional fretting corrosion behaviors of Ti6Al4V alloy in the serum solution," *Journal of Functional Materials*, vol. 43, no. 7, pp. 919-923, 2012.
- [30] L. Wu and D. Zhang, "Fretting wear study on the interface between titanium alloy ball and bone cement," *Journal of Lubrication Engineering*, vol. 36, no. 8, pp. 48-55, 2011.
- [31] L. F. Zhang and S. R. Ge, "The effect of acrylic bone cement solidification conditions on the compressive property," *Advanced Materials Research*, vol. 197-198, pp. 1694-1699, 2011.
- [32] J. S. Day, R. M. Baxter, M. L. Ramsey et al., "Characterization of wear debris in total elbow arthroplasty," *Journal of Shoulder and Elbow Surgery*, vol. 22, no. 7, pp. 924-931, 2013.
- [33] J. R. Howell, L. A. Blunt, C. Doyle, R. M. Hooper, A. J. C. Lee, and R. S. M. Ling, "In vivo surface wear mechanisms of femoral components of cemented total hip arthroplasties: the influence of wear mechanism on clinical outcome," *The Journal of Arthroplasty*, vol. 19, no. 1, pp. 88-101, 2004.
- [34] P. Sanz-Ruiz, E. Paz, J. Abenojar, J. Carlos del Real, J. Vaquero, and F. Forriol, "Effects of vancomycin, cefazolin and test conditions on the wear behavior of bone cement," *Journal of Arthroplasty*, vol. 29, no. 1, pp. 16-22, 2014.
- [35] D. R. Sumner, H. Kienapfel, J. J. Jacobs, R. M. Urban, T. M. Turner, and J. O. Galante, "Bone ingrowth and wear debris in well-fixed cementless porous-coated tibial components removed from patients," *The Journal of Arthroplasty*, vol. 10, no. 2, pp. 157-167, 1995.
- [36] V. Thomas, B. A. Halloran, N. Ambalavanan, S. A. Catledge, and Y. K. Vohra, "In vitro studies on the effect of particle size on macrophage responses to nanodiamond wear debris," *Acta Biomaterialia*, vol. 8, no. 5, pp. 1939-1947, 2012.
- [37] R. L. Buly, M. H. Huo, E. Salvati, W. Brien, and M. Bansal, "Titanium wear debris in failed cemented total hip arthroplasty. An analysis of 71 cases," *The Journal of Arthroplasty*, vol. 7, no. 3, pp. 315-323, 1992.
- [38] T. Jiao, Y. Wang, Q. Zhang, J. Zhou, and F. Gao, "Regulation of substituent groups on morphologies and self-assembly of organogels based on some azobenzene imide derivatives," *Nanoscale Research Letters*, vol. 8, article 160, 2013.
- [39] T. Jiao, Q. Huang, Q. Zhang, D. Xiao, J. Zhou, and F. Gao, "Self-assembly of organogels via new luminol imide derivatives: diverse nanostructures and substituent chain effect," *Nanoscale Research Letters*, vol. 8, article 278, 2013.

Research Article

Ball Milling to Build the Hybrid Mesocrystals of Ibuprofen and Aragonite

Kyoung A Cho, Insil Choi, and Il Won Kim

Department of Chemical Engineering, Soongsil University, Seoul 156-743, Republic of Korea

Correspondence should be addressed to Il Won Kim; iwkim@ssu.ac.kr

Received 4 July 2014; Accepted 3 September 2014

Academic Editor: Xinqing Chen

Copyright © 2015 Kyoung A Cho et al. This is an open access article distributed under the Creative Commons Attribution License, which permits unrestricted use, distribution, and reproduction in any medium, provided the original work is properly cited.

Mesocrystal formation is one of the new paradigms of the nonclassical crystallization, where the assembly of crystal domains is observed. Also, it has been recently employed in studies on drug formulation to utilize controlled dissolution of the drug domains. In this report, ibuprofen was attempted to form hybrid mesocrystals with calcium carbonate crystals. Two polymorphs of calcium carbonate (aragonite and calcite) were used during the solid-state process of ball milling. Structural analyses confirmed the mesocrystal formation of ibuprofen with aragonite but not with calcite. The origin of the observed behavior was found from the higher affinity of ibuprofen to aragonite, especially its (0 1 0) surface, compared to calcite. The hybrid mesocrystals of ibuprofen and aragonite showed the environment-responsive release behavior, where the stability of aragonite was the controlling factor for the release kinetics of ibuprofen.

1. Introduction

Mesocrystals are increasingly found as the products of nonclassical crystallization in the diverse fields of materials [1]. The examples are especially abundant in biological and bioinspired crystallization. For example, the nacre of red abalone is constructed as the layers of microcrystals that are also the assembled structures of nanocrystals [2, 3]. Similar findings have been seen in the nacre of giant oyster, the spicules of calcareous sponges, and the skeletal structure of sea urchins [4–6]. In addition, synthetic mesocrystals inspired by biomineralization have been reported in the solution crystallization, where the crystal assembly was through interparticle interactions and/or heterogeneous nucleation [7–10].

Controlled release has attracted great interest in the pharmaceutical research. The basic notion is to maintain the drug concentration in blood above the effective level and below the safe concentration for a sustained period of time, and many efforts have been made at the same time to develop environment-responsive systems that satisfy the specific needs of the drugs [11]. Mesocrystals have been also explored in this regard to control the dissolution rate of the active pharmaceutical ingredients (APIs). For example, the sustained

release of carbamazepine and adefovir dipivoxil was associated with their mesocrystal formation induced by polymeric additives [12, 13]; the enhanced release of ibuprofen was found for its mesocrystals formed with sodium dodecyl sulfate [14].

Mechanical milling was utilized to prepare hybrid structures of APIs with inorganic materials, such as silica, magnesium aluminosilicate, aluminum silicate, and aluminum hydroxide, to alter the physicochemical properties of the APIs [15–18]. It has been also extensively explored in recent years to prepare cocrystals and solvates/hydrates of APIs, and the solid-state process without or minimal use of solvents makes it attractive as a greener process than conventional procedures [19–22].

In the present study, we have attempted a simple method of ball milling to prepare hybrid mesocrystals of ibuprofen (IBU) and calcium carbonate. We explored two anhydrous polymorphs of calcium carbonate (calcite and aragonite) since the distinctive molecular arrangements of the active surfaces could contribute to the different interactions with IBU. Also, the pH-responsive dissolution behaviors of the mesocrystals were expected because of the high and sparing solubility of calcium carbonate at low and neutral pH, respectively [23].

2. Materials and Methods

2.1. Preparation of Calcite and Aragonite. Two polymorphs of anhydrous calcium carbonate were prepared following a method using water-alcohol mixtures [24]. To obtain calcite, sodium carbonate (26.0 mmol, 2.75 g; Na_2CO_3 : $\geq 99.0\%$, Sigma-Aldrich, Milwaukee, WI, USA) was completely dissolved in the solution of 100 mL ethanol (HPLC grade, 99.0%, Samchun, Pyeongtaek, South Korea) and 900 mL deionized water (DI water: resistivity of 18.2 M Ω ·cm, Direct-Q from Millipore, Billerica, MA, USA) contained in a 1000 mL volumetric flask at room temperature (ca. 25°C), and then calcium chloride (26.0 mmol, 2.89 g; CaCl_2 : 99+%, Sigma-Aldrich, Milwaukee, WI, USA) was added to the solution. The solution was vigorously mixed at all time with a stir bar (length, 30 mm) equipped with a magnetic stirrer (HS180, Misung Scientific Co., Seoul, South Korea). The procedure to obtain aragonite was the same as that for calcite except that 50 vol% ethanol (500 mL ethanol and 500 mL DI water) was used. After 24 h, the precipitated products were collected by vacuum filtration (number 20 filter paper, pore diameter 5 μm , Hyundai Micro, Seoul, South Korea), washed with DI water, and dried in a convection oven at 40°C for 12 h before further use.

2.2. Ball Milling IBU with Calcite and Aragonite. Ibuprofen (IBU: >98%) was used as obtained from Sigma-Aldrich (Milwaukee, WI, USA). IBU (100 mg) was ball-milled with calcite or aragonite (100 mg) at the frequency of 10 Hz, and the milling time was 120 or 240 min. For the procedure, a Retsch ball mill (MM 200, Haan, Germany) was used with a cylindrical stainless steel jar (about 25 mL; inner diameter ca. 26 mm and inner length ca. 52 mm) and two stainless steel balls (diameter, 9 mm), which was often utilized in pharmaceutical grinding [20]. The ball-milled products were immediately used for further characterization.

2.3. Characterization of Raw and Ball-Milled Materials. Morphologies of IBU, calcite, aragonite, and ball-milled products were characterized using field-emission scanning electron microscopy (FE-SEM: JSM-6700F, JEOL, Tokyo, Japan) after thin Au coating (Cressington Sputter Coater 108, Watford, UK) to minimize surface charging. The materials were also characterized in their crystal structures using powder X-ray diffraction (XRD: D2 PHASER, Bruker AXS, Billerica, MA, USA). XRD was performed with $\text{CuK}\alpha$ radiation ($\lambda = 1.5406 \text{ \AA}$ at 30 kV, 10 mA) in the 2θ range of 5–40° (scanning rate, 1°/min). Fourier transformation infrared spectroscopy (FT-IR) was performed using a Cary 660 FTIR Spectrometer (Agilent Technologies, Santa Clara, CA, USA). KBr (FT-IR grade, $\geq 99\%$, Sigma-Aldrich, Milwaukee, WI, USA) discs were prepared for the transmission mode, where the IR spectra were collected in the wavenumber range of 4000–400 cm^{-1} .

Thermal analyses were performed via differential scanning calorimetry (DSC: DSC 821e, Mettler-Toledo, Columbus, OH, USA) and thermogravimetric analysis (TGA: TGA/SDTA 851e, Mettler-Toledo). DSC was to check the crystalline state of IBU, and it was precalibrated for enthalpy

and temperature using indium. The scanning for the IBU containing samples (2–3 mg each in a hermetically sealed aluminum crucible) was from 25 to 100°C with a heating rate of 10°C/min, and DSC experiments were repeated in triplicate for each sample. TGA was performed from 25 to 900°C with a scanning rate of 10°C/min (10–15 mg each in an open alumina crucible). Both DSC and TGA were under nitrogen environment.

Release behaviors of IBU were studied at pH 1.2 (corresponding to the gastric fluid) and 6.8 (corresponding to the intestinal fluid) using buffer solutions of HCl–KCl and phosphate, respectively [25, 26]. Powders containing IBU (5 mg for IBU only; 10 mg for ball-milled samples of IBU and calcium carbonate) were placed in a 300 mL solution (500 mL round bottom flask) at 37°C, and the mixture was stirred at 200 rpm using an overhead stirrer (HS-30D, Wisd Laboratory Instruments, Wertheim, Germany). To analyze the concentration of IBU in the solution, 3 mL samples were removed after 5, 10, 20, 30, 60, 120, and 180 min, and the solution was refilled immediately with the original buffer solutions to keep the volume of the solution constant. The solution sample removed at a given interval was filtered through a cellulose acetate filter (pore size 0.45 μm , MFS-13, Advantec, Tokyo, Japan), and its UV absorbance was measured at 222 nm (Optizen POP, Mecasys, Daejeon, South Korea) where the absorbance was at its maximum. The UV absorbance was then converted to the concentration using a preconstructed calibration curve. The release experiments were independently repeated in triplicate for each sample.

2.4. Computational Calculations of Binding Energy. The binding energy of IBU on the surfaces of aragonite and calcite was calculated using the Materials Studio simulation software (version 7.0) from Accelrys (San Diego, CA, USA) equipped with Forcite module and COMPASS force field [27], which was known for being effective for the calculations of the binding on calcium carbonate [28]. The (0 1 0)/(1 1 0) faces of aragonite and the (1 0 4) of calcite were selected as the adsorption surfaces based on the previous morphological observations [10, 24, 29]. Electrostatic energy terms were treated using Ewald summation method, and van der Waals energy was calculated with a cutoff distance of 12.5 Å using an atom-based summation method. The crystal structures of aragonite and calcite were obtained from the previous publications [30, 31], and the partial charge was force-field assigned. The initial geometry optimization and the charge assignment of IBU were also performed before adsorption simulation. The adsorption surfaces of calcium carbonate crystals were cleaved with thickness of 17 Å , which were then expanded over 40 $\text{Å} \times 40 \text{ Å}$. The centers of geometry of calcium and carbonate were considered for them to be included in the cleaved slab. After placing the IBU molecule at the center of the surfaces, Forcite quench (5 ps with 1 fs step) was performed to find the structure of the minimum energy. The NVT ensemble (Nosé thermostat) was used at 303 K reflecting the measured temperature during the ball milling process [32]. Among the 5,000 different structures, the structures at every 500 frames were quenched and optimized. The binding energy (E_b) was calculated for

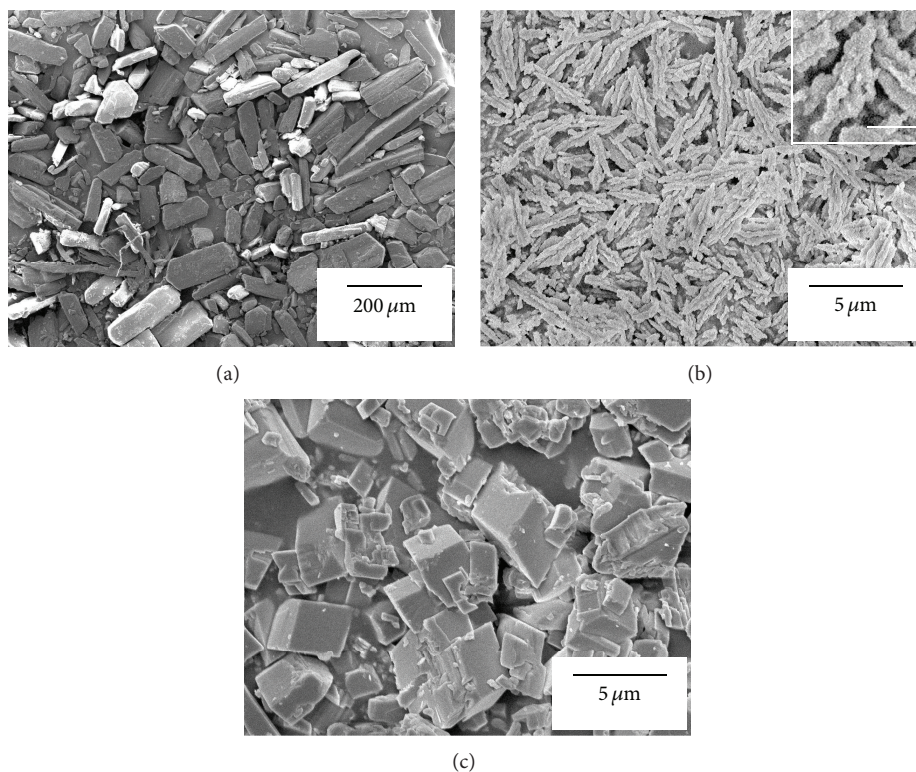


FIGURE 1: SEM images of ibuprofen (a), aragonite (b), and calcite (c) crystals. The scale bar of the inset of (b) is $1\ \mu\text{m}$.

the minimum energy structure of each surface: $E_b = E_t - (E_i + E_s)$, where E_t , E_i , and E_s are the total energy, the energy of adsorbed IBU, and the energy of surface, respectively.

3. Results and Discussion

3.1. Structures of Ball-Milled IBU with Calcite and Aragonite. The IBU crystals before milling as well as synthesized polymorphs of calcium carbonate (calcite and aragonite) were shown in Figure 1. The IBU crystals were plate-shaped with their length of about $100\text{--}200\ \mu\text{m}$ (Figure 1(a)). They were of typical morphology as previously observed: the large $\{1\ 0\ 0\}$ faces and the $\{0\ 0\ 1\}$, $\{1\ 1\ 0\}$ side faces [33, 34]. The crystal shapes of the synthesized polymorphs of calcium carbonate were also of routinely observed morphology. The aragonite crystals were needle-shaped with their length of about $2\text{--}5\ \mu\text{m}$ (Figure 1(b)). As shown in the inset, the aragonite needle was composed of submicron domains, and this observation was in agreement with the previous study using the same synthesis method [24]. The utilized method is known to generate $\{1\ 1\ 0\}$ and $\{0\ 1\ 0\}$ faces of aragonite as the enclosing surfaces, and the $\{0\ 1\ 0\}$ is also the distinct cleavage plane [24, 29]. The calcite crystals were rhombohedral with most of their size at $1\text{--}5\ \mu\text{m}$ (Figure 1(c)). The enclosing surfaces of the rhombs are known as the $\{1\ 0\ 4\}$ faces, which are also the perfect cleavage planes [10, 29, 35].

When IBU was ball-milled with the crystals of calcium carbonate, significant differences were observed between the cases with aragonite and calcite. When IBU was ball-milled with aragonite, the aragonite needles were mostly

disassembled into their individual submicron domains (Figures 2(a) and 2(b)), although some needle-shaped parts could be found (arrowheads of Figures 2(a) and 2(b)). More importantly, IBU and aragonite formed tightly integrated mesocrystal structures of the overall size about $4\text{--}10\ \mu\text{m}$. (In the case of IBU/aragonite milling, the microscopic examination did not reveal clear differences between the 120- and 240-minute samples.) In contrast, IBU ball milled with calcite did not show mesocrystal formation. IBU and calcite mostly remained as separate entities, although a small part of them appeared associated as indicated by the arrowheads of Figures 2(c) and 2(d). Note that calcite was easily distinguishable because of its $\{1\ 0\ 4\}$ cleavage surfaces. (In the case of IBU/calcite, the calcite appeared more fractured and smaller after the 240-minute milling than after 120 min.)

XRD analysis confirmed the nearly exclusive formation of calcite and aragonite during the preparation step (Figure 3). The prominent diffraction peaks of aragonite were shown at ca. 26.0 , 27.0 , 35.9 , and 38.2° for the $\{1\ 1\ 1\}$, $\{0\ 2\ 1\}$, $\{2\ 0\ 0\}$, and $\{1\ 3\ 0\}$ planes, respectively (Figure 3(a)) [36]. Those of calcite were at ca. 22.6 , 29.0 , 35.6 , and 39.0° for the $\{0\ 1\ 2\}$, $\{1\ 0\ 4\}$, $\{1\ 1\ 0\}$, and $\{1\ 1\ 3\}$ planes, respectively (Figure 3(b)) [36]. (Note that the calcite $\{1\ 0\ 4\}$ peak existed in negligible intensity in the aragonite batch.) The polymorphs of aragonite and calcite were also distinguishable using FT-IR analysis (Figure 4). The former had characteristic doublet peaks at 700 and $713\ \text{cm}^{-1}$ as well as peaks at 1082 and $1786\ \text{cm}^{-1}$ (Figures 4(a) and 4(b)), whereas the latter had a singlet at $711\ \text{cm}^{-1}$, nothing around $1080\ \text{cm}^{-1}$, and a peaks at $1799\ \text{cm}^{-1}$ (Figures 4(c) and 4(d)) [37–39].

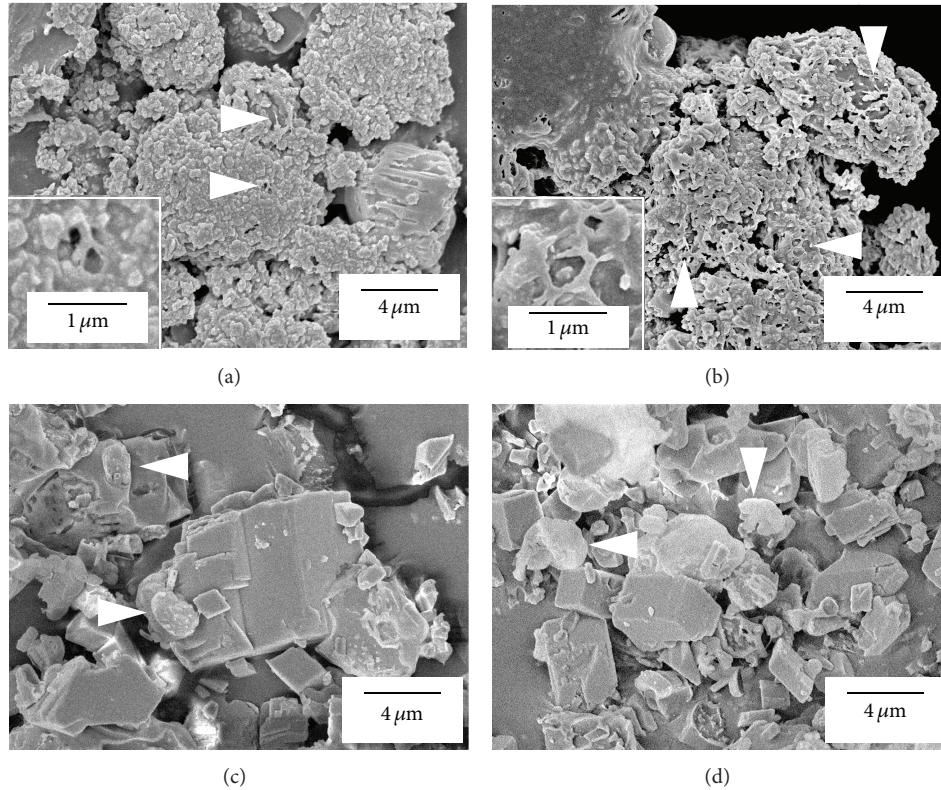


FIGURE 2: SEM images of IBU/aragonite after ball milling for (a) 120 and (b) 240 min; IBU/calcite after ball milling for (c) 120 and (d) 240 min. Arrowheads of (a) and (b) indicated the aragonite needles, and those of (c) and (d) indicated IBU. Also shown in the insets of (a) and (b) were the submicron domains as well as the needles of aragonite integrated with IBU.

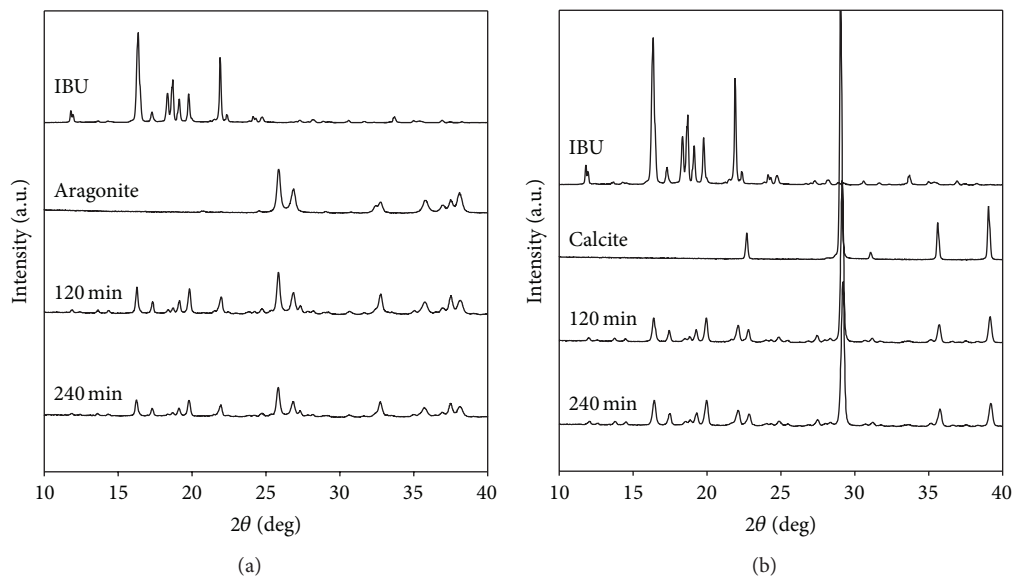


FIGURE 3: XRD patterns of IBU/aragonite (a) and IBU/calcite (b) before and after ball milling.

Ball milling did not alter the structures of IBU crystals significantly enough to generate new XRD diffraction peaks from different crystal structures (Figure 3). Major XRD diffraction peaks of IBU were at ca. 16.4, 18.7, 19.8, and 21.9° for

{2 1 0}, {2 0 -2}, {0 1 2}, and {2 0 2}, respectively [40]. All major diffraction peaks were the same after ball milling, although some alterations in the intensity, most noticeably the increased relative intensity of {0 1 2} peak at ca. 19.8°,

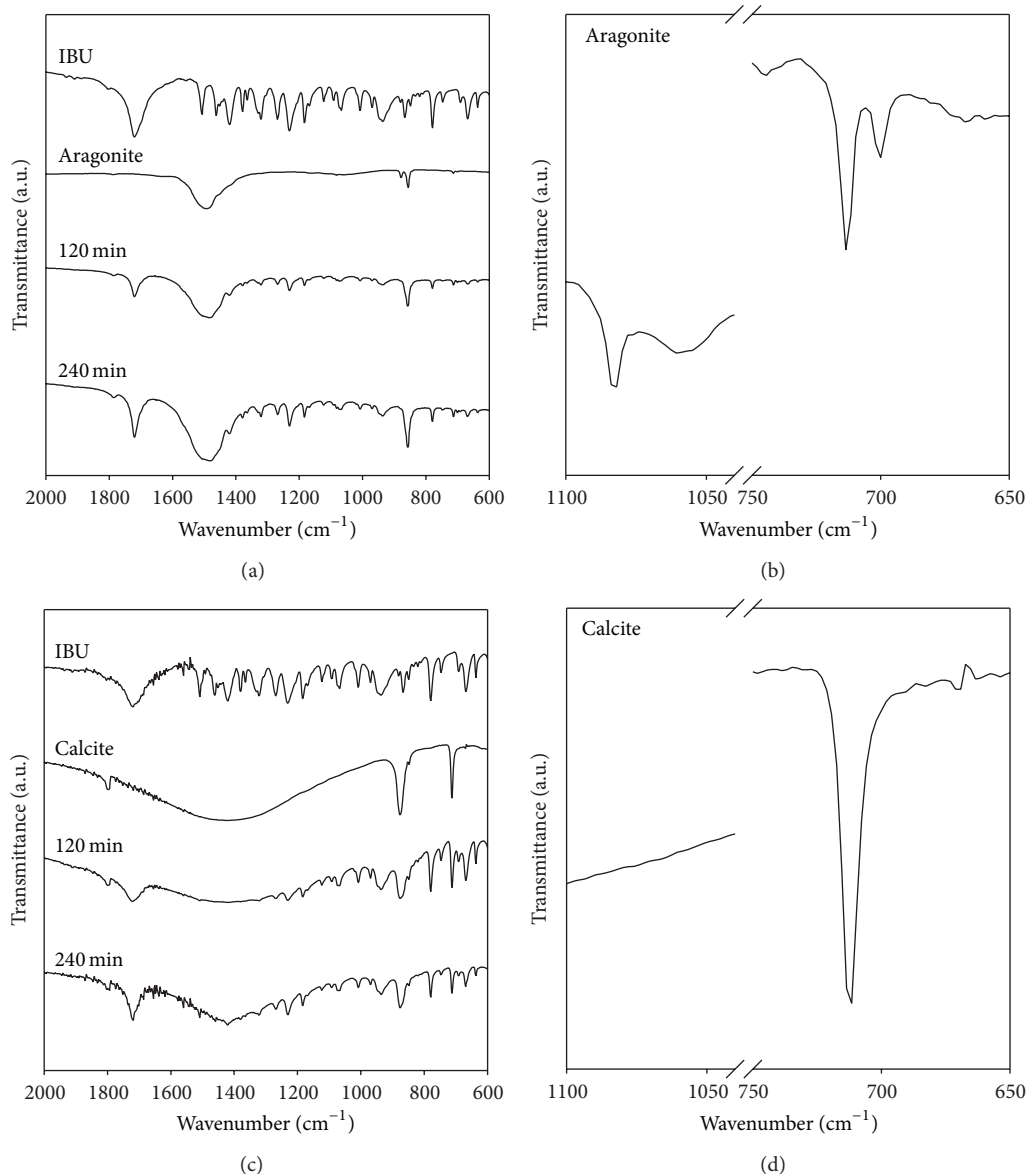


FIGURE 4: IR spectra of IBU/aragonite before and after ball milling (a); aragonite (zoomed in between 1100 and 650 cm^{-1}) (b); IBU/calcite before and after ball milling (c); calcite (zoomed in between 1100 and 650 cm^{-1}) (d).

indicated the changes in the crystal morphology. In addition, the analysis of the full width at half maximum (FWHM) was in agreement with the microscopic observation. The FWHM was analyzed based on the relatively intensified $\{0\ 1\ 2\}$ peak. The FWHM was about 0.11° before milling, and it increased after milling with aragonite or calcite. The FWHM values were 0.16 and 0.17° after 120 and 240 min of milling with aragonite, respectively. They were 0.17 and 0.19° after 120 and 240 min with calcite, respectively. Since FWHM is inversely proportional to the crystallite size, the analysis indicated the size decrease of the IBU crystallite with ball milling [41]. Note that the $\{0\ 1\ 2\}$ plane is parallel to the a -axis, which is also perpendicular to the large $\{1\ 0\ 0\}$ face of the plate-shaped IBU crystals before milling (Figure 1(a)) [33, 34]. This suggested that breakage occurred in the perpendicular

direction of the large face as would be expected from the original shape of the crystals.

The interactions between IBU and calcium carbonate were further examined with FT-IR and molecular dynamics. FT-IR showed that one of the carbonate-related peaks of aragonite noticeably changed after milling with IBU (Figure 4(a)). The frequency corresponding to asymmetric stretching was at $1495\ \text{cm}^{-1}$ [37], and it became 1485 and $1481\ \text{cm}^{-1}$ after 120 and 240 min of milling with IBU, respectively. In contrast, the corresponding change appeared absent for calcite (Figure 4(b)). Also, note that the change on the IBU side, including that for the carbonyl peak at $1720\ \text{cm}^{-1}$, was difficult to find.

The fundamental aspects of IBU interaction with aragonite and calcite were investigated by studying the binding

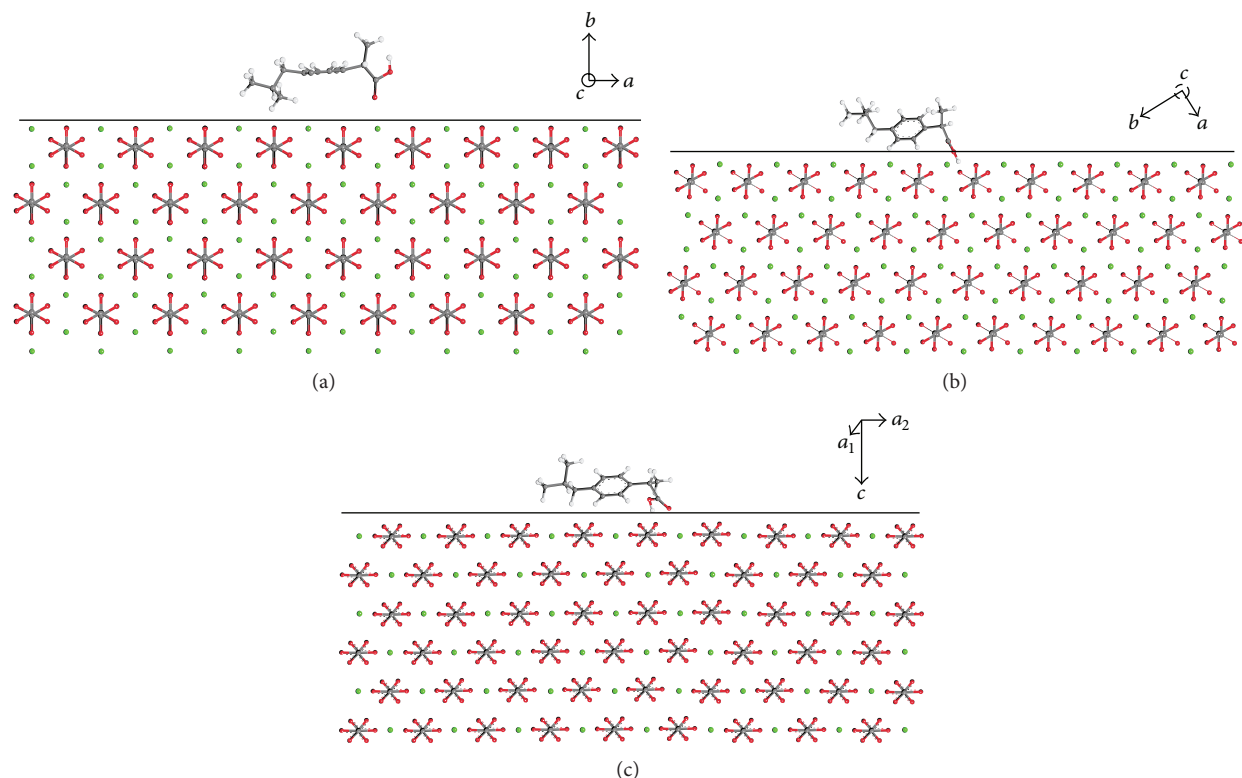


FIGURE 5: Binding conformation of IBU on the surfaces of aragonite (0 1 0) (a); aragonite (1 1 0) (b); calcite (1 0 4) (c).

energy and structures. The binding energy of IBU on the mineral surfaces was in the following order: aragonite (0 1 0), $|-212 \text{ kcal/mol}| \gg$ aragonite (1 1 0), $|-63 \text{ kcal/mol}| >$ calcite (1 0 4), $|-44 \text{ kcal/mol}|$, and the binding was predominantly of electrostatic nature in all cases. The corresponding binding conformations of IBU to the surfaces were shown in Figure 5. The binding differences seemed to originate from the dissimilar atomic arrangements of the surfaces. Each calcium ion of aragonite and calcite in bulk was coordinated with nine and six oxygens, respectively; the surface calcium of (0 1 0) and (1 1 0) lacked three coordinating oxygens out of nine, whereas that of (1 0 4) was short of only one oxygen out of six. This appeared to allow stronger electrostatic interactions of surface calcium of aragonite with the oxygens of IBU. In addition, the subtle differences in the two-dimensional periodic structures between (0 1 0) $\{4.961 \text{ \AA} \times 5.740 \text{ \AA}\}$ and (1 1 0) $\{4.694 \text{ \AA} \times 5.740 \text{ \AA}\}$ appeared to contribute to the differences of the IBU binding conformations and interactions.

Overall, the IR analysis and the computational study of the binding indicated the higher affinity of IBU to aragonite compared to calcite. This was consistent with the microscopic observation, where the intimate association of IBU was found with aragonite but not with calcite.

3.2. Properties of Ball-Milled IBU with Calcite and Aragonite.

Thermal properties of IBU ball milled with calcium carbonate were examined with DSC. The melting point of IBU was about 77°C before milling. It became about 74 and 73°C after 120 and 240 min of milling with aragonite; it was about

76 and 75°C after 120 and 240 min of milling with calcite (Figure 6(a)). The melting enthalpy showed greater changes (Figure 6(b)). The reported enthalpy was the normalized value based on the TGA analysis, which revealed the exact amount of IBU in the hybrid sample. (Calcium carbonate, both aragonite and calcite, started to experience weight loss at around 600°C to eventually leave ca. 56% of the original weight. This corresponded to the formation of calcium oxide by losing carbon dioxide; IBU decomposed nearly completely below 300°C to leave less than 1% of the original weight.) The melting enthalpy of IBU was about 172 J/g before milling. It became about 162 and 126 J/g after 120 and 240 min of milling with aragonite; it was about 173 and 151 J/g after 120 and 240 min of milling with calcite. Overall, the decrease of melting point and enthalpy of IBU was observed after milling, which was probably due to the decrease of the crystal size and crystallinity [42, 43]. Also, the effect of aragonite was more significant than that of calcite, which was in accordance with the structural analysis in the previous section.

Release behaviors of IBU from the ball-milled IBU/aragonite and IBU/calcite were studied at pH 1.2 and 6.8 (Figure 7), where the change of pH during the release was less than 0.1 in all cases. The release behavior from the IBU/aragonite hybrid was pH responsive. After milling for 240 min, the initial release (<30 min) accelerated at pH 1.2, while it decelerated at pH 6.8, compared with neat IBU. This was apparently due to the high solubility of aragonite at low pH [23], combined with its intimate association with IBU. Note that 120-minute milling was not as effective at pH 1.2, while its deceleration effect at pH 6.8 was valid. In

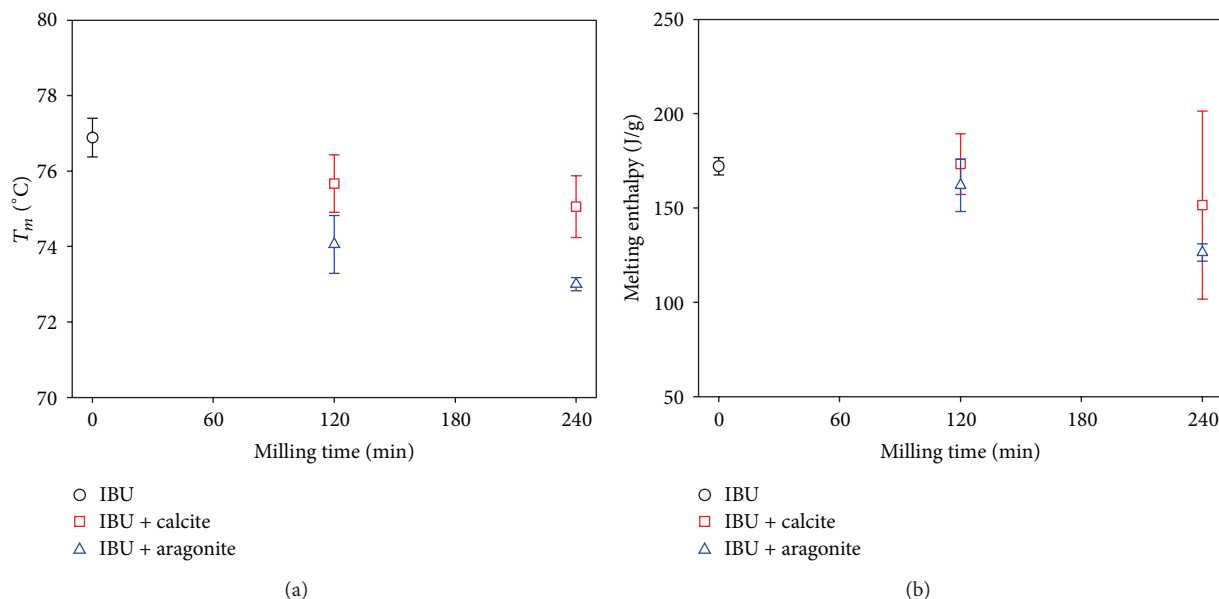


FIGURE 6: (a) Melting points and (b) melting enthalpy of IBU/argonite and IBU/calcite after ball milling.

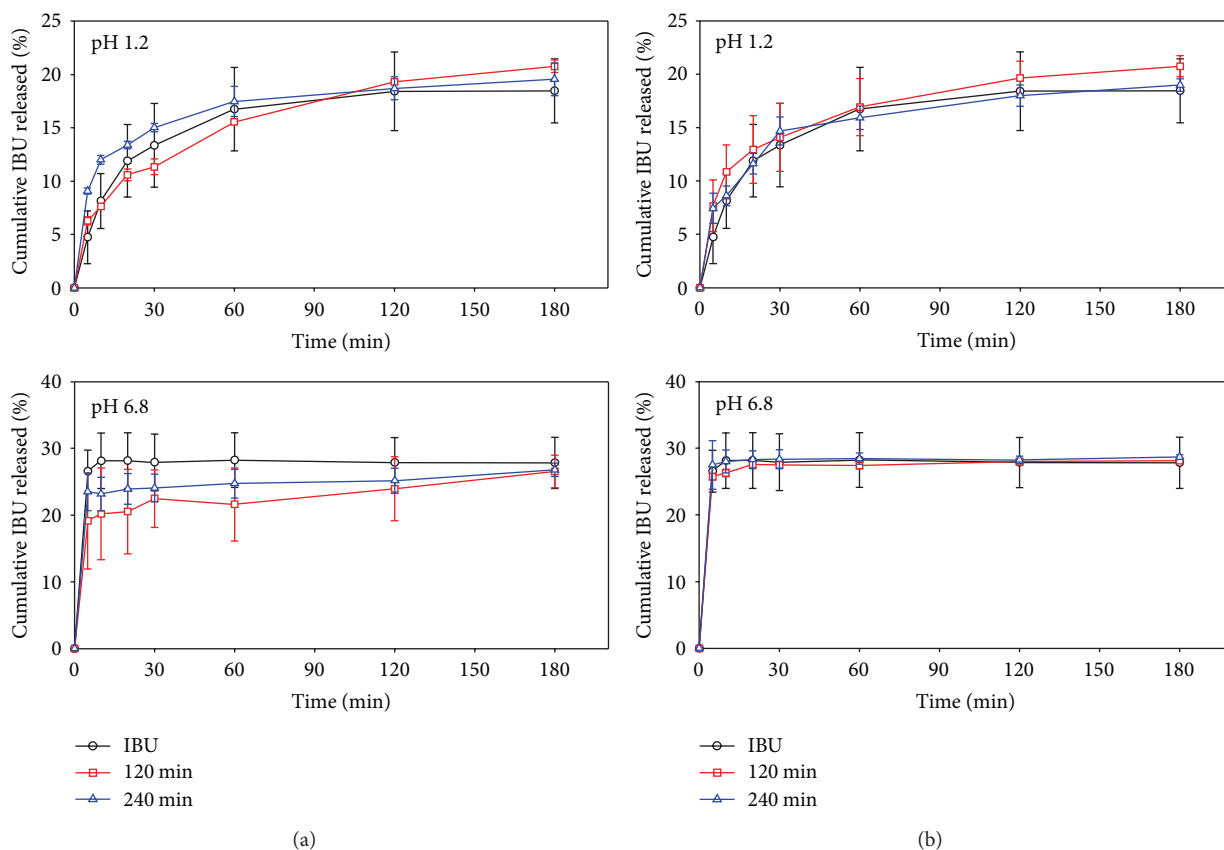


FIGURE 7: IBU release profiles at pH 1.2 and 6.8 from ball-milled IBU/argonite (a) and IBU/calcite (b).

contrast, ball milling of IBU with calcite was not effective in modulating the release rate. Overall, the release behaviors of IBU confirmed that they could be adjusted only when IBU was intimately associated with the ball-milled substrate.

When the substrate was rapidly soluble, the IBU release was expedited; when the substrate was marginally soluble, the release slowed down. Further studies on the quantitative analysis of the release kinetics and on the extended release

behavior with the fine-tuned structures would be necessary to establish the utility of the mesocrystals in the controlled drug release.

4. Conclusions

In summary, two anhydrous polymorphs of calcium carbonate (aragonite and calcite) were employed during ball milling of IBU to generate IBU/calcium carbonate hybrid materials. Aragonite polymorph was intimately integrated with IBU to form a mesocrystal-like structure, whereas calcite did not seem to be as effective under the experimental conditions employed in the present study. Aragonite and IBU kept their original crystal structures within the mesocrystals, although morphological variations occurred. Aragonite/IBU interaction was verified by the changes in the IR vibration of the carbonate of aragonite, and its strong nature was corroborated by the binding energy computationally obtained. The IBU fused with aragonite showed modulated thermal behavior, further confirming the observed structures. Finally, the IBU release behavior could be regulated through the conditions affecting the aragonite substrate. The IBU release sped up under the conditions disintegrating aragonite, and it slowed down when aragonite was stable. The present study indicates that the substrates that disintegrate at specific conditions can be utilized for the environment-responsive release of APIs. For this purpose, it also appears that the substrates need to form intimately associated structures with APIs to be delivered.

Conflict of Interests

The authors declare that there is no conflict of interests regarding the publication of this paper.

Acknowledgments

This research was supported by Basic Science Research Program through the National Research Foundation of Korea (NRF) funded by the Ministry of Education (NRF-2013R1A1A2012036).

References

- [1] H. Cölfen and M. Antonietti, *Mesocrystals and Nonclassical Crystallization*, John Wiley & Sons, Chichester, UK, 2008.
- [2] X. Li, W.-C. Chang, Y. J. Chao, R. Wang, and M. Chang, "Nanoscale structural and mechanical characterization of a natural nanocomposite material: The shell of red abalone," *Nano Letters*, vol. 4, no. 4, pp. 613–617, 2004.
- [3] L. Addadi, D. Joester, F. Nudelman, and S. Weiner, "Mollusk shell formation: a source of new concepts for understanding biomineralization processes," *Chemistry—A European Journal*, vol. 12, no. 4, pp. 980–987, 2006.
- [4] M. Rousseau, E. Lopez, P. Stempflié et al., "Multiscale structure of sheet nacre," *Biomaterials*, vol. 26, no. 31, pp. 6254–6262, 2005.
- [5] I. Sethmann, R. Hinrichs, G. Wörheide, and A. Putnis, "Nano-cluster composite structure of calcitic sponge spicules—a case study of basic characteristics of biominerals," *Journal of Inorganic Biochemistry*, vol. 100, no. 1, pp. 88–96, 2006.
- [6] Y. Oaki and H. Imai, "Nanoengineering in echinoderms: the emergence of morphology from nanobricks," *Small*, vol. 2, no. 1, pp. 66–70, 2006.
- [7] O. Grassmann, G. Müller, and P. Löbmann, "Organic-inorganic hybrid structure of calcite crystalline assemblies grown in a gelatin hydrogel matrix: relevance to biomineralization," *Chemistry of Materials*, vol. 14, no. 11, pp. 4530–4535, 2002.
- [8] H. Cölfen and M. Antonietti, "Mesocrystals: inorganic superstructures made by highly parallel crystallization and controlled alignment," *Angewandte Chemie International Edition*, vol. 44, no. 35, pp. 5576–5591, 2005.
- [9] R. Kim, C. Kim, S. Lee, J. Kim, and I. W. Kim, "In situ atomic force microscopy study on the crystallization of calcium carbonate modulated by poly(vinyl alcohol)s," *Crystal Growth & Design*, vol. 9, no. 11, pp. 4584–4587, 2009.
- [10] I. W. Kim, S. Collino, and J. S. Evans, "Cooperative modulation of mineral growth by prismatic-associated Asprich sequences and Mg(II)," *International Journal of Molecular Sciences*, vol. 13, no. 3, pp. 3949–3958, 2012.
- [11] K. Park, "Controlled drug delivery systems: past forward and future back," *Journal of Controlled Release*, vol. 190, pp. 3–8, 2014.
- [12] I. Katzhendler, R. Azoury, and M. Friedman, "Crystalline properties of carbamazepine in sustained release hydrophilic matrix tablets based on hydroxypropyl methylcellulose," *Journal of Controlled Release*, vol. 54, no. 1, pp. 69–85, 1998.
- [13] M. K. Lee, H. Lee, I. W. Kim, and J. Lee, "Novel polymorphic form of adefovir dipivoxil derived from polymer-directed crystallization," *Pharmazie*, vol. 66, no. 10, pp. 766–770, 2011.
- [14] T. Lee and C. W. Zhang, "Dissolution enhancement by bio-inspired mesocrystals: the study of racemic (R,S)-(±)-sodium ibuprofen dihydrate," *Pharmaceutical Research*, vol. 25, no. 7, pp. 1563–1571, 2008.
- [15] T. Watanabe, S. Hasegawa, N. Wakiyama, A. Kusai, and M. Senna, "Prediction of apparent equilibrium solubility of indomethacin compounded with silica by ¹³C solid state NMR," *International Journal of Pharmaceutics*, vol. 248, no. 1-2, pp. 123–129, 2002.
- [16] M. K. Gupta, A. Vanwert, and R. H. Bogner, "Formation of physically stable amorphous drugs by milling with neusilin," *Journal of Pharmaceutical Sciences*, vol. 92, no. 3, pp. 536–551, 2003.
- [17] S. Mallick, S. Pattnaik, K. Swain et al., "Formation of physically stable amorphous phase of ibuprofen by solid state milling with kaolin," *European Journal of Pharmaceutics and Biopharmaceutics*, vol. 68, no. 2, pp. 346–351, 2008.
- [18] S. Mallick, S. Pattnaik, K. Swain et al., "Physicochemical characterization of interaction of ibuprofen by solid-state milling with aluminum hydroxide," *Drug Development and Industrial Pharmacy*, vol. 34, no. 7, pp. 726–734, 2008.
- [19] W. Jones, W. D. S. Motherwell, and A. V. Trask, "Pharmaceutical cocrystals: an emerging approach to physical property enhancement," *MRS Bulletin*, vol. 31, no. 11, pp. 875–879, 2006.
- [20] T. Friščič and W. Jones, "Recent advances in understanding the mechanism of cocrystal formation via grinding," *Crystal Growth & Design*, vol. 9, no. 3, pp. 1621–1637, 2009.
- [21] S. Jung and I. W. Kim, "Effects of polymers on the cocrystallization of adefovir dipivoxil and suberic acid," *Polymer-Korea*, vol. 37, no. 5, pp. 663–668, 2013.
- [22] E. A. Losev and E. V. Boldyreva, "The role of a liquid in dry grinding: a case study of the effect of water on mechanochemical

- synthesis in a L-serine-oxalic acid system,” *CrystEngComm*, vol. 16, no. 19, pp. 3857–3866, 2014.
- [23] J.-Y. Gal, J.-C. Bollinger, H. Tolosa, and N. Gache, “Calcium carbonate solubility: a reappraisal of scale formation and inhibition,” *Talanta*, vol. 43, no. 9, pp. 1497–1509, 1996.
- [24] K. K. Sand, J. D. Rodriguez-Blanco, E. Makovicky, L. G. Benning, and S. L. S. Stipp, “Crystallization of CaCO_3 in water-alcohol mixtures: spherulitic growth, polymorph stabilization, and morphology change,” *Crystal Growth & Design*, vol. 12, no. 2, pp. 842–853, 2012.
- [25] S.-W. Song, K. Hidajat, and S. Kawi, “pH-Controllable drug release using hydrogel encapsulated mesoporous silica,” *Chemical Communications*, no. 42, pp. 4396–4398, 2007.
- [26] C. Aguzzi, M. C. Bonferoni, M. R. Osorio Fortich, S. Rossi, F. Ferrari, and C. Caramella, “Influence of complex solubility on formulations based on lambda carrageenan and basic drugs,” *AAPS PharmSciTech*, vol. 3, no. 3, pp. 83–89, 2002.
- [27] H. Sun, “COMPASS: an ab initio force-field optimized for condensed-phase applications—overview with details on alkane and benzene compounds,” *Journal of Physical Chemistry B*, vol. 102, no. 38, pp. 7338–7364, 1998.
- [28] S. E. Wolf, N. Loges, B. Mathiasch et al., “Phase selection of calcium carbonate through the chirality of adsorbed amino acids,” *Angewandte Chemie International Edition*, vol. 46, no. 29, pp. 5618–5623, 2007.
- [29] C. Klein and C. S. Hurlbut Jr., *Manual of Mineralogy*, John Wiley & Sons, New York, NY, USA, 21st edition, 1993.
- [30] D. L. Graf, “Crystallographic tables for the rhombohedral carbonates,” *The American Mineralogist*, vol. 46, no. 11-12, pp. 1283–1316, 1961.
- [31] J. P. R. de Villiers, “Crystal structures of aragonite, strontianite, and witherite,” *The American Mineralogist*, vol. 56, no. 5-6, pp. 758–767, 1971.
- [32] S. Nosé, “A unified formulation of the constant temperature molecular dynamics methods,” *Journal of Chemical Physics*, vol. 81, no. 1, pp. 511–519, 1984.
- [33] N. Shankland, A. J. Florence, P. J. Cox et al., “Crystal morphology of ibuprofen predicted from single-crystal pulsed neutron diffraction data,” *Chemical Communications*, no. 7, pp. 855–856, 1996.
- [34] H. Cano, N. Gabas, and J. P. Canselier, “Experimental study on the ibuprofen crystal growth morphology in solution,” *Journal of Crystal Growth*, vol. 224, no. 3-4, pp. 335–341, 2001.
- [35] I. W. Kim, M. R. Darragh, C. Orme, and J. S. Evans, “Molecular “tuning” of crystal growth by nacre-associated polypeptides,” *Crystal Growth & Design*, vol. 6, no. 1, pp. 5–10, 2006.
- [36] Joint Committee on Powder Diffraction Standards, Powder Diffraction File, Card No. 05-0586 (calcite), No. 41-1475 (aragonite), Swarthmore, Pa, USA, 2003.
- [37] H. H. Adler and P. F. Kerr, “Infrared study of aragonite and calcite,” *The American Mineralogist*, vol. 47, no. 5-6, pp. 700–717, 1962.
- [38] J. A. Speer, “Crystal chemistry and phase relations of orthorhombic carbonates,” in *Carbonates: Mineralogy and Chemistry*, R. J. Reeder, Ed., vol. 11, chapter 5, pp. 145–190, Mineralogical Society of America, Washington, DC, USA, 1983.
- [39] I. W. Kim, R. E. Robertson, and R. Zand, “Selected polymorphs of CaCO_3 through epitaxy with inorganic substrates aligned with an electric field,” *Advanced Materials*, vol. 15, no. 9, pp. 709–712, 2003.
- [40] K. H. Stone, S. H. Lapidus, and P. W. Stephens, “Implementation and use of robust refinement in powder diffraction in the presence of impurities,” *Journal of Applied Crystallography*, vol. 42, no. 3, pp. 385–391, 2009.
- [41] B. D. Cullity and S. R. Stock, *Elements of X-Ray Diffraction*, Prentice Hall, Upper Saddle River, NJ, USA, 3rd edition, 2001.
- [42] L. H. Sperling, “The Crystalline State,” in *Introduction to Physical Polymer Science*, chapter 6, pp. 198–278, John Wiley & Sons, New York, NY, USA, 2nd edition, 2008.
- [43] J. Chung and I. W. Kim, “Effects of some polymeric additives on the cocrystallization of caffeine,” *Journal of Crystal Growth*, vol. 335, no. 1, pp. 106–109, 2011.

Research Article

A Novel Porous Carrier Found in Nature for Nanocomposite Materials Preparation: A Case Study of *Artemia* Egg Shell-Supported TiO₂ for Formaldehyde Removal

Sufeng Wang, Fengjing Lv, Tifeng Jiao, Jingfen Ao, Xiaochun Zhang, and Fengdan Jin

Hebei Key Laboratory of Applied Chemistry, School of Environmental and Chemical Engineering, Yanshan University, Qinhuangdao 066004, China

Correspondence should be addressed to Sufeng Wang; sfwang@ysu.edu.cn

Received 17 July 2014; Revised 20 August 2014; Accepted 20 August 2014

Academic Editor: Xinqing Chen

Copyright © 2015 Sufeng Wang et al. This is an open access article distributed under the Creative Commons Attribution License, which permits unrestricted use, distribution, and reproduction in any medium, provided the original work is properly cited.

Artemia egg shells have an asymptotic sized pore structure (pore diameter: 500 nm–2500 nm), which could be used as a porous carrier for the preparation of nanocomposite materials. The objective of the present study was to prepare shell-supported TiO₂ using a naturally porous carrier, *Artemia* egg shell, and to exhibit a case study of shell-supported TiO₂ for formaldehyde removal. Characterization of shell-TiO₂ using SEM-EDS, TEM, and XRD proved that *Artemia* shell with asymptotic reduction pores (pore diameter: 500 nm–2500 nm) can be used as the carrier for nanocomposite materials. *Artemia* egg shell-supported TiO₂ in polycrystalline-like nanostructures can be used for the high efficiency removal (adsorption and degradation) of formaldehyde under visible light. Our results suggest that iron, one of the shell's components, should broaden the absorption of visible light and enhance the photocatalytic efficiency of nanotitanium dioxide under visible light. Due to their interesting absorption and formaldehyde removal qualities, *Artemia* egg shell, as a novel naturally porous carrier for nanocomposite materials preparation, especially in the preparation of nanocatalysts, is worthy of further study.

1. Introduction

The rapidly advancing field of nanotechnology has great promise for environmental remediation [1–6]. Supporter-immobilized inorganic adsorbents are one of the main environmental applications of nanotechnologies that attempt to solve the existing problems of neat nanoparticles [2, 4, 7] such as poor mechanical strength, pore collapsing, particle crush, and particles flowing away. In previous studies, researchers have loaded zirconium, iron, and cadmium onto the porous surfaces of collagen fibers, zeolite, polymer, ceramics, activated carbon, and other porous materials as a functional composite adsorbent and examined the adsorbent function for the removal of pollution [1–6]. In these studies, it was proved that the adsorptive function of composite adsorbent-based carriers is more efficient than nano-inorganic adsorbents alone [4–7]. Moreover, different carrier-supported materials showed different material-dependent performances [2]. These issues of differing performances mean that the carrier

selected to support inorganic adsorbents became the main problem.

Artemia, member of the crustacean subphylum, mainly live in coastal waters, salt ponds, and plateau salt lakes. *Artemia* are globally plentiful and it has been recorded that their habitats encompass about 600 localities around the world [8, 9]. The annual harvest yield from natural and aquacultural sources of living *Artemia* and *Artemia* eggs is about 15000 t and 300–500 t, respectively, in China alone. Unique multipore layers in *Artemia* egg shells have been reported [9–13], and researchers have documented that the pores of *Artemia* egg shells appeared to have an asymptotic size distribution (diameter: 500 nm–2500 nm) [9, 13]. In addition, *Artemia* egg shells have multiple outstanding capabilities such as nice biocompatibility, environmentally friendly characteristics, and excellent stability [14, 15]. However, when *Artemia* egg was hatched for aquacultural living food, *Artemia* egg shells have been disposed of as a waste. *Artemia* egg shells, with their novel naturally porous

structure, are worthy of further study as the carrier for nanocomposite materials in pollution removal applications.

Indoor air pollution presents an important domestic environmental concern [16, 17], since people are decorating their living spaces with plywood, coating materials, paint, and the other materials that may contain volatile organic compounds (VOCs), such as formaldehyde, benzene, and ketones. These VOCs being released from decorative materials pollute the indoor air and harm the health of inhabitants. This indicates a clear need for novel indoor air pollution remediation technologies.

One of the nano-inorganic adsorbents most commonly used in indoor harmful gas removal is nanoscale titanium dioxide (nano-TiO₂) because of its adsorption properties and degradation as a photo-catalytic [18]. Theoretically, nano-TiO₂ could provide more active surface sites for photodegradation through diffusion [19]. However, ultra-fine TiO₂ powders with large specific surface areas agglomerate easily, and its adverse effect on their catalytic performance has been observed [19, 20]. Therefore, carrier-supported TiO₂ could be used to avoid the defects stated above.

In the present paper, the composite materials were fabricated by loading nano-TiO₂ onto the porous surface of *Artemia* egg shells and a case study of *Artemia* egg shell-supported TiO₂ for formaldehyde removal was actualized.

2. Materials and Methods

2.1. Materials. *Artemia* shells were collected from the Beidaihe Central Experiment Station of the Chinese Academy of Fishery Science. Before the experiments, shells were subjected to flushing with freshwater to remove the residual impurities (including salts). All treated shells were rewashed with deionized H₂O until they reached a constant neutral pH in the range of 6.8–7.2 and vacuum desiccated at 70°C for 24 hr until reaching a constant weight.

All chemicals are of analytical grade from Aladdin Reagent Station (Beijing, China), and the orthophosphate solution (1000 mg/L) was prepared by dissolving KH₂PO₄ into the deionized water.

2.2. Preparation of Shell-TiO₂ Composite Materials. For shell-TiO₂ composite materials fabrication, 0.2 g of egg shells was immersed in a mixture of blended 5 mL butyl titanate, 20 mL absolute ethyl alcohol, and 0.5 mL hydrochloric acid (37%). Hydrochloric acid was used to prevent the butyl titanate from hydrolyzing in the absolute ethyl alcohol before the titanate could get into the egg shells. The egg shell mixture was dispersed by ultrasound (40 KHz, 50 W, 50°C) for 2 hr. Then, the butyl titanate-sucking egg shells were screened and washed with absolute ethyl alcohol and put into a 5% NaOH solution with magnetic stirring. The NaOH solution was used to accelerate the hydrolysis of the butyl titanate-sucking egg shells. After being screened and washed by the deionized H₂O, egg shells with TiO₂ (the product of the hydrolysis) were desiccated at 80°C for 24 hr until reaching a constant weight. The calcination of shell-TiO₂ was carried out under an anoxic environment inside a Muffle Furnace at 500°C for 2 hr.

2.3. Characterization of Shell-TiO₂ Composite Materials. The morphology and property characterization of shell-TiO₂ composite materials were completed using a field emission scanning electron microscope (SEM) with an energy dispersive X-ray spectrometer (EDS). All SEM specimens were mounted on standard copper stubs, coated with a layer of gold/palladium about 5 nm thick, and observed under SEM (S-4800 II, Hitachi, Japan). The chemical composition of the composite materials was characterized by EDS (Horiba, Japan), which was typically performed at an accelerating voltage of 20 kV, using an Oxford Link-ISIS X-ray EDXS microanalysis system attached to the SEM.

The TiO₂ particles loaded onto the porous surface of *Artemia* egg shells were observed with a transmission electron microscope (TEM). TEM images were recorded using a high-resolution transmission electron microscope (HRTEM, JEM2010) equipped with a Gatan CCD camera and working at an accelerating voltage of 20 kV.

The crystalline of TiO₂ particles loaded onto the porous surface of *Artemia* egg shells was characterized by X-ray diffraction (XRD) using an XTRA X-ray diffractometer (Rigaku Inc., Tokyo, Japan). The XRD pattern was obtained using CuK α radiation with an incident wavelength of 0.1542 nm under a voltage of 40 kV and a current of 30 mA. The scan rate was 0.02°/min.

The control group for the above procedures was neat *Artemia* egg shells (no TiO₂) and was treated the same way as the shell-TiO₂ composites.

2.4. Formaldehyde Removal Experiments. The removal of formaldehyde using shell-TiO₂ composite materials was carried out in an illumination culture box (GXZ-280A, Ningbo Jiangnan Co., Zhejiang, China). 0.5 mL of 36% formaldehyde was dropped into a narrow-mouth bottle (10000 mL); after formaldehyde inpouring, the narrow-mouth bottle was sealed with a silicon stopper and parafilm. A uniform rubber tube was passed through the silicon stopper before formaldehyde inpouring, and the rubber tube was linked with a KC-6D air sampler (Laoshan Electron Instrument factory, Qingdao, China). A clamp was clamped to the rubber tube between the bottle mouth and the air sampler for sample control. The sealed narrow-mouth bottle was placed in darkness at 25°C for 5 days (until the formaldehyde volatilized evenly). For formaldehyde removal, 0.25 g of shell-TiO₂ composite material was spread evenly on a glass plate with double sided adhesive tape. Next, the glass plate with the shell-TiO₂ composite material coating was put into the formaldehyde-bottle, which was then airproofed again. Air samples (flow rate: 0.2 L/min and sample time: 1.5 min) were taken from each test bottle at intervals of 1 hr by the air sampler, and the removing rate was assayed by the phenol reagent spectrophotometric method.

Formaldehyde removal (%) was calculated by

$$\frac{C_t - C_0}{C_t} \times 100\%, \quad (1)$$

where C_0 is the initial of formaldehyde concentration in narrow-mouth bottle and C_t is the formaldehyde concentrations at the time of sample taken.

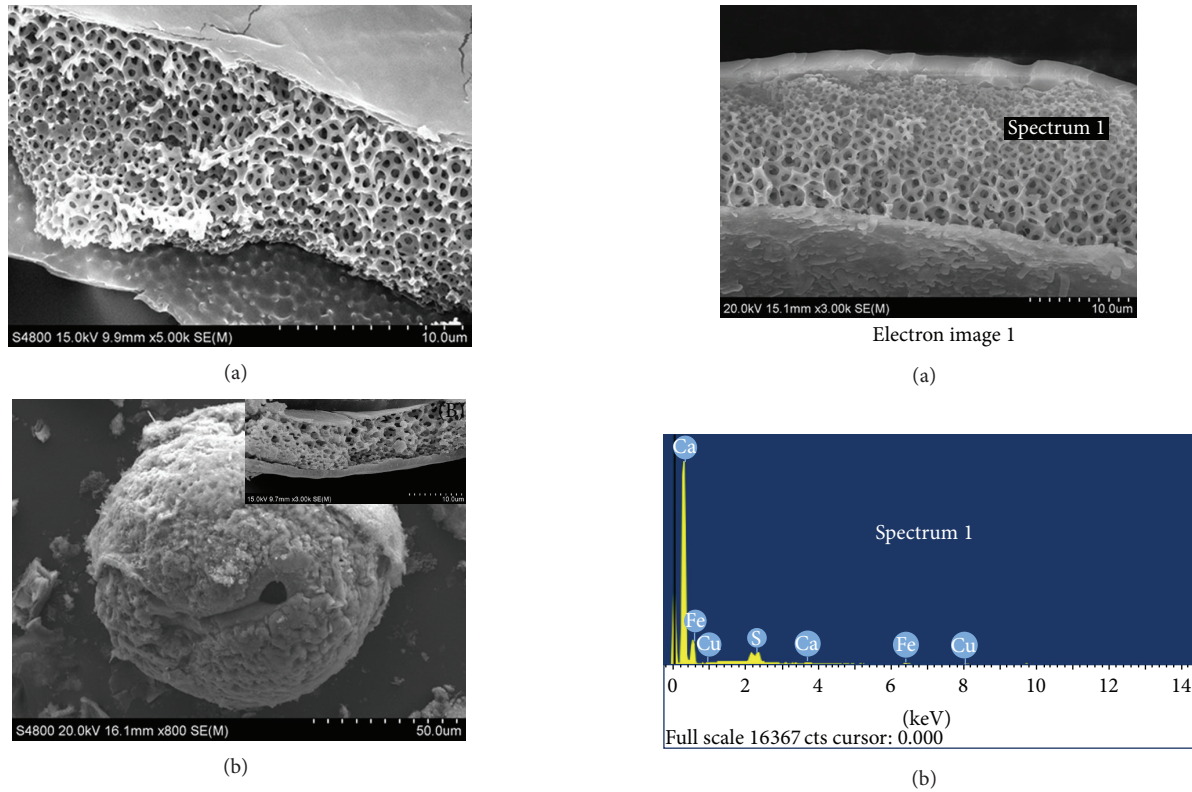


FIGURE 1: SEM images of (a) neat *Artemia* egg shell and (b) the shell-TiO₂ composite material.

The experiment was conducted in 2 replicates. One set of the formaldehyde removal experiments was carried out in darkness at 25°C; another set was actualized at 25°C under continuous illumination (about 1500 lx).

2.5. Data Analysis. Statistical analysis for formaldehyde removal was performed by SPSS 11.0 statistical software. Means were analyzed by descriptives and data are expressed as mean \pm sem ($n = 3$).

3. Results and Discussion

3.1. Characterization of Shell-TiO₂ Composite Material. The shell-TiO₂ composite material prepared in the present study was characterized by SEM-EDS, TEM, and XRD analysis. As depicted in Figure 1(b)(B), the porous region within the shell-TiO₂ composite material was filled up with TiO₂ particles. Comparatively, the surface topography of the neat *Artemia* shell showed a smooth surface without any decorations (Figure 1(a)). This suggests that TiO₂ particles have considerably filled the pores of the *Artemia* egg shells.

Titanium element scanning of the cross section with SEM-EDS (Figures 2(a)–2(d)) further demonstrates that the TiO₂ particles were fabricated in the porous region of the *Artemia* shells. The spectrum of the shell-TiO₂ composite material shows the relative elemental abundance of titanium at high levels (Figures 2(c), and 2(d)), whereas the “site of interest 1” spectrum of neat *Artemia* shell (Figures 2(a), and

FIGURE 2: Representative SEM-EDS images and spectra highlighting titanium levels: SEM image of *Artemia* egg shell (a) and EDS element scanning of a cross section (b); SEM image of shell-TiO₂ composite material (c) and EDS element scanning of a cross section (d).

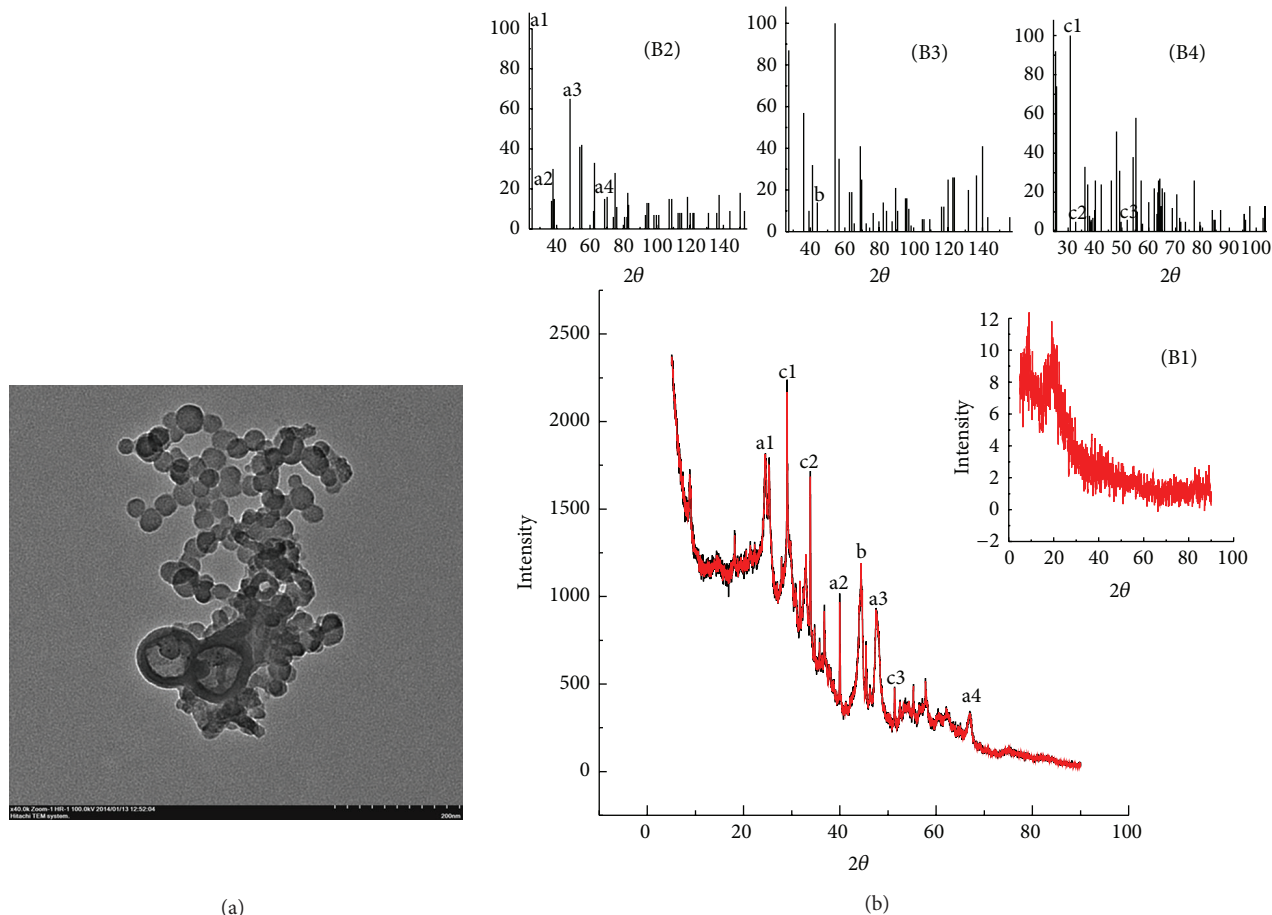


FIGURE 3: TEM images and XRD patterns of TiO_2 loaded onto the porous surface of *Artemia* egg shell: (a) TEM image of TiO_2 loaded onto the porous surface of *Artemia* egg shell; (b) XRD patterns of TiO_2 loaded onto the porous surface of *Artemia* egg shell; (B1) neat *Artemia* egg shell; (B2) standard card of anatase; (B3) standard card of rutile; and (B4) standard card of brookite.

2(b)) shows that there is no titanium in the shell pores. It appeared that the analysis of SEM-EDS corroborated the observations seen in the SEM images. The SEM image of shell- TiO_2 (Figure 2(c)) shows that the TiO_2 particles can be found everywhere within the shell pores especially when compared with the SEM image of neat *Artemia* shell (Figure 2(a)). The coverage of TiO_2 particles, spreading all over the porous region, implies that the diffusion of butyl titanate for TiO_2 formation into the deep area (the minimum pores layer) of the shell might not be restrained by pore clogging.

TEM images (Figure 3(a)) of shell- TiO_2 showed that TiO_2 significantly filled pores as nanoparticles with a size less than 50 nm. The X-ray diffraction spectra (Figure 3(b)) of the shell- TiO_2 and neat shell (Figure 3(B1)) suggest that TiO_2 nanoparticles filling shell pores were in several crystal forms. Peaks a1, a2, a3, and a4 in the angle region (2θ values, 25.3, 36.9, 48.0, and 68.8°, resp.) correspond to the XRD standard peaks for anatase (Figure 3(B2)). Peak b in the angle region (2θ values, 44.1°) corresponds to the XRD standard of rutile (Figure 3(B3)). Peaks c1, c2, and c3 in the angle region (2θ values, 30.8, 32.8, and 52.0°, resp.) correspond to the XRD standard of brookite (Figure 3(B4)). The other

peaks, unsigned in the curve (Figure 3(b)), also correspond to the amorphous forms for TiO_2 according to standard cards. Based on the results of TEM and XRD, it seems that the TiO_2 loaded within the shell pores are mainly in polycrystalline-like nanostructures.

3.2. Formaldehyde Removal Results. Formaldehyde removal percentage during the 10 hr experiment is shown in Figure 4. The formaldehyde removal percentages at the end of the experiments (10 hr) under both conditions (under continuous illumination at 25°C and under darkness at 25°C) were (70.5 ± 1.2)% and (55.4 ± 1.4)%, respectively. It was obvious that FREI (formaldehyde removal experiments that were carried out under continuous illumination at 25°C) was more efficient than the FRED (formaldehyde removal experiments that were carried out under darkness at 25°C). The formaldehyde removal percentage of FREI was rising continuously during all stages of the experiment, and the formaldehyde removal percentage of FRED was almost constant from 4 hr to 10 hr, though the formaldehyde removal percentage under both conditions did increase markedly during the first three hours (1–3 hr). It should be noted that the formaldehyde

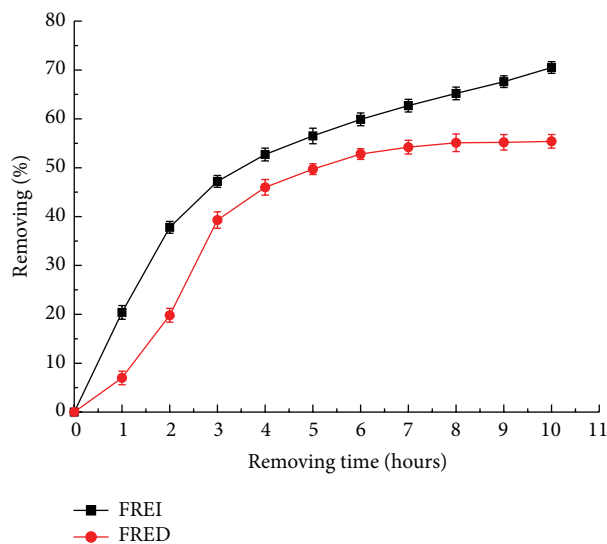


FIGURE 4: Formaldehyde removal percentages. FREI: formaldehyde removal experiments carried out under continuous illumination (about 1500 lx) at 25°C; FRED: formaldehyde removal experiments carried out under darkness at 25°C.

was only adsorbed during the FRED experiments, whereas both adsorption and degradation occurred in the FREI experiments.

It has been known that the superior photocatalytic ability of nano-TiO₂ is due to the decomposition of organic contaminants under the UV light [21, 22]. However, its practical application is limited due to the need for an ultraviolet excitation source (which accounts for only small fraction of solar light) [23]. In order to extend the photoresponse of TiO₂ to the visible region, expand the application of TiO₂, and make an efficient utilization of solar energy, researchers have doped some elements into the nano-TiO₂ matrix. It was proven that Fe-doped nanotitanium dioxide can widen the absorption of the visible light range, enhance the utilization efficiency of visible light, and improve the catalytic performance of nanotitanium dioxide [23, 24]. In the present study, it happens that iron is one of components of *Artemia* egg shells (Figures 2(b), and 2(d)), and the formaldehyde degradation experiment involving shell-TiO₂ composite materials was actualized under visible light. Moreover, the formaldehyde removal percentages in FREI (continuous illumination under visible light) can reach up to (70.5 ± 1.2)%. Therefore, the natural iron in the shells was determined to be connected to the photocatalytic performance of the shell-TiO₂ composite. To prove the function of the natural iron in *Artemia* shells, detailed research will be carried out in future studies.

4. Conclusion

The *Artemia* egg shell with asymptotic reduction pores (diameter: 500 nm–2500 nm) can be used as the carrier for nanocomposite materials. The nanocomposite materials, *Artemia* egg shell-supported TiO₂, were in polycrystalline-like nanostructures and can be used for high efficiency

formaldehyde removal (adsorption and degradation) under visible light. Our results would suggest that iron, as one of the shell's natural components, should be associated with the photocatalytic performance of shell-TiO₂ composites. To prove that natural iron in shells broadens the absorption of visible light and enhances photocatalytic efficiency under visible light, detailed research should be carried out in future studies.

Conflict of Interests

The authors declare that there is no conflict of interests regarding the publication of this paper.

Acknowledgments

The authors acknowledge and greatly appreciate the financial support from the National Natural Science Foundation of China (Grant nos. 40830746, 41271102, and 21473153). This work was also financially supported by the Natural Science Foundation of Hebei Province (B2013203108), the Science Foundation for the Excellent Youth Scholars from Universities, the colleges of Hebei Province (YQ2013026), and the Support Program for the Top Young Talents of Hebei Province.

References

- [1] X.-P. Liao and B. Shi, "Adsorption of fluoride on zirconium(IV)-impregnated collagen fiber," *Environmental Science & Technology*, vol. 39, no. 12, pp. 4628–4632, 2005.
- [2] B. C. Pan, Q. R. Zhang, W. M. Zhang et al., "Highly effective removal of heavy metals by polymer-based zirconium phosphate: a case study of lead ion," *Journal of Colloid and Interface Science*, vol. 310, no. 1, pp. 99–105, 2007.
- [3] S. Samatya, Ü. Yüksel, M. Yüksel, and N. Kabay, "Removal of fluoride from water by metal ions (Al³⁺, La³⁺ and ZrO²⁺) loaded natural zeolite," *Separation Science and Technology*, vol. 42, no. 9, pp. 2033–2047, 2007.
- [4] Q. Zhang, P. Jiang, B. Pan, W. Zhang, and L. Lv, "Impregnating zirconium phosphate onto porous polymers for lead removal from waters: effect of nanosized particles and polymer chemistry," *Industrial & Engineering Chemistry Research*, vol. 48, no. 9, pp. 4495–4499, 2009.
- [5] N. Chen, Z. Y. Zhang, C. P. Feng, M. Li, D. Zhu, and N. Sugiura, "Studies on fluoride adsorption of iron-impregnated granular ceramics from aqueous solution," *Materials Chemistry and Physics*, vol. 125, no. 1-2, pp. 293–298, 2011.
- [6] H. Tavallali and A. Daneshyar, "Cadmium selenide nanoparticles loaded on activated carbon and its efficient application for removal of fluoride from aqueous solution," *International Journal of ChemTech Research*, vol. 4, no. 3, pp. 1178–1181, 2012.
- [7] Q. R. Zhang, B. C. Pan, S. J. Zhang, J. Wang, W. Zhang, and L. Lv, "New insights into nanocomposite adsorbents for water treatment: a case study of polystyrene-supported zirconium phosphate nanoparticles for lead removal," *Journal of Nanoparticle Research*, vol. 13, no. 10, pp. 5355–5364, 2011.
- [8] G. van Stappen, "Zoogeography," in *Artemia: Basic and Applied Biology*, T. J. Abatzopoulos, J. A. Beardmore, J. S. Clegg, and

- P. Sorgeloos, Eds., pp. 171–224, Kluwer Academic Publishers, Dordrecht, The Netherlands, 2002.
- [9] S. Wang and S. Sun, “Comparative observations on the cyst shells of seven *Artemia* strains from China,” *Microscopy Research and Technique*, vol. 70, no. 8, pp. 663–670, 2007.
- [10] J. E. Morris and B. A. Afzelius, “The structure of the shell and outer membranes in encysted *Artemia salina* embryos during cryptobiosis and development,” *Journal of Ultrastructure Research*, vol. 20, no. 3-4, pp. 244–259, 1967.
- [11] E. Anderson, J. H. Lochhead, M. S. Lochhead, and E. Huebner, “The origin and structure of the tertiary envelope in thick-shelled eggs of the brine shrimp, *Artemia*,” *Journal of Ultrastructure Research*, vol. 32, no. 5-6, pp. 497–525, 1970.
- [12] M. Mazzini, “Scanning electron microscope morphology and amino-acid analysis of the egg-shell of encysted brine shrimp, *Artemia salina* Leach (Crustacea Anostraca),” *Monitore Zoologico Italiano—Italian Journal of Zoology*, vol. 12, no. 4, pp. 243–252, 1978.
- [13] K. W. Lee, M. A. Gouthro, D. Belk, and J. R. Rosowski, “Ultrastructure features of the tertiary envelope in the cyst of the brine shrimp *Artemia franciscana* (Anostraca),” in *Proceeding of the 52nd Annual Meeting of the Microscopy Society of America*, G. W. Bailey and A. J. Garratt-Reed, Eds., pp. 362–363, San Francisco Press, San Francisco, Calif, USA, August 1994.
- [14] T. Iwasaki, “Tolerance of *Artemia* dry eggs for temperature, vacuum and radiation,” *Bulletin de l’Institute International du Froid—Annexe*, vol. 5, pp. 79–88, 1973.
- [15] J. S. Clegg, “Desiccation tolerance in encysted embryos of the animal extremophile, *Artemia*,” *Integrative and Comparative Biology*, vol. 45, no. 5, pp. 715–724, 2005.
- [16] B. J. Finlayson-Pitts and J. N. Pitts, *Chemistry of the Upper and Lower Atmosphere: Theory, Experiments, and Applications*, Academic Press, San Diego, Calif, USA, 2000.
- [17] C. M. Schmidt, A. M. Buchbinder, E. Weitz, and F. M. Geiger, “Photochemistry of the indoor air pollutant acetone on Degussa P25 TiO₂ studied by chemical ionization mass spectrometry,” *The Journal of Physical Chemistry A*, vol. 111, no. 50, pp. 13023–13031, 2007.
- [18] U. Diebold, “The surface science of titanium dioxide,” *Surface Science Reports*, vol. 48, no. 5-8, pp. 53–229, 2003.
- [19] Z. Ding, H. Y. Zhu, G. Q. Lu, and P. F. Greenfield, “Photocatalytic properties of titania pillared clays by different drying methods,” *Journal of Colloid and Interface Science*, vol. 209, no. 1, pp. 193–199, 1999.
- [20] A. Rapsomanikis, D. Papoulis, D. Panagiotaras et al., “Nanocrystalline TiO₂ and halloysite clay mineral composite films prepared by sol-gel method: synergistic effect and the case of silver modification to the photocatalytic degradation of basic blue-41 azo dye in water,” *Global NEST Journal*, vol. 16, no. 3, pp. 485–498, 2014.
- [21] P. Wang, T. Xie, D. Wang, and S. Dong, “Facile synthesis of TiO₂(B) crystallites/nanopores structure: a highly efficient photocatalyst,” *Journal of Colloid and Interface Science*, vol. 350, no. 2, pp. 417–420, 2010.
- [22] S. Tieng, A. Kanaev, and K. Chhor, “New homogeneously doped Fe(III)-TiO₂ photocatalyst for gaseous pollutant degradation,” *Applied Catalysis A: General*, vol. 399, no. 1-2, pp. 191–197, 2011.
- [23] Y.-F. Tu, S.-Y. Huang, J.-P. Sang, and X.-W. Zou, “Preparation of Fe-doped TiO₂ nanotube arrays and their photocatalytic activities under visible light,” *Materials Research Bulletin*, vol. 45, no. 2, pp. 224–229, 2010.
- [24] R. M. Mohamed, D. L. McKinney, and W. M. Sigmund, “Enhanced nanocatalysts,” *Materials Science and Engineering R: Reports*, vol. 73, no. 1, pp. 1–13, 2012.

Research Article

Preparation and Investigation of the Microtribological Properties of Graphene Oxide and Graphene Films via Electrostatic Layer-by-Layer Self-Assembly

Yongshou Hu,¹ Haibing Ma,¹ Wei Liu,² Qianqian Lin,² and Bin Liu²

¹Department of Stomatology, Traditional Chinese Medicine Hospital of Gansu Province, Lanzhou 730050, China

²School of Nuclear Science and Technology, Stomatology, Lanzhou University, Lanzhou 730000, China

Correspondence should be addressed to Bin Liu; liubkq@lzu.edu.cn

Received 17 September 2014; Accepted 22 December 2014

Academic Editor: Wenwen Liu

Copyright © 2015 Yongshou Hu et al. This is an open access article distributed under the Creative Commons Attribution License, which permits unrestricted use, distribution, and reproduction in any medium, provided the original work is properly cited.

Graphene oxide (GO) films with controlled layers, deposited on single-crystal silicon substrates, were prepared by electrostatic self-assembly of negatively charged GO sheets. Afterward, graphene films were prepared by liquid-phase reduction of as-prepared GO films using hydrazine hydrate. The microstructures and microtribological properties of the samples were studied using X-ray photoelectron spectroscopy, Raman spectroscopy, X-ray diffraction, UV-*vis* absorption spectroscopy, water contact angle measurement, and atomic force microscopy. It is found that, whether GO films or graphene films, the adhesion force and the coefficients of friction both show strong dependence on the number of self-assembled layers, which both allow a downward trend as the number of self-assembled layers increases due to the interlayer sliding and the puckering effect when the tip slipped across the top surface of the films. Moreover, in comparison with the GO films with the same self-assembled layers, the graphene films possess lower adhesion force and coefficient of friction attributed to the difference of surface functional groups.

1. Introduction

With the rapid development of science and technology, especially of nanotechnology, micromechanical and high-density magnetic recording systems, the study of microtribology has attracted wide attention. In theoretical research, microtribology requires exploration deep into the atomic and molecular scale to extensively reveal the phenomena of friction processes and plays an important role in perfecting the theory of tribology [1]. In applied research, the continual emergence of advanced technologies, such as magnetic recording systems and microelectromechanical systems (MEMs), not only brings new challenges for traditional tribology and lubrication technology, but also prompts studies on friction at the microscale and development of nanolubrication technology [2].

Although MEMs are known for their superior performance and low unit cost [3], their large surface area-to-volume ratios result in serious adhesive and frictional problems that limit their operations [4]. Also, conventional

lubricants are no longer particularly desirable due to the microsize of MEMs components. Reports on improvements in the microtribological performance of MEMs are divided into two aspects: (i) preparation of a super-hard surface coating on a silicon substrate via ion implantation or thin film deposition to enhance wear resistance, and (ii) deposition of a soft coating such as Langmuir-Blodgett (LB) film to reduce the coefficient of friction (μ) of the silicon surface and further improve friction and wear properties. However, many super-hard coatings, such as SiC, diamond, and diamond-like carbon, are not easy to prepare, and LB films are limited by their poor stability, poor ability to resist external interference, and short life. For the above reasons, exploration of new methods to prepare protection films with good friction-reduction and wear-resistance is of utmost importance. As we know, an approach to preparing protection films with obvious wear-resistance behavior is the self-assembly technique [5–7]. Compared with other techniques, self-assembly has some special advantages, such as simple preparation, controlled film thickness, thermodynamic stability, and independence

from the size and shape of the base, giving it broad application prospects in the field of tribology [8]. Lio et al. [9] prepared alkanethiols and alkyl silanes self-assembly monolayers (SAMs) with different alkyl chain lengths and found that short-chain SAMs exhibit higher μ than long-chain SAMs. Beake and Leggett [10] studied mixed SAM systems composed of short- and long-chain alkanethiols and they found that the μ varies substantially with monolayer composition, especially of changes in the alkyl chain. Huang et al. [11] prepared self-assembled multilayer films consisted of nitrocontaining diazoresin and polysodium p-styrenesulfonate (NDR-PSS), and the study of their tribological behaviors showed that the 10-bilayer film exhibits better load-carrying and antiwear abilities than 1-bilayer film. Gao and Yu [12] believed that the tribological behaviors of multilayer polyelectrolyte films are closely related to the layer numbers. Ren et al. [13] prepared a stearic acid and 3-aminopropyl triethoxysilane (STA-APS) dual-layer film on a single-crystal silicon substrate via chemical self-assembly, and the tribological experiment showed that the STA-APS film has good adhesive-resistance and friction-reduction in both microscopic and macroscopic levels.

Graphene, a 2-dimensional atomic thin layer of carbon nanostructure, exhibits notable electronic, thermal, chemical, and mechanical properties, as well as unrivaled mechanical stiffness and strength [14]. Thus, it is considered highly applicable in next-generation electronic devices and MEMs [15, 16]. Lee et al. [17] found that the frictional force on graphene is smaller than that on the silicon oxide substrate, while larger than that on bulk graphite. They also compared the nanoscale friction characteristics of atomically thin sheets (including graphene, molybdenum disulfide, niobium diselenide, and hexagonal boron nitride) exfoliated onto weakly adherent silicon oxide substrates with those of their bulk counterparts and revealed that friction force of each sheet-like material monotonically increases with the number of layers decreasing [18].

However, it should be mentioned that realization of graphene application in MEMs is severely restricted by the difficulty of obtaining a stable graphene film on a device surface via exfoliation-sticking and common solution processes. The key defect is attributed to the lack of active groups on the surface of graphene, resulting in a very weak adhesion to substrate. Fortunately, the existence of abundant oxygenous groups on graphene oxide (GO) sheets makes the self-assembly technique feasible, to prepare graphene films with good adhesion to substrates [19–21]. Ou et al. [22] revealed that assembled reduced graphene oxide (RGO) monolayer film on silicon substrate possesses good friction reduction and antiwear abilities due to its intrinsic structure.

In this paper, a facile preparation of graphene multilayer films with controlled layers, deposited on silicon substrates, was realized by electrostatic self-assembly of negatively charged GO sheets followed by liquid-phase reduction using hydrazine hydrate. An investigation of the relationship between the microtribological characteristics and the number of self-assembled layers was employed in-depth. Also, comparisons of the microtribological properties between

self-assembled GO and RGO multilayer films were carried out as well.

2. Experimental

2.1. Materials. Polished single-crystal silicon (111) wafers, obtained from GRINM Semiconductor Materials Co., Ltd., Beijing, with a surface roughness of about 0.4 nm after cleaning, were used as the substrates. Poly(diallyldimethylammonium chloride) (PDDA, Mw = 400,000–500,000, 20 wt.% solution in water) was obtained from Sigma-Aldrich. GO was synthesized using a modified Hummers method [23, 24]. Other reagents were of analytical purity and used as received. Ultrapure water ($18 \text{ M}\Omega\text{-cm}^{-1}$) was used throughout the experiment.

2.2. Preparation of GO and Graphene Multilayer Films. Silicon substrates were cleaned and hydroxylated by immersing in a piranha solution (a mixture of 7 : 3 (v/v) 98% H_2SO_4 and 30% H_2O_2) at 30°C for 20 min. The substrates were then fully rinsed with ultrapure water, placed into a 0.2 wt.% PDDA aqueous solution, and then held for 15 min. A monolayer of PDDA was thus formed on each silicon surface. At the same time, a homogeneous GO aqueous suspension (0.5 mg/mL) was prepared by sonication and centrifugation. After rinsing with ultrapure water, a PDDA-coated silicon substrate was immersed in the GO suspension and kept for 15 min. A monolayer of GO was presumably produced on top of the PDDA film via electrostatic interaction between the negatively charged GO and the positively charged PDDA. By repeating the above steps, GO multilayer films with the desired layers were obtained. Subsequently, RGO multilayer films were prepared by the reduction of as-prepared GO films with hydrazine hydrate as described elsewhere [25]. In order to investigate the microstructural change of GO through the hydrazine hydrate reduction, powdery RGO was prepared as well.

Moreover, in order to certify that the graphene films with gradually increased thickness can be prepared by repeating the electrostatic layer-by-layer (LBL) self-assembly; RGO multilayer films on indium tin oxide (ITO) glass substrates were prepared according to the same LBL self-assembly followed by the hydrazine hydrate reduction. Before the self-assembly experiments, each ITO substrate was cleaned with a 3.95 wt.% ethanol solution of potassium hydroxide for 5 min using ultrasonication, thoroughly rinsed with ultrapure water and ethanol and was ready to use.

2.3. Characterization. The surface morphologies of the RGO sheets and the assembled GO and RGO films were investigated by a Nanoscope III a multimode atomic force microscope (AFM, Veeco) in tapping mode. The XPS measurements of powdery GO and RGO were performed on a Perkin-Elmer PHI-5702 multifunctional X-ray photoelectron spectroscope (Physical Electronics, USA), using $\text{Al-K}\alpha$ radiation (photon energy 1476.6 eV) as the excitation source and the binding energy of Au ($\text{Au } 4f_{7/2}$: 84.00 eV) as the reference. The crystallographic structures of the powdery samples were determined by a powder X-ray diffraction system (XRD,

TTR-III) equipped with CuK α radiation ($k = 0.15406$ nm). Raman spectroscopy (Lab RAMHR800, Horiba, Hobin Yvon, France, 532 nm laser excitation) was employed to characterize the microstructure of the film samples. UV-*vis* absorption spectra of the RGO multilayer films were monitored with a Hitachi U-2010 spectrophotometer. The water contact angle measurements of the film samples were carried out using the “sitting drop” method in atmospheric conditions at room temperature. Each measurement was repeated 10 times and reproducibility was never worse than $\pm 2^\circ$. The results of measurements were treated statistically.

2.4. Microtribological Properties of GO and Graphene Multilayer Films. The microtribological behavior was characterized with the same AFM/FFM instrument controlled by RHK electronics (RHK Technology, Rochester Hills, MI, USA) under contact mode. Mica was used to calibrate the photodetector sensitivity by measuring a force curve. Relative to the very flexible lever, the stiffness of the mica was sufficiently large; it was assumed that all deflection during the force measurement would occur in the lever. Under these circumstances, the photodetector sensitivity was the gradient of a plot of photodetector signals versus displacement while measuring repulsive forces. Commercially available Si $_3$ N $_4$ cantilevers/tips with a nominal force constant of 2.0 nN·m $^{-1}$ were employed. Friction force measurements were recorded in scope mode by obtaining friction loops from six separate areas on the monolayer surfaces. Construction of friction load plots was accomplished by varying the normal load applied to the tip. Data of μ were standardized using an internal normalization procedure previously described elsewhere [26, 27]. A single tip was used to acquire a complete set of data for an entire series of samples, and the gradients of the friction-load plots were used to obtain μ .

To obtain the adhesive force between the AFM tip and the film surface, the force distance curve was recorded and the pull-off force was assumed as the adhesive force, which was given by $F = K_c \Delta Z_p$, where K_c is the force constant of the cantilever, and ΔZ_p is the vertical displacement of the piezotube, that is, the deflection of the cantilever [28, 29]. The displacement of the retraction part from the approach part, caused by the hysteresis of the piezotube, was adjusted. To reduce the statistical error, we measured the adhesion force at many different locations on a sample surface. All the friction and adhesion tests were conducted at room temperature of 21°C and a relative humidity of 25%.

3. Results and Discussion

As Figure 1 shows, the AFM image and its corresponding height profile show that an individual RGO sheet on a silicon wafer surface has a thickness of 0.9 nm, which is accordant with the value for single-layer RGO sheet [25, 30]. The measured thickness of the RGO sheet is much larger than the theoretical value of graphene layer (0.34 nm), which is due to the fact that a small number of oxygenous groups still remain on the surface of the RGO sheet after chemical reduction.

The C1s XPS spectra of GO and RGO sheets are shown in Figure 2. The C1s XPS spectrum of GO can be fitted into

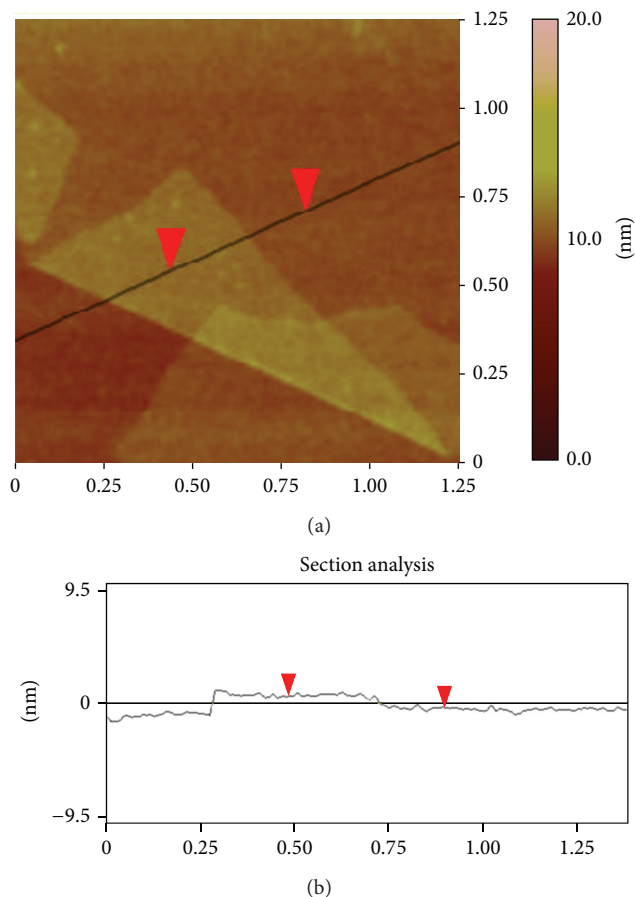


FIGURE 1: AFM image and the height profile of the RGO sheets.

four components [31]: non-oxygenated carbon at 284.8 eV, carbon in C–O at 286.2 eV, carbonyl carbon (C=O, 287.9 eV), and carboxylate carbon (O–C=O, 289.0 eV). In contrast to the C1s XPS spectrum of GO, the spectrum of RGO shows the presence of the same functionalities but with much smaller intensities, indicating that most of the oxygen functional groups were removed by reduction with hydrazine hydrate.

Structural difference between GO and RGO was further evidenced from the XRD measurements. As shown in Figure 3, the XRD pattern of GO has a diffraction peak at 12.1° , corresponding to water-bound intercalated oxidized graphite [32]. For the XRD pattern of RGO, the diffraction peaks at 24.5° and 42.8° are attributed to the graphite-like structures (002) and (100), respectively. This result indicates a relatively complete reduction from GO to RGO.

Figure 4 shows the Raman spectra of self-assembled GO and RGO multilayer films with the same layers of 20. Two spectra both exhibit two intense peaks at 1328 cm $^{-1}$ and 1595 cm $^{-1}$, corresponding to the D and G bands, respectively. 2D and D+G bands are also observed [33]. The G band is related to the vibration of sp 2 -hybridized carbon, whereas the D band corresponds to the sp 2 -hybridized carbon with defects associated with vacancies, disorder, and grain boundaries [34]. The intensity ratio of I_D/I_G in RGO spectrum (1.11) obviously increases compared with that in GO spectrum

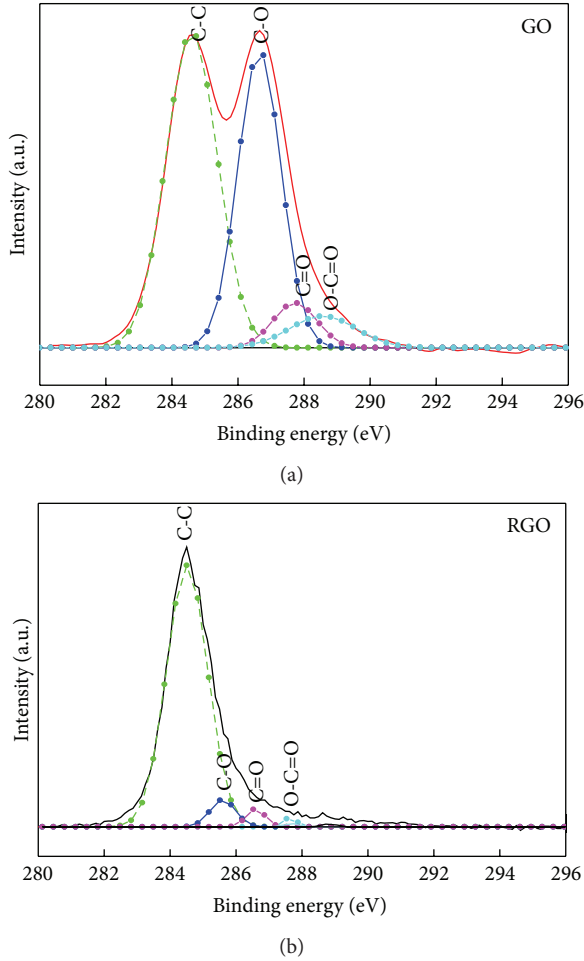


FIGURE 2: The C 1s XPS spectra of the GO (a) and RGO (b) sheets.

(1.01), indicating the realization of deoxygenation in chemical RGO film [25]. Moreover, in contrast to the ratio between the 2D and G bands, I_{2D}/I_G , of the GO films, the ratio of I_{2D}/I_G for RGO increases due to the recovering of sp^2 C=C bonds.

Figure 5 shows the UV-*vis* absorption spectra of RGO multilayer films on ITO glass substrates. The inset shows the nonlinear relationship between the absorbance of RGO films at 500 nm and the number of self-assembled layers. The absorbance at 500 nm nonlinearly increases with the increase of the self-assembled layers, suggesting that the RGO multilayer films with elevated layers were successfully by LBL self-assembly.

The surface morphologies of GO and RGO multilayer films were observed via AFM. As shown in Figure 6, the modified silicon substrate is covered by GO or RGO sheets after the self-assembly of the fifth layers. The root-mean-square roughness of the GO and RGO sheets is 4.613 and 4.098 nm, respectively, indicating that the roughness of GO films decreased after reduction with hydrazine hydrate.

The microtribological behaviors of the GO and RGO multilayer films in air were evaluated by AFM. Figure 7 shows the adhesion force curves for the GO and RGO films with the different number of layers. It is obvious seen that, the adhesion force for GO or RGO films shows strong

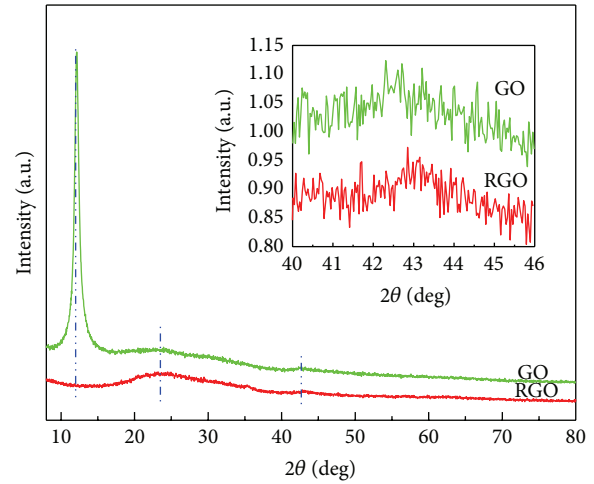


FIGURE 3: The XRD patterns of the GO and RGO sheets.

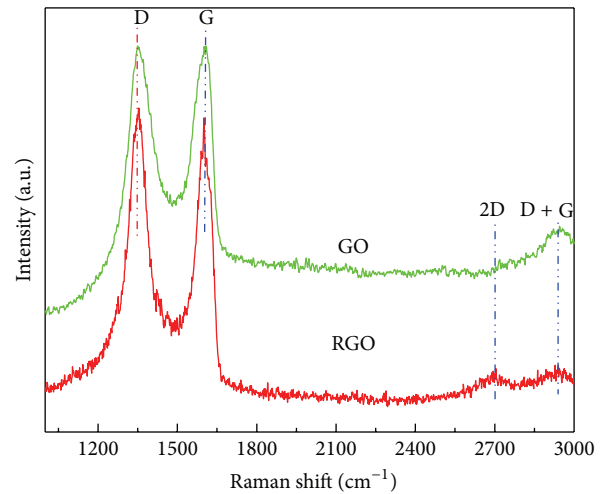


FIGURE 4: The Raman spectra of the GO and RGO multilayer films with the fifth layers.

dependence on the number of self-assembled layers, which allow a downward trend as the number of self-assembled layers increases. Moreover, in comparison with the GO films with the same self-assembled layers, the RGO films possess lower adhesion force.

In general, the adhesive force between an AFM tip and a sample surface includes the capillary force (F_c), as well as solid-solid interaction, Van der Waals force (F_{vdW}), electrostatic force (F_E), and the chemical bonding force (F_B) [28, 35]. As such, F_{ad} can be expressed as $F_{ad} = F_C + F_{vdW} + F_E + F_B$. Since the tip and sample sit in air for a relatively long time, no net charges are expected to remain in them. Thus, $F_E = 0$. The chemical bonding force can also be neglected since the surfaces of the tip and the sample are saturated with chemical bonds. Thus, no ionic or covalent bonds are expected to form during contact. Therefore, F_{ad} consists only of F_C and F_{vdW} . The capillary force F_C is closely related to surface wettability, which can be evaluated by the water contact angles (WCAs) [36].

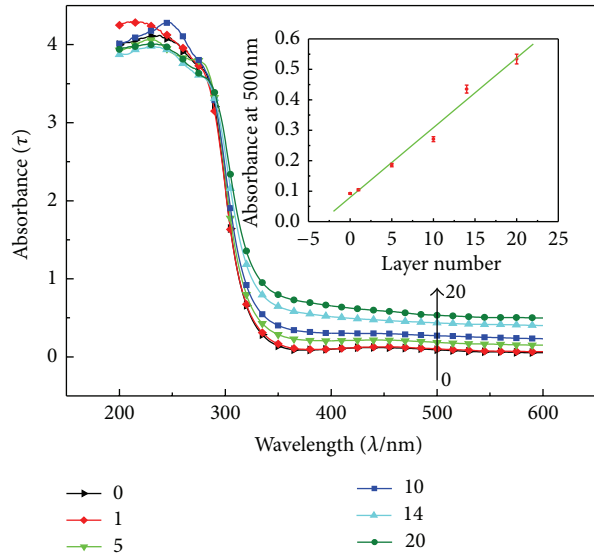


FIGURE 5: UV-vis/spectra of the RGO multilayer films on ITO glass substrates. The inset is the absorbance at 500 nm as a function of layer number.

The WCAs on the hydroxylated silicon surface and self-assembled films are shown in Figure 8. It shows that different numbers of layers of GO films or RGO films have almost no effect on their WCAs. However, after reduction, the WCA of GO films obviously increases from 60° to 81° , indicating that the RGO film surface is more hydrophobic due to the decrease of abundant oxygenous groups in GO sheets after reduction by hydrazine. This point has already been proven by the XPS data of GO and RGO and explains why the adhesive force of GO films is higher than that of RGO films. Such a phenomenon may be properly understood, since adhesive force, which depends mainly on the capillary force between a tip and a surface, is dramatically lowered or even eliminated when the surface becomes hydrophobic [13].

It has been reported that F_{vdW} also contributes to adhesion at very low humidity [28]. The difference in F_{vdW} between GO and RGO is also attributed to the oxygenous groups that exist on the surfaces of the films. Compared with RGO, the surface of the GO sheets has many oxygenous groups due to graphite oxidation, resulting in strong Van der Waals forces between the edges of GO sheets and the AFM tip. Therefore, the large F_{vdW} may be a key factor in the relatively high adhesion of GO. From the above analyses, it could be deduced that the difference in adhesion force between GO and RGO may be attributed to the quantity of surface functional groups. In addition, the adhesion force displays a downward trend as the number of layers increases, a finding that may be due to the decrease in oxygenous groups exposed to the outer edges of the GO or RGO sheets as a consequence of the closer arrangement of the sheets.

To obtain stable friction-versus-load curves, especially on the silicon surface, a typical blunting process of a Si_3N_4 tip via friction scanning on mica was performed in a manner similar to a previous report [37]. The friction-versus-load curves for GO and RGO films measured using blunt tips

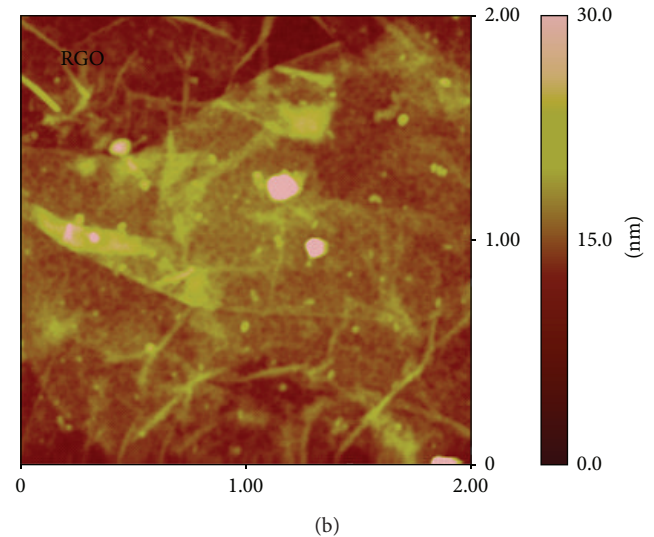
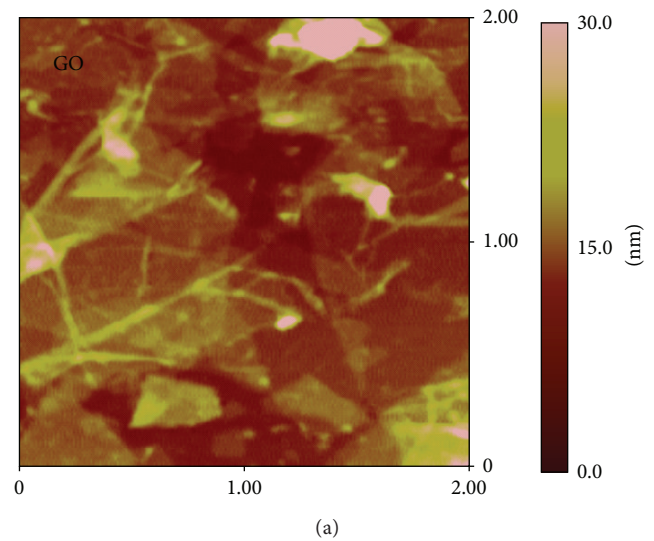
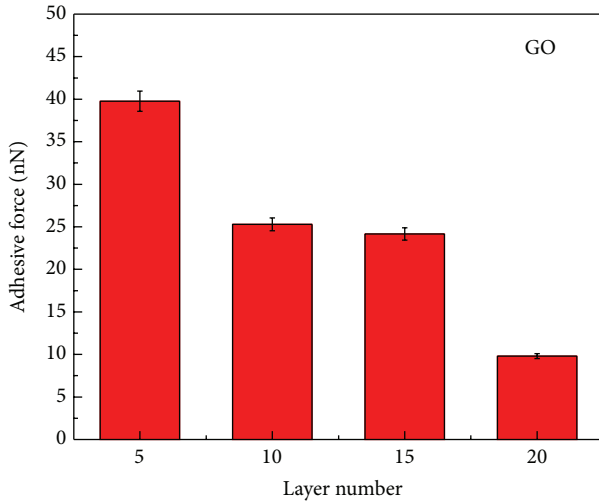
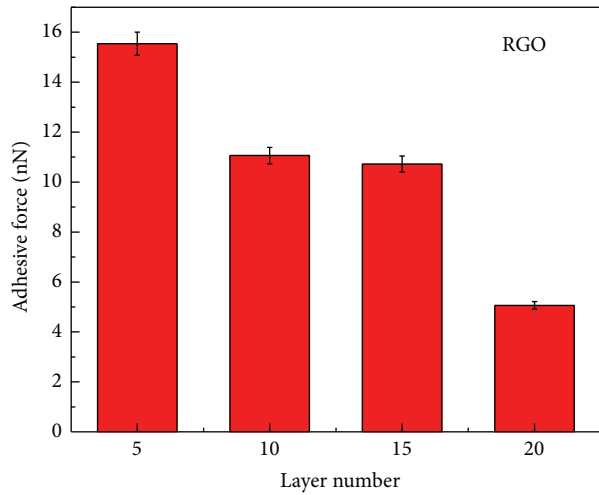


FIGURE 6: AFM images for GO (a) and RGO (b) multilayer films with the fifth layer.

are shown in Figure 9. The friction-versus-load curves show linear characteristics as the external load exceeds 360 nN, indicating that the data are in agreement with Amontons' law [26]. However, as the figure shows, not all of the friction load curves pass through the origin, suggesting that Deraguin's modification of Amontons' law should be used: $F_L = \mu F_N + F_0$, where μ is the coefficient of friction, F_N is the normal force (applied load), and F_0 is the friction force when the normal force is zero [26, 38]. According to this analysis, the gradient of a plot of the friction force against the load is equal to μ . It should be mentioned that the value of μ obtained in this study is not absolutely accurate and it is not comparable with the value obtained by other authors. However, a systemic comparison among the self-assembled GO and RGO films in our investigations is highly reliable. As shown in Figure 9, the value of μ gradually decreases with the increase in number of layers of the two films. Compared with GO films with the same self-assembled layers, RGO films possess lower μ at



(a)



(b)

FIGURE 7: Adhesion force curves for the GO (a) and RGO (b) multilayer films with the different number of layers.

the same measurement conditions, indicating that RGO films have better lubricity. Many studies have reported that friction decreases with the reduction of adhesion on a microscopic scale [39–41]. In addition, these studies further provided a manifestation for our results. Thus, for RGO film, smaller adhesion force compared with GO film results in the lower μ . It is also possible that the reduction of μ is brought about by the reduction of surface roughness after the chemical reduction, as proved by AFM images.

The possible factors that contribute to the relationship between the μ and the number of layers of GO and RGO films were analyzed. Discrepancy in the μ of GO and RGO films was also discussed. A possible explanation for the reduction in μ when the number of layers increases is that films that increasingly attach to the substrate surface via electrostatic interaction have more freedom to swing and rearrange along the sliding direction under shear stress, thus yielding smaller resistance. Interlayer sliding could have

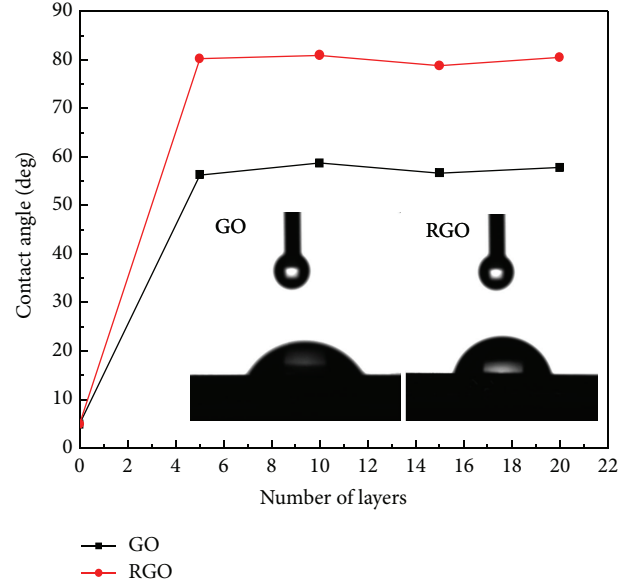


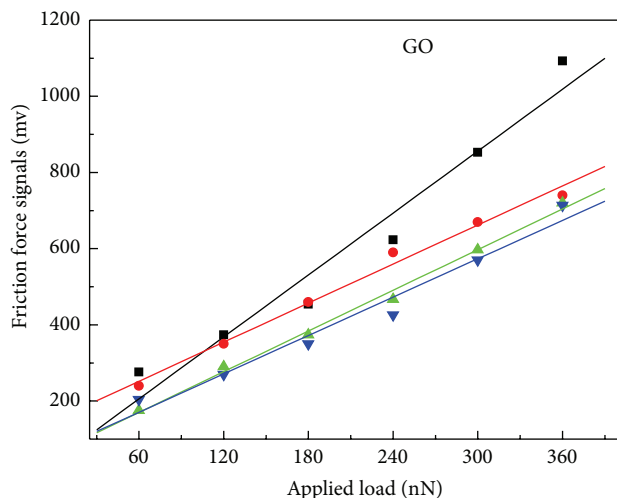
FIGURE 8: Water contact angles for the GO and RGO multilayer films with different numbers of layers. Inset is the contact angles for fifth layer.

occurred when the tip slipped across the top surface of the films in our experiments and reduced the friction of thicker samples.

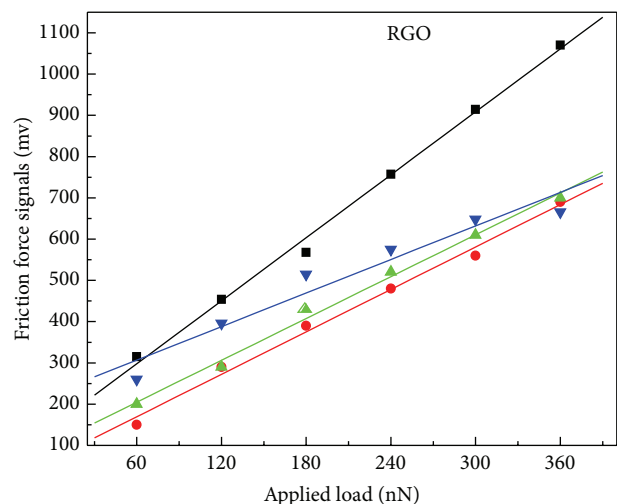
Yet another possibility that may explain the mechanism of the thickness-dependent friction behavior is based on the puckering effect proposed by Lee et. al via the simple model of a tip sliding across a flexible membrane [17]. When the tip comes into contact with the top surface of the membrane, adhesion causes the sheet to easily pucker locally because of the sheet's low bending stiffness compared with its in-plane stiffness [42]. The puckered geometry is modified at the front edge by tip-sheet friction, and the symmetry of the puckered region breaks and piles up mostly at the front edge of the contact; the geometry reverses when the tip changes direction. The enlarged contact area brought about by out-of-plane deformation requires more force to slide the tip forward [22]. For a thicker sheet, puckering is less prominent owing to the larger bending stiffness of the sheet [22]; therefore, friction is also lower.

4. Conclusion

In summary, GO and RGO multilayer films were prepared via electrostatic self-assembly on single-silicon crystal substrates. The microstructure and microtribological properties of the samples were investigated. According to the experimental results, RGO films have smaller adhesive force and lower μ compared with GO films, indicating that the former has better friction reduction properties under low applied loads in the microscopic scale. The improved tribological properties for RGO films are attributed to a decrease of abundant oxygenous groups in RGO molecules, decrease in adhesion, and a decrease of surface roughness after reduction by hydrazine. For GO films and RGO films, the adhesive



(a)



(b)

FIGURE 9: Friction-versus-load curves for the GO (a) and RGO (b) multilayer films with the different number of layers.

resistance and μ both show the downward trend as the number of layers increases. One reason is due to more freedom to swing and rearrange along the sliding direction under shear stress, thus yielding smaller resistance with the increase of number of layers. Another reason is that puckering is less prominent for a thicker sheet owing to the larger bending stiffness of the sheet; therefore, friction is also lower.

Conflict of Interests

The authors declare that they have no financial and personal relationships with other people or organizations that can

inappropriately influence their works; there is no professional or other personal interest of any nature or kind in any product, service, and/or company that could be construed as influencing the position presented in, or the review of, the paper.

Authors' Contribution

The manuscript was written through contributions of all authors. Yong shouHu and Haibing Ma contributed equally to this report. All authors have given approval to the final version of the paper.

Acknowledgments

This paper was supported by the Open Fund of Key Laboratory of Mechanics on Disaster and Environment in Western China (201203) and the Natural Science Foundation of Gansu Province (1208RJYA036).

References

- [1] S. M. Hsu, "Nano-lubrication: concept and design," *Tribology International*, vol. 37, no. 7, pp. 537–545, 2004.
- [2] Y. Qin, A. Brockett, Y. Ma et al., "Micro-manufacturing: research, technology outcomes and development issues," *International Journal of Advanced Manufacturing Technology*, vol. 47, no. 9–12, pp. 821–837, 2010.
- [3] S. M. Spearing, "Materials issues in microelectromechanical systems (MEMS)," *Acta Materialia*, vol. 48, no. 1, pp. 179–196, 2000.
- [4] Z. Rymuza, "Control tribological and mechanical properties of MEMS surfaces. Part I: critical review," *Microsystem Technologies*, vol. 5, no. 4, pp. 173–180, 1999.
- [5] Y. Lvov, G. Decher, and H. Möhwald, "Assembly, structural characterization, and thermal behavior of layer-by-layer deposited ultrathin films of poly(vinyl sulfate) and poly(allylamine)," *Langmuir*, vol. 9, no. 2, pp. 481–486, 1993.
- [6] J. C. Chen, L. Huang, L. M. Ying, G. B. Luo, X. S. Zhao, and W. X. Cao, "Self-assembly ultrathin films based on diazoresins," *Langmuir*, vol. 15, no. 21, pp. 7208–7218, 1999.
- [7] M. Ferreira and M. F. Rubner, "Molecular-level processing of conjugated polymers. 1. Layer-by-layer manipulation of conjugated polyions," *Macromolecules*, vol. 28, no. 21, pp. 7107–7114, 1995.
- [8] D. Julthongpipit, H.-S. Ahn, D.-I. Kim, and V. V. Tsukruk, "Tribological behavior of grafted polymer gel nanocoatings," *Tribology Letters*, vol. 13, no. 1, pp. 35–40, 2002.
- [9] A. Lio, D. H. Charych, and M. Salmeron, "Comparative atomic force microscopy study of the chain length dependence of frictional properties of alkanethiols on gold and alkylsilanes on Mica," *The Journal of Physical Chemistry B*, vol. 101, no. 19, pp. 3800–3805, 1997.
- [10] B. D. Beake and G. J. Leggett, "Variation of frictional forces in air with the compositions of heterogeneous organic surfaces," *Langmuir*, vol. 16, no. 2, pp. 735–739, 2000.
- [11] L. Huang, G. Luo, X. Zhao, J. Chen, and W. Cao, "Self-assembled multilayer films based on diazoresins studied by atomic force microscopy/friction force microscopy," *Journal of Applied Polymer Science*, vol. 78, no. 3, pp. 631–638, 2000.

- [12] S. Gao and L. Yu, "Preparation and investigation of the tribological behavior of small molecular weight organic dye and polycation ultra-thin films," *Acta Polymerica Sinica*, vol. 1, no. 1, pp. 18–22, 2003.
- [13] S. L. Ren, S. R. Yang, and Y. P. Zhao, "Micro- and macro-tribological study on a self-assembled dual-layer film," *Langmuir*, vol. 19, no. 7, pp. 2763–2767, 2003.
- [14] A. K. Geim, "Graphene: status and prospects," *Science*, vol. 324, no. 5934, pp. 1530–1534, 2009.
- [15] K. S. Novoselov, A. K. Geim, S. V. Morozov et al., "Electric field in atomically thin carbon films," *Science*, vol. 306, no. 5696, pp. 666–669, 2004.
- [16] I. Meric, M. Y. Han, A. F. Young, B. Ozyilmaz, P. Kim, and K. L. Shepard, "Current saturation in zero-bandgap, top-gated graphene field-effect transistors," *Nature Nanotechnology*, vol. 3, no. 11, pp. 654–659, 2008.
- [17] H. Lee, N. Lee, Y. Seo, J. Eom, and S. Lee, "Comparison of frictional forces on graphene and graphite," *Nanotechnology*, vol. 20, no. 32, Article ID 325701, 2009.
- [18] C. Lee, Q. Li, W. Kalb et al., "Frictional characteristics of atomically thin sheets," *Science*, vol. 328, no. 5974, pp. 76–80, 2010.
- [19] H. F. Yang, F. H. Li, C. S. Shan et al., "Covalent functionalization of chemically converted graphene sheets via silane and its reinforcement," *Journal of Materials Chemistry*, vol. 19, no. 26, pp. 4632–4638, 2009.
- [20] W. Q. Zhongqing, D. E. Barlow, and P. E. Sheehan, "The assembly of single-layer graphene oxide and graphene using molecular templates," *Nano Letters*, vol. 8, no. 10, pp. 3141–3145, 2008.
- [21] Y.-K. Kim and D.-H. Min, "Durable large-area thin films of graphene/carbon nanotube double layers as a transparent electrode," *Langmuir*, vol. 25, no. 19, pp. 11302–11306, 2009.
- [22] J. F. Ou, J. Wang, S. Liu et al., "Tribology study of reduced graphene oxide sheets on silicon substrate synthesized via covalent assembly," *Langmuir*, vol. 26, no. 20, pp. 15830–15836, 2010.
- [23] Y. Xu, H. Bai, G. Lu, C. Li, and G. Shi, "Flexible graphene films via the filtration of water-soluble noncovalent functionalized graphene sheets," *Journal of the American Chemical Society*, vol. 130, no. 18, pp. 5856–5857, 2008.
- [24] M. Choucair, P. Thordarson, and J. A. Stride, "Gram-scale production of graphene based on solvothermal synthesis and sonication," *Nature Nanotechnology*, vol. 4, no. 1, pp. 30–33, 2009.
- [25] S. Stankovich, D. A. Dikin, R. D. Piner et al., "Synthesis of graphene-based nanosheets via chemical reduction of exfoliated graphite oxide," *Carbon*, vol. 45, no. 7, pp. 1558–1565, 2007.
- [26] N. J. Brewer, B. D. Beake, and G. J. Leggett, "Friction force microscopy of self-assembled monolayers: influence of adsorbate alkyl chain length, terminal group chemistry, and scan velocity," *Langmuir*, vol. 17, no. 6, pp. 1970–1974, 2001.
- [27] Y.-S. Shon, S. Lee, R. Colorado Jr., S. S. Perry, and T. R. Lee, "Spiroalkanedithiol-based SAMs reveal unique insight into the wettabilities and frictional properties of organic thin films," *Journal of the American Chemical Society*, vol. 122, no. 31, pp. 7556–7563, 2000.
- [28] X. Xiao and L. Qian, "Investigation of humidity-dependent capillary force," *Langmuir*, vol. 16, no. 21, pp. 8153–8158, 2000.
- [29] V. V. Tsukruk and V. N. Bliznyuk, "Adhesive and friction forces between chemically modified silicon and silicon nitride surfaces," *Langmuir*, vol. 14, no. 2, pp. 446–455, 1998.
- [30] S. Stankovich, D. A. Dikin, G. H. B. Dommett et al., "Graphene-based composite materials," *Nature*, vol. 442, no. 7100, pp. 282–286, 2006.
- [31] S. Stankovich, R. D. Piner, X. Chen, N. Wu, S. T. Nguyen, and R. S. Ruoff, "Stable aqueous dispersions of graphitic nanoplatelets via the reduction of exfoliated graphite oxide in the presence of poly(sodium 4-styrenesulfonate)," *Journal of Materials Chemistry*, vol. 16, no. 2, pp. 155–158, 2006.
- [32] C. Hontoria-Lucas, A. J. López-Peinado, J. D. D. López-González, M. L. Rojas-Cervantes, and R. M. Martín-Aranda, "Study of oxygen-containing groups in a series of graphite oxides: physical and chemical characterization," *Carbon*, vol. 33, no. 11, pp. 1585–1592, 1995.
- [33] C.-Y. Su, Y. Xu, W. Zhang et al., "Electrical and spectroscopic characterizations of ultra-large reduced graphene oxide monolayers," *Chemistry of Materials*, vol. 21, no. 23, pp. 5674–5680, 2009.
- [34] H. Kang, A. Kulkarni, S. Stankovich, R. S. Ruoff, and S. Baik, "Restoring electrical conductivity of dielectrophoretically assembled graphite oxide sheets by thermal and chemical reduction techniques," *Carbon*, vol. 47, no. 6, pp. 1520–1525, 2009.
- [35] M. Binggeli and C. M. Mate, "Influence of capillary condensation of water on nanotribology studied by force microscopy," *Applied Physics Letters*, vol. 65, no. 4, pp. 415–417, 1994.
- [36] S.-L. Ren, S.-R. Yang, J.-Q. Wang, W.-M. Liu, and Y.-P. Zhao, "Preparation and tribological studies of stearic acid self-assembled monolayers on polymer-coated silicon surface," *Chemistry of Materials*, vol. 16, no. 3, pp. 428–434, 2004.
- [37] L. M. Qian, X. D. Xiao, and S. Z. Wen, "Tip in situ chemical modification and its effects on tribological measurements," *Langmuir*, vol. 16, no. 2, pp. 662–670, 2000.
- [38] T. T. Foster, M. R. Alexander, G. J. Leggett, and E. McAlpine, "Friction force microscopy of alkylphosphonic acid and carboxylic acids adsorbed on the native oxide of aluminum," *Langmuir*, vol. 22, no. 22, pp. 9254–9259, 2006.
- [39] A. Noy, C. D. Frisbie, L. F. Rozsnyai, M. S. Wrighton, and C. M. Lieber, "Chemical force microscopy: exploiting chemically-modified tips to quantify adhesion, friction, and functional group distributions in molecular assemblies," *Journal of the American Chemical Society*, vol. 117, no. 30, pp. 7943–7949, 1995.
- [40] V. V. Tsukruk, M. P. Everson, L. M. Lander, and W. J. Brittain, "Nanotribological properties of composite molecular films: C₆₀ anchored to a self-assembled monolayer," *Langmuir*, vol. 12, no. 16, pp. 3905–3911, 1996.
- [41] C. D. Frisbie, L. F. Rozsnyai, A. Noy, M. S. Wrighton, and C. M. Lieber, "Functional group imaging by chemical force microscopy," *Science*, vol. 265, no. 5181, pp. 2071–2074, 1994.
- [42] K. R. Shull, "Contact mechanics and the adhesion of soft solids," *Materials Science and Engineering: R: Reports*, vol. 36, no. 1, pp. 1–45, 2002.

Review Article

Fluorescent Gold Nanoclusters: Synthesis and Recent Biological Application

Xiaochao Qu, Yichen Li, Lei Li, Yanran Wang, Jingning Liang, and Jimin Liang

School of Life Science and Technology, Xidian University, Xi'an, Shannxi 710071, China

Correspondence should be addressed to Xiaochao Qu; xiaochaoqu@gmail.com

Received 16 September 2014; Accepted 14 January 2015

Academic Editor: Rajesh Naik

Copyright © 2015 Xiaochao Qu et al. This is an open access article distributed under the Creative Commons Attribution License, which permits unrestricted use, distribution, and reproduction in any medium, provided the original work is properly cited.

Fluorescent gold nanoclusters (AuNCs) have been extensively studied due to their unique construction and distinctive properties, which place them between single metal atoms and larger nanoparticles. The dimension of AuNCs is comparable to the Fermi wavelength of electrons, which lead to size-dependent fluorescence and other molecule-like properties. In this review, we summarize various synthesis strategies of fluorescent AuNCs and recent advances of biological applications such as biosensing, biolabeling, and bioimaging. The synthetic methods are considered as two routes: “Atoms to Clusters” and “Nanoparticles to Clusters.” The surface functionalization of AuNCs is described as the precondition for making future bioapplications possible, which can eventually influence their stability, biocompatibility, and other properties. And then we focus on the recent advances of AuNCs-based applications in biological sensing, biolabeling, and bioimaging and finally discuss the current challenges of AuNCs in controllable synthesis and biological application.

1. Introduction

The word “nano” is for describing something which occurs with size on nanometer range [1]. The worldwide emergence of nanoscale technology and engineering was marked by the announcement of the National Nanotechnology Initiative (NNI) in January 2000 [2]. Nanotechnology, which became an emerging and promising research field in the past decades, is the combination of medicine, chemistry, physics, and biology [3]. This multidisciplinary technology is considered dedicating to assemble molecules into objects and reverse this process. The confluence of biology and nanotechnology is defined as nanobiotechnology, which is a field that investigates biosystems and creates new biomaterials using nanoscale principles and techniques [2]. The nanostructure materials in biology and biomedical field can be useful tools for biosensing, cell labeling, and molecular imaging.

Gold is the most extensively studied material among worldwide groups due to its stable chemical property, facile synthesis, and nontoxicity. Gold on bulk- or molecular-range is highly stable; however, gold nanoparticles (NPs) exhibit distinctive properties which differ from others such as their

surface plasmon resonance (SPR) effect, size-dependent electronic properties, and their photothermal effect in biological therapy [4]. For these fascinating aspects, gold NPs have been considered as the key materials of nanoscience and nanotechnology in recent years. Due to quantum confinement effects of gold nanoparticles with a dimension below 2 nm, they are too small to support surface plasmon resonance effect [5]. The noble metal nanomaterials (which we call them gold nanoclusters) are composed of several to roughly a hundred atoms [6, 7]. The dimension occurring with gold nanoclusters (AuNCs) is comparable to the Fermi wavelength of electrons [8], which place them between single metal atoms and larger nanoparticles [9]. Due to the strong quantum confinement effect of free electrons in the particles, the continuous density of states breaks up into discrete energy levels. These lead to size-dependent fluorescence and other attractive molecule-like properties such as facile surface tailor ability and color tenability [10–13].

As to size-dependent fluorescence, the photophysical properties of AuNCs are dictated by their sizes and shapes. Recent advances make it much easier to synthesize water-soluble AuNCs with tunable size or emission colors. AuNCs

has an extremely high surface-to-volume ratio, which can make the NCs for further surface modification and controllable bioconjugation. With all the above properties, AuNCs can be used in a wide range of applications, such as biodection [14], biosensing [14], biological labeling [15–17], and bioimaging [18].

When fluorophores absorb light with a particular wavelength, fluorophores will then emit energy in a form of fluorescence equaling to the energy difference between the excited state and the ground state. Fluorescent probes are the key factor in biological fluorescent measurement. In last decades, there are several different classes of fluorescent labels: organic fluorophores such as cyanine dyes and fluorescein, the rare earth NPs (quantum dots) [19], upconverting NPs, and novel fluorescent dye-doped core-shell nanobeads. But the use of these labels is limited by the poor photostability, large physical size, and toxicity of heavy metals [17]. On the contrary, AuNCs show strong photoluminescence, good photostability and high emission rates, large Stokes shift, and size-dependent tunable fluorescence, for which they can be made as an optimum nanomaterial for biological imaging, analysis, and sensing. Moreover, the surfaces of AuNCs possess a subnanometer dimension, color tenability, facile synthesis, and low toxicity [20, 21]. Compared with common fluorophores, these advantages establish them to be a novel ultrasmall fluorophores in biomedicine application [22–24].

In this review, we firstly will discuss the origin of fluorescence of AuNCs. Then we will summarize general synthesis strategies of AuNCs and describe their distinctive properties, which are followed by highlighting their fascinating photoluminescence properties. In the second part, we will discuss the recent advances of AuNCs-based application to the biological labeling and fluorescent imaging. In the final section, we will give a brief outlook on the challenges and prospective for future research of AuNCs.

2. Gold Nanoclusters: Fluorescence Property and Synthetic Method

2.1. Fluorescence Mechanism of AuNCs. Gold nanomaterials can be broadly categorized into two kinds according to their dimensions: gold nanoparticles and gold nanoclusters. Zheng has introduced the differences in structures and other properties between these two gold nanomaterials [25]. As he mentioned, gold nanoparticles which sizes are close to the wavelength of light have similar optical properties to bulk gold. What is more, the collective oscillation of conduction electrons on the surface of gold nanoparticles can interact with light and generate SPR effect when the frequency of oscillating electrons matches the frequency of incident photons. And when the gold nanoparticles have a dimension in 3–100 nm, the SPR band locates in the visible light region, which will lead to some size-dependent effects of gold NPs. The interaction between nanoparticles, the dielectric medium, and the protective ligands also has influences on the SPR effect of gold NPs.

When size of gold nanomaterials is smaller than 3 nm, the gold nanoclusters possess some distinguished properties due to their ultrasmall dimension and special structure. Because

the energy level spacing is inversely proportional to the radius of AuNCs, AuNCs with a dimension close to Fermi wavelength of an electron possess size-dependent electronic structure [26]. The AuNCs we are discussing in this review are subnanoscale nanoparticles, which have a gold center containing a countable number of gold atoms. So AuNCs are considered as superatoms or molecular-like species. For these reasons, the energy level spacing and free electronic density of AuNCs are the key factors of transition energy of AuNCs. When the energy level spacing is large enough, the free electrons behavior can be observed in the discrete energy levels [27]. According to the structural analysis of Jin's group, the fluorescence of AuNCs originates from the LUMO-HOMO transition [28]. To sum up, the distinct optical properties (absorption and fluorescence) of molecular-like AuNCs are mainly affected by their ultrasmall size and corresponding electronic structure.

In addition to the ultrasmall size, the ligands used for AuNCs preparation also have impacts on their fluorescence properties [5]. Ligands play very important roles in the formation of AuNCs as protective agents, which can prevent the superatoms from aggregation and then keep the size-dependent fluorescence property. As for the demonstration that Jin and coworkers mentioned, surface ligands of AuNCs not only can be used as capping agent but also largely affect the fluorescence of AuNCs by charging transfer from surface ligand to the gold core. When the surface ligands have strong electron donation capability, the fluorescence can be enhanced. And the ligands with electron-rich atoms or groups have been found as a very effective choice for promising surface ligand of AuNCs to enhance the fluorescence. In this paper, we will discuss the synthesis of AuNCs by using different ligands such as glutathione, dendrimers, polymers, and protein; the as-prepared AuNCs based on different synthetic methods have various fluorescence quantum yield (QY). Lots of researches have been carried out on the origin of fluorescence from AuNCs and the enhancement of fluorescence QY for the practical application such as biological labeling, sensing, and imaging. In this section, we have summarized the different fluorescence QYs of AuNCs with different synthetic routes (Table 1).

2.2. Synthetic Methods of AuNCs. Small gold nanoclusters with robust quantum effect have been extensively investigated. The synthesis of AuNCs experiences several stages. In the early time, the research was focused on gas state metal clusters [29]. Since these metal clusters in the gas phase were short-lived and hard to be functionalized, a novel method, solution-phase synthesis, arose in the 1980s [30, 31]. These synthetic strategies lead to gold nanoclusters with enhanced stability and excellent physicochemical properties.

Since Brust et al. reported the synthesis of monolayer protected metal nanoparticles, several novel advances have emerged in the field of metal nanoclusters, especially in the field of thiol-containing AuNCs. During the decades, the synthetic strategies were generally considered as two routes: "Atoms to Clusters" and "Nanoparticles to Clusters." The approach of "Atoms to Clusters" is to reduce the gold ions into zerovalent atoms, and then AuNCs are formed with the nucleation of the Au atoms. However, the gold precursors

TABLE 1: Summary of fluorescence QYs of AuNCs obtained by different synthetic approaches.

Synthesis	Fluorescence QYs	References
Protected by monolayers of glutathione	$(3.5 \pm 1.0) \times 10^{-3}$	[32]
Alkanethiol ligands 11-mercaptoundecanoic acid (11-MUA) as stabilizer	3.1×10^{-2}	[33]
Poly(amidoamine) (PAMAM) dendrimers as stabilizer and capping agent	$41 \pm 5\%$	[34]
Pentaerythritol tetrakis(3-mercaptopropionate)-terminated Polymethacrylic acid (PTMP-pMAA) as capping agent	3%	[35]
Employed poly(N-vinylpyrrolidone) (PVP) as stabilizer of the gold clusters	12.5%	[36]
Bovine serum albumin molecules as templates and reductants	~6%	[37]
Bovine pancreatic ribonuclease A (RNase-A) as the biotemplate	~12%	[38]
DNA as template to prepare gold/silver nanoclusters from Au^{3+} , Ag^+ , and DNA (5'-CCCTTAATCCCC-3')	4.5%	[39]
Employing L-3,4-dihydroxyphenylalanine (L-DOPA) as a reducing/capping reagent	1.7%	[40]
D-penicillamine as capping agent	$1.3 \pm 0.3\%$	[41]
Mercapto-9-propyladenine as capping agent	1.2%	[42]
N,N-dimethylformamide as a weak reducing agent as well as stabilizing ligand	14.28%	[43]
Dissociation process of glutathione-gold(I) polymers in aqueous solution	$4.0 \pm 0.4\%$	[44]
GSH as reductant to form Au(I)-thiolate complexes, and the aggregation of Au(I)-thiolate complexes on the Au(0) to form Au(0)@Au(I)-thiolate NCs	~15%	[45]
11-Mercaptoundecanoic acid (11-MUA) as the protecting group to reduce Au^{3+} with NaBH_4 in methanol solutions	~6.92%	[46]
Polyethylene glycol (PEG) appended with lipoic acid (LA) anchoring groups as modular ligands	14%	[47]

can be reduced into gold nanoparticles easier than into nanoclusters due to the possibility of AuNCs to aggregate. In order to solve the problem, some kinds of ligands should be used for surface modification. Moreover, the protective ligand capped on the surface can enhance the fluorescent effect. These show that choosing appropriate ligands is the key factor in stabilizing cluster from aggregation. The other route for synthesizing the AuNCs is "Nanoparticles to Clusters" route. Pradeep and coworker used excess MSA ligands in toluene to etch (MSA-) protected large Ag nanoparticles into fluorescent Ag NCs [48]. Recently, some advances have been reported [49–51] to form more stable, monodisperse, and highly fluorescent AuNCs.

2.2.1. "Atoms to Clusters" Route

(1) *Template-Based Synthesis Methods.* AuNCs with ultrafine size and nontoxicity are very attractive for biolabeling and bioimaging application. For the reason of low fluorescent QY (10^{-4} – $10^{-1}\%$) of thiol-protected AuNCs, Dickson's group developed NCs exhibiting ~40% QY by dendrimers-assisted method in the early 2000s [34]. This synthesis can effectively enhance the fluorescent effect of AuNCs with a fairly long reaction time. According to the first template-assisted techniques, a series of templates such as polymers [35, 52], proteins [53, 54], dendrimers [55], and DNA [56, 57] have been investigated for the synthetic method of AuNCs. Compared with other synthetic techniques, template-protected techniques use mild reductant in the presence of strong stabilizer. The decreased clustering rate provides efficient sequestering by stabilizers.

(i) *Dendrimers.* Dendrimers-encapsulated AuNCs exhibited strong fluorescence in the range from blue to NIR region by adjusting the generation of PAMAM and the ratio between gold and the template [55]. Water-soluble, monodisperse, highly fluorescent Au_8 NCs had been synthesized by using the fourth generation of polyamidoamine (G4-OH PAMAM) dendrimers as reduction agent and stabilizer [58, 59] by Dickson and coworkers in the early 2000s [34, 55]. The as-prepared AuNCs exhibit a strong fluorescence (QY~40%), with an intensity of 100-fold higher than AuNCs prepared by other methods, possessing strong blue luminescence with excitation and emission peak at 385 nm and 450 nm, respectively, shown in Figure 1.

Using charged PAMAM dendrimers of generation 6–9 to prepare size-tunable fluorescent AuNCs in water have been reported. The production have been characterized by a set of methods such as transmission electron microscopy (TEM) to demonstrate gold atoms encapsulated by dendrimers. In 2007, Bao et al. unveiled a new method for synthesizing nontoxicity, highly stable AuNCs by using a mild reduction agent-ascorbic acid or no reductant at physiological temperature [60]. This approach produced highly green and red emission AuNCs without forming large gold nanoparticles. Lin and coworkers [61] exploited an amphipathic microcavity-template for sequestering gold ions and synthesizing AuNCs with high QY (20–60%) through microwave irradiation. In this strategy, the fourth generation PAMAM with amine-terminated groups (G4NH₂) had a more hydrophilic microcavity than hydroxyl-terminated G4OH PAMAM, which led to the polarity-dependent ion-pair association ($\text{AuCl}_4^-/\text{G4NH}_2^+$ pair and $\text{AuBr}_4^-/\text{G4OH}^+$ pair). The strong ion-pair association was

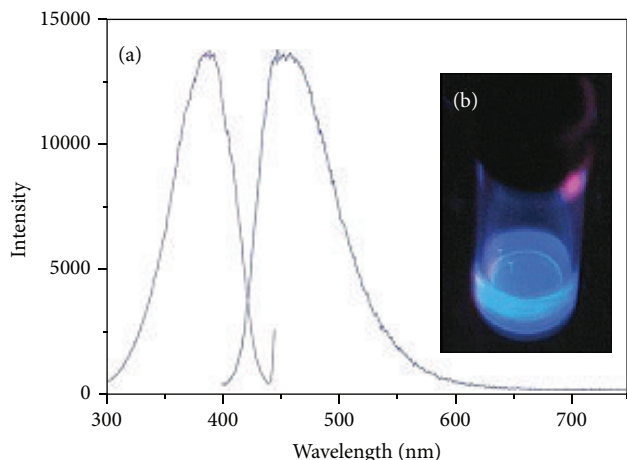


FIGURE 1: (a) Excitation and emission spectra of G4-OH PAMAM-templated AuNCs. (b) Emission from AuNCs under long-wavelength UV lamp irradiation (366 nm). Reprinted with permission from [34], ©2003, American Chemical Society.

capable of enhancing the quantum efficiency of AuNCs, and the precise control of the reaction temperature assisted by microwave irradiation could also lead to the same effects.

(ii) *Polymers*. Polymers are widespread macromolecule with abundant functional groups, which have potential to be templates for synthesizing AuNCs [62, 63]. Using polymers to prepare AuNCs has been studied by several groups. For example, AuNCs protected by multivalent polymers were synthesized by ligand exchange with dodecylamine-capped gold nanoparticles [64]. The ligand-induced etching method leads to fluorescent AuNCs with a relatively low QY (10–20%). The size of polymer-dependent AuNCs is related to several factors such as the structure of polymer, the nature of polymer functional group, and the ratio of gold to polymer [35, 65, 66]. A switch over nonfluorescent to fluorescent polymer-capped AuNCs (core diameters: 1.1–1.7 nm) can be finely tuned by adjusting the ratio of gold-to-polymer as reported by Cooper et al. Moreover, González et al. have discovered a new simple method for preparing AuNCs protected by poly(*N*-vinylpyrrolidone) (PVP), which possess the fluorescent and magnetic features [36]. In this method, an electrochemical synthesis has been used to pursue a much simpler and quicker synthetic route. Most recently, Jiang and coworkers have developed novel hybrid nanogels based on the NIR fluorescent AuNCs and poly(acrylic acid) (PAA) [67]. The core-hollow and shell-porous PAA nanogels were employed as templates followed by *in situ* reduction of HAuCl_4 in water, to synthesize AuNCs-encapsulated PAA hybrid nanogels. The PAA nanogels were prepared by the polymerization of acrylic acid monomer and then mixing the products with cysteamine water solution through interaction of COO^- group of PAA and NH_2^+ of cysteamine. Au^{3+} ions were subsequently added and reduced by thiols of cysteamine so as to encapsulate Au^+ into the cavities of PAA nanogels. Finally, NaBH_4 was chosen to reduce the Au ions into AuNCs, shown in Figure 2. This AuNCs entrapped in PAA nanogels

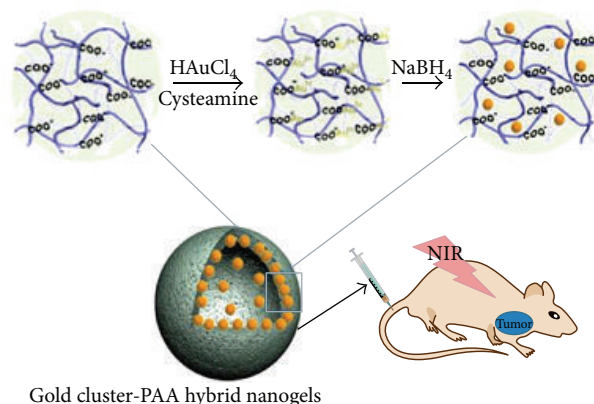


FIGURE 2: Schematic of synthetic method of gold cluster-encapsulated PAA hybrid nanogels. Reprinted with permission from [67], ©2013, American Chemical Society.

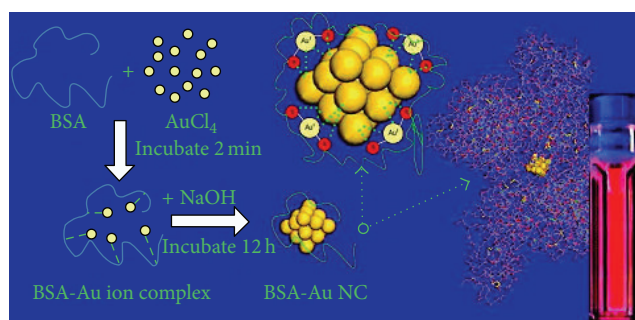


FIGURE 3: Schematic of the formation of BSA-templated AuNCs. Reprinted with permission from [37], ©2009, American Chemical Society.

possessed the NIR fluorescent property with deep tissue penetration, which was suitable for NIR live imaging.

(iii) *Proteins*. Proteins, as biological macromolecules, have certain configuration and spaces and can be utilized as templates for preparing fluorescent AuNCs. Xie and coworkers have developed a class “green” synthesis method to prepare protein-directed AuNCs [37]. In this method, a facile, one-pot, “green” synthetic technique was developed based on a common commercially available protein, bovine serum albumin (BSA), as shown in Figure 3.

BSA, a plasma protein existing in abundance, was selected as the model protein for the formation of AuNCs because of its stability, lack of effect, and low cost. Similar to the biomineralization behavior in nature, the Au^{3+} ions were added to the aqueous BSA solution, to be reduced to Au^+ with the help of tyrosine residues on the protein, and then metal ions were sequestered and entrapped by thiol groups of the protein. The as-prepared AuNCs were stable at the physiological temperature and PH with a QY~6%. The as-synthesized BSA-AuNCs have 25 gold atoms in the core, which exhibit red emission (maximum of emission wavelength locates in 640 nm), excellent stability, good biocompatibility, and easy surface modification. This striking work is not only

a novel method for creating highly fluorescent AuNCs, but a promising protocol can be used for the other proteins and noble metals. Following to this report, many groups studied this “green” synthetic route with other bioactive proteins such as insulin [68–70], lysozyme [71], transferrin [72], and egg white proteins [53]. Chou et al. have firstly selected insulin as the template for synthesizing the fluorescent AuNCs. The as-prepared insulin-AuNCs are applicable for fluorescent imaging, CT, and *in vivo* blood-glucose regulation. As innovative imaging technique involving insulin, it should be extensively studied in biolabeling and bioimaging application. The use of BSA as a reductant and stabilizer has enlightened Lu et al. to find some proteins expect BSA for preparing AuNCs. They have discovered a way to prepare highly fluorescent AuNCs by using lysozyme as reductant and stabilizer. The as-synthesized lysozyme gold fluorescent NCs (LsGFC) have a diameter of ~ 1 nm and emission wavelength centered at 657 nm, which also can be specifically quenched by Hg^{2+} . Very recently, chicken egg white (CEW), which is abundant for being available and extremely cheap, has been exploited as a template for synthesizing AuNCs by Geckerler et al. In the method, researchers developed a green, rapid synthesis of AuNCs using CEW at physiological temperature (37°C) with $\text{pH}\sim 11$. Under alkaline conditions, tyrosine and tryptophan are predominantly responsible for reduction of Au^{3+} ions and obtained highly fluorescent, water-soluble AuNCs. Most recently, Qiao and coworkers have exploited a novel fluorescent nanoprobe which contains fluorescent ovalbumin-capped AuNCs, biotarget folic acid, and homopolymers as the linker [72]. Unlike most polymer-capped nanoclusters, folic acid-functionalized fluorescent AuNCs can specifically label the cell and tumor, which have superiority in biolabeling and bioimaging applications.

(iv) *DNA*. The introduction of biological macromolecules (protein, DNA) can make the synthetic method of AuNCs greener and more biocompatible, which renders them more possible for biological application. Some reports have been published to make the affinity of DNA base pair and AuNCs evident theoretically [73, 74], which provide the foundation for the subsequent experiments to verify the feasibility of theories. Chen and coworkers have unveiled atomically monodispersed AuNCs with direction of DNA as etchant of gold nanoparticles and rods [75]. Liu and colleagues firstly reported that pH-dependent single-stranded DNA (ssDNA) was feasible in synthesizing blue-emitting AuNCs with a mild reductant [76]. Shao and colleagues developed a nanoparticle-free method for synthesizing red-emitting AuNCs in water with DNA as a template [77].

(v) *Small Molecules*. Most kinds of AuNCs are synthesized by exploiting large templates such as dendrimers, biological macromolecules (e.g. DNA, proteins) and polymers. Meanwhile, small molecules used as the templates have been paid much attention for synthesizing high fluorescent AuNCs, especially the thiol-protected (glutathione, 11-mercaptoundecanoic acid) AuNCs [79]. However, using small molecules as the templates and reductants has not drawn that much attention for synthesizing high fluorescent AuNCs compared with other templates. Several small molecules

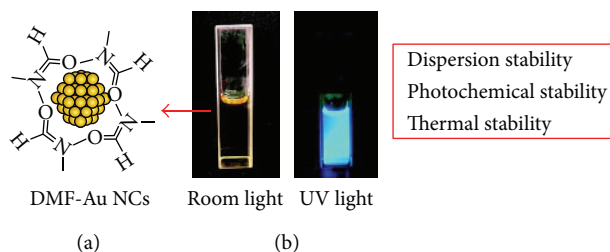


FIGURE 4: Schematic of DMF-AuNCs construction (a); the photographs of DMF-protected Au clusters in DMF under ambient light (light yellow) and UV light of 365 nm (blue) (b). Reprinted with permission from [78], ©2010, Langmuir.

have been exploited in the fabrication of AuNCs such as amino acid [80–83], peptide [84, 85], dimethylformamide [43, 78], and Good's buffers [86]. The report using amino acid as a reactant for preparing AuNCs is scarce. Chen and coworkers [83] have discovered a fast, facile method for preparing AuNCs by blending Chloroauric Acid (HAuCl_4) with histidine. It is the first time for preparing AuNCs with amino acid as the reductant and stabilizer at the same time. Kawasaki et al. have reported the DMF-protected AuNCs through the interactions of the amide groups of DMF with AuNCs, which possess high thermal stability, high dispersion stability in various solvents, and high photochemical stability, as shown in Figure 4 [78].

2.2.2. *Ligand-Protected Gold Nanoclusters*. Early studies for the AuNCs are focused on synthesizing by strong reducing agent and strong capping agents such as thiol [87, 88], dendrimers [34], and polymers [89]. For synthesizing high yield of AuNCs, a practical way was discovered involving weaker reducing agent in the present of strong capping agent. This method can form nanoparticle-free AuNCs efficiently with slower reduction rate [44]. Due to excellent optical, electronic, and chemical properties, ligand-protected gold nanoclusters have been extensively investigated, especially for their potential applications in biomedicine and nanoelectronics.

(1) *Phosphine as Ligand* [91]. In the infant stage, phosphine molecules have been widely utilized as a ligand during the preparation of AuNCs [92, 93]. The phosphine-capped AuNCs are stable to the ambient conditions and controllable over cluster core size. Generally, phosphine-capped AuNCs are synthesized by sodium borohydride reduction. In the 1960s, an 11 gold atoms phosphine-protected cluster, $\text{Au}_{11}(\text{PPh}_3)_7(\text{SCN})_3$, was firstly reported [92]. And an Au_{13} -centered icosahedral structure cluster was successfully prepared in 1981 [94]. Schmid et al. reported Au_{55} -centered nanoclusters with an average core size of ~ 1.4 nm [95]. The method was optimized by Hutchison and coworkers, who developed a more convenient, safer approach to synthesize phosphine-capped gold nanoclusters [96]. In recent development of phosphine-capped gold nanoclusters, Wan et al. isolated new phosphine-protected Au_{20} nanoclusters through the reduction of $\text{Au}(\text{PPhpy}_2)\text{Cl}$ [$\text{PPhpy}_2 = \text{bis}(2\text{-pyridyl})\text{phenylphosphine}$] by NaBH_4 , the Au_{20} core was the fusion of

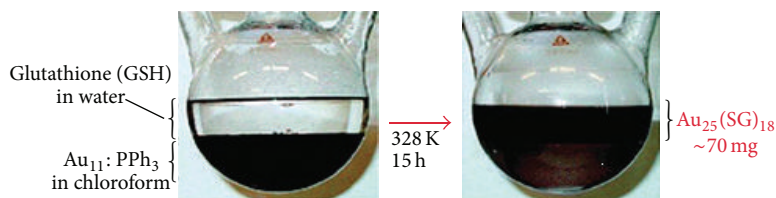


FIGURE 5: Phosphine-stabilized Au_{11} clusters in chloroform were reacted with glutathione (GSH) in water under a nitrogen atmosphere. Reprinted with permission from [90], ©2005, American Chemical Society.

two Au_{11} clusters [97]. Although phosphine-capped AuNCs are one of the important classes in the gold clusters families, the synthetic method still faces some problems such as tedious extractions, numerous steps, and unstable production tending to decompose. Since gold atoms have a good affinity to $-SH$ groups, the unstable phosphine-stabilized AuNCs could be transferred into thiol-stabilized gold clusters. Hutchison and colleagues have reported a versatile ligand-exchange reaction and first described the mechanism of thiol-phosphine ligand exchanges [98]. As shown in Figure 5, Shichibu et al. synthesized glutathione-capped AuNCs ($Au_{25}(SG)_{18}$) by ligand exchange with phosphine-stabilized Au_{11} clusters. Teranishi and coworkers recently reported a bulk solution synthetic method that permitted large scale, facile synthesis of truly monodisperse Au_{38} nanoclusters, which used a two-phase ligand exchange process based on GSH-Au clusters, and led to monodisperse Au_{38} nanoclusters in high purity [90].

(2) *Thiolate-Capped Gold Nanoclusters*. Brust et al. have done the pioneering work based on the reduction of the metal precursors and the formation of metal core [99]. Owing to a strong affinity for thiols and Au, thiol-containing small molecules were extensively used to stabilize gold nanoclusters in the aqueous solution [6]. Using thiol-containing small molecules as stabilizers rendered much more controllable AuNCs than phosphine-capped ones, contributing to the stronger Au-S covalent bonding. Thus they have been intensely pursued in last decades.

Generally, the method of synthesizing thiolate-capped AuNCs has processes as follows. Gold salts $[AuCl_4]^-$ are dissolved in water and then transferred to an organic solvent by phase transfer agent; the thiols are added to the mixture to reduce Au^{3+} ions into Au^+ ions and form Au^+-SR complexes or polymers; then the Au^+ polymers are reduced by adding the reducing agent into thiolate-protective gold nanoclusters.

The fluorescence of thiolate-protected AuNCs (referred to as $Au_n(SR)_m$, where n and m are the respective number of metal atoms and ligands) was effected by the kind of ligand and core charge state. In order to enhance fluorescence, different chain lengths of thiols will be chosen for the biolabeling and imaging applications [100]. Jin and colleagues discovered “size focusing” method to synthesize atomically monodisperse thiolate-stabilized AuNCs using different thiol ligand ($-SR$: $-SC_2H_4Ph$, $-SC_{12}H_{25}$, SG, and $SC_{10}H_{22}COOH$) [101].

Glutathione (GSH), a ubiquitous low-molecular weight thiol, played a significant role in making AuNCs which

showed good water solubility, bioactive surface, and high stability. It has been widely investigated for protecting the Au^{3+} ions when they were being reduced by sodium borohydride ($NaBH_4$) [102–104]. Whetten and coworkers have unveiled an unprecedented thiol-protective AuNCs by using the GSH (N- γ -glutamyl-cysteinyl-glycine) as the stabilizer. The as-synthesized AuNCs were fractionated by using polyacrylamide gel electrophoresis (PAGE) and characterized by mass spectrometry (MS) [102]. Tsukuda and colleagues have also reported the characterization of fractionated AuNCs protected by GSH monolayers using mass spectrometric. The as-prepared AuNCs were isolated into single-sized $Au_n(SR)_m$ clusters by the PAGE method with $n = 18, 21, 25, 28, 32, 39$ (called magic-numbered clusters) [103]. Liu and coworkers employed GSH-stabilized AuNCs (GSH-Au NCs) as the sensor of Cr (III) and Cr (VI) through fluorescence quenching [105]. In the method, GSH was used as an environment friendly reducing/protecting reagent for preparing AuNCs in physiological temperature for 24 h. The as-prepared AuNCs exhibited yellow under visible light, but the color turned into bright red when radiated by UV light, as shown in Figure 6.

Moreover, various other thiols can be used to stabilize the AuNCs such as tiopronin [106], phenylethylthiolate [107], thiolate α -Cyclodextrin [108, 109], mercaptopropionic acid [110, 111], bidentate dihydrolipoic (DHLA) [112], dodecanethiol [113], and D-penicillamine [41, 114, 115]. Using these mercaptolinkers above makes the AuNCs possess higher fluorescent yield and monodispersity. Mattoussi and coworkers [47] prepared a highly fluorescent gold nanoclusters with emission centered at ~ 750 nm NIR region using bidentate ligand as stabilizing agent. Shang et al. have reported a novel water-soluble Au-SR using the D-penicillamine (DPA) and a mild reductant. The DPA-capped AuNCs show an enhancement of the fluorescence intensity and a remarkable stability ($\sim QY = 1.3\%$), which have potential for bioimaging application.

2.3. “Nanoparticles to Clusters” Route. With the development of techniques, a novel method is reported that involves etching surface atoms of gold nanoparticles by appropriate ligands. Different small molecules and polymers have been exploited as the etchant such as thiols (e.g., glutathione, dihydrolipoic acid, and phenylethylthiol) [16, 116, 117] and biomacromolecules (e.g., BSA). Typical procedure contains the following: first, mixing the surface-stabled gold nanoparticles with excessive etchant (small molecules/polymers) and then etching the gold NPs’ surface via ligand exchange and finally, generating etchant-gold complexation. Using this method can enhance the fluorescent effect of AuNCs ($QY \sim 4\text{--}20\%$).

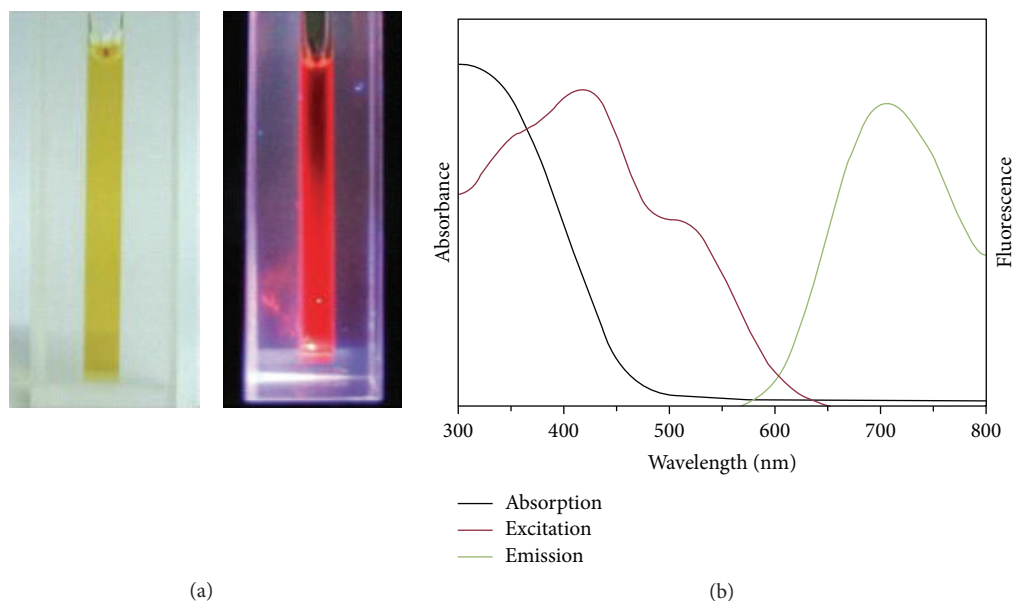


FIGURE 6: (a) GSH-protected AuNCs under visible light (left) and UV light (right), respectively. (b) UV/vis absorption, fluorescence excitation (emission at 710 nm), and emission (excitation at 410 nm) spectra of GSH-Au NCs. Reprinted with permission from [105], ©2013, Science Direction.

2.3.1. Ligand-Induced Etching. In the past decades, a series of protecting ligands have been exploited to prepare relatively controllable monolayer protected clusters (MPCs). The ligands such as phosphines, thiols, amines, and polymers have multiple functions in effecting the cluster size and physical/chemical properties. Besides the one-pot method by direct reduction of Au^{3+} ions in the presence of thiols mentioned above, fluorescent gold MPCs can be synthesized by etching Au core with excessive ligands. The study of monolayer gold MPCs has been separated into three stages: polydispersed nanoclusters; monodispersed nanoclusters; and atomically precise nanoclusters [118]. Jin et al. have discovered a kinetically controlled method based on ligand-induced etching for preparing atomically monodisperse Au-SR, called “size focusing” method. For instance, Jin and coworkers developed a facile, high yielding synthetic approach to synthesize $\text{Au}_{38}(\text{SC}_2\text{H}_4\text{Ph})_{24}$ clusters with excess phenylethylthiol. Schaaff and coworkers conducted thiol etching on a combination of 14k and 8k species, the result showed that the 8 kDa species became enriched [119]. Duan and colleague have reported synthesizing blue-emitting monodisperse AuNCs by exploiting the etching property of hyperbranched and multivalent polymers—polyethylenimine (PEI). In the approach, as-prepared Au nanocrystals in dimension for ~ 8 nm were synthesized by modified Brust-Schiffrin method. Once acting with excessive PEI, the separated AuNCs with 8 atoms emitted intense green light under UV light irradiation (365 nm), as shown in Figure 7 [64].

Parak and coworkers reported a precursor-induced etching method for the preparation of water-soluble fluorescent dihydrolipoic acid-capped AuNCs [16]. In the method, gold NPs stabilized by didodecyldimethylammonium bromide (DDAB) were synthesized in the organic phase, followed by

precursor induced etching into AuNCs. Synthesis of water-soluble AuNCs was depending on the ligand exchange with reduced lipoic acid (DHLA). Upon the production transfer to aqueous solution, they became intensely red-luminescent with QY \sim 3.45%. This report exhibited a totally novel method for preparing ultrasmall fluorescent AuNCs even if the detailed mechanisms have not yet been clearly elucidated.

2.3.2. Solvent-Induced Etching. Phase transfer is demonstrated to be an effective approach for preparing the fluorescent metal NCs via the electrostatic interaction. Yuan et al. [51] have developed a facile and versatile synthesis of highly fluorescent, stable, and monodispersed AuNCs based on a mild etching of originally polydispersed, nonfluorescent, and unstable gold nanocrystals. Thiol-protected AuNCs were synthesized by reducing the Au^+ -SR with the reducing agent (NaBH_4) in the presence of glutathione (GSH) and then transferring the polydispersed thiol-protected AuNCs into an organic phase by adding cetyltrimethylammonium bromide (CTAB) due to the electrostatic interactions between negatively charged carboxyl group in GSH and the positively charged cations of the hydrophobic salt $[(\text{CTA})^+(\text{COO})^-]$. The mild etching happened in the organic phase which led to enhanced fluorescent monodisperse AuNCs. Moreover, the fluorescent AuNCs can easily be transferred back to the aqueous solution by injecting a salt to remove the $(\text{CTA})^+$. This approach is used to fabricate highly fluorescent AuNCs with excellent stability, biocompatible protecting ligands, and monodispersion, which has a promising prospect in bioimaging and biosensing application. Xie and coworkers have also discovered a novel Au-thiolate NCs with highly luminescence (QY \sim 15%). The mechanism of aggregation-induced emission (AIE) has been discovered. Due to the discovery,

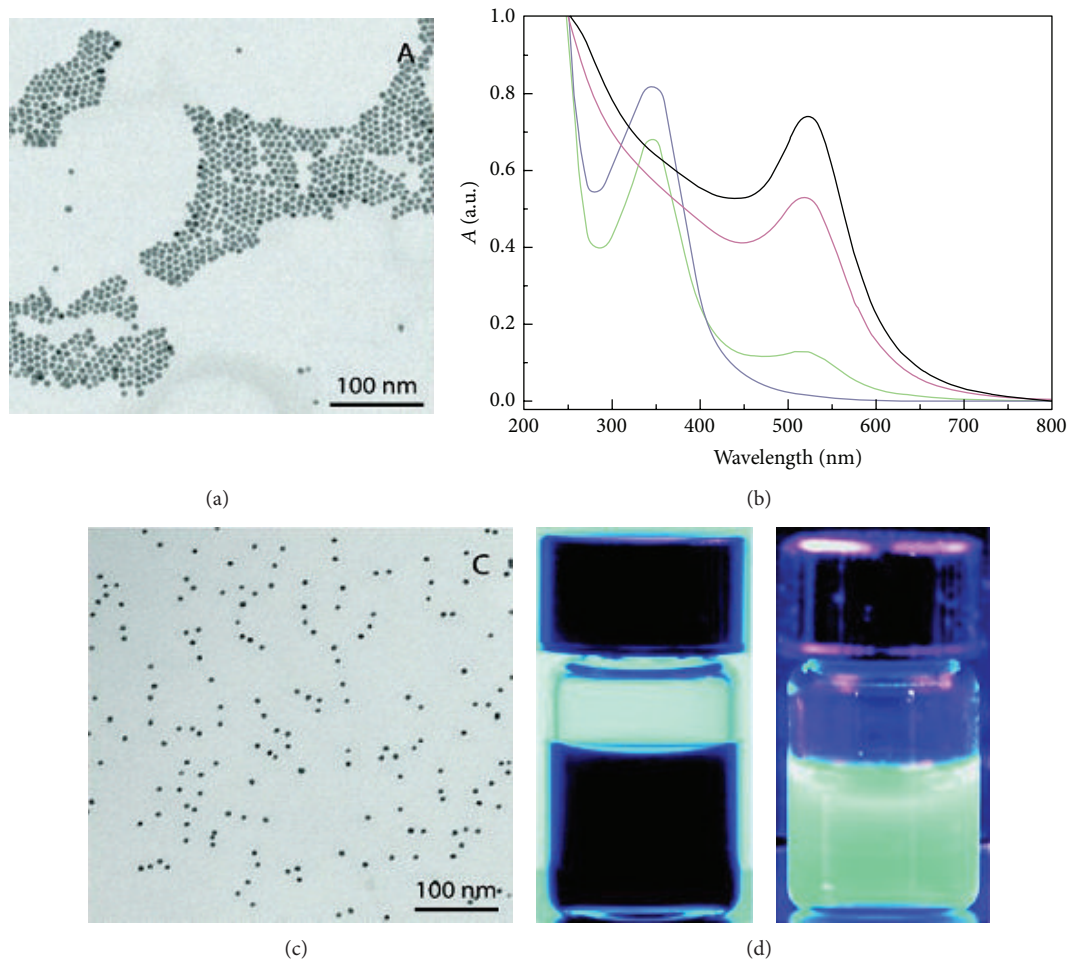


FIGURE 7: (a) and (c) are TEM of Au nanocrystals before and after ligand-induced etching. (b) UV-vis spectra of the original Au nanocrystals (black), the etched nanocrystals after separation (red), the AuNCs mixture after etching (green), and the purified AuNCs after separation (blue). (d) Color photographs of the original Au nanocrystals in chloroform (left) and the purified AuNCs in water (right). UV light (365 nm). Reprinted with permission from [64], ©(2007), American Chemical Society.

the nonfluorescent oligomeric Au (I)-thiolate complexes can generate strong luminescent under UV light depending on the degree of aggregation. The AIE properties can be used for designing AuNCs formed by the aggregation of Au (I)-thiolate complexes and *in situ* generated Au core, which aggregation was induced by adding a high concentration of ethanol in water, as shown in Figure 8 [45].

3. Application of Gold Nanoclusters: Biosensing, Biolabeling, and Bioimaging

AuNCs as nanoprobe have several advantages, as follows. AuNCs have good stability and monodispersion in the physiological environment leading to enhanced sensitivity and increased tracking lifetime; AuNCs possess ultrasmall size which can be easily uptaken by cells; the biological functions of bioentities conjugated with AuNCs will not be disturbed; photoluminescence in the form of fluorescence is an important property of AuNCs; with decreasing the core size, their fluorescence will show a blue-shift from the NIR region to ultraviolet; the QY of AuNCs is much higher than

bulk gold and gold NPs in magnitude; compared with the harsh synthetic steps and tedious surface modification of quantum dots, it is much more achievable to prepare AuNCs and the functional groups induced by the templates and stabilizers are much convenient for coupling with the dyes, peptide, DNA, and other markers; owing to the low content of metal, AuNCs have good biocompatibility for lots of *in vitro* and *in vivo* applications.

As mentioned above, fluorescent AuNCs are promising material as fluorescent biolabels and light-emitting sources in nanoscale; therefore, they can be applied in biological labeling, imaging, detection, and so on.

The precondition for making the applications possible is appropriate surface modification for AuNCs, which can eventually influence their stability, biocompatibility, targeting, and other properties. The method functionalizing AuNCs involves surface chemistry and bioconjugation, which should promise AuNCs survival in these conditions. Herein, we will summarize the strategies which are widespread in synthesizing functional AuNCs as fluorescent biological probes in biolabeling, bioimaging, and biosensing applications.

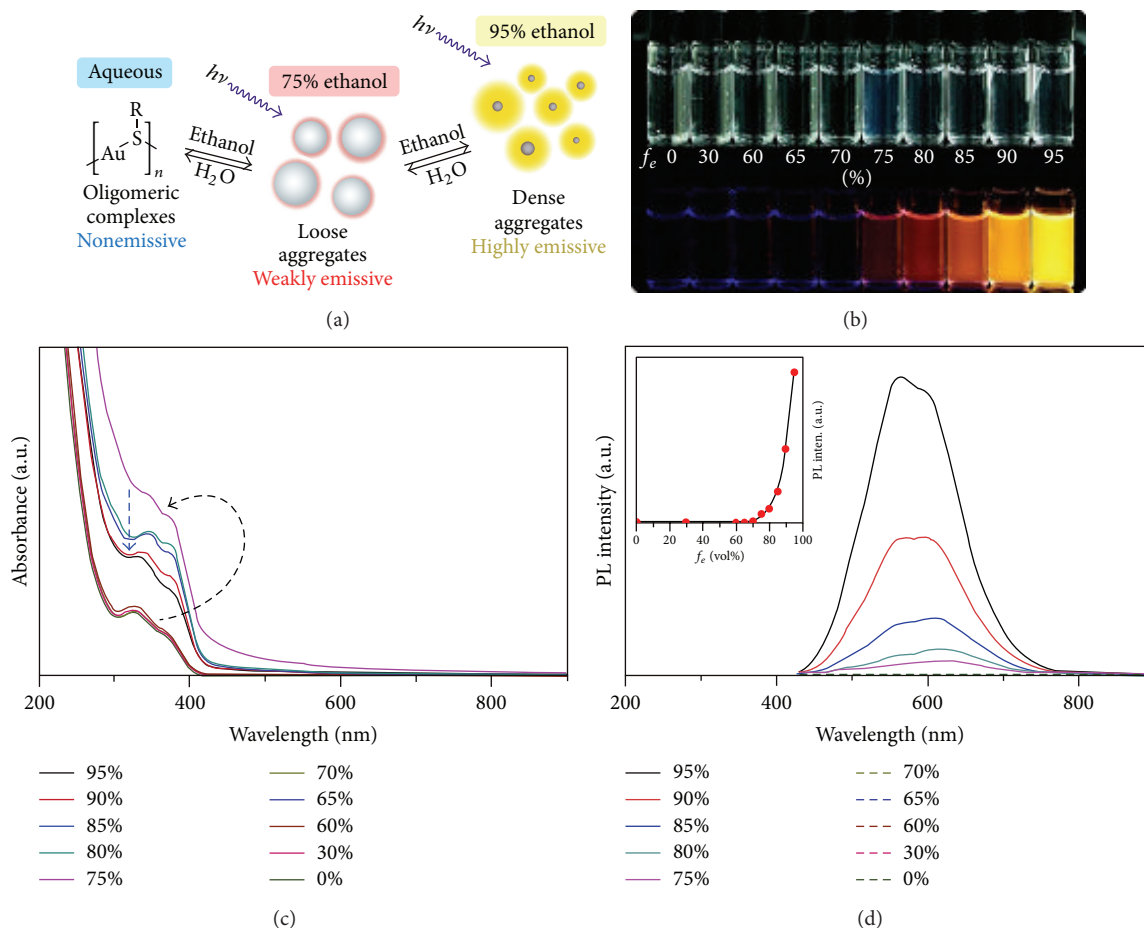


FIGURE 8: (a) Schematic illustration of solvent-induced AIE properties of oligomeric Au (I)-thiolate complexes. (b) Digital photos of Au (I)-thiolate complexes in mixed solvents of ethanol and water with different f_e under visible (top row) and UV (bottom row) light. (c) UV-vis absorption and (d) photoemission spectra of Au (I)-thiolate complexes in mixed solvents with different f_e . (Inset) Relationship between the luminescence intensity and f_e . The spectra were recorded 30 min after the sample preparation. Reprinted with permission from [45], ©(2012), American Chemical Society.

3.1. Surface Functionalization. Nanoparticles are usually modified with a variety of materials such as silica, synthetic polymers, biopolymers, dendrimers, and small molecules leading to introducing desired functionality [120, 121]. In the early days, surface modification is based on chemisorption through which bonds are weak and easy to rupture. A novel strategy offering a stronger and more robust bond has been discovered to modify NPs with more stable ligands [122], which make it possible for AuNCs holding promising applications in the biological field, *in vitro* and *in vivo*. Hence, there are several demands to AuNCs: (1) they should be water-soluble and stable in a physiological environment; (2) they should possess targeting to specific tissue with high selectivity *in vivo*; and (3) they should be efficiently discharged by the metabolic system for lowest toxicity [121]. In order to fit the bills, a mountain of work has been done to tailor functional AuNCs with various coating and bioconjugation.

The silica coating, one of the most multifunctional methods of surface functionalization, can couple the advantage of BSA-templated AuNCs with the silica particles. Guével and coworkers [123] have highlighted a novel kind of fluorescent

core-shell nanoparticles by BSA-templated AuNCs. The as-prepared AuNCs doped Si NPs show monodispersity, higher stability, NIR emission wavelength, and enhanced fluorescent intensity. Moreover, the silica shell allows AuNCs to be conjugated with bioactive entities (e.g., peptide, folic acid (FA), antibody, and polymer).

Bioconjugation is an effective route to introduce extra functionality onto nanoclusters through several functional groups such as primary amide, carboxylic acid, alcohols, and thiols [124]. According to the synthesis of AuNCs as we have discussed before, the majority of template-directed and ligand-protected clusters possess the carboxylic acids on the surface as functional groups, which can conjugate with amino-terminal biomolecules. The reaction is commonly catalyzed with 1-ethyl-3-(3-dimethylaminopropyl) carbodiimide (EDC) and sulfo-N-hydroxysuccinimide (sulfo-NHS) to form amide bond. Yan and colleagues have developed an approach to conjugate Cyclo(Arg-Gly-Asp-D-Phe-Lys) (RGD) peptide to BSA-stabilized AuNCs with the use of coupling agents [125]. A simple one-pot method has been studied by Shang and colleagues for synthesizing D-penicillamine-capped AuNCs, which have both amino and carboxylic

groups on the surface for further bioconjugation. Abad and coworkers have synthesized AuNCs capped with dihydroliipoic acid (DHLA), which possess hydrophilic carboxyl group providing an anchor for biological molecules conjugation such as covalent linkage [126]. AuNCs coated with carboxylic acid have been bonded with polymers containing amine functionalities by ion pairing without EDC and NHS. Mattoussi and coworkers have reported preparing the AuNCs stabilized with zwitterion-appended lipoic acid ligands, in which process reactive groups (amine or carboxyl group) can be inserted *in situ* on the surface of production for further bioconjugation [47].

In addition to the further steps for surface functionalization, the introduction of ultrabiocompatible interface and the protection of AuNCs have occurred simultaneously in terms of the template-directed fluorescent AuNCs. For instant, proteins such as BSA are extensively exploited as the stabilizers for preparing fluorescent AuNCs bringing in controllable functional groups [127, 128].

3.2. Biological Sensing Application. The minitype sensor in nanoscale is of interest in the wide array of biomedical applications and environmental science for detection of metal ions and biomolecules possessing high sensitivity and low cost. The surface modified AuNCs can be utilized as biosensors with the fluorescent AuNCs core as transducer and the surface functionalized molecules as recognition component.

3.2.1. Heavy Metal Ions Detection. Due to high hazard and bioaccumulation in vital organs and tissues of heavy metal ions such as mercury, copper, and chromium ions, related investigations of heavy metal ions detection have received increasing attention. For the sake of protecting our environment and health, some effective strategies are highly desirable for the sensitive and selective detection of heavy metal ions.

The detection of Hg^{2+} is based on biomolecules (proteins [129, 130], antibodies [131], oligonucleotides [132], DNAzyme [133, 134], etc.), gold nanoparticles [135, 136], small organic molecules [137, 138], and other materials such as inorganic molecules [139, 140]. Recently, AuNCs have been exploited as the sensor of Hg^{2+} . Xie et al. initially developed a method to synthesize AuNCs with BSA and further apply the BSA-templated AuNCs to the Hg^{2+} sensing in 2010 [141]. This approach utilized the specific and strong interaction between the Au^+ and Hg^{2+} , which effectively quenched the fluorescence of AuNCs. This process can specifically detect and monitor Hg^{2+} ions at minimal concentration of 0.5 nM. Tseng and Lin have reported selectively sensing Hg^{2+} and CH_3Hg^+ using lysozyme type VI-stabilized AuNCs (Lys VI-AuNCs) through the interaction between $\text{Hg}^{2+}/\text{CH}_3\text{Hg}^+$ and Au^+ on the cluster surface, as shown in Figure 9. The limit of detection (LOD) for $\text{Hg}^{2+}/\text{CH}_3\text{Hg}^+$ was 3 pM and 4 nM, respectively [54], which is much lower than the maximum concentration in the drinking water permitted by the U.S. Environmental Protection Agency (EPA).

Chang and colleagues have unveiled a new assay for the highly selective and sensitive detection of Hg^{2+} ions based on aggregation-induced quenching of the fluorescence of 11-mercaptopundecanoic acid (11-MUA) protected AuNCs. This

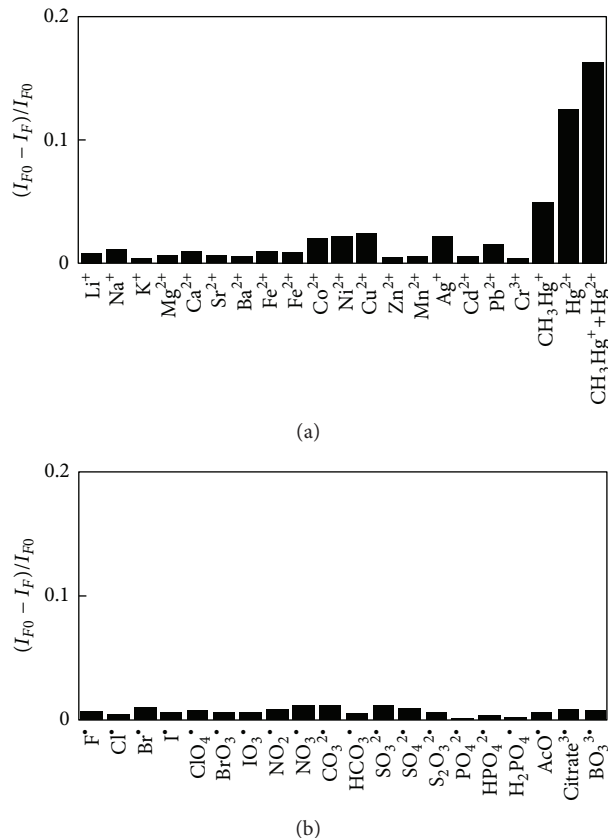


FIGURE 9: Relative fluorescence intensities $[(I_{F0} - I_F)/I_{F0}]$ at 631 nm of solutions of Lys VI-AuNCs after the addition of (a) Hg^{2+} (100 nM), CH_3Hg^+ (100 nM), and other metal ions (50 μM) and (b) anions (50 μM). The excitation wavelength was set to 400 nm. The incubation time was 10 min. It should be noted that I_{F0} and I_F are the fluorescence intensities of the AuNCs before and after adding analytes, respectively. Reprinted with permission from [54], ©2010, Analytical Chemistry.

fluorescence quenching induced by the aggregation of gold NPs in the present of Hg^{2+} was firstly reported as a method for sensing metal ions [33].

Copper widely exists and is essential for all the plants and animals for being the key factor in producing numerous enzymes and involved in various physiologic processes; however, excessive copper ions will lead to cellular toxicity, liver damage, and other damages of organisms [54, 142, 143]. Thus, considerable efforts have been made in the field of Cu^{2+} detection using fluorescent AuNCs as a sensor. Gaetke and colleagues have demonstrated a novel method using GSH-stabilized AuNCs as highly sensitive and selective fluorescent sensor for copper ions based on ion-induced aggregation of AuNCs [144]. In addition, the quenched fluorescence of AuNCs can be recovered through adding a strong metal ion chelator, ethylenediaminetetraacetate (EDTA). Guo and coworkers also reported a novel synthetic approach of NIR fluorescent AuNCs recently, which was realized by the heat-assisted reduction of an Au^+ -thiol complex. The as-prepared AuNCs are able to selectively and sensitively detect copper

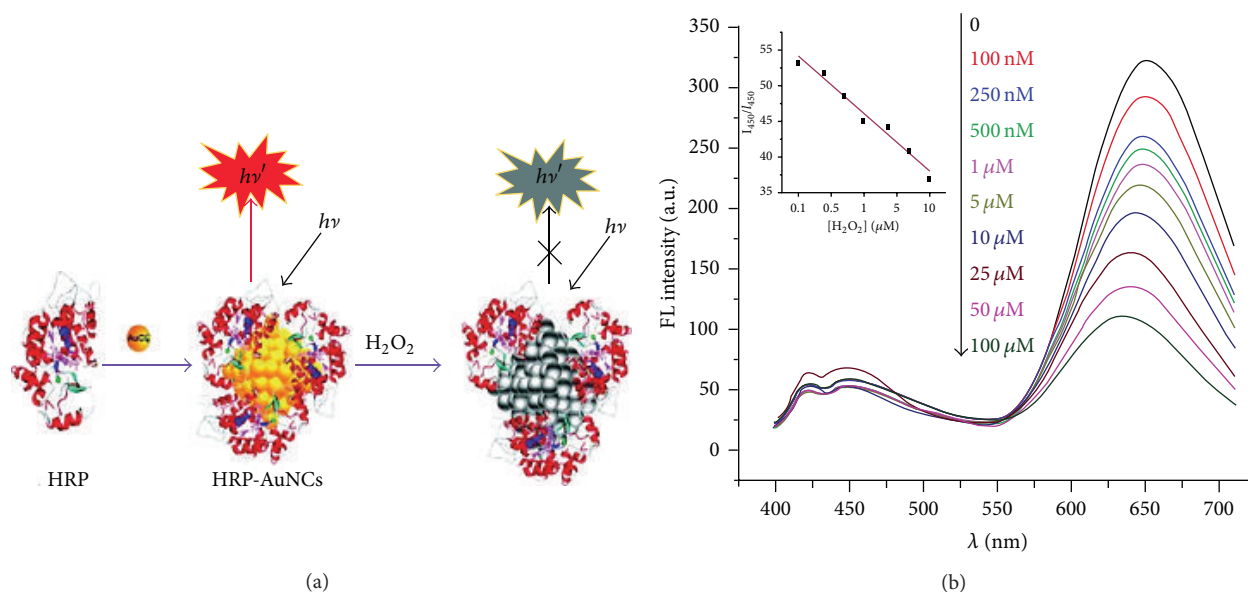


FIGURE 10: Schematic of the formation and the H₂O₂ directed quenching of HRP-AuNCs. Reprinted with permission from [127], ©2011, American Chemical Society.

ions with a minimal concentration as low as 1.6 nM [145]. Guo and coworkers published the detection method of Cu²⁺ employing lysine-functionalized AuNCs (AuNCs@Lys) as fluorescent probes [146]. The mechanism of this sensing process is the tunable fluorescent signal of AuNCs@Lys quenched by the link of copper ions and lysine. The concentration scale the probe can determine is from 10 nM to 7 μM, which is far lower than the maximum level of Cu in drinking water (20 μM) permitted by the EPA of the U.S. [147]. A masking method for improving selectivity of AuNCs has been developed by Cao and coworkers for higher selective detection of mercury and copper ions. By adding the “masking” agents, respectively, Cu²⁺ and Hg²⁺ ions are inhibited to interact with AuNCs and eliminated the corresponding quenching effect; thus the ions without being inhibited can be detected [148].

Moreover, Ho and coworkers have described a facile one-pot method to sense ferric ions by the fluorescent AuNCs stabilized and reduced by L-3, 4-dihydroxyphenylalanine (L-DOPA). The as-prepared AuNCs exhibited a fluorescent quench based on the ferric ions-induced aggregation, whose detection limit of the Fe³⁺ was lower than the maximum level allowed by the U.S. EPA (5.4 μM) [149].

3.2.2. Small Molecules and Biomacromolecules Detection. In addition to heavy metal ion detection, fluorescent AuNCs can also be exploited detecting small molecules (hydrogen peroxide [40, 150], enzymes [151–153], dopamine [154–156], nitrite [157], cholesterol [158], folic acid [159], ciprofloxacin [160], etc.) and biological macromolecules (proteins [161–166], glucose [40, 167], etc.). Zhang and coworkers have showed a biomineralization strategy for the detection of hydrogen peroxide by synthesizing the AuNCs by a functional template–Horseradish peroxidase (HRP) at physiological conditions [127]. The fluorescence of HRP-stabilized

AuNCs was quenched upon the addition of H₂O₂ in the range from 100 nM to 100 μM with a LOD of 30 nM, as shown in Figure 10.

The detection of biological thiols such as cysteine (Cys) and glutathione (GSH) has been extensively investigated. Cys plays an important role in biological system from the protein formation to being an antidote for alcoholic adverse reactions. GSH is the most abundant thiol in cells which participates in numerous biological reactions such as neutralizing free radicals and peroxides, HIV expression, and cancer therapy, which show that the altering level of GSH is related to the diabetes and HIV disease. So the level of GSH in biological organism is measured with great importance. Park and coworkers have elaborated the detection of biological thiols systematically by using the BSA-stabilized AuNCs. The method is based on Hg²⁺-induced fluorescence quenching through high affinity of Au⁺ and Hg²⁺ and blocking this interaction by selective coordination of thiols with Hg²⁺. This fluorescence-based sensing method for biothiols has advantages such as simple steps, fast reaction time, and cost-effectiveness. Recently, Huang et al. have reported a simple, immune-dependent, and label-free method for cystatin C (Cys C) detection. To achieve the detection, BSA-templated AuNCs have been employed as the fluorescent probe, which process is based on the papain-induced quenching of AuNCs and the fluorescence recovery by the coexistence of Cys C. Papain can digest the scaffold of AuNCs, BSA, based on its protease activity, and Cys C as a powerful cysteine proteinase inhibitors, capable of inhibiting the activity of papain to protect the AuNCs from aggregation. Fluorescent AuNCs enable detecting Cys C in the range of 25 ng/mL–2.0 μg/mL. Tseng et al. have also presented a method for sensing glutathione (GSH) by (Lysozyme Type VI) stabilized (Lys VI) AuNCs (contain 8 gold atoms). The PH-dependent

blue-emitting AuNCs could detect GSH resulted from the formation of GSH-Au⁺ complexes. By specific etching reaction of GSH and AuNCs core, the fluorescence of AuNCs was quenched to show the altering level of GSH with a sensing limitation of 20 nM.

Dopamine (DA), as a vital catecholamine neurotransmitter, plays a significant role in the central nervous, renal, and hormonal systems [168]. The detection of DA with simple, high performance, nontoxicity has been developed employing the AuNCs as biosensor. Qu and coworkers have firstly discussed the detection of dopamine involving BSA-templated AuNCs electrogenerated chemiluminescence (ECL) study [155]. The process was realized by injecting DA into the electrolyte, the ECL of the AuNCs exhibited a distinct linear increase response to the increase of DA's concentration. The highly sensitive and selective fluorescence and colorimetric sensing of DA was in the first time described using a BSA-stabilized AuNCs by Sony and colleague [154]. The fluorescence of BSA-AuNCs showed a decrease once adding DA due to the photoinduced electron transfer of DA to AuNCs. In the meantime, the peroxidase-like activity of AuNCs was inhibited in the present of DA leading to a visual detection with highly selectivity.

AuNCs-based fluorescent protein sensor can be achieved by coupled selective recognition molecules with the fluorescent AuNCs. Of the substantial trial for forming AuNCs-based protein sensors, Leblanc's group initially reported the conjugation of anti-human IgG to the PAMAM-stabilized AuNCs for detecting the human IgG antigen [161]. Linear fluorescence quenching coordinated with the formation of antigen-antibody immunocomplexes. Chang and colleagues unveiled a novel protein sensor by using the light switching system based on biofunctional II-MUA-protected AuNCs and bioconjugated 13 nm gold NPs [165]. Platelet-derived growth factor AA (PDGF AA), as a breast cancer marker protein, can be conjugated to AuNCs (PDGF AA- AA-L_{AuND}). Thiol-derivation aptamers (Apt) with high affinity to PDGFs interacted with gold NPs (Apt-Q_{AuNP}). PDGF AA-L_{AuND} can attach to the Apt-Q_{AuNP} leading to the fluorescence quenching by resonance energy transfer. Upon the addition of free PDGF or PDGF α -receptor, the fluorescence can be recovered as a result of competitive reaction of PDGF/Apt-Q_{AuNP} or PDGF α -receptor/PDGF AA-L_{AuND}, as shown in Figure 11. The mannose-protected AuNCs have also been synthesized for the detection of Concanavalin A (Con A) with high sensitivity and other proteins and lectins [166]. In this method, the fluorescent AuNCs were synthesized by etching the THPC-reduced AuNCs by excessive Man-SH, which showed a high sensing limitation to Con A and *E. coli* attributed to multivalent cooperative interactions between Man-AuNCs and proteins. This approach provided the lowest LOD value for Con A (75 pM) and yielded brightly fluorescent cell clusters when binding to bacteria.

Glucose on one hand is the major energy source of living cells, of significance in the synthesis of other complex molecules, and an important factor of human health condition; on the other hand, it leads to many diseases such as diabetes when holding at an abnormal level. Typically, the detection of glucose by the fluorescent AuNCs probes is

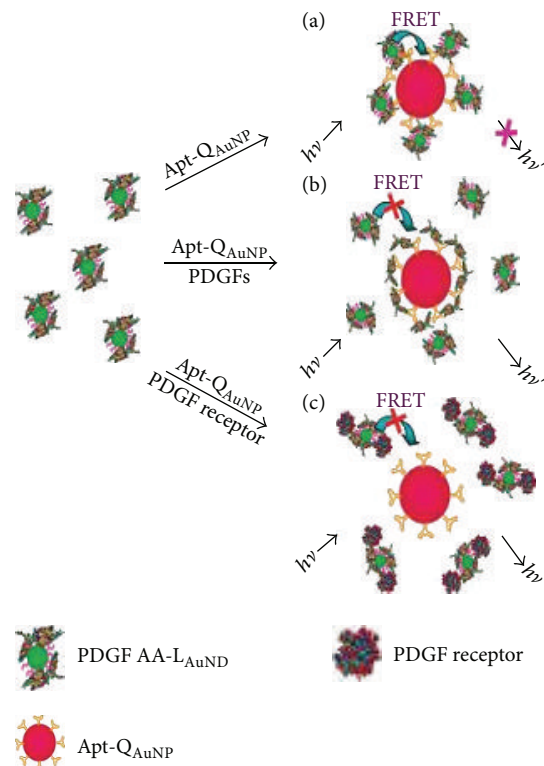


FIGURE 11: Schematic representations of PDGF and PDGF receptor biological nanosensors blocking the fluorescence quenching between PDGF AA-L_{AuND} and Apt-Q_{AuNP}. Reprinted with permission from [165], ©(2008), American Chemical Society.

as follows: the biomolecules-stabilized AuNCs were synthesized; moreover, glucose can be oxidized by oxygen incubated with glucose oxidase (GOD) which produces H₂O₂ as the intermediation. The H₂O₂-induced aggregation of AuNCs can lead to the fluorescence quenching and vicariously detecting the glucose [168, 169].

3.3. Biological Labeling and Imaging. AuNCs, as an emerging fluorescent nanomaterial, possess a dramatic number of characteristics as follows: ultrasmall size, good water solubility, biocompatibility, photostability, and large Stokes shifts; all these properties make them promising fluorescent probes for biological labeling and imaging [170, 171].

The fluorescent AuNCs as cell labels are considered to realize the long observation times and stable emission of fluorescence microscopy in live cells so as to understand the dynamics of intracellular networks better. Parak et al. have prepared water-soluble fluorescent DHLA-protected AuNCs (AuNCs@DHLA), then bioconjugated with streptavidin for specific probing of the intracellular distribution of endogenous biotin in liver cell [16]. Thereafter, an investigation was also described by Chang and coworkers to elucidate the fluorescent and biocompatibility features of AuNCs by labeling the endothelial progenitor cells (EPC) [172]. The result indicated that the fluorescence of labeled cells did not decrease as well as maintained intact angiogenic potential.

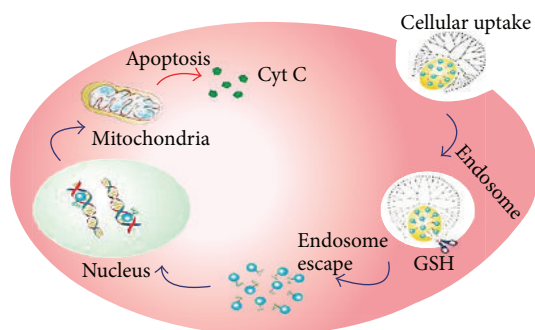


FIGURE 12: Intracellular GSH-triggered release of anticancer drugs loaded within DEGNPs. Reprinted with permission from [178], ©2013, American Chemical Society.

Furthermore, AuNCs are attractive in the biomedicine field for diagnostics and therapeutics due to ultrasmall size, strong fluorescence emission and good biocompatibility [172–176]. Irudayaraj and coworkers have described the fluorescent BSA-protected AuNCs conjugated with Herceptin (AuNCs-Her) for targeting fluorescent imaging and cancer therapy at the same time [177]. The ultrafine novel fluorescent probes were demonstrated having the ability to enter the nucleus with high targeting specificity and nuclear localization capability for effective drug delivery and therapeutic efficacy. Botella and coworkers have designed a phototheranostic agent based on chlorin e6 (Ce6) photosensitizer-conjugated silica-coated AuNCs (AuNC@SiO₂-Ce6) for fluorescent imaging-guided photodynamic therapy [175]. And most recently, Cheng and colleagues have published the first report of using Dendrimer-encapsulated gold nanoparticles (DEGNPs) as the scaffold to develop stimuli-responsive drug delivery systems, as shown in Figure 12 [178]. The DEGNPs can be loaded with thiolates anticancer drugs via Au-S bond. After triggering to the tumor cell by GSH, the drugs can be released in tumors. This strategy opened up new possibilities to exploit subnanosized NPs for an “off-on” drug release system.

In addition to achieve more effective therapeutic effect, AuNCs-based probes can also be utilized for highly specific and accurate cancer diagnosis. Most recently, to achieve high accuracy and specificity of cancer diagnosis, novel fluorescence enzyme mimetic nanoprobe have been described by Chen et al. based on folic acid modified gold nanoclusters [173]. In this method, the BSA-stabilized AuNCs were synthesized to facilitate a rapid, cost-effective, and versatile NIR imaging/visualizing cancer diagnosis system. The peroxidase mimetic AuNCs conjugated to folic acid possess enhanced targeting ability to folate receptor over-expressing tumors, and combined with other superior properties, they can be employed for a colocalization staining method which diagnoses cancer rapidly through microscopic imaging with bright field and fluorescent imaging simultaneously.

Biological imaging *in vivo* is confronted with much more challenges than cellular imaging such as difficulty in survive in complex physiological environment and weak intensity of visible light blocking by organic tissue. The emitted light

in the NIR region of AuNCs is capable of penetrating into deeper tissue and detecting stronger intensity due to weakest biological autofluorescence. Besides, unlike the toxic QDs and low-stability organic dyes, AuNCs with ultrafine size, good water-solubility, biocompatibility, and good photostability are of great interest to be fluorescent nanoprobe for biological imaging. As mentioned above, AuNCs are ideal bioprobes for bioimaging *in vivo*. Herein, we will show the latest development in bioimaging.

The two-photon excitation photoluminescence measurement was utilized to demonstrate the strong advantage in live cell imaging compared with organic dyes and quantum dots such as the ability of deeper inside tissues and the reduced phototoxicity of NIR light. Goodson and colleagues have investigated two-photon absorption (TPA) of Au₂₅ clusters in NIR region in organic phase, and TPA cross-sections increase to an extremely high level at 800 nm which make it possible for applications in optical power limiting nanolithography [182]. Xu and coworkers have investigated the one- and two-photon excitation properties of water-soluble GSH-protected AuNCs and their applications in bioimaging [183]. In this report, the TPA property and application as fluorescence imaging contrast agents of GSH-AuNCs have been explored. The TPA cross section of GSH-AuNCs is much larger compared with organic dyes and QDs as well as the low toxicity and exceptional photostability which show their as promising in live cell fluorescent imaging and other bioimaging *in vivo*. Shang et al. have studied the process that DPA-AuNCs are internalized by HeLa cells in endosomal vesicles through two-photon imaging [41]. After 2 hours of incubation of DPA-AuNCs and HeLa cells, the images were captured by confocal microscopy with two-photon excitation. The fluorescence of probes ingested by the HeLa cells can easily be seen through 3D reconstruction images which reveal the nanoclusters inside the cells as well as those attached to the outside of the plasma membrane. The study of two-photon induced luminescence of 11-MUA-AuNCs has been reported by Chou and co-workers. The two-photon induced fluorescent imaging was used to human mesenchymal stem cells (hMSCs) through the stable and nontoxic nanoprobe, which revealed that the 11-MUA-AuNCs were internalized into the cells and mainly resided in the cytoplasm nearby the nucleus, as shown in Figure 13 [179].

Compared with fluorescent intensity imaging, fluorescent lifetime imaging microscopy (FLIM) could separate the species based on differences in the exponential decay rate of fluorescence (lifetime), which is independent of the local concentration of fluorescent molecules and the excitation intensity [184]. Shang and colleagues have investigated the fluorescent DHLA-AuNCs in HeLa cells by the FLIM technique. The lifetimes of DHLA-AuNCs (>100 ns) is two order of magnitude longer than the lifetime of biological fluorescent fluorophores. Owing to this, the biological imaging can be achieved in the complete absence of cellular autofluorescence. The intensity and lifetime images of cell without and with AuNCs have been shown and indicated that the AuNCs have been internalized by the cells. The as-prepared NCs have many other features for promising candidate of wide applications in biomedical field. In the meantime, Irudayaraj

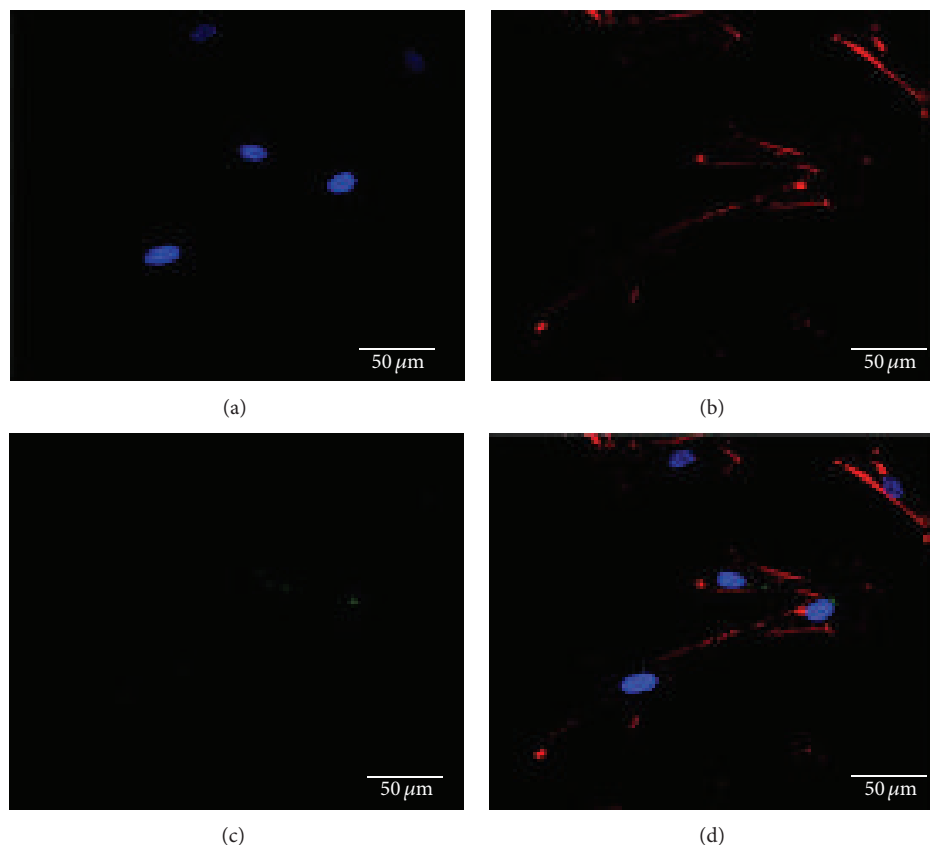


FIGURE 13: hMSCs were treated with dextran-coated 11MUA-Au nanodots for 24 h and then processed for two-photon and confocal microscopic examination. (a) Cell nucleus was stained with DAPI (blue color). (b) Actin fiber was stained with rhodamine phalloidin to confirm the cell boundary (red color). (c) Dextran-coated 11MUA-Au nanodots exhibit a two-photon emission (green luminescence) for *in vitro* bioapplication. (d) Fluorescence image overlay of the three images demonstrating the internalization of 11MUA-Au nanodots residing near the nucleus. Reprinted with permission from [179], ©2009, American Chemical Society.

and workmates have exploited FLIM combined with fluorescent correlation spectroscopy (FCS) to track the diffusion of Herceptin-conjugated AuNCs and its entry into the nucleus in SK-BR3 cells [177]. The SK-BR3 cell is a human breast cancer cell overexpressing human epidermal growth factor receptor 2 (HER2) on the cell membrane. The AuNCs-Her was specifically endocytosed into the nucleus of SK-BR3 cells causing DNA damage showed by FLIM, as shown in Figure 14.

Biological imaging *in vivo* is confronted with much more challenges than cellular imaging such as difficulty in survive in complex physiological environment and weak intensity of visible light blocking by organic tissue. The emitted light in the NIR region of AuNCs is capable of penetrating into deeper tissue and detecting stronger intensity due to weakest biological autofluorescence. Besides, unlike the toxic QDs and low-stability organic dyes, AuNCs with ultrafine size, good water-solubility, biocompatibility, and good photostability are of great interest to be fluorescent nanoprobe for biological imaging. All of these properties indicates that AuNCs are ideal bioprobes for bioimaging *in vivo*. Herein, we will show the latest development in bioimaging.

Zhang et al. have developed the utilization of AuNCs into multimodal imaging technique for early cancer diagnosis

[185]. In this method, BSA-stabilized AuNCs are synthesized as the highly fluorescent and strong X-ray absorption coefficient contrast agent for fluorescent and X-ray dual-modality imaging. Coincidentally, Cui and coworkers have prepared FA-conjugated AuNCs@SiO₂ nanoprobe for *in vivo* dual-modal fluorescent and X-ray computed tomography gastric cancer targeting imaging [180]. Nude mice model with xenograft tumor based on MGC-803 cells was injected with these targeting fluorescent nanoprobe via tail vein followed by dual-modal imaging. The experimental results demonstrated that FA-conjugated AuNCs@SiO₂ can effectively target *in vivo* gastric cancer cells and exhibited excellent NIR fluorescent imaging and presented distinguished CT signals in X-ray imaging, as shown in Figure 15.

Moreover, a multimodal imaging method blending NIR fluorescent imaging and magnetic resonance imaging (MRI) has been achieved by Koyakutty and coworkers recently with the aid of gadolinium oxide and Au (Gd₂O₃/Au) hybrid targeting nanoprobe [186]. The as-synthesized nanoclusters fabricated by biomineralization showed both intense red-emitting fluorescence and good magnetic resonance imaging ability and were further functionalized with RGD peptide for realizing the targeted tumor imaging application *in vivo*. In addition, the over expression of $\alpha_v\beta_3$ integrin in U87

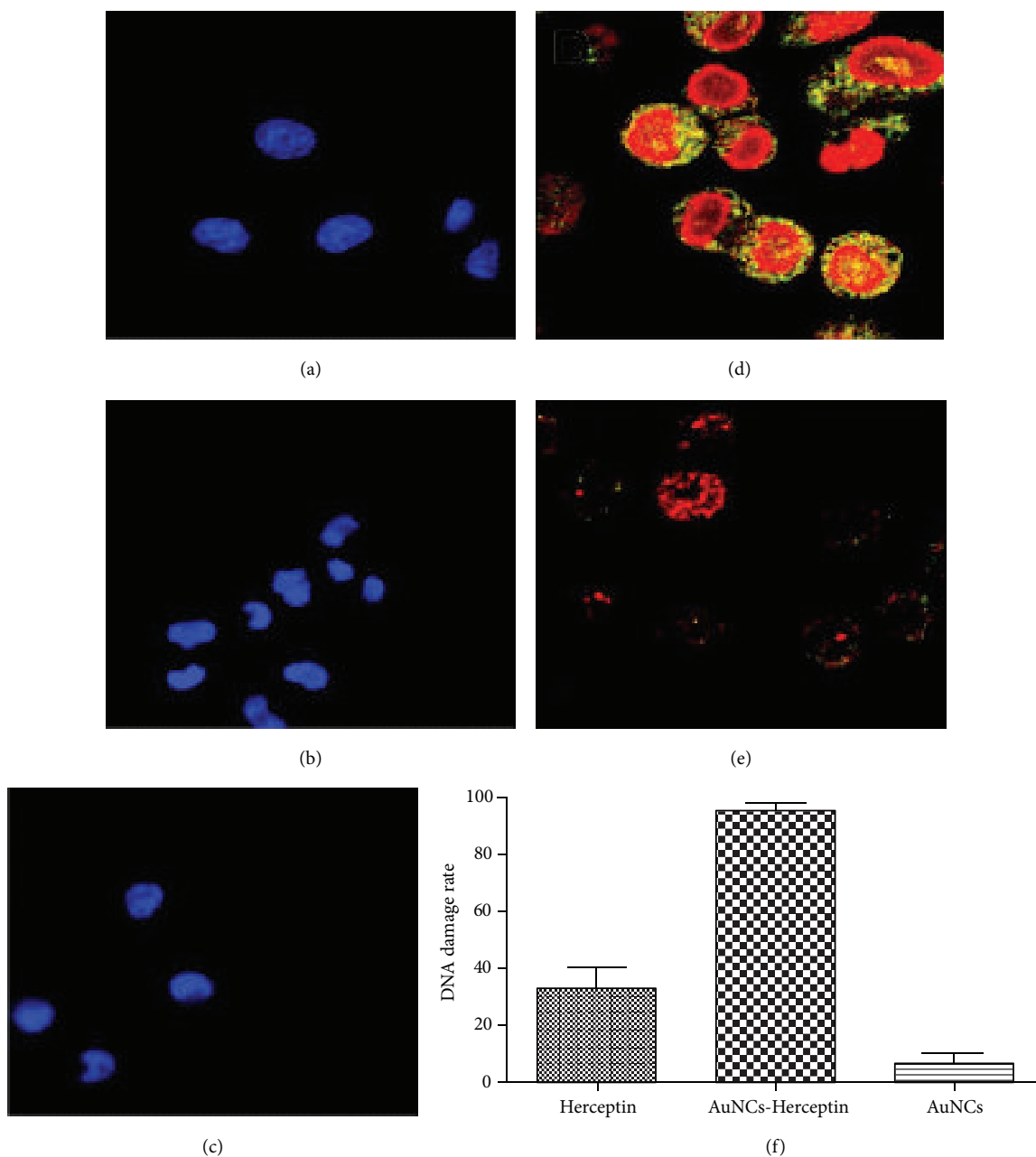


FIGURE 14: Fluorescent images showed the cell apoptosis induced by (a) AuNCs alone; (b) AuNCs-Her; (c) Herceptin by staining the nucleus with Hoechst 33258 (UV light 460 nm). FLIM shows the DNA damage of SK-BR3 cells induced by (d) AuNCs-Her; (e) Herceptin indicated by the bright yellow dots. (f) Quantitative evaluation of DNA damage of cells as a percentage of the total number of cells for different treatments. Reprinted with permission from [177], ©2011, American Chemical Society.

tumor cell can enhance the specific accumulation of RGD-Gd₂O₃/Au. RGD conjugated Gd₂O₃/Au (RGD-Gd₂O₃/Au) nanoclusters injected into U87-MG tumor-bearing mice via tail vein showed distinguished specific accumulation in U87 tumor with longer retain time for targeted bioimaging *in vivo*. Currently, the majority of nanoprobe conjugated to targetable molecules are synthesized in labs followed by the purify steps and then injected into live animals. Although possessing ultrasmall size (nanoscale), relative stability in biological systems, and validated biocompatibility, the exogenous nanoprobe will reach the specific site through organic

circulation, which inevitably triggers the clearance effect of biosystems. In order to overcome this problem, Wang and companions have created a biosynthesize method of AuNCs inside the cytoplasm through enforcing an efficient spontaneous reduction of chloroauric acid biocompatible salts by cancer cells, as shown in Figure 16 [181]. Although the mechanism of this novel bioimaging of cancer cells and tumors is still unknown, AuNCs have been successfully formed inside the cytoplasm and confirmed *in vivo* for specially labeling on the xenograft tumor mouse modal by fluorescent imaging. Thus, this novel method is remarkable not only for facilitating

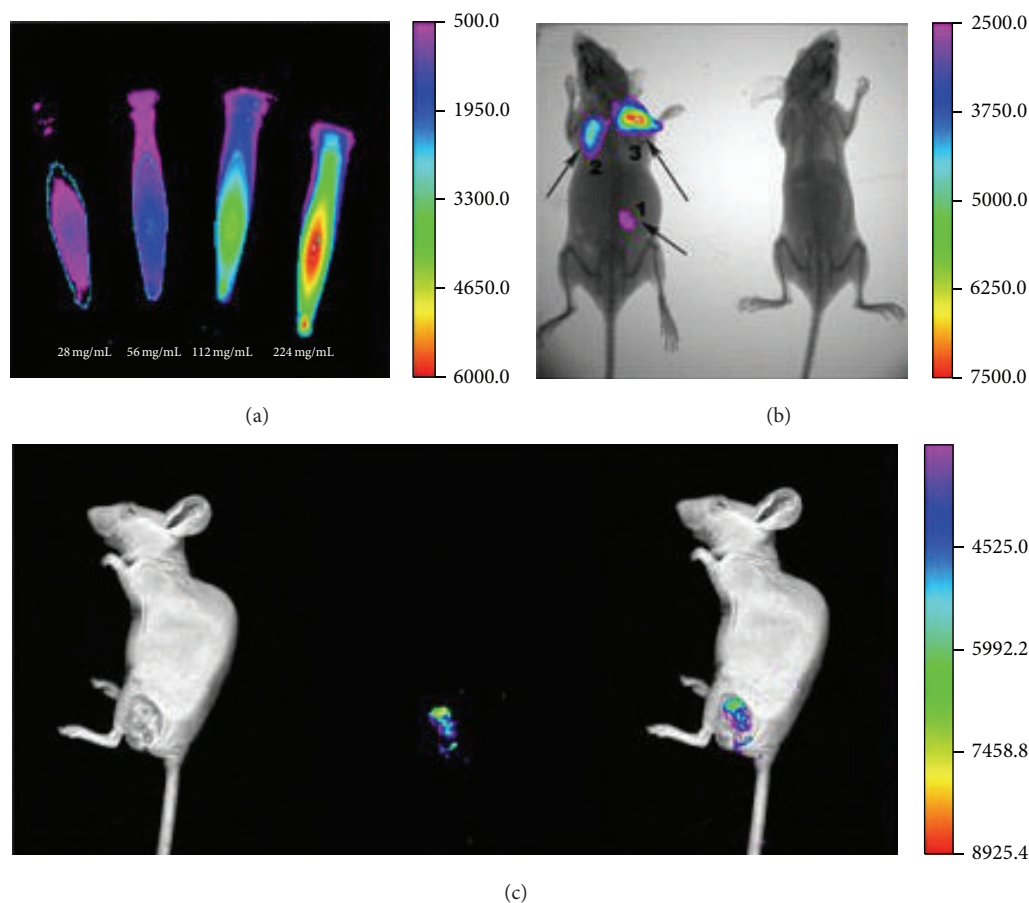


FIGURE 15: AuNCs@SiO₂-FA nanoprobes for fluorescence imaging. (a) *In vitro* fluorescence image of AuNCs@SiO₂-FA in 0.01 M PBS with different concentrations; (b) *In vivo* fluorescence image of 50 uL AuNCs@SiO₂-FA injected subcutaneously at three different doses (area-1: 56 mg/mL; area-2: 112 mg/mL; area-3: 226 mg/mL) into the left mice. The left mice without injection was selected as control; (c) fluorescence image of tumor tissues with tail vein injection at the concentration of 287 mg/mL at 6 h postinjection. Reprinted with permission from [180], ©2013, Journal of Nanobiotechnology.

fluorescent nanoprobes with biosynthetic, self-imaging, and NPs circulation elusion peculiarities but also for showing a different concept of highly sensitive and specific nanoprobes for bioimaging application compared with current system.

4. Summary and Outlook

Fluorescent AuNCs, as an emerging fluorescent nanomaterial, possess a great deal of exceptional advantages such as good water-solubility, high photostability, large Stokes shift, ultrasmall size, nontoxicity, and good biocompatibility, compared with conventional organic dyes, rare earth-based quantum dots, and other luminescent materials. Herein, first of all, we have briefly summarized various approaches that have been employed for preparing AuNCs based on two routes: “bottom-up” and “top-down” routes. Recent advances of the development of the synthetic methods have a far-reaching influence on the future functionalization of AuNCs. The surface modification of AuNCs endows a number of new functionalities for them like targeting imaging properties and therapeutic effects. In the second part, the most recent advances of bioapplications have been summed up such as

fluorescent detection of metal ions/biomolecules, fluorescent cell labeling, and bioimaging in live animal.

Although a huge progression has been achieved to develop the promising novel fluorescent nanoprobes, a variety of challenges in the way still make the future progress of AuNCs.

With regard to the synthesis method and physical properties, there are several challenges we need to face in the future study. Even with making tremendous efforts to optimize the synthetic routes, problems remain existent such as the unpurified AuNCs being polydispersed in the solvent and exhibiting quantum yield lower than 20% within a broad emission band. What is more, there is scarce strategy for preparing size-focusing AuNCs with high reactive yield and monodisperse advantage. Finally, the relationship between the structure and optical properties of AuNCs requires deeper investigation.

For the application of AuNCs, most of biological applications focus on employing them as biosensors or fluorescent nanoprobes in bioimaging, and more applications involved in the therapy of tumor can be developed. Furthermore, the interaction between biological environment and AuNCs

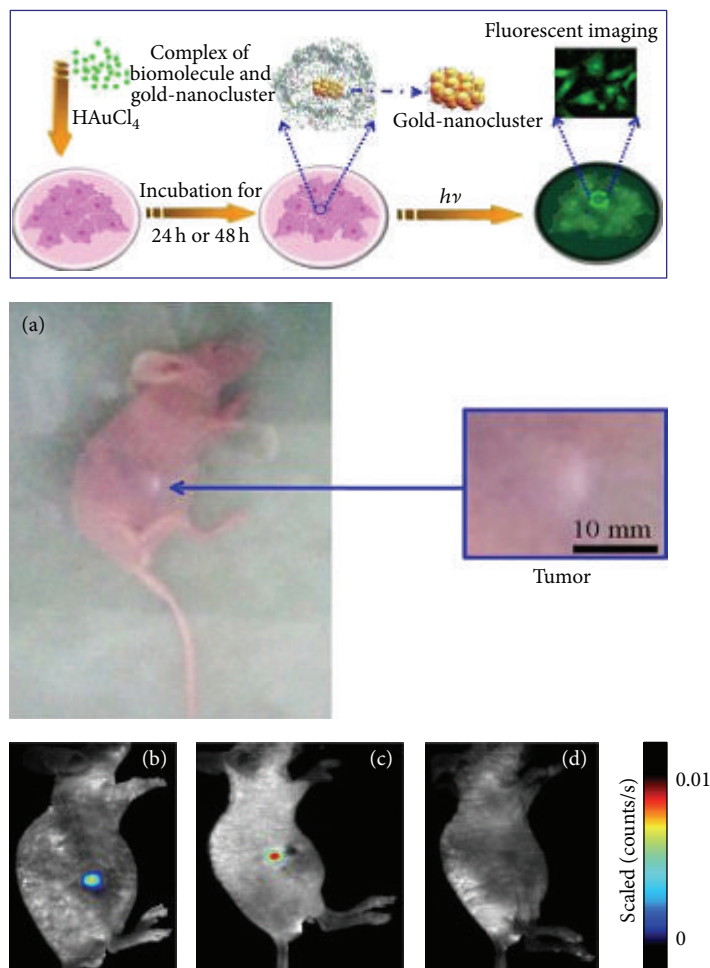


FIGURE 16: Schematic illustration of *in situ* biosynthesis of gold nanoclusters in cells and tumor imaging (top). Representative xenograft tumor mouse models of hepatocellular carcinoma observed in normal light (a) or by *in vivo* fluorescence imaging (b) 24 h after a subcutaneous injection of 10 mmol/L HAuCl_4 solution near the tumor; (c) 24 h after a subcutaneous injection of 10 mmol/L HAuCl_4 solution near the tumor. (d) Control mouse observed by *in vivo* fluorescence imaging 48 h after a subcutaneous injection of 10 mmol/L HAuCl_4 solution in the right side of their abdomen (bottom). Reprinted from the permission of [181], Copyright ©2013, Rights Managed by Nature Publishing Group.

is significant for the biological application of nanoprobes; however, most investigators judge the performance in organism centering in the matter of nanomaterial themselves (photostability, size-depending properties, etc.), but ignoring the interaction between the organism and AuNCs which is related to the safety of AuNCs used in the bionanotechnology and the mechanism of biological applications.

In a word, gold nanoclusters with fascinating properties have been extensively investigated and achieved marked advance. Nevertheless, the application of AuNCs in biological fields is still in the preliminary stage, and large amounts of study are waiting for us in the synthesis, comprehending of interaction mechanism, making full use of the decent features of AuNCs, and extending the range of biological applications.

Conflict of Interests

The authors declare that there is no conflict of interests regarding the publication of this paper.

Acknowledgments

This work is supported by the Program of the National Basic Research and Development Program of China (973) under Grant no. 2011CB707702, and the National Natural Science Foundation of China under Grant nos. 81371589, 81090272, and 81101084, and the Fundamental Research Funds for the Central Universities.

References

- [1] E. C. Dreaden, A. M. Alkilany, X. Huang, C. J. Murphy, and M. A. El-Sayed, "The golden age: gold nanoparticles for biomedicine," *Chemical Society Reviews*, vol. 41, no. 7, pp. 2740–2779, 2012.
- [2] M. C. Roco, "Nanotechnology: convergence with modern biology and medicine," *Current Opinion in Biotechnology*, vol. 14, no. 3, pp. 337–346, 2003.

- [3] L. Shang, S. Dong, and G. U. Nienhaus, "Ultra-small fluorescent metal nanoclusters: synthesis and biological applications," *Nano Today*, vol. 6, no. 4, pp. 401–418, 2011.
- [4] M.-C. Daniel and D. Astruc, "Gold nanoparticles: assembly, supramolecular chemistry, quantum-size-related properties, and applications toward biology, catalysis, and nanotechnology," *Chemical Reviews*, vol. 104, no. 1, pp. 293–346, 2004.
- [5] Z. Wu and R. Jin, "On the ligand's role in the fluorescence of gold nanoclusters," *Nano Letters*, vol. 10, no. 7, pp. 2568–2573, 2010.
- [6] R. Jin, "Quantum sized, thiolate-protected gold nanoclusters," *Nanoscale*, vol. 2, no. 3, pp. 343–362, 2010.
- [7] Q. Zhang, J. Xie, Y. Yu, and J. Y. Lee, "Monodispersity control in the synthesis of monometallic and bimetallic quasi-spherical gold and silver nanoparticles," *Nanoscale*, vol. 2, no. 10, pp. 1962–1975, 2010.
- [8] L. Zhang and E. Wang, "Metal nanoclusters: new fluorescent probes for sensors and bioimaging," *Nano Today*, vol. 9, no. 1, pp. 132–157, 2014.
- [9] J. Zheng, C. W. Zhang, and R. M. Dickson, "Highly fluorescent, water-soluble, size-tunable gold quantum dots," *Physical Review Letters*, vol. 93, no. 7, 2004.
- [10] S. W. Chen, R. S. Ingram, M. J. Hostetler et al., "Gold nanoelectrodes of varied size: transition to molecule-like charging," *Science*, vol. 280, no. 5372, pp. 2098–2101, 1998.
- [11] J. F. Hicks, A. C. Templeton, S. Chen et al., "The monolayer thickness dependence of quantized double-layer capacitances of monolayer-protected gold clusters," *Analytical Chemistry*, vol. 71, no. 17, pp. 3703–3711, 1999.
- [12] J. F. Hicks, D. T. Miles, and R. W. Murray, "Quantized double-layer charging of highly monodisperse metal nanoparticles," *Journal of the American Chemical Society*, vol. 124, no. 44, pp. 13322–13328, 2002.
- [13] B. M. Quinn, P. Liljeroth, V. Ruiz, T. Laaksonen, and K. Kontturi, "Electrochemical resolution of 15 oxidation states for monolayer protected gold nanoparticles," *Journal of the American Chemical Society*, vol. 125, no. 22, pp. 6644–6645, 2003.
- [14] K. S. Park, M. I. Kim, M.-A. Woo, and H. G. Park, "A label-free method for detecting biological thiols based on blocking of Hg^{2+} -quenching of fluorescent gold nanoclusters," *Biosensors & Bioelectronics*, vol. 45, no. 1, pp. 65–69, 2013.
- [15] N. L. Rosi and C. A. Mirkin, "Nanostructures in biodiagnostics," *Chemical Reviews*, vol. 105, no. 4, pp. 1547–1562, 2005.
- [16] C.-A. J. Lin, T.-Y. Yang, C.-H. Lee et al., "Synthesis, characterization, and bioconjugation of fluorescent gold nanoclusters toward biological labeling applications," *ACS Nano*, vol. 3, no. 2, pp. 395–401, 2009.
- [17] F. Wang, W. B. Tan, Y. Zhang, X. P. Fan, and M. Q. Wang, "Luminescent nanomaterials for biological labelling," *Nanotechnology*, vol. 17, no. 1, pp. R1–R13, 2006.
- [18] G. Wang, T. Huang, R. W. Murray, L. Menard, and R. G. Nuzzo, "Near-IR luminescence of monolayer-protected metal clusters," *Journal of the American Chemical Society*, vol. 127, no. 3, pp. 812–813, 2005.
- [19] X. Li, F. Zhang, and D. Zhao, "Highly efficient lanthanide upconverting nanomaterials: progress and challenges," *Nano Today*, vol. 8, no. 6, pp. 643–676, 2013.
- [20] I. Díez and R. H. A. Ras, "Fluorescent silver nanoclusters," *Nanoscale*, vol. 3, no. 5, pp. 1963–1970, 2011.
- [21] H. Xu and K. S. Suslick, "Water-soluble fluorescent silver nanoclusters," *Advanced Materials*, vol. 22, no. 10, pp. 1078–1082, 2010.
- [22] M. A. H. Muhammed and T. Pradeep, "Luminescent quantum clusters of gold as bio-labels," in *Advanced Fluorescence Reporters in Chemistry and Biology II*, vol. 9 of *Springer Series on Fluorescence*, pp. 333–353, Springer, Berlin, Germany, 2010.
- [23] I. Díez and R. H. A. Ras, "Few-atom silver clusters as fluorescent reporters," in *Advanced Fluorescence Reporters in Chemistry and Biology II*, vol. 9 of *Springer Series on Fluorescence*, pp. 307–332, Springer, Berlin, Germany, 2010.
- [24] C.-A. J. Lin, C.-H. Lee, J.-T. Hsieh et al., "Synthesis of fluorescent metallic nanoclusters toward biomedical application: recent progress and present challenges," *Journal of Medical and Biological Engineering*, vol. 29, no. 6, pp. 276–283, 2009.
- [25] J. Zheng, *Fluorescent Noble Metal Nanoclusters*, Georgia Institute of Technology, 2005.
- [26] J. Zheng, P. R. Nicovich, and R. M. Dickson, "Highly fluorescent noble-metal quantum dots," *Annual Review of Physical Chemistry*, vol. 58, pp. 409–431, 2007.
- [27] G. K. Wertheim, S. B. DiCenzo, and D. N. E. Buchanan, "Noble- and transition-metal clusters: the d bands of silver and palladium," *Physical Review B*, vol. 33, no. 8, pp. 5384–5390, 1986.
- [28] S. Wang, X. Meng, A. Das et al., "A 200-fold quantum yield boost in the photoluminescence of silver-doped Ag_xAu_{25-x} nanoclusters: the 13th silver atom matters," *Angewandte Chemie—International Edition*, vol. 53, no. 9, pp. 2376–2380, 2014.
- [29] G. A. Ozin and S. A. Mitchell, "Ligand-free metal clusters," *Angewandte Chemie International Edition*, vol. 22, no. 9, pp. 674–694, 1983.
- [30] Z. Q. Zhang, R. C. Patel, R. Kothari, C. P. Johnson, S. E. Friberg, and P. A. Aikens, "Stable silver clusters and nanoparticles prepared in polyacrylate and inverse micellar solutions," *Journal of Physical Chemistry B*, vol. 104, no. 6, pp. 1176–1182, 2000.
- [31] T. Huang and R. W. Murray, "Visible luminescence of water-soluble monolayer-protected gold clusters," *Journal of Physical Chemistry B*, vol. 105, no. 50, pp. 12498–12502, 2001.
- [32] S. Link, A. Beeby, S. FitzGerald, M. A. El-Sayed, T. G. Schaaff, and R. L. Whetten, "Visible to infrared luminescence from a 28-atom gold cluster," *The Journal of Physical Chemistry B*, vol. 106, no. 13, pp. 3410–3415, 2002.
- [33] C.-C. Huang, Z. Yang, K.-H. Lee, and H.-T. Chang, "Synthesis of highly fluorescent gold nanoparticles for sensing mercury(II)," *Angewandte Chemie International Edition*, vol. 46, no. 36, pp. 6824–6828, 2007.
- [34] J. Zheng, J. T. Petty, and R. M. Dickson, "High quantum yield blue emission from water-soluble Au_8 nanodots," *Journal of the American Chemical Society*, vol. 125, no. 26, pp. 7780–7781, 2003.
- [35] N. Schaeffer, B. Tan, C. Dickinson et al., "Fluorescent or not? Size-dependent fluorescence switching for polymer-stabilized gold clusters in the 1.1–1.7 nm size range," *Chemical Communications*, no. 34, pp. 3986–3988, 2008.
- [36] B. Santiago González, M. J. Rodríguez, C. Blanco, J. Rivas, M. A. López-Quintela, and J. M. G. Martinho, "One step synthesis of the smallest photoluminescent and paramagnetic PVP-protected gold atomic clusters," *Nano Letters*, vol. 10, no. 10, pp. 4217–4221, 2010.
- [37] J. Xie, Y. Zheng, and J. Y. Ying, "Protein-directed synthesis of highly fluorescent gold nanoclusters," *Journal of the American Chemical Society*, vol. 131, no. 3, pp. 888–889, 2009.
- [38] Y. Kong, J. Chen, F. Gao et al., "Near-infrared fluorescent ribonuclease-A-encapsulated gold nanoclusters: preparation, characterization, cancer targeting and imaging," *Nanoscale*, vol. 5, no. 3, pp. 1009–1017, 2013.

- [39] W.-Y. Chen, G.-Y. Lan, and H.-T. Chang, "Use of fluorescent DNA-templated gold/silver nanoclusters for the detection of sulfide ions," *Analytical Chemistry*, vol. 83, no. 24, pp. 9450–9455, 2011.
- [40] J. A. Annie Ho, H. C. Chang, and W. T. Su, "DOPA-mediated reduction allows the facile synthesis of fluorescent gold nanoclusters for use as sensing probes for ferric ions," *Analytical Chemistry*, vol. 84, no. 7, pp. 3246–3253, 2012.
- [41] L. Shang, R. M. Dörlich, S. Brandholt et al., "Facile preparation of water-soluble fluorescent gold nanoclusters for cellular imaging applications," *Nanoscale*, vol. 3, no. 5, pp. 2009–2014, 2011.
- [42] V. Venkatesh, A. Shukla, S. Sivakumar, and S. Verma, "Purine-stabilized green fluorescent gold nanoclusters for cell nuclei imaging applications," *ACS Applied Materials and Interfaces*, vol. 6, no. 3, pp. 2185–2191, 2014.
- [43] X. Liu, C. Li, J. Xu et al., "Surfactant-free synthesis and functionalization of highly fluorescent gold quantum dots," *Journal of Physical Chemistry C*, vol. 112, no. 29, pp. 10778–10783, 2008.
- [44] C. Zhou, C. Sun, M. Yu et al., "Luminescent gold nanoparticles with mixed valence states generated from dissociation of polymeric Au(I) thiolates," *Journal of Physical Chemistry C*, vol. 114, no. 17, pp. 7727–7732, 2010.
- [45] Z. Luo, X. Yuan, Y. Yu et al., "From aggregation-induced emission of Au(I)-thiolate complexes to ultrabright Au(0)@Au(I)-thiolate core-shell nanoclusters," *Journal of the American Chemical Society*, vol. 134, no. 40, pp. 16662–16670, 2012.
- [46] Y. Guo, Z. Wang, H. Shao, and X. Jiang, "Stable fluorescent gold nanoparticles for detection of Cu^{2+} with good sensitivity and selectivity," *Analyst*, vol. 137, no. 2, pp. 301–304, 2012.
- [47] F. Aldeek, M. A. H. Muhammed, G. Palui, N. Zhan, and H. Mattoussi, "Growth of highly fluorescent polyethylene glycol- and zwitterion-functionalized gold nanoclusters," *ACS Nano*, vol. 7, no. 3, pp. 2509–2521, 2013.
- [48] T. U. B. Rao and T. Pradeep, "Luminescent Ag_7 and Ag_8 clusters by interfacial synthesis," *Angewandte Chemie—International Edition*, vol. 49, no. 23, pp. 3925–3929, 2010.
- [49] J.-I. Nishigaki, S. Yamazoe, S. Kohara et al., "A twisted bicosahedral Au_{25} cluster enclosed by bulky arenethiolates," *Chemical Communications*, vol. 50, no. 7, pp. 839–841, 2014.
- [50] V. R. Jupally and A. Dass, "Synthesis of $\text{Au}_{130}(\text{SR})_{50}$ and $\text{Au}_{130-x}\text{Ag}_x(\text{SR})_{50}$ nanomolecules through core size conversion of larger metal clusters," *Physical Chemistry Chemical Physics*, vol. 16, no. 22, pp. 10473–10479, 2014.
- [51] X. Yuan, Z. Luo, Q. Zhang et al., "Synthesis of highly fluorescent metal (Ag, Au, Pt, and Cu) nanoclusters by electrostatically induced reversible phase transfer," *ACS Nano*, vol. 5, no. 11, pp. 8800–8808, 2011.
- [52] X. Huang, Y. Luo, Z. Li et al., "Biolabeling hematopoietic system cells using near-infrared fluorescent gold nanoclusters," *The Journal of Physical Chemistry C*, vol. 115, no. 34, pp. 16753–16763, 2011.
- [53] D. Joseph and K. E. Geckeler, "Synthesis of highly fluorescent gold nanoclusters using egg white proteins," *Colloids and Surfaces B: Biointerfaces*, vol. 115, pp. 46–50, 2014.
- [54] Y.-H. Lin and W.-L. Tseng, "Ultrasensitive sensing of Hg^{2+} and CH_3Hg^+ based on the fluorescence quenching of lysozyme Type VI-stabilized gold nanoclusters," *Analytical Chemistry*, vol. 82, no. 22, pp. 9194–9200, 2010.
- [55] J. Zheng and R. M. Dickson, "Individual water-soluble dendrimer-encapsulated silver nanodot fluorescence," *Journal of the American Chemical Society*, vol. 124, no. 47, pp. 13982–13983, 2002.
- [56] C. I. Richards, S. Choi, J.-C. Hsiang et al., "Oligonucleotide-stabilized Ag nanocluster fluorophores," *Journal of the American Chemical Society*, vol. 130, no. 15, pp. 5038–5039, 2008.
- [57] B. Han and E. Wang, "DNA-templated fluorescent silver nanoclusters," *Analytical and Bioanalytical Chemistry*, vol. 402, no. 1, pp. 129–138, 2012.
- [58] D. A. Tomalia and J. M. J. Fréchet, "Discovery of dendrimers and dendritic polymers: a brief historical perspective," *Journal of Polymer Science, Part A: Polymer Chemistry*, vol. 40, no. 16, pp. 2719–2728, 2002.
- [59] D. A. Tomalia, "Birth of a new macromolecular architecture: dendrimers as quantized building blocks for nanoscale synthetic organic chemistry," *Aldrichimica Acta*, vol. 37, no. 2, pp. 39–57, 2004.
- [60] B. Yuping, Z. Chang, D. M. Vu, J. P. Temirov, R. B. Dyer, and J. S. Martinez, "Nanoparticle-free synthesis of fluorescent gold nanoclusters at physiological temperature," *The Journal of Physical Chemistry C*, vol. 111, no. 33, pp. 12194–12198, 2007.
- [61] Y.-C. Jao, M.-K. Chen, and S.-Y. Lin, "Enhanced quantum yield of dendrimer-entrapped gold nanodots by a specific ion-pair association and microwave irradiation for bioimaging," *Chemical Communications*, vol. 46, no. 15, pp. 2626–2628, 2010.
- [62] L. Maya, G. Muralidharan, T. G. Thundat, and E. A. Kenik, "Polymer-mediated assembly of gold nanoclusters," *Langmuir*, vol. 16, no. 24, pp. 9151–9154, 2000.
- [63] X. Huang, B. Li, L. Li et al., "Facile preparation of highly blue fluorescent metal nanoclusters in organic media," *Journal of Physical Chemistry C*, vol. 116, no. 1, pp. 448–455, 2012.
- [64] H. Duan and S. Nie, "Etching colloidal gold nanocrystals with hyperbranched and multivalent polymers: a new route to fluorescent and water-soluble atomic clusters," *Journal of the American Chemical Society*, vol. 129, no. 9, pp. 2412–2413, 2007.
- [65] I. Hussain, S. Graham, Z. X. Wang et al., "Size-controlled synthesis of near-monodisperse gold nanoparticles in the 1–4 nm range using polymeric stabilizers," *Journal of the American Chemical Society*, vol. 127, no. 47, pp. 16398–16399, 2005.
- [66] Z. Wang, B. Tan, I. Hussain et al., "Design of polymeric stabilizers for size-controlled synthesis of monodisperse gold nanoparticles in water," *Langmuir*, vol. 23, no. 2, pp. 885–895, 2007.
- [67] Y. Chen, X. Zheng, X. Wang, C. Wang, Y. Ding, and X. Jiang, "Near-infrared emitting gold cluster-poly(acrylic acid) hybrid nanogels," *ACS Macro Letters*, vol. 3, no. 1, pp. 74–76, 2014.
- [68] C.-L. Liu, H.-T. Wu, Y.-H. Hsiao et al., "Insulin-directed synthesis of fluorescent gold nanoclusters: preservation of insulin bioactivity and versatility in cell imaging," *Angewandte Chemie International Edition*, vol. 50, no. 31, pp. 7056–7060, 2011.
- [69] A. R. Garcia, I. Rahn, S. Johnson et al., "Human insulin fibril-assisted synthesis of fluorescent gold nanoclusters in alkaline media under physiological temperature," *Colloids and Surfaces B: Biointerfaces*, vol. 105, pp. 167–172, 2013.
- [70] C. Guo and J. Irudayaraj, "Fluorescent Ag clusters via a protein-directed approach as a $\text{Hg}(\text{II})$ ion sensor," *Analytical Chemistry*, vol. 83, no. 8, pp. 2883–2889, 2011.
- [71] H. Wei, Z. Wang, L. Yang, S. Tian, C. Hou, and Y. Lu, "Lysozyme-stabilized gold fluorescent cluster: synthesis and application as Hg^{2+} sensor," *Analyst*, vol. 135, no. 6, pp. 1406–1410, 2010.

- [72] J. Qiao, X. Mu, L. Qi, J. Deng, and L. Mao, "Folic acid-functionalized fluorescent gold nanoclusters with polymers as linkers for cancer cell imaging," *Chemical Communications*, vol. 49, no. 73, pp. 8030–8032, 2013.
- [73] E. S. Kryachko and F. Remade, "Complexes of DNA bases and Watson-Crick base pairs with small neutral gold clusters," *Journal of Physical Chemistry B*, vol. 109, no. 48, pp. 22746–22757, 2005.
- [74] M. K. Shukla, M. Dubey, E. Zakar, and J. Leszczynski, "DFT investigation of the interaction of gold nanoclusters with nucleic acid base guanine and the watson-crick guanine-cytosine base pair," *Journal of Physical Chemistry C*, vol. 113, no. 10, pp. 3960–3966, 2009.
- [75] R. Zhou, M. Shi, X. Chen, M. Wang, and H. Chen, "Atomically monodispersed and fluorescent sub-nanometer gold clusters created by biomolecule-assisted etching of nanometer-sized gold particles and rods," *Chemistry—A European Journal*, vol. 15, no. 19, pp. 4944–4951, 2009.
- [76] T. A. C. Kennedy, J. L. MacLean, and J. Liu, "Blue emitting gold nanoclusters templated by poly-cytosine DNA at low pH and poly-adenine DNA at neutral pH," *Chemical Communications*, vol. 48, no. 54, pp. 6845–6847, 2012.
- [77] G. Liu, Y. Shao, K. Ma, Q. Cui, F. Wu, and S. Xu, "Synthesis of DNA-templated fluorescent gold nanoclusters," *Gold Bulletin*, vol. 45, no. 2, pp. 69–74, 2012.
- [78] H. Kawasaki, H. Yamamoto, H. Fujimori, R. Arakawa, Y. Iwasaki, and M. Inada, "Stability of the DMF-protected Au nanoclusters: photochemical, dispersion, and thermal properties," *Langmuir*, vol. 26, no. 8, pp. 5926–5933, 2010.
- [79] S. Palmal, S. Basiruddin, A. R. Maity, S. C. Ray, and N. R. Jana, "Thiol-directed synthesis of highly fluorescent gold clusters and their conversion into stable imaging nanopobes," *Chemistry*, vol. 19, no. 3, pp. 943–949, 2013.
- [80] H. Chen, B. Li, C. Wang et al., "Characterization of a fluorescence probe based on gold nanoclusters for cell and animal imaging," *Nanotechnology*, vol. 24, no. 5, Article ID 055704, 2013.
- [81] Y. Zhang, Q. Hu, M. C. Paau et al., "Probing histidine-stabilized gold nanoclusters product by high-performance liquid chromatography and mass spectrometry," *Journal of Physical Chemistry C*, vol. 117, no. 36, pp. 18697–18708, 2013.
- [82] X. Mu, L. Qi, P. Dong et al., "Facile one-pot synthesis of l-proline-stabilized fluorescent gold nanoclusters and its application as sensing probes for serum iron," *Biosensors and Bioelectronics*, vol. 49, pp. 249–255, 2013.
- [83] X. Yang, M. Shi, R. Zhou, X. Chen, and H. Chen, "Blending of HAuCl₄ and histidine in aqueous solution: a simple approach to the Au₁₀ cluster," *Nanoscale*, vol. 3, no. 6, pp. 2596–2601, 2011.
- [84] R. de la Rica, L. W. Chow, C.-M. Horejs et al., "A designer peptide as a template for growing Au nanoclusters," *Chemical Communications*, vol. 50, no. 73, pp. 10648–10650, 2014.
- [85] Y. Wang, Y. Cui, Y. Zhao et al., "Bifunctional peptides that precisely biomineralize Au clusters and specifically stain cell nuclei," *Chemical Communications*, vol. 48, no. 6, pp. 871–873, 2012.
- [86] Y. Bao, H.-C. Yeh, C. Zhong et al., "Formation and stabilization of fluorescent gold nanoclusters using small molecules," *Journal of Physical Chemistry C*, vol. 114, no. 38, pp. 15879–15882, 2010.
- [87] C. A. Simpson, C. L. Farrow, P. Tian et al., "Tiopronin gold nanoparticle precursor forms aurophilic ring tetramer," *Inorganic Chemistry*, vol. 49, no. 23, pp. 10858–10866, 2010.
- [88] X. Yuan, Y. Yu, Q. Yao, Q. Zhang, and J. Xie, "Fast synthesis of thiolated Au₂₅ nanoclusters via protection-deprotection method," *Journal of Physical Chemistry Letters*, vol. 3, no. 17, pp. 2310–2314, 2012.
- [89] Y. Bao, C. Zhong, D. M. Vu, J. P. Temirov, R. B. Dyer, and J. S. Martinez, "Nanoparticle-free synthesis of fluorescent gold nanoclusters at physiological temperature," *The Journal of Physical Chemistry C*, vol. 111, no. 33, pp. 12194–12198, 2007.
- [90] Y. Shichibu, Y. Negishi, T. Tsukuda, and T. Teranishi, "Large-scale synthesis of thiolated Au₂₅ clusters via ligand exchange reactions of phosphine-stabilized Au₁₁ clusters," *Journal of the American Chemical Society*, vol. 127, no. 39, pp. 13464–13465, 2005.
- [91] M. Yu, C. Zhou, J. Liu, J. D. Hankins, and J. Zheng, "Luminescent gold nanoparticles with pH-dependent membrane adsorption," *Journal of the American Chemical Society*, vol. 133, no. 29, pp. 11014–11017, 2011.
- [92] M. McPartlin, R. Mason, and L. Malatesta, "Novel cluster complexes of gold(0)-gold(I)," *Journal of the Chemical Society D: Chemical Communications*, no. 7, p. 334, 1969.
- [93] B. K. Teo, X. Shi, and H. Zhang, "Pure gold cluster of 1:9:9:1:9:9:1 layered structure: a novel 39-metal-atom cluster [(Ph₃P)₁₄Au₃₉C₁₆]C₁₂ with an interstitial gold atom in a hexagonal antiprismatic cage," *Journal of the American Chemical Society*, vol. 114, no. 7, pp. 2743–2745, 1992.
- [94] C. E. Briant, B. R. C. Theobald, J. W. White, L. K. Bell, D. M. P. Mingos, and A. J. Welch, "Synthesis and X-ray structural characterization of the centred icosahedral gold cluster compound [Au₁₃(PMe₂Ph)₁₀Cl₂](PF₆)₃; the realization of a theoretical prediction," *Journal of the Chemical Society, Chemical Communications*, no. 5, pp. 201–202, 1981.
- [95] G. Schmid, R. Pfeil, R. Boese et al., "Au₅₅[P(C₆H₅)₃]₁₂Cl₆-agold-clusterofanexceptional size," *Chemische Berichte/Recueil*, vol. 114, no. 11, pp. 3634–3642, 1981.
- [96] W. W. Weare, S. M. Reed, M. G. Warner, and J. E. Hutchison, "Improved synthesis of small (d(CORE)approximateto 1.5 nm) phosphine-stabilized gold nanoparticles," *Journal of the American Chemical Society*, vol. 122, no. 51, pp. 12890–12891, 2000.
- [97] X. K. Wan, S. F. Yuan, Z. W. Lin, and Q. M. Wang, "A chiral gold nanocluster Au₂₀ protected by tetradentate phosphine ligands," *Angewandte Chemie - International Edition*, vol. 53, no. 11, pp. 2923–2926, 2014.
- [98] G. H. Woehrle, L. O. Brown, and J. E. Hutchison, "Thiol-functionalized, 1.5-nm gold nanoparticles through ligand exchange reactions: scope and mechanism of ligand exchange," *Journal of the American Chemical Society*, vol. 127, no. 7, pp. 2172–2183, 2005.
- [99] M. Brust, M. Walker, D. Bethell, D. J. Schiffrin, and R. Whyman, "Synthesis of thiol-derivatised gold nanoparticles in a two-phase liquid-liquid system," *Journal of the Chemical Society, Chemical Communications*, no. 7, pp. 801–802, 1994.
- [100] R. Jin, H. Qian, Z. Wu et al., "Size focusing: a methodology for synthesizing atomically precise gold nanoclusters," *Journal of Physical Chemistry Letters*, vol. 1, no. 19, pp. 2903–2910, 2010.
- [101] Z. Wu, J. Suhan, and R. Jin, "One-pot synthesis of atomically monodisperse, thiol-functionalized Au₂₅ nanoclusters," *Journal of Materials Chemistry*, vol. 19, no. 5, pp. 622–626, 2009.
- [102] T. G. Schaaff, G. Knight, M. N. Shafiqullin, R. F. Borkman, and R. L. Whetten, "Isolation and selected properties of a 10.4 kDa gold: glutathione cluster compound," *Journal of Physical Chemistry B*, vol. 102, no. 52, pp. 10643–10646, 1998.

- [103] Y. Negishi, Y. Takasugi, S. Sato, H. Yao, K. Kimura, and T. Tsukuda, "Magic-numbered Au_n clusters protected by glutathione monolayers ($n = 18, 21, 25, 28, 32, 39$): Isolation and spectroscopic characterization," *Journal of the American Chemical Society*, vol. 126, no. 21, pp. 6518–6519, 2004.
- [104] Y. Negishi, K. Nobusada, and T. Tsukuda, "Glutathione-protected gold clusters revisited: bridging the gap between gold(I)-thiolate complexes and thiolate-protected gold nanocrystals," *Journal of the American Chemical Society*, vol. 127, no. 14, pp. 5261–5270, 2005.
- [105] H. Zhang, Q. Liu, T. Wang et al., "Facile preparation of glutathione-stabilized gold nanoclusters for selective determination of chromium (III) and chromium (VI) in environmental water samples," *Analytica Chimica Acta*, vol. 770, pp. 140–146, 2013.
- [106] A. C. Templeton, S. Chen, S. M. Gross, and R. W. Murray, "Water-soluble, isolable gold clusters protected by tiopronin and coenzyme a monolayers," *Langmuir*, vol. 15, no. 1, pp. 66–76, 1999.
- [107] D. Lee, R. L. Donkers, G. Wang, A. S. Harper, and R. W. Murray, "Electrochemistry and optical absorbance and luminescence of molecule-like Au₃₈ nanoparticles," *Journal of the American Chemical Society*, vol. 126, no. 19, pp. 6193–6199, 2004.
- [108] M. C. Paau, C. K. Lo, X. Yang, and M. M. F. Choi, "Synthesis of 1.4 nm α -cyclodextrin-protected gold nanoparticles for luminescence sensing of mercury(II) with picomolar detection limit," *Journal of Physical Chemistry C*, vol. 114, no. 38, pp. 15995–16003, 2010.
- [109] E. S. Shibu and T. Pradeep, "Quantum clusters in cavities: trapped Au₁₅ in cyclodextrins," *Chemistry of Materials*, vol. 23, no. 4, pp. 989–999, 2011.
- [110] H. Zhang, X. Huang, L. Li et al., "Photoreductive synthesis of water-soluble fluorescent metal nanoclusters," *Chemical Communications*, vol. 48, no. 4, pp. 567–569, 2012.
- [111] Y. Shiraishi, D. Arakawa, and N. Toshima, "pH-dependent color change of colloidal dispersions of gold nanoclusters: effect of stabilizer," *European Physical Journal E*, vol. 8, no. 4, pp. 377–383, 2002.
- [112] L. Shang, N. Azadfar, F. Stockmar et al., "One-pot synthesis of near-infrared fluorescent gold clusters for cellular fluorescence lifetime imaging," *Small*, vol. 7, no. 18, pp. 2614–2620, 2011.
- [113] N. K. Chaki, P. Singh, C. V. Dharmadhikari, and K. P. Vijayamohan, "Single-electron charging features of larger, dodecanethiol-protected gold nanoclusters: electrochemical and scanning tunneling microscopy studies," *Langmuir*, vol. 20, no. 23, pp. 10208–10217, 2004.
- [114] H. Yao, K. Miki, N. Nishida, A. Sasaki, and K. Kimura, "Large optical activity of gold nanocluster enantiomers induced by a pair of optically active penicillamines," *Journal of the American Chemical Society*, vol. 127, no. 44, pp. 15536–15543, 2005.
- [115] X. Yang, L. Gan, L. Han, D. Li, J. Wang, and E. Wang, "Facile preparation of chiral penicillamine protected gold nanoclusters and their applications in cell imaging," *Chemical Communications*, vol. 49, no. 23, pp. 2302–2304, 2013.
- [116] M. A. H. Muhammed, S. Ramesh, S. S. Sinha, S. K. Pal, and T. Pradeep, "Two distinct fluorescent quantum clusters of gold starting from metallic nanoparticles by pH-dependent ligand etching," *Nano Research*, vol. 1, no. 4, pp. 333–340, 2008.
- [117] H. Qian, Y. Zhu, and R. Jin, "Size-Focusing synthesis, optical and electrochemical properties of monodisperse Au₃₈(SC₂H₄Ph)₂₄ nanoclusters," *ACS Nano*, vol. 3, no. 11, pp. 3795–3803, 2009.
- [118] H. Qian, M. Zhu, Z. Wu, and R. Jin, "Quantum sized gold nanoclusters with atomic precision," *Accounts of Chemical Research*, vol. 45, no. 9, pp. 1470–1479, 2012.
- [119] T. G. Schaaff and R. L. Whetten, "Controlled Etching of Au: SR cluster Compounds," *Journal of Physical Chemistry B*, vol. 103, no. 44, pp. 9394–9396, 1999.
- [120] R. A. Sperling and W. J. Parak, "Surface modification, functionalization and bioconjugation of colloidal inorganic nanoparticles," *Philosophical Transactions of the Royal Society A: Mathematical, Physical and Engineering Sciences*, vol. 368, no. 1915, pp. 1333–1383, 2010.
- [121] S. Jiang, K. Y. Win, S. Liu, C. P. Teng, Y. Zheng, and M.-Y. Han, "Surface-functionalized nanoparticles for biosensing and imaging-guided therapeutics," *Nanoscale*, vol. 5, no. 8, pp. 3127–3148, 2013.
- [122] N. Erathodiyil and J. Y. Ying, "Functionalization of inorganic nanoparticles for bioimaging applications," *Accounts of Chemical Research*, vol. 44, no. 10, pp. 925–935, 2011.
- [123] X. Le Guével, B. Hötzer, G. Jung, and M. Schneider, "NIR-emitting fluorescent gold nanoclusters doped in silica nanoparticles," *Journal of Materials Chemistry*, vol. 21, no. 9, pp. 2974–2981, 2011.
- [124] C. A. J. Lin, R. A. Sperling, J. K. Li et al., "Design of an amphiphilic polymer for nanoparticle coating and functionalization," *Small*, vol. 4, no. 3, pp. 334–341, 2008.
- [125] S.-K. Sun, L.-X. Dong, Y. Cao, H.-R. Sun, and X.-P. Yan, "Fabrication of multifunctional Gd₂O₃/Au hybrid nanoprobe via a one-step approach for near-infrared fluorescence and magnetic resonance multimodal imaging in vivo," *Analytical Chemistry*, vol. 85, no. 17, pp. 8436–8441, 2013.
- [126] J. M. Abad, S. F. L. Mertens, M. Pita, V. M. Fernández, and D. J. Schiffrin, "Functionalization of thioctic acid-capped gold nanoparticles for specific immobilization of histidine-tagged proteins," *Journal of the American Chemical Society*, vol. 127, no. 15, pp. 5689–5694, 2005.
- [127] F. Wen, Y. Dong, L. Feng, S. Wang, S. Zhang, and X. Zhang, "Horseradish peroxidase functionalized fluorescent gold nanoclusters for hydrogen peroxide sensing," *Analytical Chemistry*, vol. 83, no. 4, pp. 1193–1196, 2011.
- [128] Y. Chen, Y. Wang, C. Wang et al., "Papain-directed synthesis of luminescent gold nanoclusters and the sensitive detection of Cu²⁺," *Journal of Colloid and Interface Science*, vol. 396, pp. 63–68, 2013.
- [129] C. Banerjee, J. Kuchlyan, D. Banik et al., "Interaction of gold nanoclusters with IR light emitting cyanine dyes: a systematic fluorescence quenching study," *Physical Chemistry Chemical Physics*, vol. 16, no. 32, pp. 17272–17283, 2014.
- [130] Z. Wang, J. H. Lee, and Y. Lu, "Highly sensitive 'turn-on' fluorescent sensor for Hg²⁺ in aqueous solution based on structure-switching DNA," *Chemical Communications*, no. 45, pp. 6005–6007, 2008.
- [131] Z. Gu, M. Zhao, Y. Sheng, L. A. Bentolila, and Y. Tang, "Detection of mercury ion by infrared fluorescent protein and its hydrogel-based paper assay," *Analytical Chemistry*, vol. 83, no. 6, pp. 2324–2329, 2011.
- [132] M. Matsushita, M. M. Meijler, P. Wirsching, R. A. Lerner, and K. D. Janda, "A blue fluorescent antibody-cofactor sensor for mercury," *Organic Letters*, vol. 7, no. 22, pp. 4943–4946, 2005.
- [133] B. Ruttkey-Nedecky, J. Kudr, L. Nejdil, D. Maskova, R. Kizek, and V. Adam, "G-quadruplexes as sensing probes," *Molecules*, vol. 18, no. 12, pp. 14760–14779, 2013.

- [134] J. Liu and Y. Lu, "Rational Design of 'turn-On' allosteric DNAzyme catalytic beacons for aqueous mercury ions with ultrahigh sensitivity and selectivity," *Angewandte Chemie*, vol. 46, no. 40, pp. 7587–7590, 2007.
- [135] P. J. J. Huang and J. Liu, "Sensing parts-per-trillion Cd^{2+} , Hg^{2+} , and Pb^{2+} collectively and individually using phosphorothioate DNAzymes," *Analytical Chemistry*, vol. 86, no. 12, pp. 5999–6005, 2014.
- [136] B.-C. Ye and B.-C. Yin, "Highly sensitive detection of mercury(II) ions by fluorescence polarization enhanced by gold nanoparticles," *Angewandte Chemie International Edition*, vol. 47, no. 44, pp. 8386–8389, 2008.
- [137] C.-W. Tseng, H.-Y. Chang, J.-Y. Chang, and C.-C. Huang, "Detection of mercury ions based on mercury-induced switching of enzyme-like activity of platinum/gold nanoparticles," *Nanoscale*, vol. 4, no. 21, pp. 6823–6830, 2012.
- [138] M. Suresh, S. K. Mishra, S. Mishra, and A. Das, "The detection of Hg^{2+} by cyanobacteria in aqueous media," *Chemical Communications*, no. 18, pp. 2496–2498, 2009.
- [139] Nuriman, B. Kuswandi, and W. Verboom, "Selective chemosensor for Hg(II) ions based on tris[2-(4-phenyldiazenyl)phenylaminoethoxy]cyclootrimeratrylene in aqueous samples," *Analytica Chimica Acta*, vol. 655, no. 1-2, pp. 75–79, 2009.
- [140] S. Voutsadaki, G. K. Tsikalas, E. Klontzas, G. E. Froudakis, and H. E. Katerinopoulos, "A 'turn-on' coumarin-based fluorescent sensor with high selectivity for mercury ions in aqueous media," *Chemical Communications*, vol. 46, no. 19, pp. 3292–3294, 2010.
- [141] J. Xie, Y. Zheng, and J. Y. Ying, "Highly selective and ultrasensitive detection of Hg^{2+} based on fluorescence quenching of Au nanoclusters by Hg^{2+} - Au^+ interactions," *Chemical Communications*, vol. 46, no. 6, pp. 961–963, 2010.
- [142] T. Mayr, I. Klimant, O. S. Wolfbeis, and T. Werner, "Dual lifetime referenced optical sensor membrane for the determination of copper(II) ions," *Analytica Chimica Acta*, vol. 462, no. 1, pp. 1–10, 2002.
- [143] M. E. Letelier, A. M. Lepe, M. Faúndez et al., "Possible mechanisms underlying copper-induced damage in biological membranes leading to cellular toxicity," *Chemico-Biological Interactions*, vol. 151, no. 2, pp. 71–82, 2005.
- [144] L. M. Gaetke and C. K. Chow, "Copper toxicity, oxidative stress, and antioxidant nutrients," *Toxicology*, vol. 189, no. 1-2, pp. 147–163, 2003.
- [145] W. Chen, X. Tu, and X. Guo, "Fluorescent gold nanoparticles-based fluorescence sensor for Cu^{2+} ions," *Chemical Communications*, no. 13, pp. 1736–1738, 2009.
- [146] X. Tu, W. Chen, and X. Guo, "Facile one-pot synthesis of near-infrared luminescent gold nanoparticles for sensing copper (II)," *Nanotechnology*, vol. 22, no. 9, Article ID 095701, 2011.
- [147] Y. Xu, X. Yang, S. Zhu, and Y. Dou, "Selectively fluorescent sensing of Cu^{2+} based on lysine-functionalized gold nanoclusters," *Colloids and Surfaces A: Physicochemical and Engineering Aspects*, vol. 450, pp. 115–120, 2014.
- [148] D. Cao, J. Fan, J. Qiu, Y. Tu, and J. Yan, "Masking method for improving selectivity of gold nanoclusters in fluorescence determination of mercury and copper ions," *Biosensors & Bioelectronics*, vol. 42, no. 1, pp. 47–50, 2013.
- [149] J.-A. Annie Ho, H.-C. Chang, and W.-T. Su, "DOPA-mediated reduction allows the facile synthesis of fluorescent gold nanoclusters for use as sensing probes for ferric ions," *Analytical Chemistry*, vol. 84, no. 7, pp. 3246–3253, 2012.
- [150] Y.-C. Shiang, C.-C. Huang, and H.-T. Chang, "Gold nanodot-based luminescent sensor for the detection of hydrogen peroxide and glucose," *Chemical Communications*, no. 23, pp. 3437–3439, 2009.
- [151] L. Hu, S. Han, S. Parveen, Y. Yuan, L. Zhang, and G. Xu, "Highly sensitive fluorescent detection of trypsin based on BSA-stabilized gold nanoclusters," *Biosensors & Bioelectronics*, vol. 32, no. 1, pp. 297–299, 2012.
- [152] Q. Wen, Y. Gu, L. J. Tang, R. Q. Yu, and J.-H. Jiang, "Peptide-templated gold nanocluster beacon as a sensitive, label-free sensor for protein post-translational modification enzymes," *Analytical Chemistry*, vol. 85, no. 24, pp. 11681–11685, 2013.
- [153] X. Yang, Y. Luo, Y. Zhuo, Y. Feng, and S. Zhu, "Novel synthesis of gold nanoclusters templated with l-tyrosine for selective analyzing tyrosinase," *Analytica Chimica Acta*, vol. 840, pp. 87–92, 2014.
- [154] B. Aswathy and G. Sony, " Cu^{2+} modulated BSA-Au nanoclusters: a versatile fluorescence turn-on sensor for dopamine," *Microchemical Journal*, vol. 116, pp. 151–156, 2014.
- [155] Y. Tao, Y. Lin, J. Ren, and X. Qu, "A dual fluorometric and colorimetric sensor for dopamine based on BSA-stabilized Au nanoclusters," *Biosensors & Bioelectronics*, vol. 42, no. 1, pp. 41–46, 2013.
- [156] L. Li, H. Liu, Y. Shen, J. Zhang, and J. J. Zhu, "Electrogenerated chemiluminescence of Au nanoclusters for the detection of dopamine," *Analytical Chemistry*, vol. 83, no. 3, pp. 661–665, 2011.
- [157] H. Liu, G. Yang, E. S. Abdel-Halim, and J.-J. Zhu, "Highly selective and ultrasensitive detection of nitrite based on fluorescent gold nanoclusters," *Talanta*, vol. 104, pp. 135–139, 2013.
- [158] X. Chen and G. A. Baker, "Cholesterol determination using protein-templated fluorescent gold nanocluster probes," *Analyst*, vol. 138, no. 24, pp. 7299–7302, 2013.
- [159] B. Hemmateenejad, F. Shakerizadeh-Shirazi, and F. Samari, "BSA-modified gold nanoclusters for sensing of folic acid," *Sensors and Actuators, B: Chemical*, vol. 199, pp. 42–46, 2014.
- [160] Z. Chen, S. Qian, J. Chen, J. Cai, S. Wu, and Z. Cai, "Protein-templated gold nanoclusters based sensor for off-on detection of ciprofloxacin with a high selectivity," *Talanta*, vol. 94, pp. 240–245, 2012.
- [161] G.-H. Yang, J.-J. Shi, S. Wang et al., "Fabrication of a boron nitride-gold nanocluster composite and its versatile application for immunoassays," *Chemical Communications*, vol. 49, no. 91, pp. 10757–10759, 2013.
- [162] R. C. Triulzi, M. Micic, S. Giordani, M. Serry, W. A. Chiou, and R. M. Leblanc, "Immunoassay based on the antibody-conjugated PAMAM-dendrimer-gold quantum dot complex," *Chemical Communications*, no. 48, pp. 5068–5070, 2006.
- [163] H. Lin, L. Li, C. Lei et al., "Immune-independent and label-free fluorescent assay for Cystatin C detection based on protein-stabilized Au nanoclusters," *Biosensors and Bioelectronics*, vol. 41, no. 1, pp. 256–261, 2013.
- [164] K. Selvaprakash and Y.-C. Chen, "Using protein-encapsulated gold nanoclusters as photoluminescent sensing probes for biomolecules," *Biosensors & Bioelectronics*, vol. 61, pp. 88–94, 2014.
- [165] C.-C. Huang, C.-K. Chiang, Z.-H. Lin, K.-H. Lee, and H.-T. Chang, "Bioconjugated gold nanodots and nanoparticles for protein assays based on photoluminescence quenching," *Analytical Chemistry*, vol. 80, no. 5, pp. 1497–1504, 2008.

- [166] C. C. Huang, C. T. Chen, Y. C. Shiang, Z. H. Lin, and H. T. Chang, "Synthesis of fluorescent carbohydrate-protected Au nanodots for detection of Concanavalin A and *Escherichia coli*," *Analytical Chemistry*, vol. 81, no. 3, pp. 875–882, 2009.
- [167] J. Zhang, M. Sajid, N. Na, L. Huang, D. He, and J. Ouyang, "The application of Au nanoclusters in the fluorescence imaging of human serum proteins after native PAGE: enhancing detection by low-temperature plasma treatment," *Biosensors and Bioelectronics*, vol. 35, no. 1, pp. 313–318, 2012.
- [168] A. M. P. Hussain, S. N. Sarangi, J. A. Kesarwani, and S. N. Sahu, "Au-nanocluster emission based glucose sensing," *Biosensors & Bioelectronics*, vol. 29, no. 1, pp. 60–65, 2011.
- [169] L. Jin, L. Shang, S. Guo et al., "Biomolecule-stabilized Au nanoclusters as a fluorescence probe for sensitive detection of glucose," *Biosensors & Bioelectronics*, vol. 26, no. 5, pp. 1965–1969, 2011.
- [170] W. J. Stark, "Nanoparticles in biological systems," *Angewandte Chemie International Edition*, vol. 50, no. 6, pp. 1242–1258, 2011.
- [171] L. Shang and G. U. Nienhaus, "Small fluorescent nanoparticles at the nano-bio interface," *Materials Today*, vol. 16, no. 3, pp. 58–66, 2013.
- [172] H.-H. Wang, C. A. J. Lin, C. H. Lee et al., "Fluorescent gold nanoclusters as a biocompatible marker for in vitro and in vivo tracking of endothelial cells," *ACS Nano*, vol. 5, no. 6, pp. 4337–4344, 2011.
- [173] P.-H. Chan, S.-Y. Wong, S.-H. Lin, and Y.-C. Chen, "Lysozyme-encapsulated gold nanocluster-based affinity mass spectrometry for pathogenic bacteria," *Rapid Communications in Mass Spectrometry*, vol. 27, no. 19, pp. 2143–2148, 2013.
- [174] D. Hu, Z. Sheng, S. Fang et al., "Folate receptor-targeting gold nanoclusters as fluorescence enzyme mimetic nanoprobe for tumor molecular colocalization diagnosis," *Theranostics*, vol. 4, no. 2, pp. 142–153, 2014.
- [175] P. Botella, Í. Ortega, M. Quesada et al., "Multifunctional hybrid materials for combined photo and chemotherapy of cancer," *Dalton Transactions*, vol. 41, no. 31, pp. 9286–9296, 2012.
- [176] P. Huang, J. Lin, S. Wang et al., "Photosensitizer-conjugated silica-coated gold nanoclusters for fluorescence imaging-guided photodynamic therapy," *Biomaterials*, vol. 34, no. 19, pp. 4643–4654, 2013.
- [177] Y. Wang, J. Chen, and J. Irudayaraj, "Nuclear targeting dynamics of gold nanoclusters for enhanced therapy of HER2⁺ breast cancer," *ACS Nano*, vol. 5, no. 12, pp. 9718–9725, 2011.
- [178] X. Wang, X. Cai, J. Hu et al., "Glutathione-triggered 'Off-On' release of anticancer drugs from dendrimer-encapsulated gold nanoparticles," *Journal of the American Chemical Society*, vol. 135, no. 26, pp. 9805–9810, 2013.
- [179] C.-L. Liu, M.-L. Ho, Y.-C. Chen et al., "Thiol-functionalized gold nanodots: two-photon absorption property and imaging in vitro," *Journal of Physical Chemistry C*, vol. 113, no. 50, pp. 21082–21089, 2009.
- [180] Z. Zhou, C. Zhang, Q. Qian et al., "Folic acid-conjugated silica capped gold nanoclusters for targeted fluorescence/X-ray computed tomography imaging," *Journal of Nanobiotechnology*, vol. 11, article 17, 2013.
- [181] J. Wang, G. Zhang, Q. Li et al., "In vivo self-bio-imaging of tumors through in situ biosynthesized fluorescent gold nanoclusters," *Scientific reports*, vol. 3, 2013.
- [182] G. Ramakrishna, O. Varnavski, J. Kim, D. Lee, and T. Goodson, "Quantum-sized gold clusters as efficient two-photon absorbers," *Journal of the American Chemical Society*, vol. 130, no. 15, pp. 5032–5033, 2008.
- [183] L. Polavarapu, M. Manna, and Q.-H. Xu, "Biocompatible glutathione capped gold clusters as one- and two-photon excitation fluorescence contrast agents for live cells imaging," *Nanoscale*, vol. 3, no. 2, pp. 429–434, 2011.
- [184] T. W. J. Gadella Jr., T. M. Jovin, and R. M. Clegg, "Fluorescence lifetime imaging microscopy (FLIM): spatial resolution of microstructures on the nanosecond time scale," *Biophysical Chemistry*, vol. 48, no. 2, pp. 221–239, 1993.
- [185] A. Zhang, Y. Tu, S. Qin et al., "Gold nanoclusters as contrast agents for fluorescent and X-ray dual-modality imaging," *Journal of Colloid and Interface Science*, vol. 372, no. 1, pp. 239–244, 2012.
- [186] A. Retnakumari, S. Setua, D. Menon et al., "Molecular-receptor-specific, non-toxic, near-infrared-emitting Au cluster-protein nanoconjugates for targeted cancer imaging," *Nanotechnology*, vol. 21, no. 5, Article ID 055103, 2010.

Research Article

Mössbauer Spectroscopy, Structural and Magnetic Studies of Zn²⁺ Substituted Magnesium Ferrite Nanomaterials Prepared by Sol-Gel Method

Yun He,¹ Xingxing Yang,¹ Jinpei Lin,¹ Qing Lin,^{1,2} and Jianghui Dong³

¹College of Physics and Technology, Guangxi Normal University, Guilin 541004, China

²Department of Information Technology, Hainan Medical College, Haikou 571101, China

³School of Natural and Built Environments, University of South Australia, Adelaide, SA 5095, Australia

Correspondence should be addressed to Qing Lin; hy@gxnu.edu.cn

Received 8 August 2014; Accepted 26 August 2014

Academic Editor: Xinqing Chen

Copyright © 2015 Yun He et al. This is an open access article distributed under the Creative Commons Attribution License, which permits unrestricted use, distribution, and reproduction in any medium, provided the original work is properly cited.

Zinc substituted magnesium ferrite nanomaterials Mg_{1-x}Zn_xFe₂O₄ ($x = 0, 0.1, 0.3, 0.5, 0.7$) powders have been prepared by a sol-gel autocombustion method. The lattice parameter increases with increase in Zn concentration, but average crystallite size tends to decrease by increasing the zinc content. SEM results indicate the distribution of grains and morphology of the samples. Some particles are agglomerated due to the presence of magnetic interactions among particles. Room temperature Mössbauer spectra of Mg_{1-x}Zn_xFe₂O₄ shows that the A Mössbauer absorption area decreases and the B Mössbauer absorption area increases with zinc concentration increasing. The change of the saturation magnetization can be explained with Néel's theory. It was confirmed that the transition from ferrimagnetic to superparamagnetic behaviour depends on increase in zinc concentration by Mössbauer spectra at room temperature. Saturation magnetization increases and coercivity decreases with Zn content increasing.

1. Introduction

Magnesium ferrite is a soft magnetic n-type semiconducting material, which is used in catalysis, gas sensors, transformers, ferrofluids, fuel cells, and magnet core of coils [1, 2]. It has been reported [3, 4] that the structure of magnesium ferrite is partially inverse spinel, with 0.1 of Mg²⁺ ions and 0.9 of Mg²⁺ ions distributed over the A and B sites in the following way (Mg_{0.1}Fe_{0.9})[Mg_{0.9}Fe_{1.1}]O₄. The magnetic properties of nonmagnetic Zn substituted ferrites have attracted considerable attention because of the importance of these materials for high-frequency applications [5, 6]. Zinc ferrite possesses a normal spinel structure, and all Zn²⁺ ions reside on tetrahedral A sites. Therefore, substitution of Mg by Zn in Mg_{1-x}Zn_xFe₂O₄ is expected to increase the magnetic moment up to a certain limit; thereafter, it decreases for the canting of spins in octahedral B sites. Choodamani et al. [7] investigated thermal effect on magnetic properties of Mg-Zn ferrite nanoparticles, and magnetic properties were found to be affected by particle size. In this paper,

ferrite Mg_{1-x}Zn_xFe₂O₄ ($x = 0, 0.1, 0.3, 0.5, 0.7$) powders were prepared by a sol-gel autocombustion method. The aim of this study is to investigate variation structural and magnetic properties of magnesium ferrite powders by partial replacement of nonmagnetic zinc cations.

2. Experimental

2.1. Sample Preparation. Zinc substituted magnesium ferrite Mg_{1-x}Zn_xFe₂O₄ ($x = 0, 0.1, 0.3, 0.5, 0.7$) powders were prepared by a sol-gel autocombustion method. The analytical grades Mg(NO₃)₂·6H₂O, Zn(NO₃)₂·6H₂O, Fe(NO₃)₃·9H₂O, citric acid (C₆H₈O₇·H₂O), and ammonia (NH₃·H₂O) were used as raw materials. The molar ratio of metal nitrates to citric acid was taken as 1:1. The metal nitrates and citric acid were, respectively, dissolved into deionized water to form solution. The solution of metal nitrates was added to ammonia to change the pH value from 7 to 9. The mixed solution was poured into a thermostat water bath and heated at 80°C under constant stirring to transform into a dried gel.

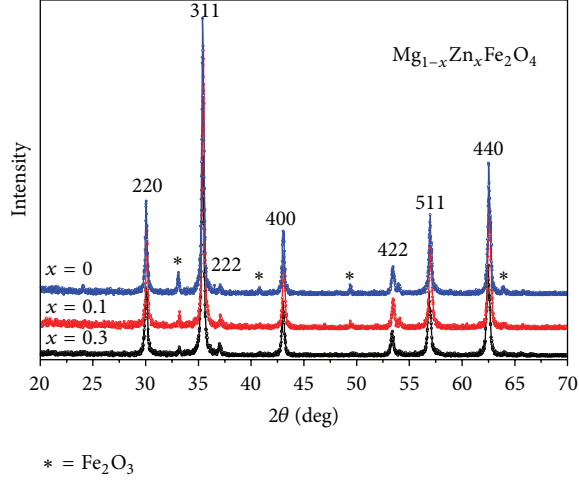


FIGURE 1: Room temperature X-ray diffraction patterns of $\text{Mg}_{1-x}\text{Zn}_x\text{Fe}_2\text{O}_4$ annealed at 800°C .

Citric acid was dropped continually in the process of heating. The gel was dried at 120°C in a dry oven for 2 h and, being ignited in air at room temperature, the dried gel burnt in a self-propagating combustion way to form loose powder. The powder was ground and annealed at temperature of 800°C for 3 h.

2.2. Characterization. The crystalline structure was investigated by X-ray diffraction (D/max-2500V/PC, Rigaku) with $\text{Cu K}\alpha$ radiation ($\lambda = 0.15405 \text{ nm}$). The micrographs were obtained by scanning electron microscopy (NoVa Nano SEM 430). The Mössbauer spectrum was performed at room temperature (25°C), using a conventional Mössbauer spectrometer (Fast Com Tec PC-moss II), in constant acceleration mode. The γ -rays were provided by a ^{57}Co source in a rhodium matrix. Magnetization measurements were carried out with super conducting quantum interference device (MPMS-XL-7, Quantum Design) at room temperature.

3. Results and Discussion

3.1. XRD Patterns Analysis. Figure 1 shows the XRD patterns of $\text{Mg}_{1-x}\text{Zn}_x\text{Fe}_2\text{O}_4$ ($x = 0, 0.1, 0.3$) ferrites calcined at 800°C for 3 h. The impurity peak of Fe_2O_3 is detected in the samples with $x = 0, 0.1$ and 0.3 , and increasing the content of Zn is favorable for the synthesis of pure Mg-Zn ferrites. Similar results also were reported in the other literature [6].

Table 1 indicates that the lattice constant increases with the increasing substitution of Zn^{2+} ions. The increase in lattice parameter is probably due to replacement of smaller Mg^{2+} ions (0.72 \AA) by larger Zn^{2+} ions (0.74 \AA) [8, 9].

The X-ray density was calculated using the relation [4, 10, 11]:

$$\rho_x = \frac{8M}{Na^3}, \quad (1)$$

where M is relative molecular mass, N is Avogadro's number, and " a " is the lattice parameter. Table 1 shows the X-ray

TABLE 1: Lattice parameters, average crystallite size, and X-ray densities date of $\text{Mg}_{1-x}\text{Zn}_x\text{Fe}_2\text{O}_4$ annealed at 800°C .

Sample (x)	Lattice parameter (\AA)	Average crystallite size (\AA)	Density ($\text{g}\cdot\text{cm}^{-3}$)
0	8.39786	411	4.4859
0.1	8.39491	356	4.5829
0.3	8.40864	322	4.7440
0.5	8.43133	377	4.8879
0.7	8.43576	385	5.0620

density increase with Zn^{2+} concentration for all samples. The atomic weight of Zn is greater than that of Mg, so the relative molecular mass increases with Zn concentration increasing. The increase in X-ray density is attributed to the fact that relative molecular mass increases more than the negligible rise of the lattice parameter.

The average crystallite size of the investigated samples estimated by Scherrer's formula [10–12] is found to be around $32\sim 41 \text{ nm}$. The slight decrease in the crystallite size by the addition of Zn indicates that the presence of zinc obstructs the crystal growth [13, 14].

3.2. Structures and Grain Sizes. The SEM micrographs of MgFe_2O_4 annealed 800°C for 3 h are shown in Figure 2. The distribution of grains with almost uniform size can be observed. Figure 3 shows the histogram of grain size distribution of MgFe_2O_4 ferrites. The average grain size of MgFe_2O_4 is approximately 96.26 nm by using a statistical method. The average grain size is slightly larger than the average crystallite size determined by XRD.

The SEM micrographs of $\text{Mg}_{0.5}\text{Zn}_{0.5}\text{Fe}_2\text{O}_4$ annealed 800°C for 3 h are shown in Figure 4. The distribution of grains with almost uniform size can be observed, well crystallized for $\text{Mg}_{1-x}\text{Zn}_x\text{Fe}_2\text{O}_4$ ($x = 0.5$). Some particles are agglomerated due to the presence of magnetic interactions among particles [14].

Figure 5 shows the histogram of grain size distribution of $\text{Mg}_{0.5}\text{Zn}_{0.5}\text{Fe}_2\text{O}_4$ ferrites. The average grain size of $\text{Mg}_{0.5}\text{Zn}_{0.5}\text{Fe}_2\text{O}_4$ ($x = 0.5$) is approximately 90.74 nm by using a statistical method. It shows that the ferrite powers are nanoparticles, and the average grain size decreases with Zn content increasing. This shows that every particle is formed by a number of crystallites [15, 16].

3.3. Mössbauer Spectroscopy. The Mössbauer spectra recorded at room temperature are shown in Figure 6 for $\text{Mg}_{1-x}\text{Zn}_x\text{Fe}_2\text{O}_4$. All samples have been analyzed using Mösswinn 3.0 program. For the $\text{Mg}_{1-x}\text{Zn}_x\text{Fe}_2\text{O}_4$ with $x = 0, 0.1$, the spectra exhibit two normal Zeeman-split sextets due to Fe^{3+} at tetrahedral and octahedral sites, indicating the ferromagnetic behavior of the samples.

The sextet with the larger isomer shift is assigned to the Fe^{3+} ions at the B site and the one with the smaller isomer shift is assumed to arise from the Fe^{3+} ions occupying the A site. May be it is due to difference in $\text{Fe}^{3+}-\text{O}^{2-}$ internuclear separation. Compared with A site ions, the bond separation

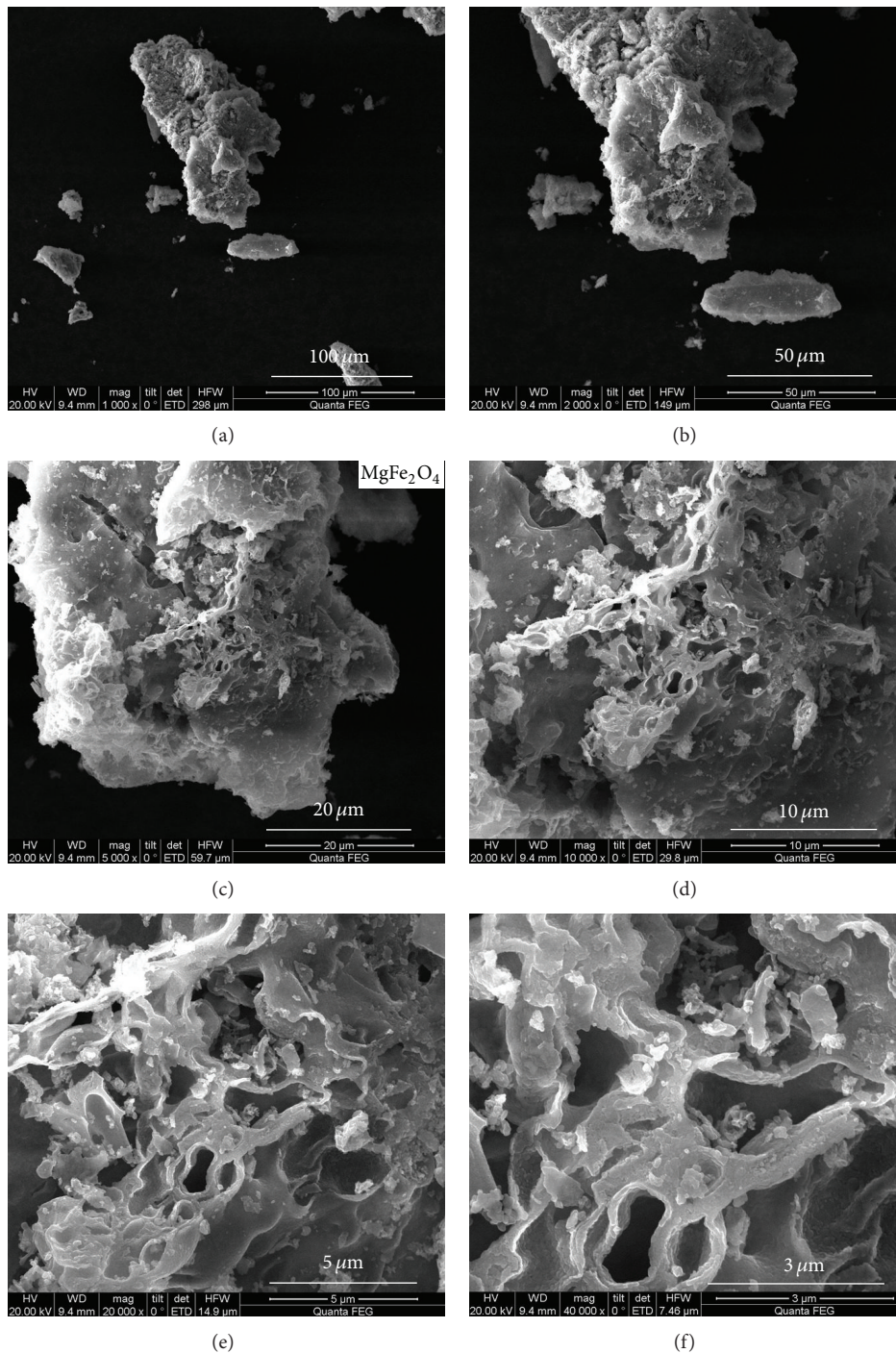


FIGURE 2: SEM micrographs depict MgFe₂O₄ ferrites with diameters of 100 μm (a), 50 μm (b), 20 μm (c), 10 μm (d), 5 μm (e), and 3 μm (f).

is larger for B site Fe³⁺ ions. In addition, overlap-ping of orbit is smaller for Fe³⁺ and O²⁺ ions at B site, which results in smaller covalency and larger isomer shift for Fe³⁺ ions at B site [17, 18]. It is reported that the values of IS for Fe²⁺ ions lie in the range 0.6~1.7 mm/s, while for Fe³⁺ they lie in the range 0.1~0.5 mm/s [19]. From Table 2, values for IS in our study indicate that iron is in Fe³⁺ state.

Table 2 shows the values of magnetic hyperfine field at A and B sites decrease by increasing nonmagnetic zinc substitution. The value of quadrupole shift of the A and B magnetic sextets is very small in the samples indicating that the local symmetry of the ferrites obtained is close to cubic [20]. The A Mössbauer absorption area decreases and the B Mössbauer absorption area increases with increasing zinc

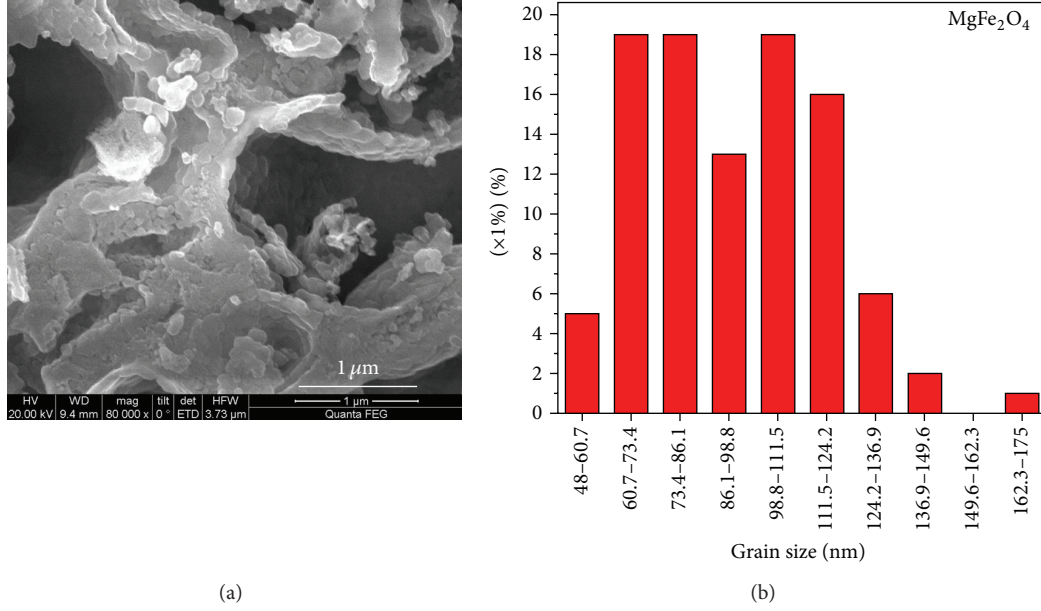


FIGURE 3: Histogram of grain size distribution of MgFe₂O₄ ($x = 0$) annealed at 800°C.

TABLE 2: Mössbauer parameters of isomer shift (IS), quadrupole splitting (QS), magnetic hyperfine field (H), line width (Γ), and absorption area (A_0) for Mg_{1-x}Zn_xFe₂O₄ annealed at 800°C.

Sample (x)	Component	IS (mm/s)	QS (mm/s)	H (T)	Γ (mm/s)	A_0 (mm/s)
0	Sextet (A)	0.163	0.011	45.871	0.503	17
	Sextet (B)	0.332	0.032	43.306	0.325	83
0.1	Sextet (A)	0.224	0.077	45.059	0.473	15
	Sextet (B)	0.294	-0.028	41.322	0.313	85
0.3	Sextet (B)	0.291	-0.009	34.072	0.363	100
0.5	Sextet (B)	0.318	0.005	24.234	0.268	100
0.7	Double	0.336	0.472	—	0.357	100

concentration, since Zn²⁺ substitutes Mg ferrite and occupies the A site, leading to transfer of Fe³⁺ from A site to B site.

When $x = 0.3, 0.5$, the spectra of Mg_{1-x}Zn_xFe₂O₄ are only the B magnetic sextet, and the magnetic sextet of A site vanishes which indicates the presence of Fe³⁺ ions only in the octahedral B site [21]. The spectrum obtained for the composition with $x = 0.5$ shows features of relaxation effects and was analyzed to a single sextet. Mössbauer spectra for the samples with $x = 0.7$ consist only of a central doublet, and it exhibits superparamagnetic character. The central doublet can be attributed to the magnetically isolated Fe³⁺ ions which do not participate in the long-range magnetic ordering due to a large number of nonmagnetic nearest neighbors [20, 21].

3.4. Magnetic Property of Particles. Figure 7 shows hysteresis loops of Mg_{1-x}Zn_xFe₂O₄ at room temperature. The magnetization of all samples nearly reaches saturation at the external field of 5000 Oe. It is observed from Table 3 that saturation magnetization increases as Zn content x increases.

The saturation magnetization could be expressed by means of the following relation [22, 23]:

$$\sigma_s = \frac{5585 \times n_B}{M}, \quad (2)$$

where n_B is magnetic moment with Bohr magneton as the unit and M is relative molecular mass. The relative molecular mass of Mg_{1-x}Zn_xFe₂O₄ decreases as Zn content x increases.

The change of magnetic moment n_B can be explained with Néel's theory. The magnetic moment for Zn²⁺, Mg²⁺, and Fe³⁺ ions is 0_{μ_B} , 0_{μ_B} , and 5_{μ_B} , respectively [3, 4]. According to Néel's two sublattice model of ferrimagnetism, using the cation distribution of (Zn_xMg_yFe_{1-x-y}) [Mg_{1-x-y}Fe_{1+x+y}]O₄, since Zn²⁺ ions have a stronger preference for the tetrahedral sites [11, 12], and Mg²⁺ ions exist in both sites but have a preference for the octahedral

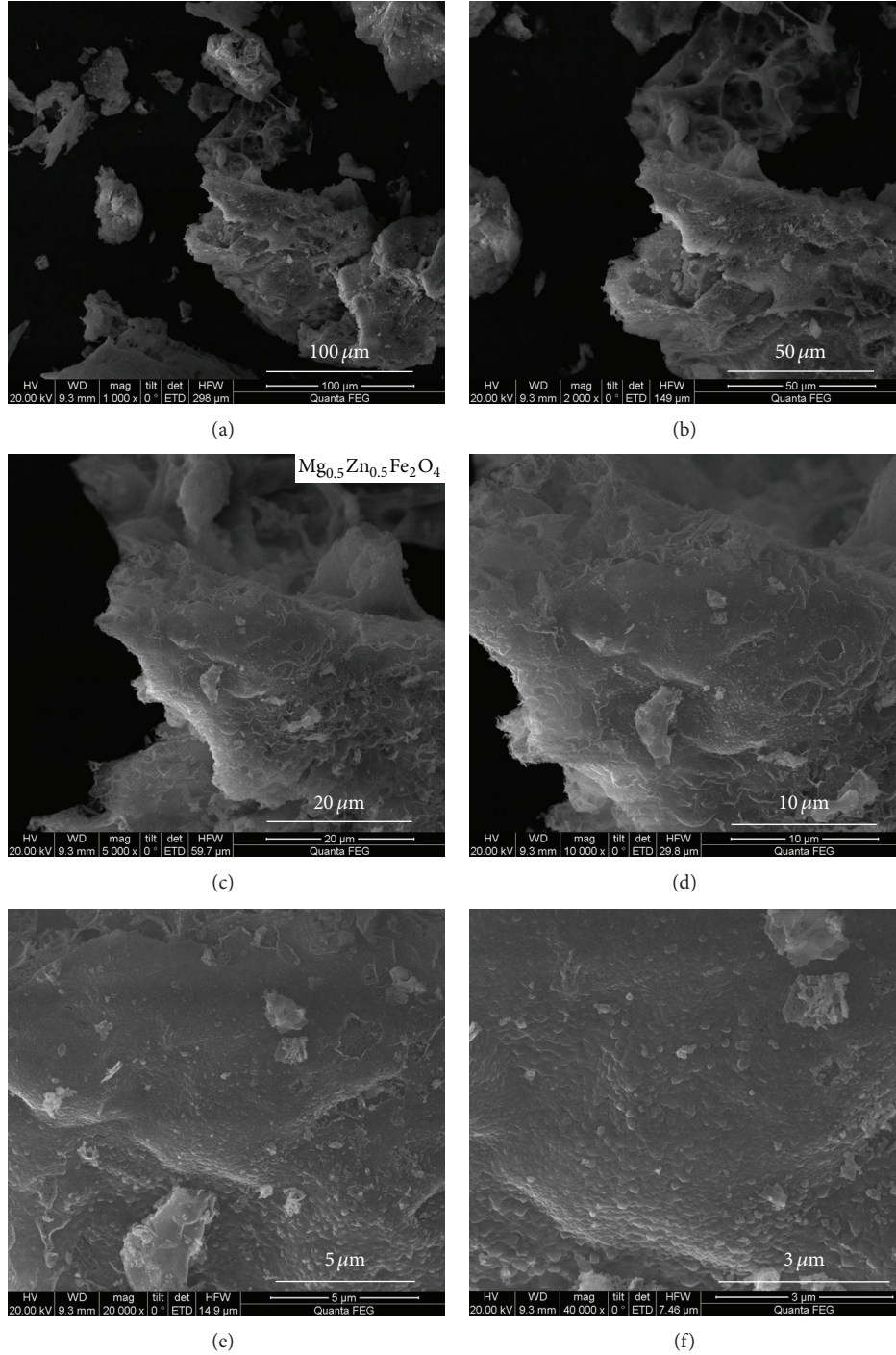


FIGURE 4: SEM micrographs depict $\text{Mg}_{0.5}\text{Zn}_{0.5}\text{Fe}_2\text{O}_4$ ferrites with diameters of 100 μm (a), 50 μm (b), 20 μm (c), 10 μm (d), 5 μm (e), and 3 μm (f).

site [3, 4, 10–12]. The magnetic moment n_B is expressed as [4, 5, 11].

$$\begin{aligned} n_B &= M_B - M_A = 5(1 + x + y) - 5(1 - x - y) \\ &= 10x + 10y, \end{aligned} \quad (3)$$

where M_B and M_A are the B and A sublattice magnetic moments. According to the literature [3], we assumed that

the value of y is equal to 0.1. Figure 8 shows the change in experimental and theoretical magnetic moments with Zn content x .

From Figure 8, the experimental and theoretical magnetic moments increase as Zn content x increases. Furthermore, according to (3), the theoretical saturation magnetization increases with Zn content x increasing. The result of the experimental is in a good agreement with theoretical

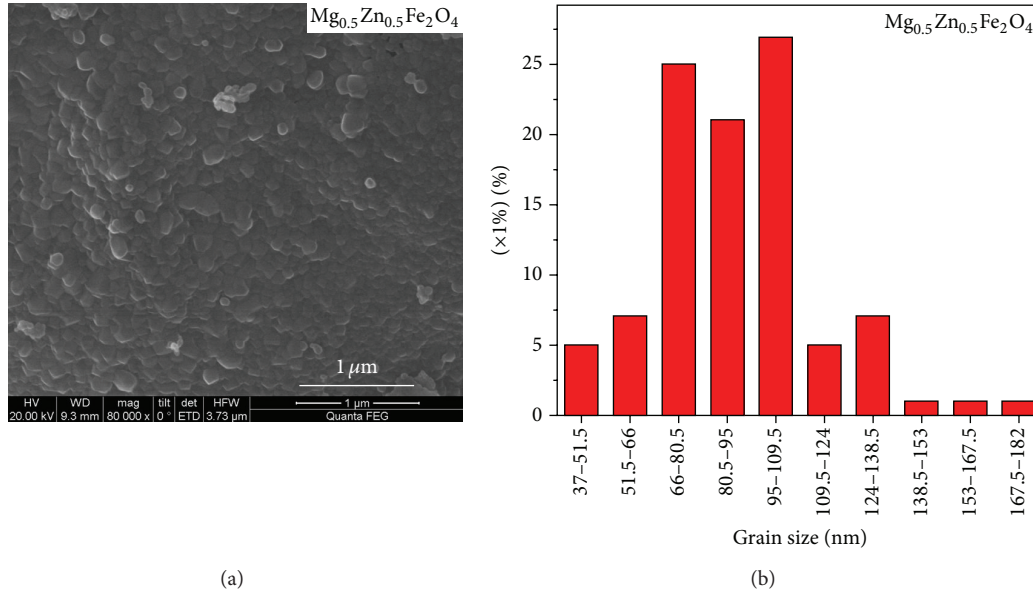


FIGURE 5: Histogram of grain size distribution of $\text{Mg}_{0.5}\text{Zn}_{0.5}\text{Fe}_2\text{O}_4$ ($x = 0.5$) annealed at 800°C .

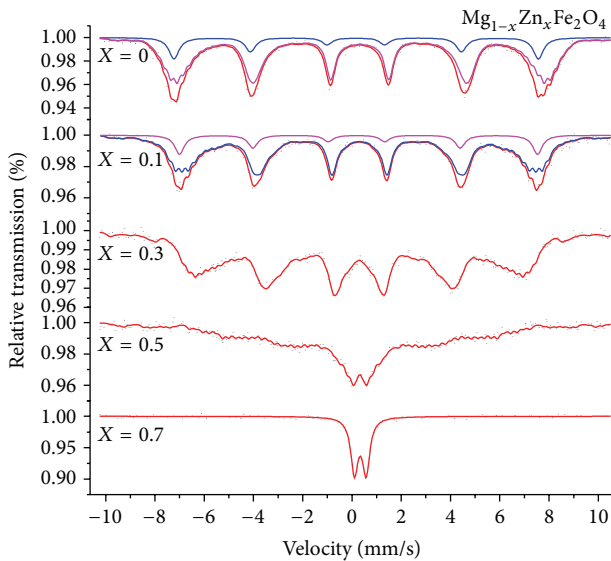


FIGURE 6: Room temperature Mössbauer spectra of $\text{Mg}_{1-x}\text{Zn}_x\text{Fe}_2\text{O}_4$ annealed at 800°C .

saturation magnetization for all samples. However, the saturation magnetization of $\text{Mg}_{1-x}\text{Zn}_x\text{Fe}_2\text{O}_4$ with $x = 0.1$ and 0.5 has no significant changes, maybe because the average grain size decreases with increasing Zn content from the SEM. It is known that porosity is inversely proportional, while the particle size is directly proportional to the magnetization for nanoferrites [24, 25].

It is observed from Table 3 that the coercivity of $\text{Mg}_{1-x}\text{Zn}_x\text{Fe}_2\text{O}_4$ is less than 100 Oe, which indicating the all sample is soft magnetic materials. And the coercivity tends to decrease with Zn content x increasing. The magnetic coercivity of the particles depends significantly on

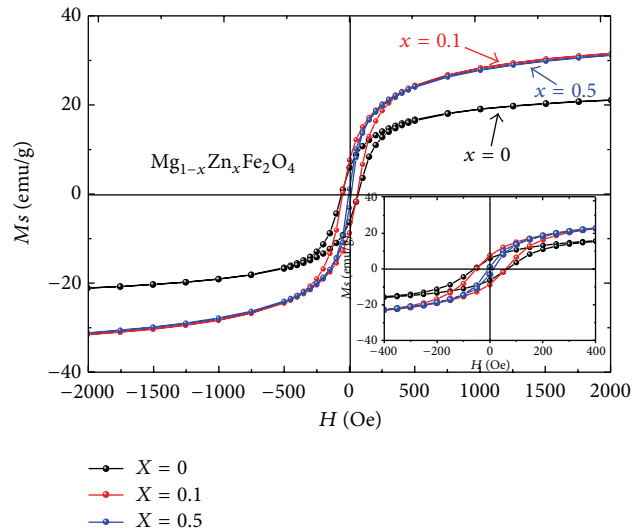


FIGURE 7: Room temperature hysteresis loops of $\text{Mg}_{1-x}\text{Zn}_x\text{Fe}_2\text{O}_4$ annealed at 800°C .

their magnetocrystalline anisotropy, microstrain, interparticle interaction, temperature, size, and shape [9, 26, 27]. However the Zn^{2+} and Mg^{2+} ions have no unpaired electrons and lead to zero total electron spin. So replacing Mg^{2+} ions with the Zn^{2+} ions will not have much effect on the magnetic anisotropy constant. The reduction in magnetic coercivity is related to the grain size [28–30].

4. Conclusion

The analysis of XRD patterns for $\text{Mg}_{1-x}\text{Zn}_x\text{Fe}_2\text{O}_4$ ($x = 0, 0.1, 0.3, 0.5, 0.7$) annealed at 800°C show that the increase in lattice constant is due to replacement of smaller Mg^{2+} ions

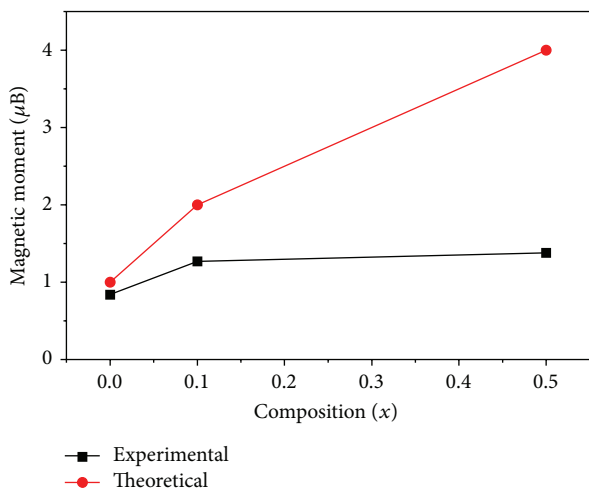


FIGURE 8: Variation in experimental and theoretical magnetic moment with zinc content x .

TABLE 3: Magnetic data for $\text{Mg}_{1-x}\text{Zn}_x\text{Fe}_2\text{O}_4$ annealed at 800°C .

Sample (x)	M_S (emu/g)	H_C (Oe)	M_r (emu/g)	n_B
0	23.36	50.13	6.36	0.84
0.1	34.83	50.13	7.65	1.27
0.5	34.98	0.18	1.10	1.38

by larger Zn^{2+} ions. SEM results indicate the distribution of grains and morphology of the samples. Some particles are agglomerated due to the presence of magnetic interactions among particles. And the ferrite particles are nanoparticles. Room temperature Mössbauer spectra of $\text{Mg}_{1-x}\text{Zn}_x\text{Fe}_2\text{O}_4$ display that the A Mössbauer absorption area decreases and the B Mössbauer absorption area increases with increasing zinc concentration. The change of the saturation magnetization can be explained with Néel's theory. The coercivity decreases with increasing Zn content is attributed to the grain size.

Conflict of Interests

The authors declare that they have no conflict of interests regarding this work.

Acknowledgments

This work was financially supported by the National Natural Science Foundation of China (nos. 11364004 and 11164002) and Innovation Project of Guangxi Graduate Education under Grant (no. 2010106020702M47).

References

- [1] N. M. Deraz and A. Alarifi, "Novel preparation and properties of magnesioferrite nanoparticles," *Journal of Analytical and Applied Pyrolysis*, vol. 97, pp. 55–61, 2012.
- [2] S. H. Hosseini and A. Asadnia, "Synthesis, characterization, and microwave-absorbing properties of polypyrrole/ MnFe_2O_4 nanocomposite," *Journal of Nanomaterials*, vol. 2012, Article ID 198973, 6 pages, 2012.
- [3] A. Franco Jr. and M. S. Silva, "High temperature magnetic properties of magnesium ferrite nanoparticles," *Journal of Applied Physics*, vol. 109, no. 7, Article ID 07B505, 2011.
- [4] M. Manjurul Haque, M. Huq, and M. A. Hakim, "Effect of Zn^{2+} substitution on the magnetic properties of $\text{Mg}_{1-x}\text{Zn}_x\text{Fe}_2\text{O}_4$ ferrites," *Physica B*, vol. 404, no. 21, pp. 3915–3921, 2009.
- [5] M. M. Eltabey, A. M. Massoud, and C. Radu, "Microstructure and superparamagnetic properties of Mg-Ni-Cd ferrites nanoparticles," *Journal of Nanomaterials*, vol. 2014, Article ID 492832, 7 pages, 2014.
- [6] A. Xia, S. Liu, C. Jin, L. Chen, and Y. Lv, "Hydrothermal $\text{Mg}_{1-x}\text{Zn}_x\text{Fe}_2\text{O}_4$ spinel ferrites: phase formation and mechanism of saturation magnetization," *Materials Letters*, vol. 105, pp. 199–201, 2013.
- [7] C. Choodamani, G. P. Nagabhushana, B. Rudraswamy, and G. T. Chandrappa, "Thermal effect on magnetic properties of Mg-Zn ferrite nanoparticles," *Materials Letters*, vol. 116, pp. 227–230, 2014.
- [8] K. Verma, A. Kumar, and D. Varshney, "Dielectric relaxation behavior of $\text{A}_x\text{Co}_{1-x}\text{Fe}_2\text{O}_4$ ($A = \text{Zn}, \text{Mg}$) mixed ferrites," *Journal of Alloys and Compounds*, vol. 526, pp. 91–97, 2012.
- [9] H. Mohseni, H. Shokrollahi, I. Sharifi, and K. Gheisari, "Magnetic and structural studies of the Mn-doped Mg-Zn ferrite nanoparticles synthesized by the glycine nitrate process," *Journal of Magnetism and Magnetic Materials*, vol. 324, no. 22, pp. 3741–3747, 2012.
- [10] K. A. Mohammed, A. D. Al-Rawas, A. M. Gismelseed et al., "Infrared and structural studies of $\text{Mg}_{1-x}\text{Zn}_x\text{Fe}_2\text{O}_4$ ferrites," *Physica B: Condensed Matter*, vol. 407, no. 4, pp. 795–804, 2012.
- [11] B. Babić-Stojić, V. Jokanović, D. Milivojević et al., "Magnetic and structural studies of CoFe_2O_4 nanoparticles suspended in an organic liquid," *Journal of Nanomaterials*, vol. 2013, Article ID 741036, 9 pages, 2013.
- [12] S. J. Haralkar, R. H. Kadam, S. S. More et al., "Substitutional effect of Cr^{3+} ions on the properties of Mg-Zn ferrite nanoparticles," *Physica B*, vol. 407, no. 21, pp. 4338–4346, 2012.
- [13] W. A. A. Bayoumy, "Synthesis and characterization of nanocrystalline Zn-substituted Mg-Ni-Fe-Cr ferrites via surfactant-assisted route," *Journal of Molecular Structure*, vol. 1056–1057, pp. 285–291, 2014.
- [14] S. Kanagesan, M. Hashim, S. Tamilselvan, N. B. Alitheen, I. Ismail, and G. Bahmanrokh, "Cytotoxic effect of nanocrystalline MgFe_2O_4 particles for cancer cure," *Journal of Nanomaterials*, vol. 2013, Article ID 865024, 8 pages, 2013.
- [15] S. Hajarpour, K. Gheisari, and A. Honarbakhsh Raouf, "Characterization of nanocrystalline $\text{Mg}_{0.6}\text{Zn}_{0.4}\text{Fe}_2\text{O}_4$ soft ferrites synthesized by glycine-nitrate combustion process," *Journal of Magnetism and Magnetic Materials*, vol. 329, pp. 165–169, 2013.
- [16] L. Bih, M. Azrou, B. Manoun, M. P. F. Graça, and M. A. Valente, "Raman spectroscopy, X-Ray, SEM, and DTA analysis of alkali-phosphate glasses containing WO_3 and Nb_2O_5 ," *Journal of Spectroscopy*, vol. 2013, Article ID 123519, 10 pages, 2013.
- [17] Y. Zhang, J. Lin, and D. Wen, "Structure, infrared radiation properties and mössbauer spectroscopic investigations of $\text{Co}_{0.6}\text{Zn}_{0.4}\text{Ni}_x\text{Fe}_{2-x}\text{O}_4$ ceramics," *Journal of Materials Science and Technology*, vol. 26, no. 8, pp. 687–692, 2010.
- [18] M. Siddique and N. M. Butt, "Effect of particle size on degree of inversion in ferrites investigated by Mössbauer spectroscopy," *Physica B: Condensed Matter*, vol. 405, no. 19, pp. 4211–4215, 2010.

- [19] S. Kumar, A. M. M. Farea, K. M. Bato, C. G. Lee, B. H. Koo, and A. Yousef, "Mössbauer studies of $\text{Co}_{0.5}\text{Cd}_x\text{Fe}_{2.5-x}\text{O}_4$ (0.0–0.5) ferrite," *Physica B*, vol. 403, no. 19–20, pp. 3604–3607, 2008.
- [20] M. Gupta and B. S. Randhawa, "Mössbauer, magnetic and electric studies on mixed Rb-Zn ferrites prepared by solution combustion method," *Materials Chemistry and Physics*, vol. 130, no. 1–2, pp. 513–518, 2011.
- [21] W. Bayoumi, "Structural and electrical properties of zinc-substituted cobalt ferrite," *Journal of Materials Science*, vol. 42, no. 19, pp. 8254–8261, 2007.
- [22] M. V. Chaudhari, S. E. Shirsath, A. B. Kadam, R. H. Kadam, S. B. Shelke, and D. R. Mane, "Site occupancies of Co-Mg-Cr-Fe ions and their impact on the properties of $\text{Co}_{0.5}\text{Mg}_{0.5}\text{Cr}_x\text{Fe}_{2-x}\text{O}_4$," *Journal of Alloys and Compounds*, vol. 552, pp. 443–450, 2013.
- [23] X.-M. Liu and W.-L. Gao, "Preparation and magnetic properties of NiFe_2O_4 nanoparticles by modified pechini method," *Materials and Manufacturing Processes*, vol. 27, no. 9, pp. 905–909, 2012.
- [24] S. Thankachan, B. P. Jacob, S. Xavier, and E. M. Mohammed, "Effect of neodymium substitution on structural and magnetic properties of magnesium ferrite nanoparticles," *Physica Scripta*, vol. 87, no. 2, Article ID 025701, 2013.
- [25] Q. Lin, Z. Ye, C. Lei, H. Huang, Y. Xu, and Y. He, "Microstructure and magnetic research of NiCuZn ferrite by Co, Bi compound doped," *Materials Research Innovations*, vol. 17, no. 1, pp. 287–291, 2013.
- [26] V. Lilkov, O. Petrov, Y. Tzvetanova, P. Savov, and M. Kadiyski, "Mössbauer, XRD, and complex thermal analysis of the hydration of cement with fly ash," *Journal of Spectroscopy*, vol. 2013, Article ID 231843, 9 pages, 2013.
- [27] T. Jiao, Y. Wang, Q. Zhang et al., "Self-assembly and headgroup effect in nanostructured organogels via cationic amphiphilic-graphene oxide composites," *PLoS ONE*, vol. 9, no. 7, Article ID e101620, 2014.
- [28] J. Lin, Y. He, Q. Lin, R. Wang, and H. Chen, "Microstructural and Mössbauer spectroscopy studies of $\text{Mg}_{1-x}\text{Zn}_x\text{Fe}_2\text{O}_4$ ($x = 0.57, 0.7$) nanoparticles," *Journal of Spectroscopy*, vol. 2014, Article ID 540319, 5 pages, 2014.
- [29] M. J. Iqbal, Z. Ahmad, Y. Melikhov, and I. C. Nlebedim, "Effect of CuCr co-substitution on magnetic properties of nanocrystalline magnesium ferrite," *Journal of Magnetism and Magnetic Materials*, vol. 324, no. 6, pp. 1088–1094, 2012.
- [30] T. Jiao, Q. Huang, Q. Zhang, D. Xiao, J. Zhou, and F. Gao, "Self-assembly of organogels via new luminol imide derivatives: diverse nanostructures and substituent chain effect," *Nanoscale Research Letters*, vol. 8, article 278, 2013.

Research Article

Morphological Investigation of Calcium Carbonate during Ammonification-Carbonization Process of Low Concentration Calcium Solution

Huairang Cheng, Xiaoxi Zhang, and Huiping Song

Institute of Resources and Environment Engineering, State Environment Protection Key Laboratory of Efficient Utilization of Coal Waste Resources, Shanxi University, Taiyuan 030006, China

Correspondence should be addressed to Huiping Song; songhp@sxu.edu.cn

Received 15 July 2014; Accepted 5 August 2014; Published 2 September 2014

Academic Editor: Xinqing Chen

Copyright © 2014 Huairang Cheng et al. This is an open access article distributed under the Creative Commons Attribution License, which permits unrestricted use, distribution, and reproduction in any medium, provided the original work is properly cited.

Ultrafine calcium carbonate is a widely used cheap additive. The research is conducted in low degree supersaturation solution in order to study the polymorphic phases' change and its factors of the calcium carbonate precipitate in the ammonification-carbonization process of the solution with calcium. Fine particles of calcium carbonate are made in the solution containing 0.015 mol/L of Ca^{2+} . Over 98% of the calcium carbonate precipitate without ammonification resembles the morphology of calcite, while the introduction of ammonia can benefit the formation of vaterite. It was inferred that the main cause should be serious partial oversaturation or steric effects. Ammonia also helps to form the twin spherical calcium carbonate. However, particles formed in the process of ammonification-carbonization in solution with low concentration degree of calcium are not even with a scale of the particle diameter from 5 to 12 μm . Inorganic salts, alcohol, or organic acid salts have significant controlling effect on the particle diameter of calcium carbonate and can help to decrease the particle diameter to about 3 μm . Anionic surfactants can prevent the agglomeration of calcium carbonate particles and shrink its diameter to 500 nm–1 μm .

1. Introduction

Ultrafine calcium carbonate of nano- and submicron size is widely used as cheap additive in manufacturing plastic, rubber, varnish, ink, paper, paint, medicine, and other fields [1, 2]. Calcium carbonate and inorganic oxide have good affinity; therefore, it can be used as the model material [3, 4] to make inorganic hollow microsphere such as SiO_2 and TiO_2 . The reason why calcium carbonate can be so widely used is that it has a unique crystal structure and particle size.

Calcium carbonate has three kinds of crystal polymorphs [5], namely, spherical vaterite, aragonite in the shape of a needle, and rhomboidal calcite. The energy level decreases according to this order, while the stability increases. Calcium carbonate of calcite type can stay stable at room temperature, while those of vaterite and aragonite type with metastability are easier to be transformed into the calcite type. Spherical calcium carbonate is commonly used for its smoothness and fluidity. Usually, it is a porous structure and resembles

the clustering with microcrystal of nanosize (25–35 nm). Large amounts of expensive biological macromolecules, dendronized polymers, or compound additives as crystalline controller are used to form spherical calcium carbonate, and less cheap acid, alkali, and salt are used to control the crystal shape.

There are many ways to compose calcium carbonate including carbonization, precipitate method, and high gravity method. Carbonization refers to the method of adding CO_2 gas to suspension with Ca^{2+} and adding morph regulator to control the growing rate of each face of the crystal to achieve morphology control. Precipitate method is to mix the solution of Ca^{2+} and CO_3^{2-} to make calcium carbonate particles. High gravity method is to create the condition for the intensive mixing of liquid and raise the reaction rate of calcium carbonate with centrifugal force. Ultrafine calcium carbonate is mainly synthesized in liquid. Controlling the operation conditions, like temperature, pH, and

supersaturation, or adding crystalline regulator, it can influence nucleation, formation, and the final polymorph of calcium carbonate [6]. Commonly used crystalline regulators include chelating agent [7], organic compound [8, 9], inorganic salt, minerals, organic acid [10], alcohol, amino acid [11], and chitosan. The morphology of calcium carbonate can also be induced by biological factors [12]. From the dynamics perspective, mixed solution can help to form the crystal of metastability, for example, the mixture of alcohol and water. With ammonia, hexagonal calcium carbonate crystal can be formed by the self-assembly of vaterite nanoparticles. While in the reaction of CO₂ gas and CaCl₂ solution, ammonia can function to shape the CaCO₃ into spherical vaterite of metastability [13]. In addition, the spherical CaCO₃ after thermal decomposition becomes spherical CaO which can be used as catalyst in biodiesel or to manufacture the organic light-emitting diode. Magnesium also plays an important role in the precipitation of calcium carbonate. When the Mg²⁺ concentration degree is low, calcite is formed; when it is high, aragonite is formed.

Making ultrafine calcium carbonate, mix solution with Ca²⁺ and solution with CO₃²⁻ or add organic substance to regulate the mass transfer of Ca²⁺ and CO₃²⁻ to control nucleation and formation of crystal. What is more, CO₂ gas can be added to Ca(OH)₂ solution [14]. The method of the reaction of Ca(OH)₂ solution and CO₂ gas [15] is the major way for industrial ultrafine calcium carbonate making considering the production cost. However, in this method, Ca(OH)₂ solution can also be replaced by other solutions with Ca²⁺, such as CaCl₂ solution. The solution should be changed to alkaline in order to make the reaction with CO₂ happen faster, and the process of alkalization is usually achieved by using ammonia solution. Also, the method of adding ammonia and CO₂ gas to gypsum serum to make ammonia sulfate is to recycle the gypsum to solid wastes and has produced calcium carbonate as well. The common method of making calcium carbonate in existing findings is basically using solution with high concentration of Ca²⁺ as source of calcium, through which enough calcium carbonate can be obtained. However, solution with low concentration of Ca²⁺ is also worth being studied [16, 17]. The supersaturation degree will remain at a low level. Theoretically, in the system with low degree of supersaturation, the control of the morphology of calcium carbonate particles will be easier. In the process of formation and precipitation of crystal, the solution becomes supersaturated and the crystal nucleus is formed with the clashes of ions. Then the ions that constructed the crystal in the solution diffuse and precipitate on the surface of crystal nucleus, which is called the crystal nucleus growth. Crystal nuclei form crystal particles gradually, and particles concentrate and form crystal with orientation arrangement. If the supersaturation degree is too high, it is easy to form amorphous precipitate. With a low supersaturation degree, the growth velocity of crystal is slow, and the surface of crystal is well formed. When the supersaturation degree is too high, the reaction of Ca²⁺ and CO₃²⁻ will be too quick to control the crystal morphology. Thus, the control of reaction speed is usually achieved by controlling the concentration

of participating substances [18, 19]; for example, in the formation process of biological mineralization (such as the formation of shell), semipermeable membrane is used to control the release of Ca²⁺ or CO₃²⁻. It will function to control the crystal morphology of calcium carbonate.

The focus of this paper is to analyze the morphology of the calcium carbonate precipitate of low concentration degree and the way to control its morphology to infer the formation mechanism of calcium carbonate materials. It is of great importance to research on making nano- and submicron calcium carbonate materials in solutions with Ca²⁺, such as CaCl₂. It can also explain how solutions with low concentration of Ca²⁺, such as calcium sulfate, can form the calcium carbonate materials with unique morphology.

2. Experimental Details

Calcium carbonate precipitate is made by adding CO₂ gas to solution with Ca²⁺. Calcium sulfate saturated solution with about 0.015 mol/L of Ca²⁺ is used since it will be a proper concentration for the calcium carbonate precipitating. If we need a higher concentration of Ca²⁺, CaCl₂ solution is used. Since calcium sulfate or CaCl₂ solution is neutral, Ca²⁺ and CO₂ will not react. Thus, ammonia liquid is added to the solution as follows:



The reagents and additives used in this experiment include calcium sulfate, calcium chloride, sodium carbonate, sodium chloride, ammonia, alcohol, and sodium acetate, which are all analytical reagents (BOLT Tianjin Chemical Co., Ltd., China). A CO₂ cylinder (99.5% in purity) is used to provide carbon source. The anionic surfactant (Nafine Chemical Industry Group Co., Ltd., China) including sodium alkane sulfonate and poly(oxy-1,2-ethanediyl),a-sulfo-w-(dodecyloxy)-, sodium salt (1:1) which is usually used as a detergent is used to control the crystal morphology.

Scanning electron microscope (SEM, JEOL JSM-6701F, Japan) is applied to inspect the morphology of the formed calcium carbonate and X-ray powder diffraction (XRD, Bruker D2 Advance Phaser, Germany) to analyze its crystalline phase. When XRD is used to analyze the crystal morphology, lattice planes 104, 113, 202, 024, 116, 221, and 122 correspond to the diffraction peaks of crystal planes of the calcite, while 110, 112, 114, and 300 correspond to the diffraction peaks of crystal plane of vaterite. According to the literature [20], the proportion of vaterite (f_v) can be calculated as follows:

$$f_v = \frac{(I_{110v} + I_{112v} + I_{114v})}{(I_{110v} + I_{112v} + I_{114v} + I_{104c})}, \quad (2)$$

where I is the intensity of diffraction peak, the subscript v represents the vaterite, and c represents calcite.

3. Results and Discussion

3.1. Influence of Ammonia on the Crystal Phase of Calcium Carbonate. To investigate the influence of ammonia on

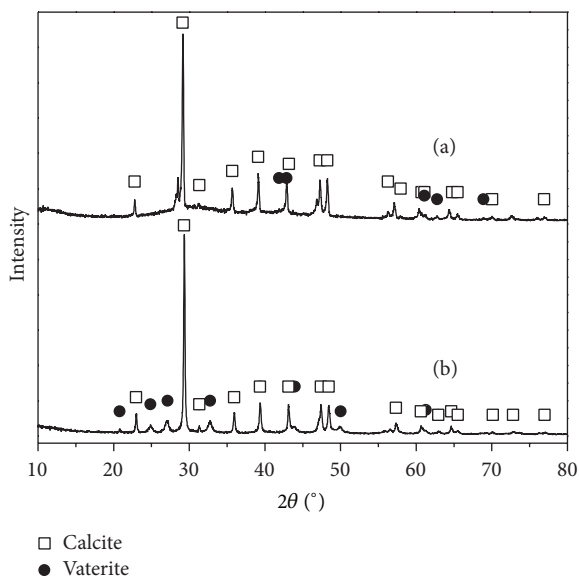


FIGURE 1: Crystal phase of calcium carbonate precipitate. (a) Solutions: CaCl_2 , 0.18 mol/L; Na_2CO_3 , 0.18 mol/L. (b) Solutions: CaCl_2 , 0.13 mol/L; NH_3 , 0.74 mol/L. CO_2 gas: 60 ml/min \times 20 min.

crystal polymorphs of calcium carbonate precipitate, the XRD spectra of calcium carbonate obtained in two reaction systems, one with ammonia and the other without, were compared, as shown in Figure 1. The calcium carbonate obtained by mixing calcium chloride and sodium carbonate solutions is shown in Figure 1(a). Figure 1(b) is the calcium carbonate obtained by mixing calcium sulfate solution with ammonia liquid and CO_2 gas. The concentration degrees of Ca^{2+} of two experiments are similar.

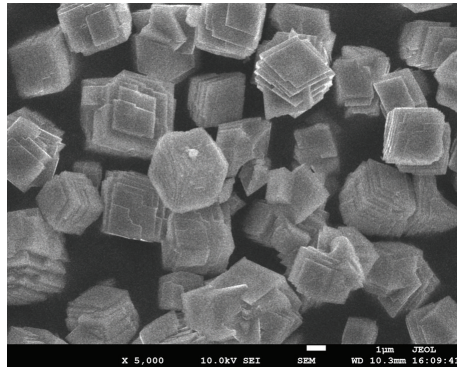
Figure 1(a) shows that when ammonia is not added, calcite is the major crystal morphology of calcium carbonate precipitate, containing a little crystal morphology of vaterite. According to (2), the proportion of calcite is 98.52%, while the remaining 1.48% is the vaterite, in terms of their total amount. When ammonia is added to the solution, the characteristic peak of vaterite is intensified, as shown in Figure 1(b). The precipitate at this time contains crystal morphology of both calcite and vaterite and a little aragonite. The calculation in (2) shows that the proportion of calcite reaches 87.83% of the total amount of calcite and vaterite, while the rest 12.17% is vaterite. It shows that adding ammonia functions to form vaterite.

When ammonia is used to form calcium carbonate precipitate, the pH is controlled between 8 and 11 [13], which is the interval to form spherical vaterite steadily. The reaction process includes CO_2 dissolving in water, ammonia and water forming NH_4^+ , and OH^- , CO_2 , and OH^- forming HCO_3^- . Finally, CO_3^{2-} is formed, and calcium carbonate is formed with Ca^{2+} and CO_3^{2-} . In this process, the speed controlling step is the formation of HCO_3^- . Supersaturation degree of calcium carbonate around the CO_2 gas bubbles is very high, which provides condition to create the new solid particles. When degree of supersaturation is maintained at a relatively high value, new vaterite will form its nucleus around the

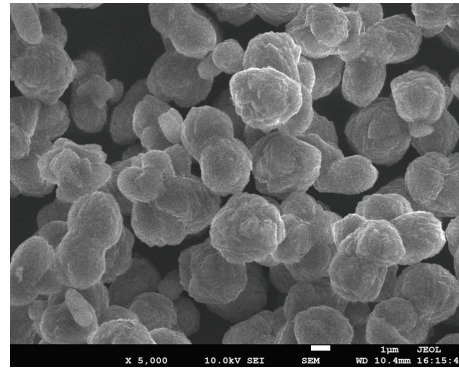
CO_2 bubbles. The dense nucleation of vaterite prevents it from dissolving and renucleation and prevents the growth of more stable calcite crystal. High degree of supersaturation can benefit to form the metastable vaterite in the dynamics perspective and stop it from transforming into calcite. The supersaturation degree can be achieved with high pH since when pH is high, the speed of dissolving CO_2 and forming CO_3^{2-} is fast, which can be achieved by adding ammonia. Thus, when ammonia exists in solution, it is easy to form calcium carbonate precipitate with crystal morphology of vaterite.

3.2. Influence of Ammonia on the Morphology of Calcium Carbonate Precipitate. Figure 2 shows, under different operation, ammonia has impact on the morphology of calcium carbonate precipitate. Figure 2(a) indicates that when solutions with Ca^{2+} and CO_3^{2-} are mixed, the calcium carbonate precipitate is cubic, which is the morphology of calcite. After ammonia is added, as shown in Figure 2(b), the precipitate embodies the rough spherical shape, ellipsoidal shape, and twin spherical shape. On the one hand, the reason can be that ammonia raised the supersaturation degree of calcium carbonate to form spherical calcium carbonate. On the other hand, the amount of Ca^{2+} and CO_3^{2-} decreased as the reaction went on, and degree of supersaturation decreases, which makes spherical calcium carbonate tends to form more stable cube. Thus, the crystal manifests the topograph of calcite, and edges and corners become sharper. These two conditions affect each other. As a result, the calcium carbonate precipitate shows the rough spherical morphology. Meanwhile, it is assumed that calcium carbonate particles in the solution form cubic or spindle-shaped crystal nucleus. The crystal nuclei have high surface energy in the direction of edge and corner. With the steric effect of ammonia, partial Ca^{2+} and CO_3^{2-} at the edge and corner direction concentrate and grow quickly, and partial degree of supersaturation is very high. Many small crystal particles formed in the process of nucleation. Particles formed twin spherical calcium carbonate by combining themselves to achieve the minimization of surface area.

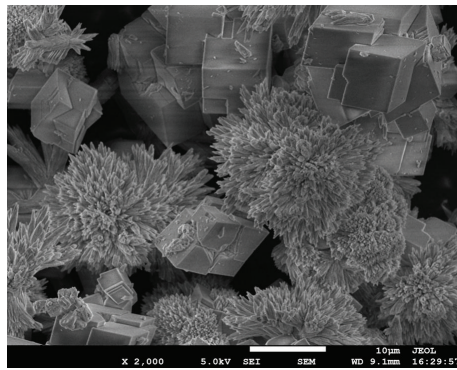
Figures 2(c) and 2(d) show another growth type of crystal. It is in the system of Ca^{2+} solution and CO_2 gas bubbles. Since CO_2 gas is continuously added to the solution, the degree of supersaturation in the reaction will not be decreased and can be maintained at a certain level. When the amount of ammonia is small and cannot maintain the degree of supersaturation at the level of producing vaterite, the calcium carbonate includes cube and needle-cluster shape. When the amount of ammonia is big, most of the calcium carbonate precipitate is spherical, which shows that ammonia has influence on the topograph of calcium carbonate. It means that ammonia can help the calcium carbonate to precipitate in the morphology of vaterite. In most cases, it is well known that the calcium carbonate tends to form the stable cube shape. Therefore, the needle-cluster calcium carbonate may be assumed to be the transition morphology between the cubic and spherical shape under the effect of ammonia.



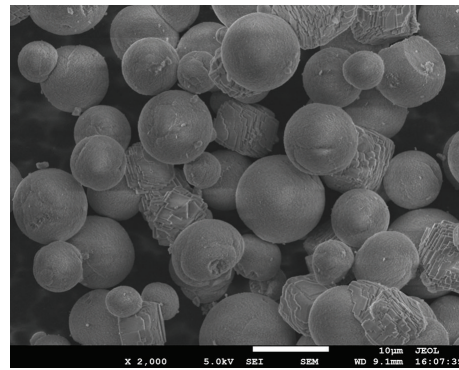
(a) Solutions: CaCl_2 , 0.18 mol/L; Na_2CO_3 , 0.18 mol/L



(b) Solutions: CaCl_2 , 0.18 mol/L; Na_2CO_3 , 0.18 mol/L; NH_3 , 3.39 mol/L



(c) Solutions: NH_3 , 0.36 mol/L; CaSO_4 , 0.15 mol/L. CO_2 gas: 60 mL/min \times 20 min



(d) Solutions: NH_3 , 1.47 mol/L; CaSO_4 , 0.15 mol/L. CO_2 gas: 60 mL/min \times 20 min

FIGURE 2: Morphology of calcium carbonate precipitate with and without ammonification.

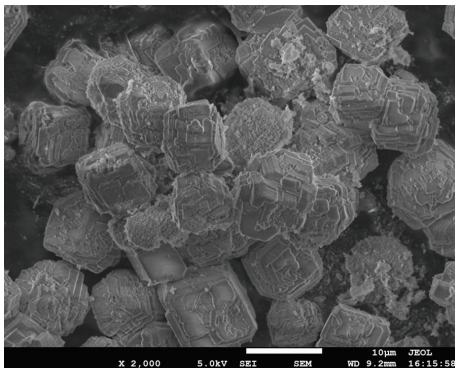
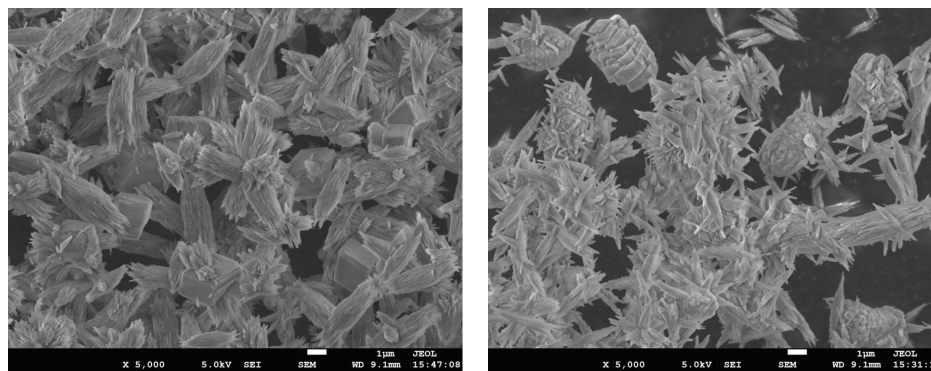


FIGURE 3: Morphology of calcium carbonate precipitate. Solutions: CaSO_4 , 0.15 mol/L. CO_2 gas: 55 mL/min \times 20 min. Final pH = 10.

Figure 3 shows the precipitate of calcium carbonate in another reaction system. Constantly adding CO_2 in the saturated solution of calcium sulfate until pH decreases from 7 to 4.6 and adding ammonia liquid and controlling the pH of the solution at 10, the precipitate of the calcium carbonate is shown in Figure 3. Before adding ammonia liquid, the Ca^{2+} , SO_4^{2-} , and H_2CO_3 will not react. After adding ammonia, calcium carbonate precipitate and ammonia sulfate are formed instantly. The reason inferred is

that the degree of supersaturation became high suddenly. Therefore, the crystal morphology is the spherical vaterite. However, without new supplementing CO_2 , the amount of Ca^{2+} and H_2CO_3 decreased as the reaction went on, and the degree of supersaturation is decreased as well. The shape of vaterite gradually transforms into calcite. Figure 3 shows the intermediate state of spherical crystal morphology transforming into cubic crystal morphology, and the comparison with Figure 2(a) explains that the effect of ammonia in the calcium carbonate crystal growing process is to accelerate the precipitate into spherical morphology.

The ultrasound usually has an influence on the precipitation of calcium carbonate [21]. Ultrasound can make the suspended particles dispersed and has a role in preventing the formation of large particles precipitated. Therefore, under the effect of ultrasound, the precipitate formed will be relatively small. With the interference of ultrasound, we can see clearer the effect of ammonia on shaping particle morphology of precipitate. Without ammonia, calcium carbonate precipitate with ultrasound shows the cubic and spindle-shaped morphology, like in Figure 4(a). Figure 4(b) indicates that when increasing the amount of ammonia, ammonia accelerates the transformation of cubic calcium carbonate particles into rough spherical morph and egg-shaped morphology, as shown in Figure 4(a). Apparently, the surface is a bit sharp, which means the formation still



(a) Solutions: NH_3 , 1.47 mol/L; CaSO_4 , 0.15 mol/L. CO_2 gas: 1560 mL/min \times 20 min. CO_2 (v%) = 3.88%

(b) Solutions: NH_3 , 3.39 mol/L; CaSO_4 , 0.15 mol/L. CO_2 gas: 1560 mL/min \times 20 min. CO_2 (v%) = 3.88%

FIGURE 4: Morphology of calcium carbonate precipitate under ultrasound.

obeys the rule of forming calcite, while the look is more like a sphere. Ammonia can influence the morphology of calcium carbonate precipitate developing into sphere. Apart from increasing the degree of supersaturation, steric effect may be used to accelerate the spherical formation of calcium carbonate.

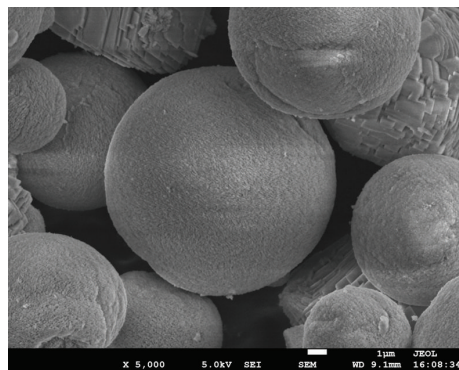
3.3. Controlling the Morphology of Calcium Carbonate by Electrolyte and Surfactant. With different types of electrolyte, ammonia can have different effects on calcium carbonate particles, as shown in Figures 5(a) and 5(b). When adding inorganic salt to increase the ion strength, morphology of calcium carbonate particles has two conspicuous changes. First, the diameter decreases from 5~12 μm to 5 μm . Second, clustering of particles and twin spherical polymorph appear. Figures 5(c) and 5(d) show that, by adding alcohol and organic acid and salt, the diameter of calcium carbonate particles decreases to about 3 μm and the clustering effect becomes more conspicuous. In Figure 5(e), the anionic surfactant can decrease the diameter of calcium carbonate particles to 500 nm~1 μm .

In most of the conditions, calcium carbonate in calcite crystal type shows the spindle-shaped and cubic polymorph, while the vaterite type resembles the spherical shape. In the formation process of calcium carbonate, calcite is the stable crystal polymorph. Thus, the crystal grows into the prism shaped calcite without additives. Sphere is shaped since the ions have different effects in the electrolyte or the additives have large steric effect to deter the growth of calcium carbonate crystal. According to the dynamics of crystal growing, the nucleation rate of calcium carbonate is positive to the degree of supersaturation. Adding dissolvable salt can cause the salt effect to increase supersaturation degree of calcium carbonate. The critical dimension of particle nucleus and energy required in the nucleation process are decreased, while the nucleation rate increases. The rates of nucleation and growth are of competing relation, which means when the nucleation rate is high, the growth rate is low. On a macrolevel, the particle diameter decreases and, meanwhile, the gradient of concentration increases when the degree of supersaturation is high. Clustering or other polymorphs will

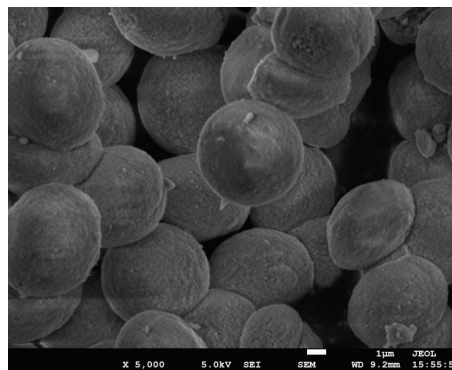
be shaped since corners and edges of the crystal have larger areas than the center of the surface to take the accumulation of mass points. That is why in Figure 5 adding inorganic salt, alcohol, and organic acid salt, the particle diameter and polymorph of calcium carbonate will change significantly. In addition, the surfactant can change the surface state of the solution system and make the indissoluble particles disperse. In terms of Figure 5(e), the interaction of surfactant and Ca^{2+} helps the nucleation of vaterite in supersaturation solution and stops the growth and clustering of calcium carbonate particles. Thus, the diameter is shrunk.

4. Conclusion

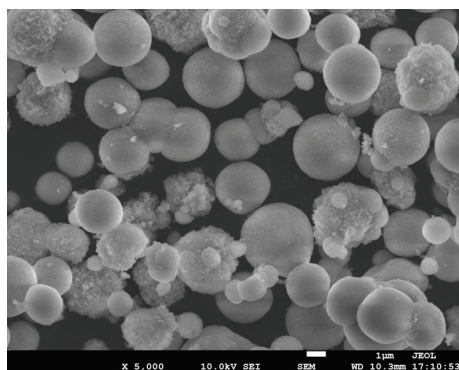
In the solution of low degree of concentration with about 0.015 mol/L Ca^{2+} and under the condition of low degree of supersaturation, ammonification and carbonization methods are applied to make ultrafine particles of calcium carbonate. With low degree of supersaturation, the reaction rates of Ca^{2+} and CO_3^{2-} are not that quick, so that it is expected to be easy to control the crystal polymorph. When the reaction system does not include ammonia, the precipitate of calcium carbonate is mainly of the crystal morphology of calcite and a little crystal morphology of vaterite. The proportion of calcite will be over 98%. Adding ammonia to the solution helps to form the vaterite, and the precipitate of calcium carbonate is the mixture of calcite and vaterite. At the same time, a little aragonite is also formed. The influence of ammonia on crystal morphology of calcium carbonate precipitate is achieved by creating great partial degree of supersaturation. Ultrasound can also be applied to infer that ammonia can form calcium carbonate into spherical shape with steric effect. In addition, with forming the cubic or spindle-shaped crystal nucleus of calcium carbonate in the solution, ammonia can also function to concentrate partial Ca^{2+} and CO_3^{2-} at the edge and corner direction and form the twin spherical calcium carbonate. Without other additives, the calcium carbonate formed is with a diameter of about 5~12 μm . Inorganic salt, alcohol, or organic acid and salt can have significant effect on controlling the particle diameter of calcium carbonate and will trigger salt effect, which increases the degree of supersaturation of



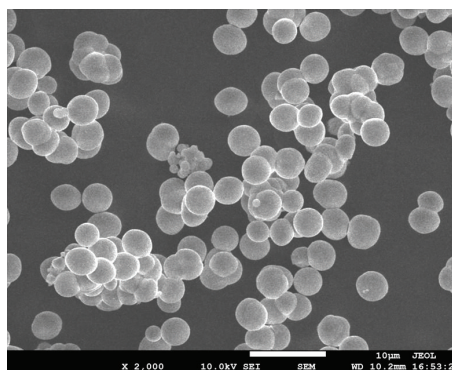
(a) Solutions: NH_3 , 1.47 mol/L; CaSO_4 , 0.15 mol/L. CO_2 gas: 55 mL/min \times 20 min



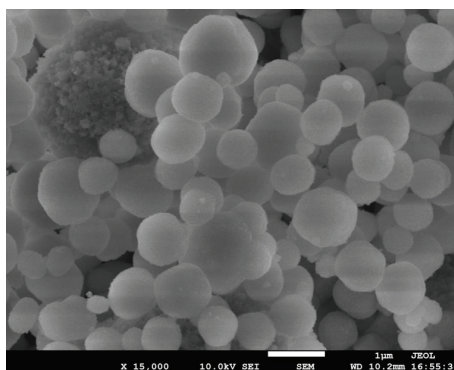
(b) Solutions: NH_3 , 1.47 mol/L; CaSO_4 , 0.15 mol/L; NaCl , 1.65 mol/L. CO_2 gas: 55 mL/min \times 20 min



(c) Solutions: NH_3 , 0.29 mol/L; CaSO_4 , 0.15 mol/L; $\text{CH}_3\text{CH}_2\text{OH}$, 1.72 mol/L. CO_2 gas: 40 mL/min \times 20 min



(d) Solutions: NH_3 , 0.29 mol/L; CaSO_4 , 0.15 mol/L; CH_3COONa , 1.21 mol/L. CO_2 gas: 40 mL/min \times 20 min



(e) Solutions: NH_3 , 0.29 mol/L; CaSO_4 , 0.15 mol/L; anionic surfactant, 2 mL/L. CO_2 gas: 40 mL/min \times 20 min

FIGURE 5: Morphology of calcium carbonate precipitate with different additives.

calcium carbonate and shrinks its size to about $3\ \mu\text{m}$. What is more, clustering occurs and the anionic surfactant can deter the clustering of calcium carbonate particles and shrink its size to $500\ \text{nm}\sim 1\ \mu\text{m}$.

Conflict of Interests

The authors declare that they have no financial and personal relationships with other people or organizations that can inappropriately influence their works; there is no professional

or other personal interest of any nature or kind in any product, service, and/or company that could be construed as influencing the position presented in, or the review of, the paper.

Acknowledgments

This work was financially supported by National Natural Science Foundation of China (51104097), the National Key Technology R&D Program (2013BAC14B05), the Provincial

Research Projects (2012021010-2, 20120313014-1), and the Program of International Science and Technology Cooperation (2012DFA91500).

References

- [1] T. Sasaki, H. Mizuuchi, and K. Sakurai, "Chitosan derivatives/calcium carbonate composite capsules prepared by the layer-by-layer deposition method II stabilization of the shell by crosslinking," *Journal of Nanomaterials*, vol. 2011, Article ID 476752, 7 pages, 2011.
- [2] C. Aniruddha and M. Satyendra, "Nano-Calcium carbonate (CaCO_3)/Polystyrene (PS) core-shell nanoparticle: its effect on physical and mechanical properties of high impact polystyrene (HIPS)," *Journal of Polymer Research*, vol. 20, article 249, pp. 10–1007, 2013.
- [3] J. P. Paques, L. M. C. Sagis, C. J. M. van Rijn, and E. van der Linden, "Nanospheres of alginate prepared through w/o emulsification and internal gelation with nanoparticles of CaCO_3 ," *Food Hydrocolloids*, vol. 40, pp. 182–188, 2014.
- [4] V. Parakhonskiy Bogdan, M. Yashchenok Alexey, K. Manfred, and G. Skirtach Andre, "Colloidal micro- and nano-particles as templates for polyelectrolyte multilayer capsules," *Advances in Colloid and Interface Science*, vol. 207, pp. 253–264, 2014.
- [5] A. Shafiu Kamba, M. Ismail, T. A. Tengku Ibrahim, and Z. A. B. Zakaria, "Synthesis and characterisation of calcium carbonate aragonite nanocrystals from cockle shell powder (Anadara granosa)," *Journal of Nanomaterials*, vol. 2013, Article ID 398357, 9 pages, 2013.
- [6] W. Li, W.-S. Chen, P.-P. Zhou, L. Cao, and L.-J. Yu, "Influence of initial pH on the precipitation and crystal morphology of calcium carbonate induced by microbial carbonic anhydrase," *Colloids and Surfaces B: Biointerfaces*, vol. 102, pp. 281–287, 2013.
- [7] S. P. Gopi and V. K. Subramanian, "Polymorphism in CaCO_3 —effect of temperature under the influence of EDTA (di sodium salt)," *Desalination*, vol. 297, pp. 38–47, 2012.
- [8] S. Kirboga and M. Öner, "Application of experimental design for the precipitation of calcium carbonate in the presence of biopolymer," *Powder Technology*, vol. 249, pp. 95–104, 2013.
- [9] A. Verch, I. E. G. Morrison, R. V. D. Loch, and R. Kröger, "In situ electron microscopy studies of calcium carbonate precipitation from aqueous solution with and without organic additives," *Journal of Structural Biology*, vol. 183, no. 2, pp. 270–277, 2013.
- [10] S. Bai, G. Naren, M. Nakano, Y. Okaue, and T. Yokoyama, "Effect of polysilicic acid on the precipitation of calcium carbonate," *Colloids and Surfaces A: Physicochemical and Engineering Aspects*, vol. 445, pp. 54–58, 2014.
- [11] B. Njegić-Džakula, G. Falini, L. Brečević, Ž. Skoko, and D. Kralj, "Effects of initial supersaturation on spontaneous precipitation of calcium carbonate in the presence of charged poly-L-amino acids," *Journal of Colloid and Interface Science*, vol. 343, no. 2, pp. 553–563, 2010.
- [12] W. Li, L. Liu, W. Chen, L. Yu, W. Li, and H. Yu, "Calcium carbonate precipitation and crystal morphology induced by microbial carbonic anhydrase and other biological factors," *Process Biochemistry*, vol. 45, no. 6, pp. 1017–1021, 2010.
- [13] M.-A. Popescu, R. Isopescu, C. Matei, G. Fagarasan, and V. Plesu, "Thermal decomposition of calcium carbonate polymorphs precipitated in the presence of ammonia and alkylamines," *Advanced Powder Technology*, vol. 25, pp. 500–507, 2014.
- [14] Y. Liang, G. Chu, J. Wang et al., "Controllable preparation of nano- CaCO_3 in a microporous tube-in-tube microchannel reactor," *Chemical Engineering and Processing: Process Intensification*, vol. 79, pp. 34–39, 2014.
- [15] J.-H. Bang, Y. N. Jang, W. Kim et al., "Precipitation of calcium carbonate by carbon dioxide microbubbles," *Chemical Engineering Journal*, vol. 174, no. 1, pp. 413–420, 2011.
- [16] K. Song, Y.-N. Jang, W. Kim et al., "Precipitation of calcium carbonate during direct aqueous carbonation of flue gas desulfurization gypsum," *Chemical Engineering Journal*, vol. 213, pp. 251–258, 2012.
- [17] K. Song, Y. N. Jang, W. Kim, and et al, "Factors affecting the precipitation of pure calcium carbonate during the direct aqueous carbonation of flue gas desulfurization gypsum," *Energy*, vol. 65, pp. 527–532, 2014.
- [18] W. Li, W.-S. Chen, P.-P. Zhou, S.-L. Zhu, and L.-J. Yu, "Influence of initial calcium ion concentration on the precipitation and crystal morphology of calcium carbonate induced by bacterial carbonic anhydrase," *Chemical Engineering Journal*, vol. 218, pp. 65–72, 2013.
- [19] I. A. Bundeleva, L. S. Shirokova, O. S. Pokrovsky et al., "Experimental modeling of calcium carbonate precipitation by cyanobacterium *Gloeocapsa sp.*," *Chemical Geology*, vol. 374–375, pp. 44–60, 2014.
- [20] Y. Sheng Han, G. Hadiko, M. Fuji, and M. Takahashi, "Crystallization and transformation of vaterite at controlled pH," *Journal of Crystal Growth*, vol. 289, no. 1, pp. 269–274, 2006.
- [21] A. Stoica-Guzun, M. Stroescu, S. Jinga, I. Jipa, T. Dobre, and L. Dobre, "Ultrasound influence upon calcium carbonate precipitation on bacterial cellulose membranes," *Ultrasonics Sonochemistry*, vol. 19, no. 4, pp. 909–915, 2012.

Research Article

Gold Nanoparticles: Synthesis, Stability Test, and Application for the Rice Growth

Aiwu Wang,^{1,2,3} Hoi Pong Ng,² Yi Xu,² Yuyu Li,² Yuhong Zheng,¹ Jingping Yu,¹
Fugui Han,¹ Feng Peng,¹ and Li Fu⁴

¹ Institute of Botany, Jiangsu Province and Chinese Academy of Sciences,
Nanjing Botanical Garden, Memorial Sun Yat-Sen, Nanjing 210014, China

² Department of Physics and Materials Science and Centre for Functional Photonics (CFP), City University of Hong Kong,
88 Tat Chee Avenue, Kowloon, Hong Kong

³ Faculty of Science and Technology, University of Macau, Macau

⁴ Department of Chemistry and Biotechnology, Faculty of Science, Engineering and Technology, Swinburne University of Technology,
Hawthorn, VIC 3122, Australia

Correspondence should be addressed to Yuhong Zheng; friend266@163.com

Received 8 July 2014; Accepted 10 August 2014; Published 2 September 2014

Academic Editor: Tifeng Jiao

Copyright © 2014 Aiwu Wang et al. This is an open access article distributed under the Creative Commons Attribution License, which permits unrestricted use, distribution, and reproduction in any medium, provided the original work is properly cited.

In today's science, with the use of nanotechnology, nanomaterials, which behave very differently from the bulk solid, can be made. One of the capable uses of nanomaterials is bioapplications which make good use of the specific properties of nanoparticles. However, since the nanoparticles will be used both *in vivo* and *in vitro*, their stability is an important issue to the scientists, concern. In this dissertation, we are going to test the stability of gold nanoparticles in a number of media including the biocompatible medium and their behaviors will be illustrated in terms of optical properties change and aggregation degree. Herein, we report the synthesis of gold nanoparticles of different shapes and applications for the rice growth with significant difference. The gold nanoparticles can inhibit the elongation of rice root without inhibiting the germination of rice seeds.

1. Introduction

Gold nanoparticles (AuNPs) are also called colloidal gold or gold colloids. Similar to semiconductors, when metals decrease their size from bulk to the nanoscale, they also experience quantum confinement effect [1]. The conduction band electrons of the metal nanoparticles will resonate with the electromagnetic field, that is, light, and hence cause light absorption; this phenomenon is known as surface plasmon resonance [2–5]. Surface plasmon resonance was explained by Mie in 1908 [6]. However, at that time, Mie's theory could only be applied on metal nanoparticles which are much smaller than wavelength of light (about 25 nm) due to the assumption of the theory. The theory shows that plasmon absorption is size independent [7–9]. By the full expression of Mie's theory, it can be applied to large metal nanoparticles (>25 nm) and

can show size dependence of plasmon absorption [10–13].

Since the plasmon absorption maximum of AuNPs is size dependent [14–19], by tuning their size, their absorption maximum and color can be tuned.

Although gold is one of the most stable elements in the world, when AuNPs with diameter smaller than 5 nm are deposited on select metal oxides, they exhibit extraordinary selectivities and/or activities in some reactions such as combustion of carbon monoxide and saturated hydrocarbons [20] which show catalytic property.

In the presence of light, the conduction band electrons of AuNPs oscillate due to surface plasmon resonance. The oscillating electrons interact with the crystal lattice of AuNPs and transfer thermal energy to the lattice. Thus, AuNPs are heated up and can further dissipate their thermal energy to the surrounding medium to achieve the heating effect [21].

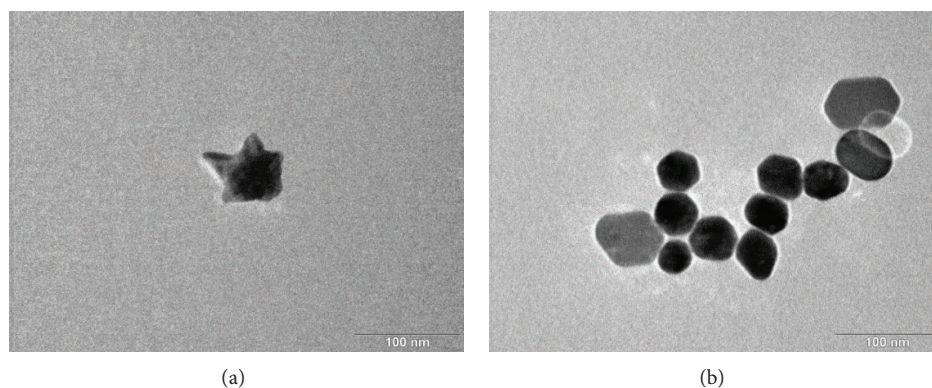


FIGURE 1: (a) TEM image of CTAB AuNPs. (b) TEM image of citrate AuNPs.

2. Experimental Parts

2.1. Synthesis of Citrate Gold Nanoparticles. First, 25 mL of water and a magnetic stir bar were added into a flask and the flask was placed on stirrer and heated to 100°C. Second, 52.4 mg of HAuCl_4 was weighed in a dry 100 mL flask and was placed on a stirrer. Then, 75 mL of water was added and the gold salt was dissolved under stirring. After all of the gold salt was dissolved, 10 mL of the solution was poured into the hot water flask. Next, citrate stock solution was prepared by dissolving 506.3 mg $\text{Na}_3\text{C}_6\text{H}_5\text{O}_7 \cdot 2\text{H}_2\text{O}$ in 75 mL of Milli-Q water. After the gold solution was boiled, 4 mL of citrate stock solution was added and the solution was boiled for 1.5 hours. After 1.5 hours, the flask was put onto a table and we waited till it cools down. Finally, the solution was stored in a 50 mL test tube at room temperature without any special treatment.

2.2. Synthesis of CTAB Gold Nanoparticles. First, 100 mL of 0.1 M CTAB, 10 mL of 0.01 M HAuCl_4 , 5 mL of 0.1 M of ascorbic acid, and 10 mL of 0.01 M of AgNO_3 solution were prepared. The CTAB solution was heated to 30°C in a water bath. Then, 3 mL of 0.1 M CTAB was added into a test tube. 1.748 mL of Milli-Q water, 200 μL HAuCl_4 , and 32 μL ascorbic acid were added one by one. The solution was mixed gently after each addition. Next, 20 μL of 0.01 M silver nitrate was added into the test tube and we waited for 4 seconds before gently mixing it. After the solution was prepared, it was placed inside a 30°C water bath and we waited for 3 hours for complete reaction. Finally, the solution was washed twice by centrifuging at 4500 rpm for 5 min each time and then it was stored at room temperature.

3. Results and Discussion

From Figure 1(a), we can observe that the CTAB AuNPs are star shaped with the longest dimension in between 80 and 90 nm. So it is expected that we can observe two peaks or one peak and one shoulder from the absorption spectra.

Figure 1(b) shows that the citrate AuNPs are almost spherical in shape with the diameter from about 30 to 50 nm. The larger, brighter, and irregular shaped particles on the left hand side should be the precipitated citrate.

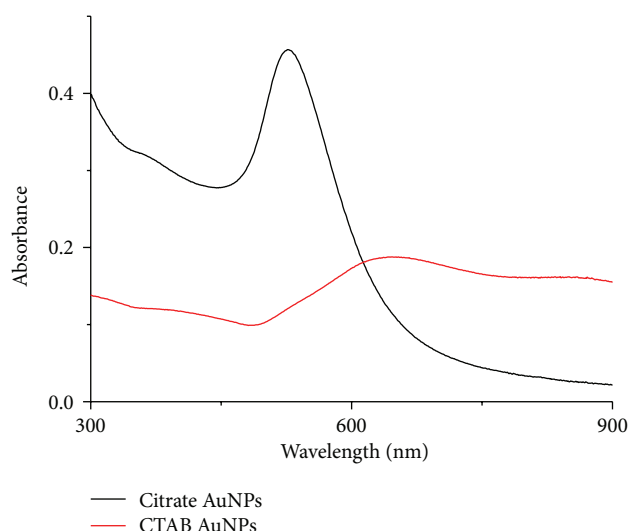


FIGURE 2: Absorption spectra of citrate and CTAB AuNPs.

From Figure 2, we can observe that citrate AuNPs have a peak and a shoulder while citrate AuNPs only have one peak.

3.1. Stability of CTAB AuNPs in Different Media. Table 1 showed the absorption peak position and intensity of CTAB AuNPs.

3.1.1. CTAB AuNPs in Milli-Q Water and Biobuffer. The absorption intensities of CTAB AuNPs in both Milli-Q water and biobuffer are very stable within the time of inspection. And their absorption peak positions were very stable too. These mean that CTAB AuNPs were very stable in both Milli-Q water and biobuffer.

3.1.2. CTAB AuNPs in pH 4, pH 7, pH 8, and pH 10 Buffers. CTAB AuNPs behave similarly in pH 4, pH 7, pH 8, and pH 10 buffers. They showed a rapid drop in absorption intensities in the first 15 minutes and decreased slowly afterwards. Meanwhile, their absorption peak positions also demonstrated a blue shift in the first 15 minutes and remained unchanged up

TABLE 1: Absorption peak position and intensity variation of CTAB AuNPs with time in different media.

	Hour	Position 1	Position 2	Intensity 1%	Intensity 2%
Water	0	639	840—	100	100
	0.25	639	840—	100	100
	0.5	639	840—	100	100
	1	639	840—	100	100
	2	639	840—	100	100
	72	639	840—	94	93
	168	639	840—	102	102
pH 4 buffer	0	640	852.2—	90	104
	0.25	617	852.2—	63	87
	0.5	617	852.2—	57	79
	1	617	852.2—	53	73
	2	617	852.2—	48	66
	72	640—	852.2—	7	9
	168	640—	852.2—	25	29
pH 7 buffer	0	623	851	80	98
	0.25	620	851—	57	74
	0.5	620	851—	53	67
	1	620	851—	50	63
	2	620	851—	44	57
	72	623—	851—	1	2
	168	623—	851—	14	16
pH 8 buffer	0	629	850	84	105
	0.25	607	850—	56	78
	0.5	607	850—	52	70
	1	607	850—	48	65
	2	607	850—	43	60
	72	629—	850—	1	1
	168	629—	850—	18	21
pH 10 buffer	0	631	836	90	97
	0.25	611	836—	53	71
	0.5	611	836—	47	64
	1	611	836—	42	53
	2	611	836—	36	48
	72	631—	836—	2	2
	168	631—	836—	17	21
Biobuffer	0	560	584	61	68
	0.25	560	585	60	67
	0.5	560	586	60	66
	1	560	587	59	67
	2	560	588	59	67
	3	560	588	59	67
	72	560	584—	59	65
168	560	584—	57	64	

**For the number with “—” behind means no clear peak can be observed and we measure the intensity at that wavelength.

to 2 hours. Subsequently, their absorption intensities dropped to a few intensity percentages and no peaks can be observed at the third day. However, their absorption intensities increased again at the seventh day; this may be because the CTAB

AuNPs form larger aggregates than those at the third day; therefore, scattering of the CTAB AuNPs increased. These represented that CTAB AuNPs are not stable in pH 4, pH 7, pH 8, and pH 10 buffers.

TABLE 2: Zeta potential and size of citrate AuNPs in Milli-Q water.

Time (hour)	Zeta potential (mV)	Zeta potential (mV) (second measure)	Size 1 (nm)	Size 2 (nm)
0	-27.5	—	5.6	50.8
1	-16.1	—	5.6	50.8
2	-19.0	—	5.6	50.8
3	-17.1	-32.2	5.6	50.8
24	-37.5	—	5.6	50.8
72	-33.4	—	5.6	50.8
168	-39.9	—	5.6	50.8

“—” means no measurement has been done.

To sum up, CTAB AuNPs were very stable in Milli-Q water and biobuffer; this indicated that they can be used for bioapplications. But they were unstable in pH 4, pH 7, pH 8, and pH 10 buffers.

3.2. Stability of Citrate AuNPs in Different Media. Citrate has a shorter carbon length than CTAB. As there is no big difference in peak position, only the absorption peak intensity variation was shown in Figure 3.

3.2.1. Citrate AuNPs in Milli-Q Water and Biobuffer. We can observe that the absorption peak intensities of citrate AuNPs in Milli-Q water and biobuffer were very stable within the period of inspection. And their absorption peak position in Milli-Q water and biobuffer was always the same in the experimental time. These represented that citrate AuNPs were very stable in Milli-Q water and biobuffer.

3.2.2. Citrate AuNPs in pH 4, pH 7, and pH 10 Buffers. Citrate AuNPs perform similarly in pH 4, pH 7, and pH 10 buffers. All of them showed fast drop in absorption peak intensity in the first 15 minutes and then dropped slowly thereafter. At the fourth day, they only have about 5% absorption peak intensity. Moreover, the absorption peak position of pH 4 buffer showed small red shift from 524 nm at 0 minutes to 533 nm at 2 hours which may be because of the increase in aggregate size and showed a large blue shift to 507 nm at the fourth day; this may be due to the degradation of citrate AuNPs which have a smaller size than their size at 0 minutes. But the absorption peak positions of citrate AuNPs in pH 7 and pH 10 buffers were almost the same within the first 2 hours and then no peaks can be found afterwards. These phenomena mean that citrate AuNPs are unstable in pH 4, pH 7, and pH 10 buffers.

3.2.3. Citrate AuNPs in pH 8 Buffer. The absorption peak intensity of citrate AuNPs in pH 8 buffer decreases slowly within the first 2 hours and then drops to about 40% intensity thereafter. And their absorption peak position was almost the same with the experimental time. Thus, they are unstable in pH 8 buffer in terms of absorption peak intensity.

To sum up, citrate AuNPs were very stable in Milli-Q water and biobuffer which made them able to be used for bioapplications. But they were unstable in pH 4, pH 7, pH 8,

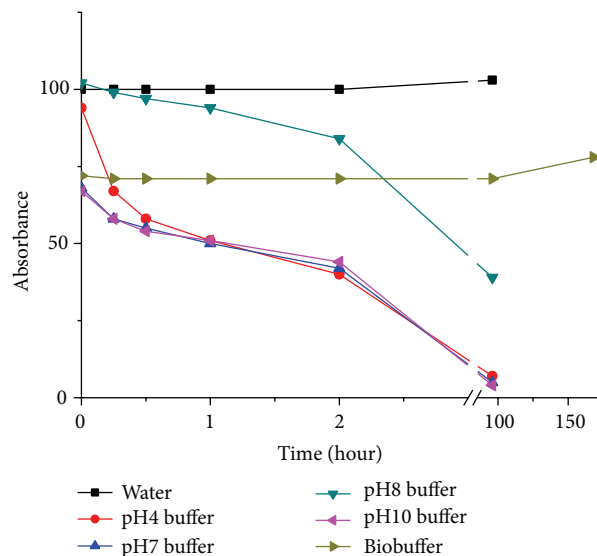


FIGURE 3: Absorption peak intensity of citrate AuNPs in different media varies with time.

and pH 10 buffers. Compared with the first absorption peak of CTAB AuNPs, both of them showed similar behavior for all buffers, that is, being unstable in pH 4, pH 7, pH 8, and pH 10 buffers but very stable in Milli-Q water and biobuffer, which allows them to be used for bioapplications.

3.3. Zeta Potential and Size of Citrate AuNPs. For the citrate AuNPs in Milli-Q water, referring to Table 2, it is noted that the zeta potential is very good at 0 hours but decreased with time in the first 3 hours. At the same time, the color of the citrate AuNPs in the zeta cell for zeta potential measurement fades out after each measurement. This may be because in the measurement of zeta potential the citrate AuNPs adhere to the surface of the gold-plated electrodes.

But if the citrate AuNPs in the zeta cell were replaced by the spare solution that has not been used for measurement before, a good zeta potential can be observed again, that is, zeta potential of second measurement of the 3 hours and measurement after 3 hours.

And the size of the citrate AuNPs was the same for all time ranges. These were in good agreement with the absorption spectrum.

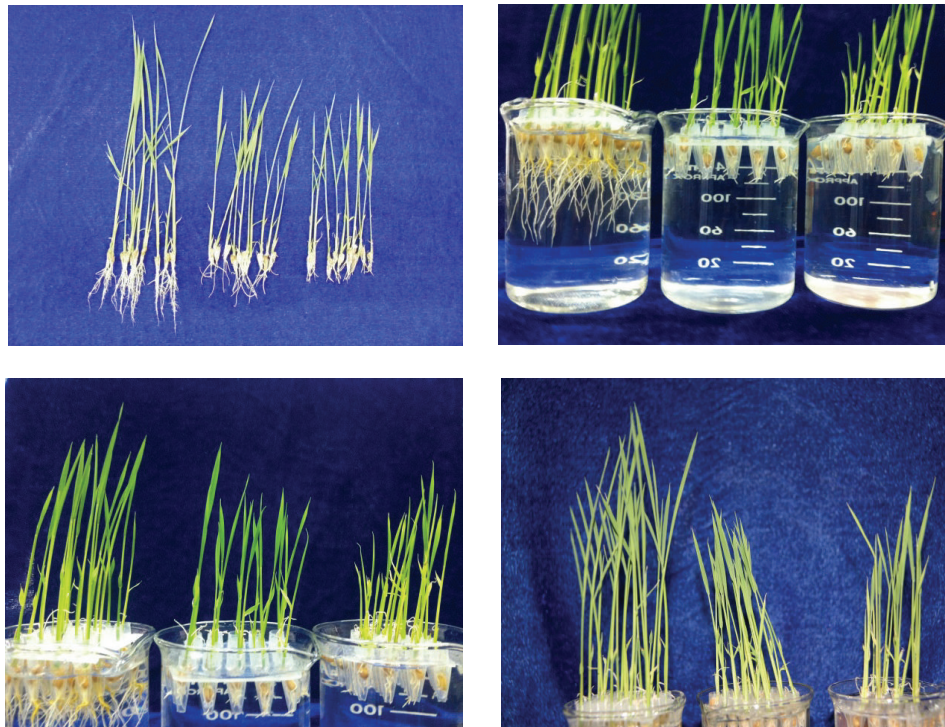


FIGURE 4: Images of rice: no gold nanoparticles, $5 * 10^{-6}$ M gold nanoparticles, and $5 * 10^{-8}$ M gold nanoparticles.

TABLE 3: Zeta potential and size of citrate AuNPs in pH 4 buffer.

Time (hour)	Zeta potential (mV)	Size (nm)
0	-46.1	342.0
1	-39.4	825.0
2	-38.8	531.2
3	-36.0	255.0
24	-33.0	295.3
72	-29.9	712.4
168	-13.9	141.8

From Table 3, the zeta potential of the citrate AuNPs in pH 4 buffer was evenly more negative than that in Milli-Q water. But aggregation happened because some components in the buffer adsorb on the surface of the citrate AuNPs and crosslinks form in between AuNPs. These results agreed with the absorption spectrum.

According to Table 4, the zeta potential of citrate AuNPs in biobuffer was about 5 times lower than that in Milli-Q water at 0 hours. And size 1 was due to the biobuffer and size 2 was the size of the citrate AuNPs which was almost the same within the measurement period. As the zeta potential and size were stable with time, so it was in a good agreement with the absorption spectrum.

To sum up, the zeta potentials of citrate AuNPs in Milli-Q water and biobuffer were very stable while those in pH 4 buffer were decreasing during the experiment. Moreover, their size in Milli-Q water and biobuffer was also stable for

TABLE 4: Zeta potential and size of citrate AuNPs in biobuffer.

Time (hour)	Zeta potential (mV)	Size 1 (nm)	Size 2 (nm)
0	-9.54	10.1	78.8
1	-10.6	5.6	122.4
2	-10.2	10.1	91.3
3	-10.5	10.1	78.8
24	-11.4	13.5	78.8
72	-11	11.7	78.8
168	-10.6	10.1	78.8

all times within the experimental period while they showed aggregation in pH 4 buffer.

3.4. Application for the Rice Growth. As citrate AuNPs were rather stable in water and biobuffer, they were used in the application for the rice growth.

From Figure 4 and Table 5 we can observe that with the AuNPs in a rather low concentration the rice roots stopped growing and the height of seedlings got influenced too; however the presence of AuNPs did not inhibit the germination of rice seed.

4. Conclusions

In Milli-Q water, both AuNPs are very stable. In pH 4, pH 7, pH 8, and pH 10 buffers, both of them are unstable.

TABLE 5: The height, number, and length for rice.

	The height of seedlings	The number of roots	The length of roots	The ratio of root length and seedling height
CK	17.78 ± 1.82 Aa	7.50 ± 1.80 Aa	3.39 ± 1.35 Aa	0.191 Aa
T1	10.79 ± 3.03 Bb	6.90 ± 1.29 Aa	1.90 ± 0.74 Bb	0.176 Bb
T2	11.60 ± 0.15 Bb	7.30 ± 1.42 Aa	1.67 ± 0.50 Bb	0.144 Bb

Aa Bb are Significant symbols which commonly used in the Data Analysis. Use the uppercase and lowercase letters (A a) due to the significant results.

In biobuffer, they were very stable which indicated that both CTAB and citrate AuNPs can be used for bioapplications.

To conclude, we found important information for the practical use of nanoparticles in bioapplications. Both CTAB and citrate AuNPs are also very good for bioapplications. And citrate AuNPs can inhibit the elongation of rice root to a large degree without inhibiting the germination of rice seed.

Conflict of Interests

The authors declare that there is no conflict of interests regarding the publication of this paper.

Acknowledgments

The authors thank the support from Institute of Botany, Jiangsu Province, Chinese Academy of Sciences, Nanjing Botanical Garden, Department of Physics and Materials Science and Centre for Functional Photonics (CFP), City University of Hong Kong, Department of Chemistry and Biotechnology, Faculty of Science and Technology, University of Macau, Macau Faculty of Science, Engineering and Technology, and Swinburne University of Technology.

References

- [1] T. Vossmeier, L. Katsikas, M. Giersig, I. G. Popovic, K. D. Chemseddine, and A. Eychmüller, "Simultaneous control of nanocrystal size and nanocrystal-nanocrystal separation in CdS nanocrystal assembly," *The Journal of Physical Chemistry*, vol. 65, no. 4, pp. 565–570, 1994.
- [2] H. S. Choi, W. Liu, P. Misra et al., "Renal clearance of quantum dots," *Nature Biotechnology*, vol. 25, no. 2, pp. 1165–1170, 2007.
- [3] A. L. Rogach, A. Kornowski, M. Gao, A. Eychmüller, and H. Weller, "Synthesis and characterization of a size series of extremely small thiol-stabilized CdSe nanocrystals," *The Journal of Physical Chemistry B*, vol. 103, no. 16, pp. 3065–3069, 1999.
- [4] A. L. Rogach, L. Katsikas, A. Kornowski, S. Dangsheng, A. Eychmüller, and H. Weller, "Synthesis and characterization of thiol-stabilized CdTe nanocrystals," *Berichte der Bunsengesellschaft für Physikalische Chemie*, vol. 100, no. 11, pp. 1772–1778, 1996.
- [5] A. L. Rogach, "Fluorescence energy transfer in hybrid structures of semiconductor nanocrystals," *Nano Today*, vol. 6, no. 4, pp. 355–365, 2011.
- [6] A. Rogach, S. Kershaw, M. Burt et al., "Optical properties of semiconductor nanostructures," *Advanced Materials*, vol. 11, pp. 552–555, 1999.
- [7] U. Resch-Genger, M. Grabolle, S. Cavaliere-Jaricot, R. Nitschke, and T. Nann, "Quantum dots versus organic dyes as fluorescent labels," *Nature Methods*, vol. 5, no. 9, pp. 763–775, 2008.
- [8] M. Green, "Semiconductor quantum dots as biological imaging agents," *Angewandte Chemie*, vol. 43, no. 32, pp. 4129–4131, 2004.
- [9] J. K. Jaiswal and S. M. Simon, "Potentials and pitfalls of fluorescent quantum dots for biological imaging," *Trends in Cell Biology*, vol. 14, no. 9, pp. 497–504, 2004.
- [10] M. Bruchez Jr., M. Moronne, P. Gin, S. Weiss, and A. P. Alivisatos, "Semiconductor nanocrystals as fluorescent biological labels," *Science*, vol. 281, no. 5385, pp. 2013–2016, 1998.
- [11] A. M. Derfus, W. C. W. Chan, and S. N. Bhatia, "Probing the cytotoxicity of semiconductor quantum dots," *Nano Letters*, vol. 4, no. 1, pp. 11–18, 2004.
- [12] S. T. Selvan, T. T. Tan, and J. Y. Ying, "Robust, non-cytotoxic, silica-coated CdSe quantum dots with efficient photoluminescence," *Advanced Materials*, vol. 17, no. 13, pp. 1620–1625, 2005.
- [13] T. Vossmeier, L. Katsikas, M. Giersig et al., "CdS nanoclusters: synthesis, characterization, size dependent oscillator strength, temperature shift of the excitonic transition energy, and reversible absorbance shift," *Journal of Physical Chemistry*, vol. 98, no. 31, pp. 7665–7673, 1994.
- [14] M. V. Khodakovskaya, B.-S. Kim, J. N. Kim et al., "Carbon nanotubes as plant growth regulators: effects on tomato growth, reproductive system, and soil microbial community," *Small*, vol. 9, no. 1, pp. 115–123, 2013.
- [15] S. Wu, J. Dou, J. Zhang, and S. Zhang, "A simple and economical one-pot method to synthesize high-quality water soluble CdTe QDs," *Journal of Materials Chemistry*, vol. 22, no. 29, pp. 14573–14578, 2012.
- [16] A. L. Rogach, T. Franzl, T. A. Klar et al., "Aqueous synthesis of thiol-capped CdTe nanocrystals: state-of-the-art," *The Journal of Physical Chemistry C*, vol. 111, no. 40, pp. 14628–14637, 2007.
- [17] P. Alivisatos, "The use of nanocrystals in biological detection," *Nature Biotechnology*, vol. 22, no. 1, pp. 47–52, 2004.
- [18] C. A. Mirkin, R. L. Letsinger, R. C. Mucic, and J. J. Storhoff, "A DNA-based method for rationally assembling nanoparticles into macroscopic materials," *Nature*, vol. 382, no. 6592, pp. 607–609, 1996.
- [19] J. D. Gosnell, M. A. S. Schreuderb, M. J. Bowers II, S. J. Rosenthal, and S. M. Weiss, "Cadmium selenide nanocrystals as white-light phosphors," in *6th International Conference on Solid State Lighting*, vol. 6337 of *Proceedings of the SPIE*, p. 63370A, 2006.
- [20] J.-H. Kim, Y. Lee, E.-J. Kim et al., "Exposure of iron nanoparticles to Arabidopsis thaliana enhances root elongation by triggering cell wall loosening," *Environmental Science & Technology*, vol. 48, no. 6, pp. 3477–3485, 2014.
- [21] M. Haruta, "Size- and support-dependency in the catalysis of gold," *Catalysis Today*, vol. 36, no. 2, pp. 153–166, 1997.

Research Article

Synthesis and Catalytic Performance of Graphene Modified CuO-ZnO-Al₂O₃ for CO₂ Hydrogenation to Methanol

Zheng-juan Liu,^{1,2} Xing-jiang Tang,¹ Shan Xu,¹ and Xiao-lai Wang¹

¹ State Key Laboratory for Oxo Synthesis and Selective Oxidation, Lanzhou Institute of Chemical Physics, Chinese Academy of Sciences, Lanzhou 730000, China

² University of Chinese Academy of Sciences, Beijing 100049, China

Correspondence should be addressed to Shan Xu; xushan@licp.cas.cn

Received 3 July 2014; Accepted 25 July 2014; Published 24 August 2014

Academic Editor: Tifeng Jiao

Copyright © 2014 Zheng-juan Liu et al. This is an open access article distributed under the Creative Commons Attribution License, which permits unrestricted use, distribution, and reproduction in any medium, provided the original work is properly cited.

CuO-ZnO-Al₂O₃ and graphene nanosheet (GNS) were synthesized by coprecipitation route and reduction of exfoliated graphite oxides method, respectively. GNS modified CuO-ZnO-Al₂O₃ nanocomposites were synthesized by high energy ball milling method. The structure, morphology, and character of the synthesized materials were studied by BET, XRD, TEM, and H₂-TPR. It was found that by high energy ball milling method the CuO-ZnO-Al₂O₃ nanoparticles were uniformly dispersed on GNS surfaces. The catalytic performance for the methanol synthesis from CO₂ hydrogenation was also tested. It was shown experimentally that appropriate incorporation of GNS into the CuO-ZnO-Al₂O₃ could significantly increase the catalyst activity for methanol synthesis. The 10 wt.% GNS modified CuO-ZnO-Al₂O₃ catalyst gave a methanol space time yield (STY) of 92.5% higher than that on the CuO-ZnO-Al₂O₃ catalyst without GNS. The improved catalytic performance was attributed to the excellent promotion of GNS to dispersion of CuO and ZnO particles.

1. Introduction

The concentration of atmospheric CO₂ had risen from ~280 ppm before 1860 to ~390 ppm in 2010, which is further predicted to be ~570 ppm by the end of the century [1]. The increase in CO₂ emissions arguably causes to the increase in global temperatures and climate changes, which is called the “greenhouse effect.” Hence, the comprehensive utilization of CO₂ has drawn more and more attention from the entire world. Because converting CO₂ to methanol not only could promote the efficient utilization of CO₂ but also has found a new way of methanol production, CO₂ hydrogenation to methanol has become a hot topic of academic research [2]. But due to the fact that CO₂ is inert molecule and very difficult to be activated, so making an appropriate catalyst that could bring the enhancement of CO₂ conversion and methanol yield will be the key topic of this research.

A conventional CuO-ZnO-Al₂O₃ catalyst for methanol production from synthesis gas (mixture of CO, CO₂, and H₂)

is now accepted [3–5]. But it is not adequate for methanol synthesis from a H₂/CO₂ mixture at temperatures below 250°C [6–8]. Hence, several modifications have been used to improve conventional CuO-ZnO-Al₂O₃ methanol synthesis catalysts. The key is to keep a high dispersion of the Cu/Zn crystallites where the active sites are as stated in [9, 10]. A lot of works have been done by doping other metal elements in CuO-ZnO-based catalyst for investigation, for example, Cr, Zr, V, Ce, Ti, Ga, and Pd [11–13]. In addition, some works tried to find the suitable method to synthesis CuO-ZnO-Al₂O₃ catalyst, such as sol-gel, hydrothermal, reverse microemulsion, and organic chelating agent to the common coprecipitation method [14, 15].

In comparison to the other preparation techniques, high energy ball milling has been used as an effective and easy method for preparation of high dispersed and refining grains including nanocrystalline as well as amorphous materials [16]. High energy ball milling process can change not only the size but also the structure of the material, so that makes

the active species in the secondary distribution of the sample surface [17, 18]; moreover, the particles undergo heavy pressure and mechanical deformation forming high-density fault structure and high concentration of lattice defects [19]. As a result, it makes the catalytic activity significantly improves due to the dynamic performance of the catalyst increasing.

Graphene nanosheet (GNS) is considered an excellent catalytic carrier and additives owing to its unique physical chemical properties [20], such as, special electronic transmission characteristics, huge specific surface area, and excellent electrical and thermal conductivity. So far, the research of graphene in catalyst fields primarily appears to be on photoelectric catalysis, fuel cell, lithium ion battery, and so on.

In this paper, we doped GNS with CuO-ZnO-Al₂O₃ composite oxides by high energy ball milling method. The prepared catalysts exhibit high dispersion of nanocomposite particles and high activity for CO₂ hydrogenation to methanol.

2. Experimental

2.1. Material Synthesis. Graphene nanosheet (GNS) was synthesized by reduction of graphite oxides. Firstly, we prepare graphite oxide by a modified Hummers method [21]. Then, the prepared graphite oxide was dispersed in deionized water, followed by ultrasonic as graphene suspension and the hydrazine hydrate was added as the reducing agent. After that the mixture was refluxed at 100°C. In the end, GNS was obtained after filtering, washing, and drying the resulting mixture.

The mixed aqueous solution of Cu(NO₃)₂, Zn(NO₃)₂, and Al(NO₃)₃ (the mole ratio is 6:3:1) with a total concentration of 1 mol/L and the aqueous solution of 1 mol/L Na₂CO₃ were prepared. The CuO-ZnO-Al₂O₃ catalysts were prepared by concurrently dropping Na₂CO₃ solution and mixed nitrates solution into an around-bottomed flask at 70°C under the water bath with vigorous stirring. The mixed nitrates solution was dropped at a rate of 5 mL/min and the pH was kept constant at 7-8. Then, the precursor was filtered and washed followed by dried overnight at 80°C. Finally the precursor was calcined at 350°C for 6 h to produce the CuO-ZnO-Al₂O₃ catalysts.

In our experiment Fritsch 7 Pulverisette planetary ball mill was applied. The anhydrous ethanol was used as ball mill solvent and WC balls ($\Phi = 10$ mm) were used as grinding balls. The milling rotational speed was 500 r/min. And ball mill could stop running for 15 min after working for 30 min. The cumulative milling time is 6 h. The mixture was dried at 60°C for 24 h after ball milling. The catalysts are denoted as CZA (without GNS), 5G-CZA (5 wt.% GNS), 10G-CZA (10 wt.% GNS), and 15G-CZA (15 wt.% GNS), respectively, in terms of graphene contents variations.

2.2. Material Characterization. Panalytical X'Pert Pro polycrystal X-ray diffraction (XRD) was performed with Cu-K α radiation, $\lambda = 0.15406$ nm, tube voltage being 40 kV, and

tube current being 40 mA in crystal structure of material characterization. The grain size of material is calculated by the Scherrer formula based on the strongest half peak width of the diffraction peak. The Brunauer-Emmett-Teller (BET) surface area of the catalyst was measured with an ASAP-2010 surface analyzer. The samples were degassed at approximately 200°C for 4 h before analysis. Hydrogen temperature-programmed reduction (H₂-TPR) was conducted with a GC-7890II Gas chromatograph equipped with a thermal conductive detector (TCD) made from Shanghai Tianmei Company. The quality of the catalyst tested was 10 mg with the 5% H₂-N₂ mixture gas as the reducing gas at a flow rate of 50 mL/min and heating rate of 10°C/min. Tecnai G2-F30 transmission electron microscopy (TEM) was used to test the morphology of catalyst with 300 kV accelerating voltage.

2.3. Catalytic Tests. The activity tests were carried out in a stainless steel fixed bed microreactor. The catalyst (20–40 mesh size, 0.5 g) was packed into a stainless steel fixed bed microreactor (15 mm Φ) and reduced in a mixed (V(H₂)/V(N₂) = 5/95) flow at 280°C for 6 h. After the reduction, the gas feed was switched to the reactant gas (V(H₂)/V(CO₂)/V(N₂) = 69/23/8). The reaction was tested at a pressure of 3.0 MPa and temperature of 250°C with a space velocity of 12000 mL/h·g_{catal.}. The CO₂ and CO were separated and regulated by carbon packed molecular sieve column and thermal conductivity detector (TCD). Methanol and other organic matters were separated and regulated by PoraPak Q column and hydrogen flame ionization detector (FID).

3. Results and Discussion

3.1. Structure Properties of Catalysts. The XRD patterns of the pure CuO-ZnO-Al₂O₃ samples and the CuO-ZnO-Al₂O₃ doped by varying contents of GNS samples are compared in Figure 1. No matter how much is the amount of GNS added in the samples, the characteristic diffraction peaks of CuO appeared at $2\theta = 35.6^\circ$, 38.8° , and 48.9° and the ZnO special diffraction peaks appeared at $2\theta = 31.8^\circ$, 34.5° , and 36.3° in all the samples. The peak at $2\theta = 26^\circ$ is the typical diffraction peak (002) of graphite material. With the added GNS increasing, the typical diffraction peak (002) intensity weakened a lot compared with the natural graphite. As part of the crystal structure of the incomplete oxidation of flake graphite damaged to some extent, so that its peak intensity is greatly decreased.

The physicochemical properties of CuO-ZnO-Al₂O₃ doped with different amounts of GNS are summarized in Table 1. For comparison, the physicochemical properties of pure CuO-ZnO/Al₂O₃ are also included. The surface areas of CZA, 5G-CZA, 10G-CZA, and 15G-CZA are 40.9, 113.3, 147.8, and 186.3 m²/g, respectively. The surface areas of the samples increase with the increase of GNS doping amount and it proves that specific surface area of sample is proportional to the GNS addition. From Table 1, we could get the crystallite size data of CuO and ZnO calculated from their corresponding diffraction peak by Scherrer equation. And

TABLE 1: Physicochemical properties of CuO-ZnO-Al₂O₃ doped with different amounts of GNS.

Catalysts	Surface area (m ² /g)	CuO crystallite size (nm)	ZnO crystallite size (nm)
CZA	40.9	13.6	17.3
5G-CZA	113.3	12.6	16.4
10G-CZA	147.8	12.4	14.0
15G-CZA	186.3	14.5	20.6

CuO and ZnO crystallite sizes were calculated from XRD data using Scherrer equation.

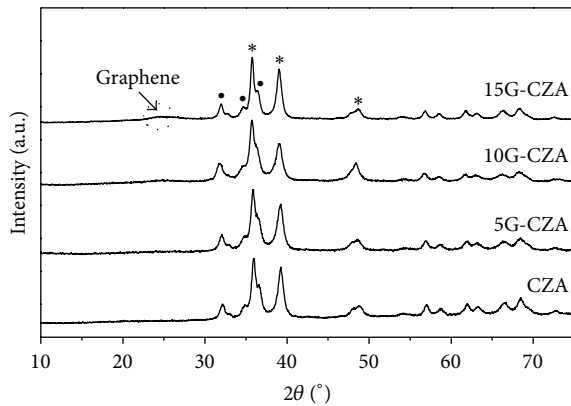


FIGURE 1: XRD patterns of CuO-ZnO-Al₂O₃ doped with different amounts of GNS [*] CuO; [•] ZnO.

the crystallite size of CuO particles decreased from 13.6 nm of CZA to 12.4 nm of 10G-CZA and the size of ZnO particles decreased from 18.3 nm to 14.0 nm. When milling time was constant, the minimum crystallite size of the samples is the sample powder with 10 wt.% GNS doped. For this result, there might be two reasons: (1) the CuO-ZnO/Al₂O₃ particles adsorb on the surface of GNS, which reduce the surface energy of the particles and prevent the recombination between breaking chemical bonds, leading to the decrease of mechanical strength of the particles and the external force for dislocation extension and finally resulting in reinforcement of the crushing effect. (2) The compatibility of the powder with ethanol increases by the addition of GNS, which improves the rheological properties of the slurry. As a result, the slurry viscosity is decreased and the fluidity and dispersal ability of particles are promoted making the collision frequency between the ball mill and powder particle higher. However, for the sample with 15 wt.% GNS doped the crystallite size of CuO increased to 14.5 nm and the size of ZnO increased to 20.6 nm. This result illustrates the excessive addition of graphene reduced the collision frequency between the ball mill and particles, so that the particles were bigger for aggregating. Such a conclusion suggests that crystallite size is the smallest when GNS doped in the composite is 10 wt.% and the crushing grain effect is weakened over this doped amount.

3.2. *TEM.* The morphology of CuO-ZnO/Al₂O₃ doped with different amounts of GNS is shown in the TEM images in Figure 2. In Figure 2(a), the particle sizes are larger with obvious agglomeration of the pure CuO-ZnO-Al₂O₃ catalysts which could be seen after ball milling. In Figures 2(b), 2(c), and 2(e), the transparent cicada's wing shape of nanographene sheets characteristic could be seen and the composite metal oxides particles are evenly distributed on the GNS. The stacks of graphene layers are clearly observed in the high-resolution image of Figure 2(d). Due to the fact that the GNS has a large specific surface area and the big π electron delocalization system, it is beneficial to the anchoring of the metal oxide nanoparticles and increases the electrostatic repulsion between the particles. GNS made by chemical reduction method has a certain amount of lattice defects and some residual oxygen functional groups making the distribution of the catalyst nanoparticles more uniform. The ball mill method made the metal oxide particles distributed evenly on GNS with the shape more regular and the size smaller. Figure 2(c) shows the CuO-ZnO-Al₂O₃ catalysts doped with 10 wt.% GNS with the smallest size distributed on the GNS sheets most uniformly which is consistent with the change of the grain size of CuO and ZnO.

3.3. *Reduction Properties of the Catalysts.* The H₂-TPR patterns of CuO-ZnO/Al₂O₃ doped with different amounts of GNS are given in Figure 3 and the four samples are all reduced in the temperature range of 150–290°C. For the pure CuO-ZnO/Al₂O₃ catalyst, there is a big side-by-side peak which can be decomposed into two peaks noted as β and γ , respectively. Because ZnO and Al₂O₃ are not reduced under the experimental conditions described here [22], so the two peaks appeared in the TPR profile stand for CuO existing in two different ways. The low temperature reduction peak (β peak) is assigned to reduction of CuO highly dispersed on the surface of catalysts and the high temperature reduction peak (γ peak) is assigned to reduction of CuO in bulk phase. It is noticeable that there is a new small peak appearing at lower temperature in the H₂-TPR patterns of other three samples doped with GNS. We name the lower temperature peak as α peak and assume that it is the contribution of GNS. GNS makes the shifts of reduction peak of the highly dispersed CuO toward lower temperature; that is, it makes part of CuO being more easily reduced by H₂. This is because GNS has high adsorption and activation ability for hydrogen species [23] and implies that in the reaction GNS is not only a carrier but also a good promoter. In order to prove that the appearance of α peak has nothing to do with the reduction of GNS, we run a H₂-TPR test in the same steps as before to pure GNS, getting a curve which is almost a straight line parallel to the baseline without any peaks. The areas of reduction peaks and their contributions to the TPR pattern over catalysts are given in Table 2. We can see that the proportion of areas of α and β peaks together is as high as 69.1% when the amounts of GNS doped is 10 wt.% indicating a higher content of highly dispersed CuO. The result is in accordance with the conclusion of aforementioned XRD, TEM characterization.

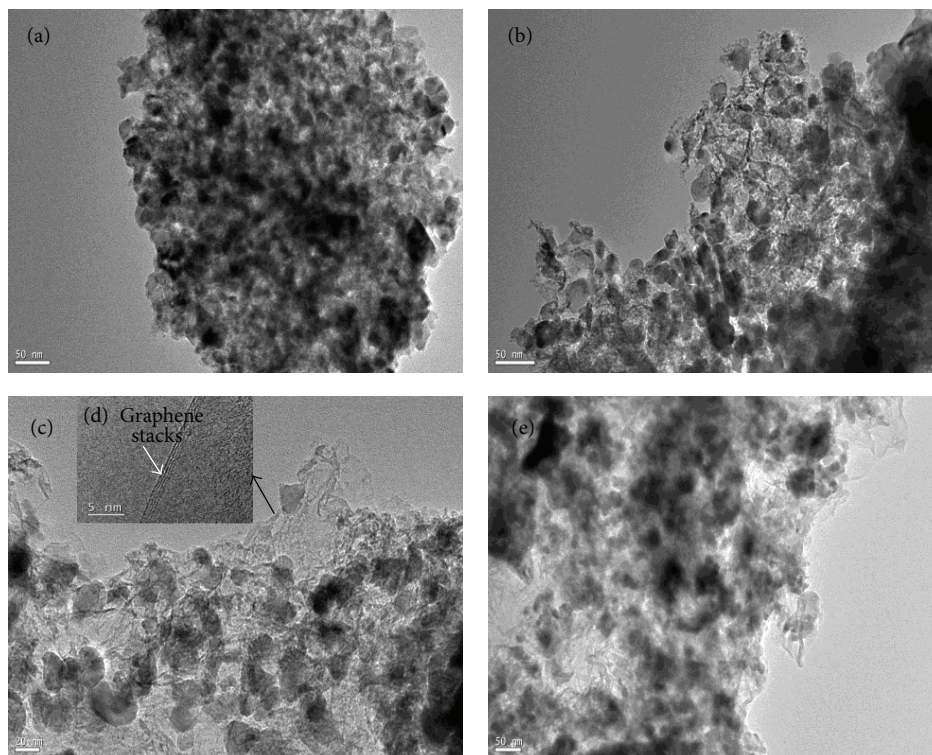


FIGURE 2: TEM photos of CuO-ZnO/ Al_2O_3 doped with different amounts of GNS: (a) CZA, (b) 5G-CZA, (c) 10G-CZA, (d) the HRTEM photos of 10G-CZA, and (e) 15G-CZA.

TABLE 2: Temperatures of reduction peaks and their contributions to the TPR pattern over catalysts.

Catalysts	T_α ($^\circ\text{C}$)	T_β ($^\circ\text{C}$)	T_γ ($^\circ\text{C}$)	$(A_\alpha + A_\beta)/(A_\alpha + A_\beta + A_\gamma)$ (%)
CZA	—	215	240	43.8
5G-CZA	197	224	245	58.7
10G-CZA	204	227	246	69.1
15G-CZA	215	230	249	56.0

A_α , A_β , and A_γ represent the areas of α , β , and γ peaks, respectively.

3.4. The Performance and Stability of the Catalysts. The activity evaluation of CO_2 hydrogenation to methanol is carried out in the fixed bed microreactor and methanol and CO are the main carbonaceous products with a small amount of CH_4 . In Table 3, the copper dispersion (D_{Cu}) and active surface area (MSA) of the catalysts are showed by calculation from N_2O chemisorption data. We could find that D_{Cu} and MSA values are increased with the amount of the GNS increased till 10 wt.%, and then those are reduced when the GNS amount is up to 15 wt.%. As shown in Table 3, the CO_2 conversion and methanol space time yield (STY) are in accordance with D_{Cu} and MSA. The 10G-CZA has the highest CO_2 conversion and STY of 14.6% and 360 mg/g·h, which are 71.8% and 92.5% higher than that on the CZA catalyst, respectively. These results suggest that the dispersion and particle size of active components of CuO and ZnO have a significant influence on the catalytic activity. The 10G-CZA catalyst, which has the most highly dispersion and the smallest particle size, is most conducive to the improvement

of the catalytic performance. The result is in agreement with the XRD, TEM, and H_2 -TPR and other analysis conclusions.

Figure 4 shows the assay results of conversion and methanol selectivity at 230–280 $^\circ\text{C}$ over the catalysts of CZA and 10G-CZA. The CO_2 conversion of the both catalysts went up as the temperature increased because appropriately raising the reaction temperature could promote the CO_2 reaction. On the other hand, both the methanol selectivity decreased with the temperature increased because the methanol formation from the hydrogenation of CO_2 is thermodynamically restricted within low conversion under the operating conditions [24]. It can be showed that the CO_2 conversion and the methanol selectivity of 10G-CZA catalyst were always higher than that of the CZA catalyst, confirming that graphene is an excellent promoter for CuO-ZnO- Al_2O_3 catalysts on CO_2 hydrogenation to methanol.

The 10G-CZA as the best catalyst performance was selected for the stability test, and the results are shown in Figure 5. The CO_2 conversion and methanol selectivity

TABLE 3: Catalytic properties and N₂O chemisorption data of CuO-ZnO-Al₂O₃ doped with different amounts of GNS.

Catalysts	D_{Cu} (%)	MSA (m ² /g _{Cu})	Conversion of CO ₂ (%)	Selectivity of CH ₃ OH (%)	STY of CH ₃ OH (mg/g·h)
CZA	7.2	10.8	8.5	55.7	187
5G-CZA	8.2	11.7	12.1	59.9	287
10G-CZA	9.4	12.6	14.6	62.3	360
15G-CZA	7.7	11.3	12.3	57.7	281

Reaction conditions: temperature = 250 °C; pressure = 3.0 MPa; SV = 12000 ml/h·g_{catal.}

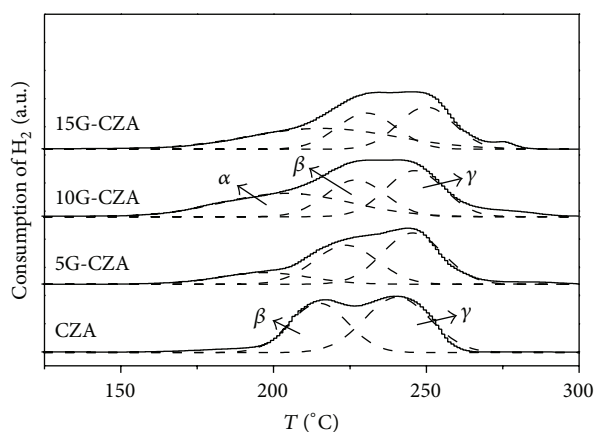


FIGURE 3: H₂-TPR patterns of CuO-ZnO-Al₂O₃ doped with different amounts of GNS.

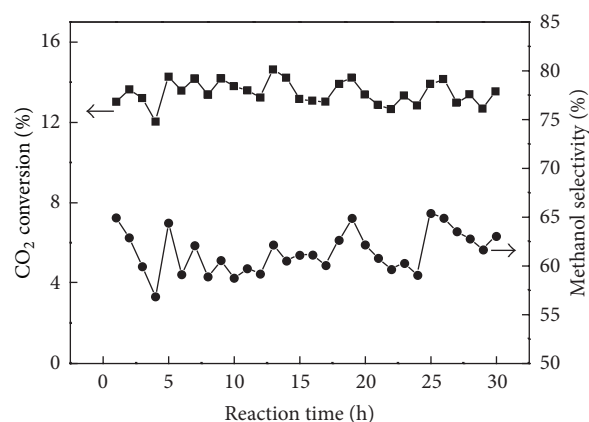


FIGURE 5: Variation of CO₂ conversion and methanol selectivity with reaction time over 10G-CZA catalyst ($T = 250^{\circ}\text{C}$, $P = 3.0\text{ MPa}$, $SV = 12000\text{ mL/h}\cdot\text{g}_{\text{catal.}}$).

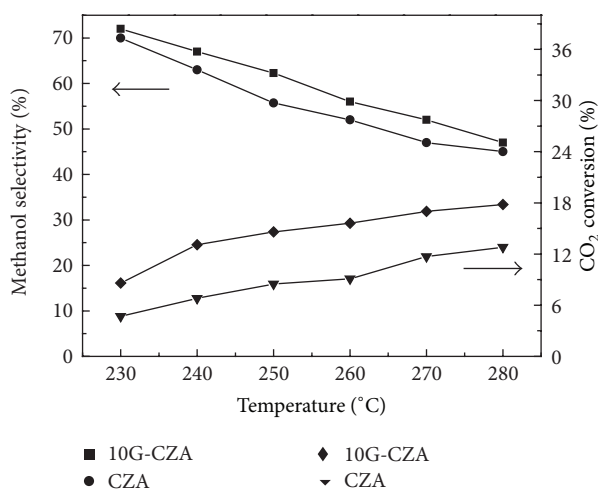


FIGURE 4: Variation of CO₂ conversion and methanol selectivity with reaction temperature over CZA and 10G-CZA catalyst ($P = 3.0\text{ MPa}$, $SV = 12000\text{ mL/h}\cdot\text{g}_{\text{catal.}}$).

of 10G-CZA catalyst remain unchanged after continuous operation for 30 h in the fixed bed microreactor under $T = 250^{\circ}\text{C}$, $P = 3.0\text{ MPa}$, and $SV = 12000\text{ mL/h}\cdot\text{g}_{\text{catal.}}$. The results show that the catalyst prepared by ball milling method has very good stability.

4. Conclusions

The high energy ball milling method has been used to prepare GNS modified CuO-ZnO-Al₂O₃ nanocomposites catalysts for methanol synthesis from CO₂ hydrogenation. GNS/CuO-ZnO-Al₂O₃ nanocomposites catalyst with 10 wt.% GNS showed the best catalytic activity with CO₂ conversion and methanol space time yield is 71.8% and 92.5% higher separately than the catalyst without GNS addition. The GNS modified CuO-ZnO-Al₂O₃ nanocomposites catalysts prepared by high energy ball milling method make the dispersion of active components of CuO and ZnO higher and smaller particle size and exhibit a much enhancement in catalytic performance. The ball mill operation is simple with low energy consumption, environmentally friendly, and suitable for large-scale preparation of industrialization.

Conflict of Interests

The authors declared that they have no conflict of interests regarding this paper.

Acknowledgments

This work was financially supported by the National Natural Science Foundation of China (no. 21103205) and the “Western Light” Project (2013) of Chinese Academy of Sciences.

References

- [1] X. Xiaoding and J. A. Moulijn, "Mitigation of CO₂ by chemical conversion: plausible chemical reactions and promising products," *Energy and Fuels*, vol. 10, no. 2, pp. 305–325, 1996.
- [2] G. A. Olah, A. Goepfert, and G. K. S. Prakash, "Chemical recycling of carbon dioxide to methanol and dimethyl ether: from greenhouse gas to renewable, environmentally carbon neutral fuels and synthetic hydrocarbons," *Journal of Organic Chemistry*, vol. 74, no. 2, pp. 487–498, 2009.
- [3] F. Pontzen, W. Liebner, V. Gronemann, M. Rothaemel, and B. Ahlers, "CO₂-based methanol and DME—efficient technologies for industrial scale production," *Catalysis Today*, vol. 171, no. 1, pp. 242–250, 2011.
- [4] Z. Hong, Y. Cao, J. Deng, and K. Fan, "CO₂ hydrogenation to methanol over Cu/ZnO/Al₂O₃ catalysts prepared by a novel gel-network-coprecipitation method," *Catalysis Letters*, vol. 82, no. 1-2, pp. 37–44, 2002.
- [5] K. Jun, W. Shen, K. S. Rama Rao, and K. Lee, "Residual sodium effect on the catalytic activity of Cu/ZnO/Al₂O₃ in methanol synthesis from CO₂ hydrogenation," *Applied Catalysis A: General*, vol. 174, no. 1-2, pp. 231–238, 1998.
- [6] X. Liu, G. Q. Lu, Z. Yan, and J. Beltramini, "Recent Advances in Catalysts for Methanol Synthesis via Hydrogenation of CO and CO₂," *Industrial and Engineering Chemistry Research*, vol. 42, no. 25, pp. 6518–6530, 2003.
- [7] J. L. G. Fierro, I. Melián-Cabrera, and M. López Granados, "Reverse topotactic transformation of a Cu-Zn-Al catalyst during wet Pd impregnation: Relevance for the performance in methanol synthesis from CO₂/H₂ mixtures," *Journal of Catalysis*, vol. 210, no. 2, pp. 273–284, 2002.
- [8] J. L. G. Fierro, I. Melián-Cabrera, and M. López Granados, "Pd-modified Cu-Zn catalysts for methanol synthesis from CO₂/H₂ mixtures: catalytic structures and performance," *Journal of Catalysis*, vol. 210, no. 2, pp. 285–294, 2002.
- [9] J. Wang, S. Funk, and U. Burghaus, "Indications for metal-support interactions: the case of CO₂ adsorption on Cu/ZnO(0001)," *Catalysis Letters*, vol. 103, no. 3-4, pp. 219–223, 2005.
- [10] V. E. Ostrovskii, "Mechanisms of methanol synthesis from hydrogen and carbon oxides at Cu-Zn-containing catalysts in the context of some fundamental problems of heterogeneous catalysis," *Catalysis Today*, vol. 77, no. 3, pp. 141–160, 2002.
- [11] I. Melián-Cabrera, M. L. Granados, and J. L. G. Fierro, "Effect of Pd on Cu-Zn catalysts for the hydrogenation of CO₂ to methanol: Stabilization of Cu metal against CO₂ oxidation," *Catalysis Letters*, vol. 79, no. 1-4, pp. 165–170, 2002.
- [12] S. Schuyten and E. E. Wolf, "Selective combinatorial studies on Ce and Zr promoted Cu/Zn/Pd catalysts for hydrogen production via methanol oxidative reforming," *Catalysis Letters*, vol. 106, no. 1-2, pp. 7–14, 2006.
- [13] I. Melián-Cabrera, M. López Granados, and J. L. G. Fierro, "Structural reversibility of a ternary CuO-ZnO-Al₂O₃ ex hydrotalcite-containing material during wet Pd impregnation," *Catalysis Letters*, vol. 84, no. 3-4, pp. 153–162, 2002.
- [14] G. Busca, U. Costantino, F. Marmottini et al., "Methanol steam reforming over ex-hydrotalcite Cu-Zn-Al catalysts," *Applied Catalysis A: General*, vol. 310, no. 1-2, pp. 70–78, 2006.
- [15] X. Zhang, L. Wang, C. Yao et al., "A highly efficient Cu/ZnO/Al₂O₃ catalyst via gel-coprecipitation of oxalate precursors for low-temperature steam reforming of methanol," *Catalysis Letters*, vol. 102, no. 3-4, pp. 183–190, 2005.
- [16] M. Varga, Á. Molnár, G. Mulas, M. Mohai, I. Bertóti, and G. Cocco, "Cu-MgO samples prepared by mechanochemistry for catalytic application," *Journal of Catalysis*, vol. 206, no. 1, pp. 71–81, 2002.
- [17] V. A. Zazhigalov, J. Haber, J. Stoch, L. V. Bogutskaya, and I. V. Bacherikova, "Mechanochemistry as activation method of the V-P-O catalysts for n-butane partial oxidation," *Applied Catalysis A: General*, vol. 135, no. 1, pp. 155–161, 1996.
- [18] S. Mori, W.-C. Xu, T. Ishidzuki, N. Ogasawara, J. Imai, and K. Kobayashi, "Mechanochemical activation of catalysts for CO₂ methanation," *Applied Catalysis A: General*, vol. 137, no. 2, pp. 255–268, 1996.
- [19] C. Feng, G. Fan, and Y. Wang, "Progress in synthesis methods of ceria-based oxygen storage materials for automotive catalysts," *Modern Chemical Industry*, vol. 24, no. 11, pp. 10–14, 2004.
- [20] Y. Lu, M. Zhou, C. Zhang, and Y. Feng, "Metal-embedded graphene: a possible catalyst with high activity," *Journal of Physical Chemistry C*, vol. 113, no. 47, pp. 20156–20160, 2009.
- [21] W. S. Hummers Jr. and R. E. Offeman, "Preparation of graphitic oxide," *Journal of the American Chemical Society*, vol. 80, no. 6, p. 1339, 1958.
- [22] E. Samei, M. Taghizadeh, and M. Bahmani, "Enhancement of stability and activity of Cu/ZnO/Al₂O₃ catalysts by colloidal silica and metal oxides additives for methanol synthesis from a CO₂-rich feed," *Fuel Processing Technology*, vol. 96, pp. 128–133, 2012.
- [23] A. Ghosh, K. S. Subrahmanyam, K. S. Krishna et al., "Uptake of H₂ and CO₂ by graphene," *The Journal of Physical Chemistry C*, vol. 112, no. 40, pp. 15704–15707, 2008.
- [24] W. Shen, K. Jun, H. Choi, and K. Lee, "Thermodynamic Investigation of Methanol and Dimethyl Ether Synthesis from CO₂ Hydrogenation," *Korean Journal of Chemical Engineering*, vol. 17, no. 2, pp. 210–216, 2000.

Research Article

Study on Thermal Insulation Zeolite by Coal Fly Ash

Huiping Song, Nan Zheng, Fangbin Xue, and Fangqin Cheng

State Environment Protection Key Laboratory of Efficient Utilization Technology of Coal Waste Resources,
Institute of Resources and Environmental Engineering, Shanxi University, Taiyuan 030006, China

Correspondence should be addressed to Huiping Song; songhp@sxu.edu.cn

Received 17 June 2014; Accepted 16 July 2014; Published 6 August 2014

Academic Editor: Tifeng Jiao

Copyright © 2014 Huiping Song et al. This is an open access article distributed under the Creative Commons Attribution License, which permits unrestricted use, distribution, and reproduction in any medium, provided the original work is properly cited.

This paper takes the coal fly ash as the material and makes zeolite with low thermal conductivity under a two-step synthesis for the purpose of thermal insulation. It studies main factors affecting zeolite such as the different concentration of NaOH, the solid-liquid ratio, the silica-alumina ratio, and the crystallization temperature. The optimal conditions were obtained that the NaOH concentration was 3 mol/L, the solid-liquid ratio was 10:1, the silica-alumina ratio was 2, and the crystallization temperature was 12°C. Zeolites have multiple pores and skeletal structures under SEM observation. The mean particle size was 2.78 μm of concentrated distribution. The pore volume was 0.148 m³/g measured by BET analysis, the specific surface was 118.6 m²/g, and the thermal conductivity was 0.153 W/(m·K). Zeolite was proved to be a qualified insulation material which can be used in thermal insulation coating as a new material of energy conservation.

1. Introduction

Fly ash is the largest amount of industrial waste in the world. There is still a proportion of CFA that is discharged into ponds or landfills, which causes serious environmental problems and significant distress to local communities [1, 2]. Therefore, recycling CFA has important economic and environmental implications. The components of fly ash are some oxides derived from inorganic compounds, which remain after combustion of the coal. The main components of fly ash are SiO₂ and Al₂O₃, which are compositionally similar to natural zeolites [3]. Because of these similarities, more than 150 zeolites have been synthesized from CFA in the past few years [4].

Höller and Wirsching first reported how to create zeolites from fly ash in 1985 [5]. Then, many attempts have been made to derive zeolites from CFA using a one-stage hydrothermal method. The main obstacle to synthesizing zeolites from CFA is that, to speed up the reaction, temperatures in the range of 100–200°C must be applied in order to dissolve the silica and alumina [6, 7]. Over a decade later, Hollman et al. [8] pioneered the two-stage hydrothermal method, which reportedly yielded very pure zeolite. As a result, the two-stage hydrothermal method gained considerable interest

in the following years [9]. The main disadvantages of the two-stage method are fairly long incubation times (~72 h) and the high temperatures (>500°C) required to prefuse the CFA with a solid alkali [10]. Studies in the literature suggest that it is possible to synthesize zeolites from natural materials and industrial residues, but all of these processes employ large quantities of sodium hydroxide (NaOH) and require high temperatures for performing the alkaline fusion [11]. Such processes have significant costs and are not always reproducible [12].

Zeolites were usually applied to environmental technology for ion exchange, soil improvement, and air purification [13, 14]. In addition, zeolites can be used in wastewater purification because they efficiently adsorb positively charged pollutants in wastewater, such as heavy metals [15–17]. But they have not been applied to thermal insulation. Zeolites have multiple pores filled with air of low thermal conductivity. There is a good reason to take them as a thermal insulation material.

In this study, a homogeneous-phase reactor was explored to reduce the temperatures and reaction times required to synthesize zeolites from deironed CFA. We selected qualified zeolites of low thermal conductivity by changing experimental conditions.

2. Materials and Methods

2.1. Raw Materials of Experiment. The main chemical components of CFA (sampled from Taiyuan First Thermal Power Plant) were SiO_2 (51.63%) and Al_2O_3 (35.00%). The main crystal phases of the ash included mullite ($3\text{Al}_2\text{O}_3 \cdot 2\text{SiO}_2$) and quartz (SiO_2) [18], the composition of which was very close to that of zeolite molecular sieves. These phases are very good raw materials for producing zeolite [5]. The raw material also includes 4.96% Fe_2O_3 , which is not favorable for the preparation of zeolite molecular sieves. Thus, Fe_2O_3 must be removed from the materials prior to synthesizing zeolite.

2.2. Zeolites Synthesis. Based on the optimized experimental conditions determined earlier, the two-step synthesis of zeolites in this study was performed. In hot alkali solution, iron compound in the coal fly ash reacted with NaOH to produce $\text{Fe}(\text{OH})_3$ sediment that reduced the alkali concentration and resulted in a reduction of crystallinity and whiteness [19]. Therefore, the CFA was pretreated several times using a permanent magnet (6000 Gs, Ningbo, China) to remove the iron in it. Then, CFA was added to reaction tanks in a JBJX-8 homogenous reactor (Jianbang, China) containing NaOH (analytical reagent, >96%) solutions. After the self-pressure alkali-leaching reaction, the supernatants in the reaction tanks were collected to determine the amount of silicon in the alkaline leaching solution by means of silicon molybdenum yellow spectrophotometry. The aluminum content in solution was also measured by means of test method for analysis of coal ash (GB/T 1547-2007). Sodium metaaluminate (analytical reagent, >99.5%) was added to adjust the molar ratio of $\text{SiO}_2/\text{Al}_2\text{O}_3$. The solution was then placed in the reactor again. The crystallized products were filtered and washed until pH 9-10. The products were dried at 100°C and stored overnight.

2.3. Analyses Methods. X-Ray Powder Diffractometer (D8 Advance, Bruker, Germany) was used to analyze the phase of the zeolites synthesized from CFA. The sample was pressed into a tablet using a mold with a diameter of 2 cm. Cu-K α radiation was adopted. The accelerating voltage was 40 kV, the electrical current was 40 mA, and the scans ranged from 10° to 80° at a speed of $6^\circ/\text{min}$. The thermal conductivities of samples were measured by the Thermal Conductivity Tester (DRL-II, Xiangtan, China). After the samples had been gold-sprayed, the surface topography of the samples was observed by the Field Emission Scanning Electron Microscope (S-4800, Hitachi, Japan). The size and distribution of the sample were measured by the Particle Size Analyser (Eyetechnology/CIS, Ankersmid B.V., Holland). Based on N_2 adsorption, BET method was used to measure specific surface area of the samples by the Surface Area and Pore Size Analyzer (ASAP 2020M, Micromeritics, USA).

3. Results and Discussion

3.1. The Influence of Sodium Hydroxide Concentration on Zeolite. In the process of synthesis, NaOH concentration

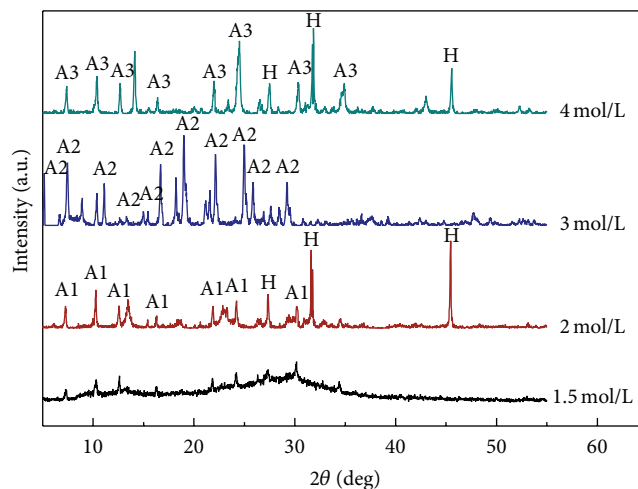


FIGURE 1: XRD pattern of samples synthesized with different concentration of sodium hydroxide. H-Halite, syn (PDF number 05-0628); A1-Zeolite A, [Na] (PDF number 39-0223), A2-Zeolite 4A (PDF number 43-0142); and A3-Zeolite A (PDF number 46-0564).

determined the water-sodium ratio and the equilibrium state. As a result, the reaction headed to the synthesis of some kind of zeolite. The product's state changed with NaOH concentration. This paper studied the influence of coal fly ash on zeolite with four NaOH concentrations (1.5, 2, 3, and 4 mol/L). Experimental conditions were as follows: solid-liquid ratio was 10:1 (quality of NaOH solution and coal fly ash); alkaline-leaching temperature was 100°C ; alkaline-leaching time was 2 h; the silica-alumina ratio was 2; the crystallization temperature was 100°C ; the crystallization time was 3 h. Synthesized zeolites were applied to XRD analysis. The results are shown in Figure 1.

Qualitative phase analyses with the XRD data were performed. When NaOH concentration was 1.5 mol/L, the product was in the form of amorphous silica. When NaOH concentration was more than 2 mol/L, it became very pure NaA zeolite. Zeolite synthesis with hot water composed of two processes: first was the production of silica-alumina gel; then the gel turned into crystallized synthesized zeolites. When NaOH concentration was very low, silica and alumina could not react fully to produce the gel. As the concentration increased, silica and alumina could gradually react and reached the condition to synthesize zeolites [20].

Zeolites were different under various NaOH concentrations. Their structure and performance varied for each kind. Their thermal conductivities were tested, as was shown in Figure 2. Within the selected NaOH concentration, the thermal conductivity was less than $0.25 \text{ W}/(\text{m}\cdot\text{K})$, capable of being thermal materials. The thermal conductivity was the smallest, $0.179 \text{ W}/(\text{m}\cdot\text{K})$, when NaOH concentration was 3.0 mol/L. Thus, 3.0 mol/L was the optimal concentration for NaOH.

3.2. The Influence of the Solid-Liquid Ratio on Zeolite. We explored the quality ratio of NaOH solution to coal fly ash (adjusted solid-liquid ratio was 3:1, 7:1, 10:1, 13:1, and 15:1).

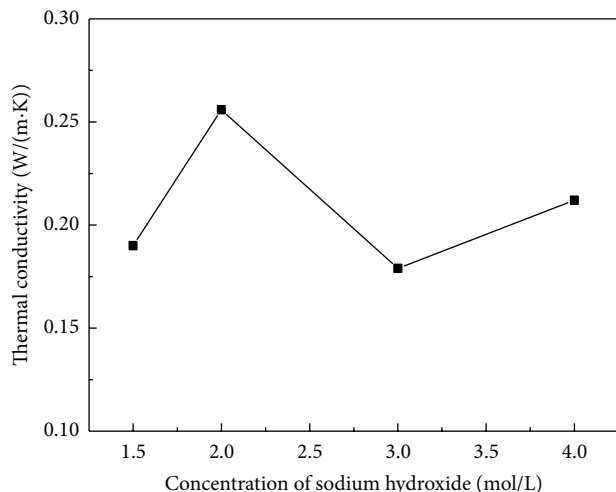


FIGURE 2: Thermal conductivity of samples synthesized with different concentration of sodium hydroxide.

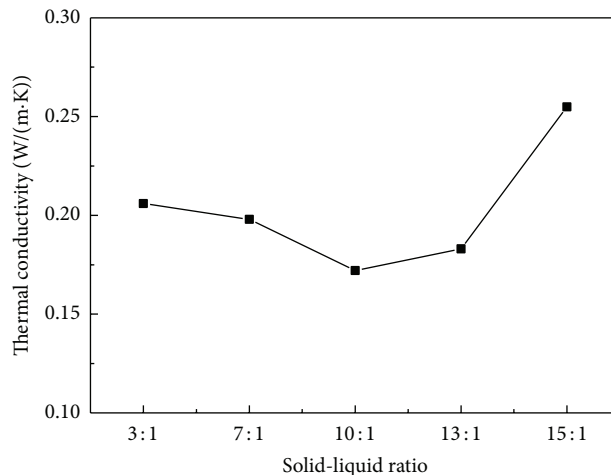


FIGURE 4: Thermal conductivity of samples synthesized with different solid-liquid ratio.

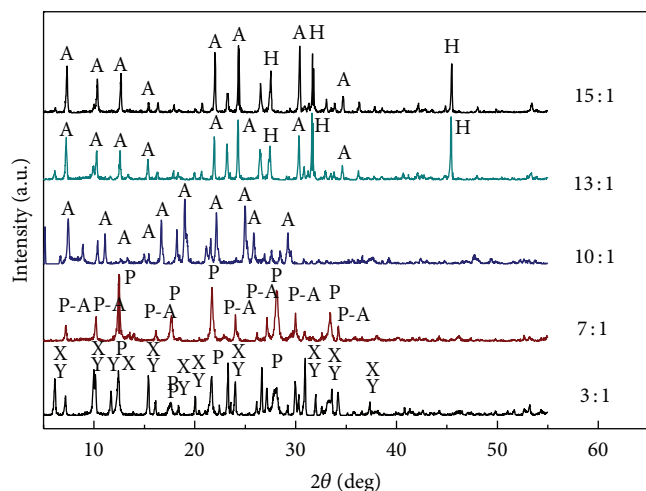


FIGURE 3: XRD pattern of samples synthesized with different solid-liquid ratio. Y-Faujasite Na, (PDF number 12-0246), X-Zeolite X (PDF number 41-0118), P-Zeolite P, [Na] (PDF number 44-0052), P-A-Zeolite P-A (PDF number 38-0323), A-Zeolite 4A (PDF number 43-0142), and H-Halite, syn (PDF number 05-0628).

Experimental conditions were as follows: the concentration of NaOH is 3 mol/L; alkaline-leaching temperature was 100°C; alkaline-leaching time was 2 h; solid-liquid ratio was 10 : 1; silica-alumina ratio was 2.5; crystallization time was 3 h. Synthesized zeolites were applied to XRD analysis. The results were shown in Figure 3.

When the solid-liquid ratio was 3:1, the product concentration in coal fly ash solution was high. The crystallized speed was fast but the reaction was uneven. This brought about many mixed crystals, including Y-type zeolite, Faujasite Na (PDF number 12-0246), X-type zeolite (PDF number 41-0118), and P-type zeolite (PDF number 44-0052). As solid-liquid ratio increased, reactants were able to be dissolved with more silica and alumina. When solid-liquid ratio was 7:1, characteristic peak of NaA zeolite showed up with

synthesized products of high crystallinity such as P-A-Zeolite P-A (PDF number 38-0323), A-Zeolite 4A (PDF number 43-0142), and H-Halite, syn (PDF number 05-0628). Zeolites were very pure when the ratio was 10 : 1.

To study the thermal insulation property, we tested the thermal conductivity of products with different solid-liquid ratios. The results were shown in Figure 4. When solid-liquid ratio was less than 15:1, the thermal conductivities were smaller than 0.25 W/(m·K), which fitted the standard of thermal insulation material. When the ratio was 10 : 1, the thermal conductivity was the smallest, 0.172 W/(m·K), which was the optimal ratio.

3.3. The Influence of the Silica-Alumina Ratio on Zeolite.

The properties of synthesized zeolitic materials from coal fly ash are also affected by the silica-alumina ratio. The series experiments with different silica-alumina ratio were studied by adjusting the dose of sodium metaaluminate. Other experiment conditions were as follows: the concentration of NaOH is 3 mol/L; alkaline-leaching temperature was 100°C; alkaline-leaching time was 2 h; solid-liquid ratio was 10 : 1; crystallization time was 3 h; crystallization temperature was 100°C. Figure 5 shows the XRD pattern of samples synthesized with different silica-alumina ratio. Tanaka et al. [21] thought alumina affected the solubility of silica in the silica-alumina gel. They presented a negative correlation. Therefore, an adjusted silica-alumina ratio was the key to produce qualified zeolite.

When silica-alumina ratio was 1.5, the synthesized product was mainly in the form of NaA-type zeolite. When it was adjusted to 2, 2.5, and 3, there were NaX-type zeolites and NaA-type. And these two types of zeolites are all with special pore and skeletal structure. After the test of thermal conductivity of synthesized zeolites with different silica-alumina ratio (as was shown in Figure 6), it was found out that the thermal conductivity was the smallest at 0.181 W/(m·K) when silica-alumina ratio was 2. Given soluble result of silica

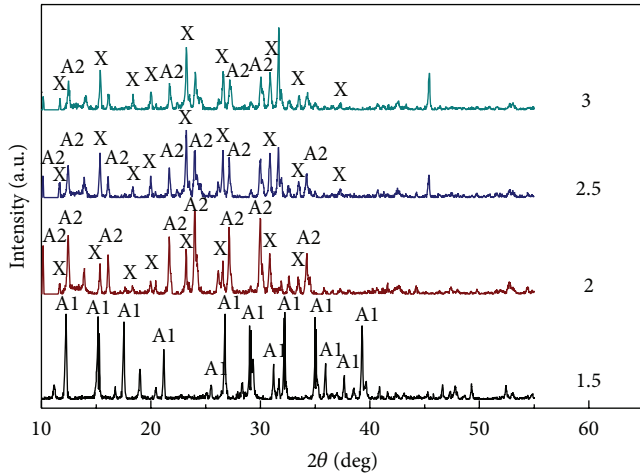


FIGURE 5: XRD pattern of samples synthesized with different silica-alumina ratio. A1-Zeolite A [Na] (PDF number 39-0222), A2-Zeolite 4A (PDF number 43-0142), and X-Zeolite (PDF number 41-0118).

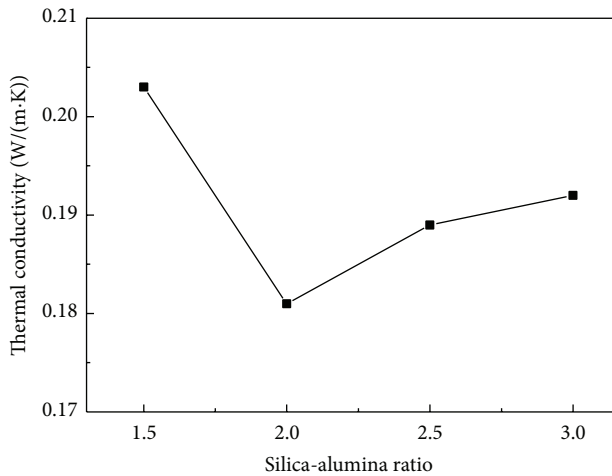


FIGURE 6: Thermal conductivity of samples synthesized with different silica-alumina ratio.

and alumina in the coal fly ash solution as well as the property of the product, the ratio was set as 2 in latter experiments.

3.4. The Influence of Crystallization Temperature on Zeolite.

Crystallization temperature was important in the process of zeolite crystallization. Experiment conditions were as follows: the concentration of NaOH is 3 mol/L; alkaline-leaching temperature was 100°C; alkaline-leaching time was 2 h; solid-liquid ratio was 10 : 1; silica-alumina ratio was 2.5; crystallization time was 3 h; adjusted crystallization temperature was 80, 100, 120, and 140°C. Figure 7 shows the variation of samples synthesized with different crystallization temperatures. When the temperature was 80°C, the product was mainly in the form of amorphous silica and there was no zeolite. When it reached 100°C, the synthesized product was mainly in the form of NaA-type zeolite. When it reached 120°C, NaX-type zeolite with multiple pores was synthesized.

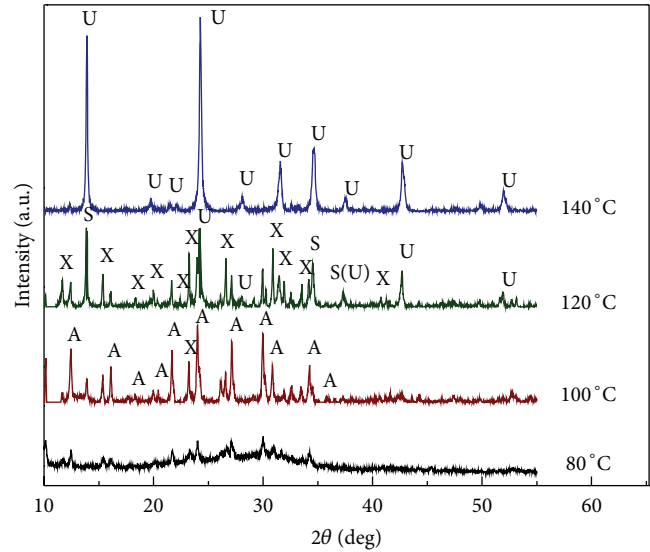


FIGURE 7: XRD pattern of samples synthesized with different crystallization temperature. A-Zeolite 4A (PDF number 43-0142), S-Sodalite (PDF number 41-0118), X-Zeolite (PDF number 41-0118), and U-Unnamed (PDF number 38-0221).

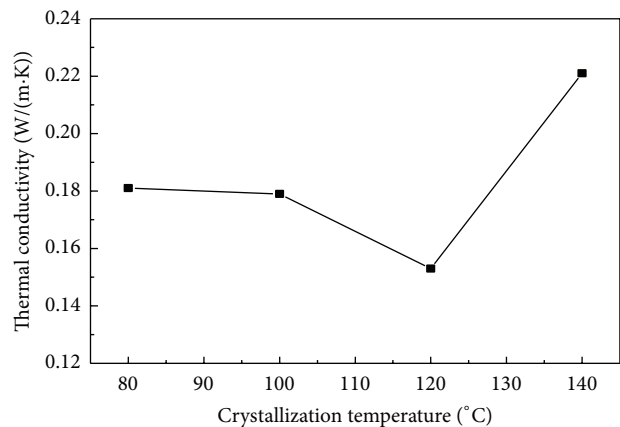


FIGURE 8: Thermal conductivity of samples synthesized with different crystallization temperature.

When the temperature was 140°C, there was an unnamed zeolite with high crystallinity and purity. There was almost no characteristic peak of mixed crystal.

According to thermal conductivity test (as was shown in Figure 8), when the crystallization temperature was 140°C, the thermal conductivity was the biggest at 0.221 W/(m·K). When it was 120°C, the thermal conductivity was the smallest at 0.153 W/(m·K). Thus, crystallization temperature did have a great influence on the crystallinity of samples. If the crystallization temperature was too low, the reaction was hard to continue. As the temperature increased, the solubility of silica-alumina gel rose up. So did the number of crystal nucleus. The crystallization speed would be accelerated and the crystal was getting bigger, resulting in an increase of the thermal conductivity [22]. Therefore, the optimal crystallization temperature was 120°C.

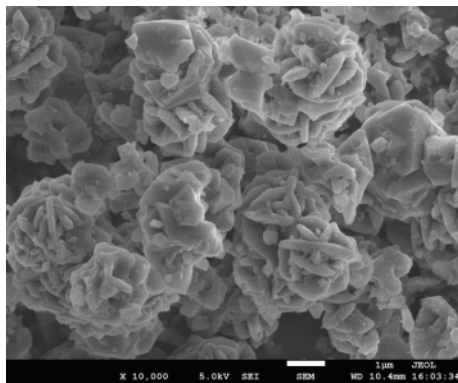


FIGURE 9: SEM observation for zeolite synthesized with different crystallization temperatures.

Therefore, with the coal fly ash as the material, the optimal condition for making zeolite with low thermal conductivity under a two-step synthesis was as follows: the concentration of NaOH was 3 mol/L with a solid-liquid ratio of 10:1, the silica-alumina ratio of 2, and the crystallization temperature of 120°C.

3.5. The Appearance Performance Analysis of Synthesized Zeolites. Make the zeolites under the optimal condition and observe their appearances by SEM observation. They had multiple pores and skeletal structures as were shown in Figure 9. According to laser particle size analyzer, mean particle size of zeolite was 2.78 µm of concentrated distribution. About 70% of particles were from 700 nm to 2 µm. By BET analysis, the pore volume of zeolite was 0.148 m³/g, the specific surface is 118.6 m²/g, and the thermal conductivity is 0.153 W/(m·K). Zeolite is proved to be a qualified insulation material, which can be used in thermal insulation coating as a new material of energy conservation.

4. Conclusion

This paper concludes the optimal condition for making zeolite with low thermal conductivity coefficient by deironing coal fly ash under two-step synthesis. The concentration of NaOH is 3 mol/L with a solid-liquid ratio of 10:1, silica-alumina ratio of 2, and crystallization temperature of 120°C. Zeolites have multiple pores and skeletal structures. The mean particle size is 2.78 µm, the pore volume is 0.148 m³/g, the specific surface is 118.6 m²/g, and the thermal conductivity is 0.153 W/(m·K). Zeolite is proved to be a qualified insulation material which can be used in thermal insulation coating as a new material of energy conservation.

Conflict of Interests

The authors declare that there is no conflict of interests regarding the publication of this paper.

Acknowledgments

This work was financially supported by the National Natural Science Foundation of China (51104097 and 20906053), the Research Projects of Shanxi Province (20120313014-1), and the National Key Technology R&D Program (2013BAC14B05).

References

- [1] M. Ahmaruzzaman, "A review on the utilization of fly ash," *Progress in Energy and Combustion Science*, vol. 36, no. 3, pp. 327–363, 2010.
- [2] P. Brown, T. Jones, and K. Bérubé, "The internal microstructure and fibrous mineralogy of fly ash from coal-burning power stations," *Environmental Pollution*, vol. 159, no. 12, pp. 3324–3333, 2011.
- [3] J. Kugbe, N. Matsue, and T. Henmi, "Synthesis of Linde type A zeolite-goethite nanocomposite as an adsorbent for cationic and anionic pollutants," *Journal of Hazardous Materials*, vol. 164, no. 2-3, pp. 929–935, 2009.
- [4] K. S. Hui, C. Y. H. Chao, and S. C. Kot, "Removal of mixed heavy metal ions in wastewater by zeolite 4A and residual products from recycled coal fly ash," *Journal of Hazardous Materials*, vol. 127, no. 1-3, pp. 89–101, 2005.
- [5] H. Höller and U. Wirsching, "Zeolites formation from fly ash," *Fortschr Mineral*, vol. 63, pp. 21–43, 1985.
- [6] R. S. Blissett and N. A. Rowson, "A review of the multi-component utilisation of coal fly ash," *Fuel*, vol. 97, pp. 1–23, 2012.
- [7] C.-F. Wang, J.-S. Li, L.-J. Wang, and X.-Y. Sun, "Influence of NaOH concentrations on synthesis of pure-form zeolite A from fly ash using two-stage method," *Journal of Hazardous Materials*, vol. 155, no. 1-2, pp. 58–64, 2008.
- [8] G. G. Hollman, G. Steenbruggen, and M. Janssen-Jurkovičová, "Two-step process for the synthesis of zeolites from coal fly ash," *Fuel*, vol. 78, no. 10, pp. 1225–1230, 1999.
- [9] H. Tanaka and A. Fujii, "Effect of stirring on the dissolution of coal fly ash and synthesis of pure-form Na-A and -X zeolites by two-step process," *Advanced Powder Technology*, vol. 20, no. 5, pp. 473–479, 2009.
- [10] N. Shigemoto, S. Sugiyama, H. Hayashi, and K. Miyaura, "Characterization of Na-X, Na-A, and coal fly ash zeolites and their amorphous precursors by IR, MAS NMR and XPS," *Journal of Materials Science*, vol. 30, no. 22, pp. 5777–5783, 1995.
- [11] Y. Yaping, Z. Xiaoqiang, Q. Weilan, and W. Mingwen, "Synthesis of pure zeolites from supersaturated silicon and aluminum alkali extracts from fused coal fly ash," *Fuel*, vol. 87, no. 10-11, pp. 1880–1886, 2008.
- [12] L. Bieseki, F. G. Penha, and S. B. C. Pergher, "Zeolite a synthesis employing a brazilian coal ash as the silicon and aluminum source and its applications in adsorption and pigment formulation," *Materials Research*, vol. 16, no. 1, pp. 38–43, 2013.
- [13] X. Querol, N. Moreno, J. C. Umaña et al., "Synthesis of zeolites from coal fly ash: an overview," *International Journal of Coal Geology*, vol. 50, no. 1-4, pp. 413–423, 2002.
- [14] R. Juan, S. Hernández, X. Querol, J. M. Andrés, and N. Moreno, "Zeolitic material synthesised from fly ash: use as cationic exchanger," *Journal of Chemical Technology and Biotechnology*, vol. 77, no. 3, pp. 299–304, 2002.
- [15] S. Babel and T. A. Kurniawan, "Low-cost adsorbents for heavy metals uptake from contaminated water: a review," *Journal of Hazardous Materials*, vol. 97, no. 1-3, pp. 219–243, 2003.

- [16] V. K. Jha, M. Matsuda, and M. Miyake, "Sorption properties of the activated carbon-zeolite composite prepared from coal fly ash for Ni^{2+} , Cu^{2+} , Cd^{2+} and Pb^{2+} ," *Journal of Hazardous Materials*, vol. 160, no. 1, pp. 148–153, 2008.
- [17] R. Apiratikul and P. Pavasant, "Sorption of Cu^{2+} , Cd^{2+} , and Pb^{2+} using modified zeolite from coal fly ash," *Chemical Engineering Journal*, vol. 144, no. 2, pp. 245–258, 2008.
- [18] X. J. Chen, *Research on the modified methods of fly ash for ammonia-nitrogen wastewater treatment [M.S. thesis]*, Shanxi University, 2011 (Chinese).
- [19] A. Molina and C. Poole, "A comparative study using two methods to produce zeolites from fly ash," *Minerals Engineering*, vol. 17, no. 2, pp. 167–173, 2004.
- [20] R. R. Xu, W. Q. Pang, and J. H. Yu, *Chemistry—Zeolites and Porous Materials*, Science press, Beijing, China, 2004 (Chinese).
- [21] H. Tanaka, H. Eguchi, S. Fujimoto, and R. Hino, "Two-step process for synthesis of a single phase Na-A zeolite from coal fly ash by dialysis," *Fuel*, vol. 85, no. 10-11, pp. 1329–1334, 2006.
- [22] Z. H. Wei, L. S. Jin, and W. X. Cao, "The optimum transport process of synthesis of 4(A)-zeolite with coal fly ash," *China Resources Comprehensive Utilization*, vol. 25, pp. 9–12, 2007 (Chinese).